

Sheffield Hallam University

The microstructure and properties of unbalanced magnetron sputtered CrN[x] coatings.

HURKMANS, Antonius Petrus Arnoldus.

Available from the Sheffield Hallam University Research Archive (SHURA) at:

<http://shura.shu.ac.uk/19846/>

A Sheffield Hallam University thesis

This thesis is protected by copyright which belongs to the author.

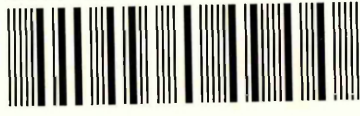
The content must not be changed in any way or sold commercially in any format or medium without the formal permission of the author.

When referring to this work, full bibliographic details including the author, title, awarding institution and date of the thesis must be given.

Please visit <http://shura.shu.ac.uk/19846/> and <http://shura.shu.ac.uk/information.html> for further details about copyright and re-use permissions.

CITY CAMPUS, HOWARD STREET
SHEFFIELD S1 1WB

101 698 954 7



REFERENCE

ProQuest Number: 10697152

All rights reserved

INFORMATION TO ALL USERS

The quality of this reproduction is dependent upon the quality of the copy submitted.

In the unlikely event that the author did not send a complete manuscript and there are missing pages, these will be noted. Also, if material had to be removed, a note will indicate the deletion.



ProQuest 10697152

Published by ProQuest LLC (2017). Copyright of the Dissertation is held by the Author.

All rights reserved.

This work is protected against unauthorized copying under Title 17, United States Code
Microform Edition © ProQuest LLC.

ProQuest LLC.
789 East Eisenhower Parkway
P.O. Box 1346
Ann Arbor, MI 48106 – 1346

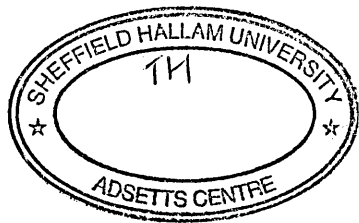
THE MICROSTRUCTURE AND PROPERTIES
OF UNBALANCED MAGNETRON SPUTTERED
CrN_x COATINGS

Antonius Petrus Arnoldus Hurkmans

A thesis submitted in partial fulfilment of the
requirements of Sheffield Hallam University for
the degree of Doctor of Philosophy

March 2002

Collaborating organisation:
Hauzer Techno Coating B.V.



Abstract

The most widely used surface treatment to protect engineering components is the deposition of hard chromium by electroplating. The coatings are known to be quite thick (up to 20 μm), reasonably hard ($\sim\text{HV}1000$), but contain micro-cracks. This wet deposition process is well understood, but it has technical limitations and is under high political pressure because of the environmental pollution by hexavalent chromium. The physical vapour deposition (PVD) technique is an alternative method to produce high quality coatings. PVD is an almost pollution free technique, because the process occurs under vacuum. CrN by PVD is one of the most promising PVD coatings as a candidate to replace eventually electroplated hard chromium. The growth characteristics of CrN coatings are less understood than those of TiN, the well-known PVD coating material. This thesis anticipates to fill this technological gap. Along a wide range of experiments based on the deposition of CrN_x coatings, XRD, SEM, SNMS and tribological analysis have been used to complete a thorough understanding of CrN_x growth.

The experiments show that there exist several different phases within the Cr-N system: bcc-Cr, hcp- Cr_2N , fcc-CrN, and mixed phases. This is not fundamentally new, but the work has resulted in two new modifications, which are highly interesting candidates for the industry, including electroplating replacements, namely high nitrogen containing metallic bcc-Cr (solid solution with up to 18 at.% nitrogen) in the hardness range up to HV1800 and a very hard fcc-CrN phase with hardness values between HV1500 and HV3000, similar to TiN.

The solid solution bcc-Cr-N is very dense fine-grained, reasonably hard (almost twice as hard as electroplated hard chromium), very smooth, and with a Young's modulus very similar to that of (hardened) steel. The hard fcc-CrN phase (approximately three times harder than electroplated hard chromium) could only be obtained by the current experiments in a rather non-conventional magnetron sputtering parameter window: a combination of a high substrate bias voltage (> -200 V) and a high partial pressure of nitrogen (a multitude of the argon partial pressure). This phase shows a strong {100} preferred crystallographic orientation and shows an excellent behaviour against corrosion and wear.

Acknowledgements

The author would like to sincerely thank the following persons and companies:

- Professor Dieter Münz for his highly knowledgeable input in this thesis, but also for making me familiar with several cultural parts of life.
- Dr. Brian Lewis for his dedication and excellent support as my supervisor.
- All employees and students of Bodycote/SHU and the MRI who have helped me in whatever way. The XTEM evaluations by Dr. Quanshun Luo and the wear and corrosion data by Dr. Papken Hovsepian were of great importance.
- Hauzer Techno Coating B.V. and all the employees that helped me in a direct or indirect way. Dr. Gerrit-Jan van der Kolk is especially mentioned for his support and encouragement throughout. Mr. Wim van Ijzendoorn's contribution in sample preparation and evaluation of mechanical coating properties was highly appreciated.
- Dr. Jiri Vyskocil and his co-workers from HVM-Plasma.
- Mr. Frans Hauzer for his support to start this part-time PhD. He is the person who realised the dream of PVD hard coatings from Venlo.
- Dr. Hamid Kheyrandish and Dr. Simon Romani for their SNMS contributions.
- My wife Janny and our children Lotte, Pim, and Wies for the sacrifices made and their unlimited support.

Dedicated to:

My parents / mijn ouders:

Grad & Pieta Hurkmans

“Get the maximum out of yourself”

Advanced Studies

During the course of the studies, the following conferences were attended:

- ICMCTF-1996, April 1996, San Diego, CA, USA
- SVC-1996, May 1996, Philadelphia, PA, USA
- 2nd ABS-days, July 1996, Sheffield, UK
- PSE, September 1996, Garmisch-Partenkirchen, Germany
- SVC-1997, April 1997, New Orleans, LA, USA
- ICMCTF-1997, April 1997, San Diego, CA, USA
- ICMCTF-1998, April 1998, San Diego, CA, USA
- ICMCTF-1999, April 1999, San Diego, CA, USA
- 5th ABS-days, July 1999, Sheffield, UK
- ICMCTF-2000, April 2000, San Diego, CA, USA
- SVC-2000, April 2000, Denver, CO, USA
- AESF/Surfin, June 2000, Chicago, IL, USA
- AVS, October 2000, Boston, MA, USA
- Gorham, November 2000, Atlanta, GA, USA
- ASME-ME, November 2000, Orlando, FL, USA
- SVC-2001, April 2001, Philadelphia, PA, USA
- ICMCTF-2001, May 2001, San Diego, CA, USA
- Gorham, May 2001, Atlanta, GA, USA
- AESF/Surfin, June 2001, Nashville, TN, USA
- AVS, October 2001, San Francisco, CA, USA
- MRS, November 2001, Boston, MA, USA

For Hauzer Techno Coating B.V. there was also strong involvement in the following BRITE-EURAM projects:

- “Steered arc ion plating for the development of new ternary and quaternary ceramic coatings for cutting and forming tools”
RIIB-0201-C (AM)
- “Advanced super-finish wire-EDM and coating technologies for improved tool production”
BE 4117-90/CT91-0461; “WECAT”
- “Development of industrial low temperature PVD technique of cubic Boron Nitride for long lifetime products”
BRE 2-CT92-0292/BE 5745; “LTcBN”
- “Environmentally friendly and hardness enhanced PVD CrN/TaN superlattice coatings, a novel alternative to plated hard chrome”
BE 96-3305/BR PR-CT96-00329; “NEWCHROME”
- “Developing less pollutant cutting technologies”
BR PR-CT95-0107; “LEPOCUT”

Involvement in the Society of Vacuum Coaters (SVC):

- 2001-conference: Assistant chair of TAC “Decorative and Functional Coatings”
- 2002-conference: Chair of TAC “Decorative and Functional Coatings”

Publications

An all-round performer in the physical vapour deposition laboratory
W.-D. Münz, K. Vannisselroy, R. Tietema, T. Hurkmans, G. Keiren
Surface and coatings technology, 58, 1993, 205-212

Multilayered Titanium Tungsten Nitride Coatings with a Superlattice Structure
Grown by Unbalanced Magnetron Sputtering.
T. Hurkmans, T. Trinh, D.B. Lewis, J.S. Brooks, W.-D. Münz
Surface and coatings technology, 76-77, 1995, 159-166

Comparison of TiAlN coatings grown by unbalanced magnetron and arc bond
sputtering techniques
W.-D. Münz, T. Hurkmans, G. Keiren, T. Trinh
Journal of Vac. Sci & Techn. A, Vol.11, no. 5, Sept/Oct 1993, 2583-2589

Defects in TiN and TiAlN coatings grown by combined cathodic arc / unbalanced
magnetron technology
W.-D. Münz, D.B. Lewis, S. Creasey, T. Hurkmans, T. Trinh, W. v. Ijzendoorn
Vacuum, vol. 46, no. 4, 1994, 323-330

Formation of high temperature phases in sputter deposited Ti-based films below
100 °C
J. Musil, A.J. Bell, J. Vlcek, T. Hurkmans
J. Vac. Sci. Technol. A 14(4), Jul/Aug 1996

Ion-assisted growth of $Ti_{1-x}Al_xN$ / $Ti_{1-y}Nb_yN$ multilayers by combined cathodic arc /
magnetron sputter deposition
I. Petrov, P. Losbichler, D. Bergstrom, J.E. Greene, W.-D. Münz, T. Hurkmans, T.
Trinh
Thin Solid Films, 302, 1997, 179-192

Large-scale fabrication of hard superlattice thin films by combined steered arc
evaporation and unbalanced magnetron sputtering
L.A. Donohue, W.-D. Münz, D. B. Lewis, J. Cawley, T. Hurkmans, T. Trinh, I. Petrov,
J.E. Greene
Surface and coatings techn. 93, 1997, 69-87

Wear and corrosion resistant decorative hard coatings in large volume PVD units
T. Hurkmans, D. Bass
39th Annual Technical Conference Proceedings SVC, 1996, 91-96

Properties of metal containing carbon (Me-C:H) films
G.J. van der Kolk, T. Hurkmans, T. Trinh, W. Fleischer
40th Annual Technical Conference Proceedings SVC, 1997, 94-97

PVD coating on engine parts for energy efficient vehicles
W. Fleischer, T. Hurkmans
ISATA Proceedings, Florence, Italy, 1996

Physical vapour deposited films in the automotive industry
T. Hurkmans, W. Fleischer
ISATA Proceedings, Florence, Italy, 1996

A new large volume PVD coating system using advanced controlled arc and combined arc / unbalanced magnetron (ABSTM) deposition techniques
T. Hurkmans, F. Hauzer, B. Buil, K. Engel, R. Tietema
Surface and coatings techn. 92, 1997, 62-68

Chromium nitride coatings grown by unbalanced magnetron (UBM) and combined arc / unbalanced magnetron (ABSTM) deposition techniques
T. Hurkmans, D. B. Lewis, J. S. Brooks, W.-D. Münz
Surface and coatings techn. 86-87, 1996, 192-199

High performance Me-C:H coating for precision components
K. Bewilogua, M. Grischke, J. Schröder, T. Michler, G.J. van der Kolk, T. Trinh, T. Hurkmans, W. Fleischer
41st Annual Technical Conference Proceedings SVC, 1998, 75-79

Decorative PVD hard coatings in a wide colour range on different substrate materials
W. Fleischer, T. Trinh, G.J. van der Kolk, T. Hurkmans, M. Franck
41st Annual Technical Conference Proceedings SVC, 1998, 33-37

Coating evaluations of decorative PVD finishes
G.J. van der Kolk, T. Hurkmans, T. Trinh, W. Fleischer, M. Griepentrog, U. Beck
41st Annual Technical Conference Proceedings SVC, 1998, 44-50

PVD coatings for dry cutting of Al-alloy and bronze
W. Fleischer, M. Franck, G.J. van der Kolk, T. Trinh, T. Hurkmans, F. Klocke, G. Eisenblätter, W. Hockauf, C. Sanz
41st Annual Technical Conference Proceedings SVC, 1998, 80-88

Influence of ion bombardment on structure and properties of unbalanced magnetron grown CrN_x coatings
T. Hurkmans, D.B. Lewis, H. Paritong, J.S. Brooks, W.-D. Münz
Surface and Coatings Technology, 114, 1999, 52-59

Setting up mass production of decorative coatings on consumer goods
T. Hurkmans, G.J. van der Kolk, M. Eerden, T. Trinh, W. Fleischer
42nd Annual Technical Conference Proceedings SVC, 1999, 58-63

The next generation of deposition equipment for wear protection coatings
E. Bergmann, B. Buil, T. Hurkmans, G.J. van der Kolk
Surface and Coatings Technology, 114, 1999, 101-10

Perspective for replacement of hard chrome by PVD
T. Hurkmans, J. Kubinski, T. Trinh, W. Fleischer, G.J. van der Kolk
42nd Annual Technical Conference Proceedings SVC, 1999, 364-367

PVD coatings voor tribologische toepassingen
G.J. van der Kolk, T. Hurkmans, T. Trinh, K. Bewilogua, T. Eckardt
NEVACBLAD, Jaargang 37, 1999, Nr. 1, 11-15

Improving tribological properties of sputtered boron carbide coatings by process modifications
T. Eckardt, K. Bewilogua, G.J. van der Kolk, T. Hurkmans, T. Trinh, W. Fleischer
Surface and coatings Technology, 126, 2000, 69-75

Surface oxidation on decorative hard coatings with enriched carbon content
W. Fleischer, T. Trinh, G.J. van der Kolk, T. Hurkmans, P. Willich
43rd Annual Technical Conference Proceedings SVC, 2000, 46-51

PVD coatings for cutting tools under minimum lubrications conditions
G.J. van der Kolk, W. Fleischer, T. Hurkmans, Y. Stockmann
Ipsen on top, Issue no. 1, 2001

Hard coatings – past, present, and future
W. Fleischer, G.J. van der Kolk, A. Hurkmans, T. Trinh, B. Buil
44th Annual Technical Conference Proceedings SVC, 2001, 39-45

Mechanical and tribological properties of metal containing diamond-like coatings (Me-DLC) deposited under different plasma confinement conditions
C. Strondl, G.J. van der Kolk, T. Hurkmans, W. Fleischer, N. Carvalho, J. de Hosson
44th Annual Technical Conference Proceedings SVC, 2001, 67-71

Properties and characterization of multilayers of carbides and diamond like carbon
C. Strondl, G.J. van der Kolk, T. Hurkmans, W. Fleischer, T. Trinh, N. Carvalho, J. de Hosson
Surface and coatings Technology, 142-144, 2001, 707-713

Presentations

New applications of TiAlN coatings grown by combined cathodic arc / unbalanced magnetron PVD deposition in tooling

W.-D. Münz, D.B. Lewis, W. Fleischer, T. Hurkmans, T. Trinh
Oral presentation, PSE, 1994, Garmisch-Partenkirchen, Germany

Ta and TaN_x coatings grown by unbalanced magnetron sputtering

T. Hurkmans, D.B. Lewis, J.S. Brooks, W.-D. Münz
Poster presentation, PSE, 1996, Garmisch-Partenkirchen, Germany

PVD hard coatings for high speed dry cutting of hard materials

W. Fleischer, M. Franck, G.J. van der Kolk, T. Hurkmans
Oral presentation, ICMCTF-1998, April 1998, San Diego, CA, USA

PVD coatings with multilayer and mixed layer structures on cutting- and forming tools in dry or MQL operations

W. Fleischer, T. Trinh, G.J. van der Kolk, T. Hurkmans, E. Pflüger, A. Savan
Poster presentation, ICMCTF-1998, April 1998, San Diego, CA, USA

Properties of boron containing and tungsten containing diamond like carbon films

G.J. van der Kolk, T. Hurkmans, C. Strondl, W. Fleischer, T. Eckardt, K. Bewilogua
Poster presentation, Diamond, 1999, Prague, Czech Republic.

Engineered properties of decorative coatings by combined arc evaporation and unbalanced magnetron sputtering

T. Hurkmans, M. Eerden, G.J. van der Kolk, W. Fleischer
Oral presentation, ICMCTF-2000, 2000, San Diego, CA, USA

Effect of composition modulation on the tribological performance of metal containing diamond like carbon

C. Strondl, G.J. van der Kolk, T. Hurkmans, T. Trinh, W. Fleischer
Oral presentation, ICMCTF-2000, April 2000, San Diego, CA, USA

Unbalanced magnetron sputter deposited CrN coatings with enhanced hardness properties

T. Hurkmans, W. van Ijzendoorn, D.B. Lewis, H. Paritong, P. Hovsepian, W.-D. Münz
Oral presentation, ICMCTF-2000, 2000, San Diego, CA, USA

Industrial applications of tribological PVD coatings

T. Hurkmans, G.J. van der Kolk, C. Strondl
Oral presentation, ASME-ME, 2000, Orlando, FL, USA

Application of PVD coatings on the surface of plastic injection moulds to increase productivity and product quality

W. Fleischer, G.J. van der Kolk, T. Hurkmans, C. Strondl, B. Buil, N. Baranski, T. Eulenstein, U. Hinzpeter

Oral presentation, ICMCTF-2001, May 2001, San Diego, CA, USA

Influence of different plasma confinement conditions on mechanical and tribological properties for deposition of Me-DLC coatings
C. Strondl, G.J. van der Kolk, T. Hurkmans, W. Fleischer, N. Carvalho, J. de Hosson
Oral presentation, ICMCTF-2001, May 2001, San Diego, CA, USA

The effect of deposition conditions on the properties of W-DLC coatings
C. Strondl, T. Hurkmans, R. Dielis, G.J. van der Kolk
Oral presentation, MRS-fall, 2001, Boston, MA, USA

Patents

PVD-verfahren zur abscheidung von mehrkomponentigen hartstoffschichten
W.-D. Münz, T. Trinh, A. Hurkmans
21.02.94 DE 4405477

Bauteil mit verschleißschutzschicht und verfahren zu dessen herstellung
W. Fleischer, A. Hurkmans
12.04.96 DE 19614557

Mehrlagenschicht und Verfahren zu deren Herstellung
T. Trinh, G.J. van der Kolk, A. Hurkmans
20.07.98 DE 19832571 A1

Low friction carbon-carbide multilayer PVD coatings
C. Strondl, G.J. van der Kolk, A. Hurkmans
Application submitted

Verfahren zur herstellung eines Gegenstandes und Gegenstand
G.J. van der Kolk, A. Hurkmans, C. Strondl
09.02.00 DE 10005612

Substrat mit einer Chrom-Nitrid-Schicht
A. Hurkmans, G.J. van der Kolk, D.B. Lewis, W.-D. Münz
Application no. 00122894.9-2119/EP1098014A1

Method of applying a coating by physical vapour deposition
A. Hurkmans, M. Eerden, G.J. van der Kolk, D. Hall, G. Hein, W. McCarthy
13.01.00 GB 0000638
13.01.00 GB 0000635

PVD process for manufacturing a colored coating insensitive to fingerprints on
articles and articles having such a coating
M. Eerden, A. Hurkmans, G.J. van der Kolk
14.01.00 DE 10001381

Contents

Page

Chapter 1 – Introduction

1

1.1. Surface modification

1.2. Thin film deposition by PVD

1.3. Why CrN by PVD?

Chapter 2 – Literature Review: Chromium (Cr) and chromiumnitride (CrN_x) deposited by PVD

14

2.1. Cr and CrN_x standards

2.2. CrN_x by different PVD methods

2.3. CrN_x by sputtering

2.3.1. bcc-Cr by sputtering

2.3.2. hcp-Cr₂N by sputtering

2.3.3. fcc-CrN by sputtering

2.4. CrN_x by cathodic arc evaporation

2.4.1. bcc-Cr by cathodic arc evaporation

2.4.2. hcp-Cr₂N by cathodic arc evaporation

2.4.3. fcc-CrN by cathodic arc evaporation

Chapter 3 – Experimental

30

3.1. PVD deposition

3.1.1. HTC-625 deposition equipment

3.1.2. Targets

3.1.3. Sample preparation prior to PVD

3.1.3.1. Substrates

3.1.3.2. Chemical cleaning of substrates

3.1.4. PVD process sequence

3.1.5. Deposition rate estimation for Cr

3.2. Characterisation techniques

- 3.2.1. X-Ray diffraction (XRD)
 - 3.2.1.1. Bragg-Brentano
 - 3.2.1.2. Glancing angle parallel beam geometry
- 3.2.2. Scanning electron microscopy (SEM)
- 3.2.3. Transmission electron microscopy (TEM)
- 3.2.4. Sputtered neutral mass spectrometry (SNMS)
- 3.2.5. Hardness measurement
- 3.2.6. Scratchtest
- 3.2.7. Rockwell indentation test
- 3.2.8. Ball-cratering thickness test
- 3.2.9. Surface roughness profiling
- 3.2.10. Stess measurement by the deflection method
- 3.2.11. Pin-on-disc
- 3.2.12. Corrosion testing
- 3.2.13. Colourimetry

Chapter 4 – Results

52

- 4.1. Influence of nitrogen flow rate on unbalanced magnetron sputtered CrN_x
 - 4.1.1. Overview of the experiments
 - 4.1.2. Influence of the nitrogen flow rate on the deposition parameters
 - 4.1.3. X-Ray diffraction (Bragg Brentano high angle scan)
 - 4.1.3.1. Phase development
 - 4.1.3.2. Texture
 - 4.1.3.3. Interplanar spacing and peak broadening
 - 4.1.4. SEM cross sections
 - 4.1.5. Cross section TEM
 - 4.1.6. Composition
 - 4.1.7. Hardness and Young's modulus
 - 4.1.8. Residual stress
 - 4.1.9. Surface roughness
 - 4.1.10. Colour
- 4.2. Influence of substrate bias voltage on unbalanced magnetron sputtered CrN_x
 - 4.2.1. Overview of the experiments

4.2.2. Influence of the substrate bias voltage on the deposition parameters

4.2.3. X-Ray diffraction (Bragg Brentano high angle scan)

4.2.3.1. Phase development

4.2.3.2. Texture

4.2.3.3. Interplanar spacing and peak broadening

4.2.4. SEM cross sections

4.2.5. Cross section TEM

4.2.6. Composition

4.2.7. Hardness and Young's modulus

4.2.8. Residual stress

4.2.9. Surface roughness

4.2.10. Colour

4.3. Influence of the substrate bias current density on unbalanced magnetron sputtered CrN_x

4.3.1. Overview of the experiments

4.3.2. Influence of the substrate bias current density on the deposition parameters

4.3.3. X-Ray diffraction (Bragg Brentano high angle scan)

4.3.3.1. Phase development

4.3.3.2. Texture

4.3.3.3. Interplanar spacing and peak broadening

4.3.4. SEM cross sections

4.3.5. Composition

4.3.6. Hardness and Young's modulus

4.3.7. Residual stress

4.3.8. Surface roughness

4.3.9. Colour

4.3.10. Adhesion

4.4. Influence of type of ion etching on unbalanced magnetron sputtered CrN_x

4.4.1. Overview of the experiments

4.4.2. X-Ray diffraction (Bragg Brentano high angle scan)

4.4.2.1. Phase development

4.4.2.2. Texture

4.4.2.3. Interplanar spacing and peak broadening

4.4.3. SEM cross sections

4.4.4. Kalotest

4.4.5. Hardness

4.4.6. Surface roughness

4.4.7. Adhesion

4.5. Engineered properties of hard sputtered CrN_x

4.5.1. Overview of the experiments

4.5.2. Film properties

4.5.3. Corrosion properties of unbalanced magnetron sputtered CrN_x coatings

4.5.4. Pin-on-disc and wear results of CrN_x coatings

Chapter 5 – Discussion **145**

5.1. (expanded) bcc-Cr

5.2. hcp-Cr₂N

5.3. fcc-CrN

Chapter 6 – Conclusions **152**

References **154**

Appendix **161**

An all-round performer in the physical vapour deposition laboratory

W.-D. Münz, K. Vannisselroy, R. Tietema, T. Hurkmans, G. Keiren

Surface and coatings techn. 58, 1993, 205-212

Multilayered Titanium Tungsten Nitride Coatings with a Superlattice Structure

Grown by Unbalanced Magnetron Sputtering.

T. Hurkmans, T. Trinh, D.B. Lewis, J.S. Brooks, W.-D. Münz

Surface and coatings techn. 76-77, 1995, 159-166

Comparison of TiAlN coatings grown by unbalanced magnetron and arc bond sputtering techniques

W.-D. Münz, T. Hurkmans, G. Keiren, T. Trinh

Journal of Vac. Sci & Techn. A, Vol.11, no. 5, Sept/Oct 1993, 2583-2589

Defects in TiN and TiAlN coatings grown by combined cathodic arc / unbalanced magnetron technology

W.-D. Münz, D.B. Lewis, S. Creasey, T. Hurkmans, T. Trinh, W. v. Ijzendoorn

Vacuüm, vol. 46, no. 4, 1994, 323-330

Ion-assisted growth of $Ti_{1-x}Al_xN$ / $Ti_{1-y}Nb_yN$ multilayers by combined cathodic arc / magnetron sputter deposition

I. Petrov, P. Losbichler, D. Bergstrom, J.E. Greene, W.-D. Münz, T. Hurkmans, T. Trinh

Thin Solid Films, 302, 1997, 179-192

Chromium nitride coatings grown by unbalanced magnetron (UBM) and combined arc / unbalanced magnetron (ABSTM) deposition techniques

T. Hurkmans, D. B. Lewis, J. S. Brooks, W.-D. Münz

Surface and coatings techn. 86-87, 1996, 192-199

Influence of ion bombardment on structure and properties of unbalanced magnetron grown CrN_x coatings

T. Hurkmans, D.B. Lewis, H. Paritong, J.S. Brooks, W.-D. Münz

Surface and Coatings Techn. 114, 1999, 52-59

Perspective for replacement of hard chrome by PVD

T. Hurkmans, J. Kubinski, T. Trinh, W. Fleischer, G.J. van der Kolk

42nd Annual Technical Conference Proceedings, 1999, 364-367

Substrat mit einer Chrom-Nitrid-Schicht

A. Hurkmans, G.J. van der Kolk, D.B. Lewis, W.-D. Münz

Application no. 00122894.9-2119/EP1098014A1

Chapter 1 - Introduction

1.1. Surface modification

In many practical circumstances it is desirable to have engineered products with surface properties which are different from bulk material properties. There are several technologies available to treat material in order to modify the surface. A classification is presented in table 1.1. There are basically four groups: 1) removing material, 2) changing the structure of the top surface, 3) bringing material into the surface, and 4) adding material on top of the surface. Combinations are also being used today.

Coatings ("adding material on top")	Hard Facing	Thermal Spray	Flame; Spray & Fuse; Plasma Arc; Low pressure Plasma; Detonation Gun; Electric Arc
		Welding	Flame; Electric Arc; Plasma Arc
		Cladding	Deformation; Diffusion; Brazing; Welding; Laser
	Vapour Deposition	Physical Vapour	Evaporation; Ion Plating; Sputtering
		Chemical Vapour	CVD
		Physical-Chemical Vapour	Plasma-Enhanced CVD; Reactive Pulsed Plasma; Chemical Vapour Polymerisation
	Miscellaneous Techniques		Atomised liquid spray; Dip; Fluidised-Bed; Spin-on; Sol-gel; Screening & Lithography; Electrochemical; Chemical conversion; Intermetallic compound; Spark Hardening
Treatments	Micro-structural ("structure change")	Thermal	Induction; Flame; Laser; Electron Beam; Chill Casting; Work Hardening
		Mechanical	Cold working
	Chemical ("Adding material into surface")	Diffusion	Carburising; Carbonitriding; Nitriding; Nitrocarburising; Boriding; Chromising; Aluminising; Siliconising; Sherardising
		Implantation	Ion Implantation; Ion Beam Mixing

Table 1.1. Classification of various coating deposition and surface treatment techniques [1].

Within this thesis Physical Vapour Deposition technology (PVD) has been used in order to add material on top of the surface. Additionally a special type of low energy ion implantation was employed to create a modification of the surface prior to deposition to improve adhesion [2].

The PVD technology is very suitable for creating engineered films. In general the engineering concentrates on four areas, 1) surface modification in the substrate, 2) the interface microchemistry between substrate and coating, 3) the microstructure and composition of the coating, and 4) the surface of the coating (morphology and roughness). For coating to substrate adhesion the surface modification and interface play a dominant role. Prior to deposition, chemical cleaning ion bombardment are the usual pre-treatment steps. The application of the coating gives the desired property changes of the product. It can be deposited as either a single layer or in a multi-layer geometry. In the multi-layer configuration it is for example possible to design coatings with high hardness and a high ductility [3,4,5,6,7,8]. When the thickness of the individual layers within the multi-layer stack is in the range of the lattice dimensions, the material is considered to be a "superlattice". Material properties of the superlattice are different from the material properties of the individual layers [9,10,11,12,13,14]. Hardness values up to half of that of diamond has been observed. The properties of the surface of the coating can be engineered in such a way that the coating shows negligible interaction with the counter face materials. Chemical stability between the coating and counter face material is of prime importance in surface engineering applications. Examples of various modes of interactions are observed, e.g. on differently coated cutting tools (TiN, TiCN, TiAlN) or as anti-wear coatings (W-C:H and MoS₂). A special example of surface modification of the coating is on TiAlN coated cutting tools where an Al₂O₃ top coating is formed with low chemical interaction to steel and a high oxidation resistance [15]. The layer is a result of high temperature oxidation at the cutting edge [16,17].

1.2. Thin film deposition by PVD

The PVD process can be split in two main steps [18]:

- 1) Substrate cleaning by ion bombardment (“etching”)
- 2) Deposition, with the following phenomena:
 - 2.1) Generation of the vapour flux from source materials (targets)
 - 2.2) Transport through plasma
 - 2.3) Condensation

Substrate cleaning:

In most PVD processes chemical substrate cleaning is used to remove dirt from the surfaces. Typically the majority of hydrocarbon contamination (oil and greases) is removed in chemical cleaning lines supported by ultrasonic means. Special care has to be taken because a variety of substrate surfaces lose their protection against oxidation. The thin native oxides have to be removed prior to any film growth in order to achieve sufficient coating to substrate adhesion. Bombarding the substrate surface in vacuo with accelerated ions removes these oxides within the PVD etching cycle.

Deposition:

After the cleaning step the deposition of the coating is initiated. The source material is delivered by the target material, which can be vaporised in two fundamentally different ways; thermal evaporation or sputtering. Resistance heating, cathodic arc, electron beam, and laser beam are the most widely used tools to deliver the required energy for thermal evaporation. Sputtering, particularly magnetron sputtering, is the other important vaporisation method. Magnetron sputtering, cathodic arc and electron beam evaporation are the main techniques used for coating cutting and forming tools. Evaporation by laser beams [19,20] is for example investigated for the deposition of carbon based tribological films.

In the experiments described in this thesis, the cathodic arc evaporation technique is only used for the generation of Cr and Ta ions. In a pre-treatment step the energy of such metallic ions has to be of such high values that ion implantation occurs as utilised in the Arc Bond Sputtering (ABS) technology [21,2]. The main drawback of coating by cathodic arc evaporation is the generation of target material clusters, so called droplets or macro-particles. Because of their size, in range of micrometers, the droplets increase surface roughness and lead to a non-uniform elemental distribution

in the growing coatings either by their own dimensions or as nucleation sites which form growth defects of even larger dimensions than the droplets themselves [22]. Magnetic filtering is possible in order to reduce the number and size of the droplets arriving on the surface [23]. In order to minimise the generation of macro-particles the velocity of the arc spot can be increased (steered arc) [24] or the partial pressure of any present reactive gas (for example nitrogen or oxygen) can be increased.

Vaporising target materials by sputtering is possible by energetic bombardment of the target surface with ions or neutral species. The energy required for release of atoms from the surface is achieved by energy (momentum) transfer from bombarding atoms to near surface atoms resulting in atoms being ejected from the target. In practice glow discharges and ion beams are used to sputter the target. Within this work an argon DC glow discharge has been used between a Cr target (cathode potential) and the vacuum chamber wall (anode potential). In a low-pressure gas atmosphere there are several different plasma regions between the cathode and the anode, figure 1.1. There are three main areas: cathode glow region, cathode dark space, and the negative glow region.

The luminous glow region adjacent to the cathode surface is called the cathode glow region. In this area the incoming gas ions and the cathode ions are neutralised. The emitted light is characteristic for the target material and the sputtering gas. In the cathode glow area the secondary target electrons begin to accelerate away from the cathode. Next to the cathode glow area is the cathode dark space ("sheath"). In this area most of the plasma voltage is dropped and provides the accelerating force for the positive ions to move to the target surface. The positive net space charging in this area is a result of the slow moving ions, compared to the fast moving electrons. The bombardment of the target surface by the sputtering ions results in heat generation, removal of neutrals, removal of ions and secondary electron emission. These secondary electrons are accelerated to the negative glow region, resulting in ionisation of the sputtering gas. Typically there is an ionisation yield of 10 to 20 ions per electron, resulting in a self-sustaining discharge. The Faraday dark space and the positive column are essentially connecting electrically the negative glow to the anode and they are not essentially in the sputtering process.

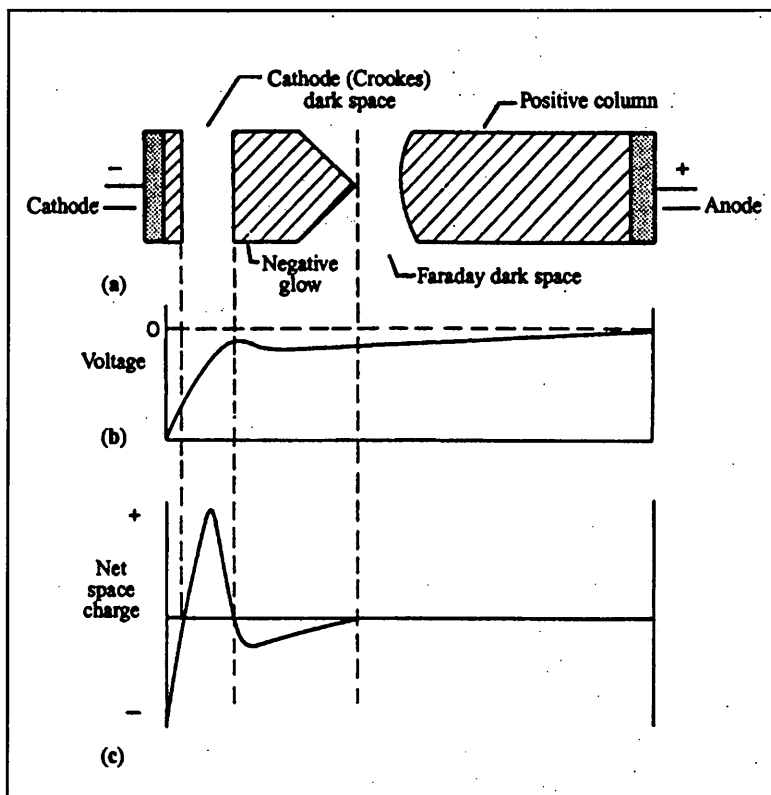


Figure 1.1. Schematic of a DC diode glow discharge. a) plasma regions, b) Voltage characteristics, and c) net space charges [25].

The current-voltage characteristic of the glow discharge is plotted in figure 1.2. With increasing voltage applied voltage between two electrodes the natural available electrons will generate more ions and secondary electrons, because the kinetic energy (as a result of the acceleration voltage) reaches the level of the ionisation energy of the gas species. In the Townsend discharge more charge is created and herewith the current increases. The bombarding ions generate secondary electrons, which generate again more ions and so on. In a self-sustaining discharge the number of electrons generated at the target surface is just enough to produce sufficient ions to regenerate again the same amount of electrons. Then the glow discharge is called a normal glow discharge and is characterised by a drop in voltage and a rise in current. Further increase of the power results in an increased uniformity of the plasma over the cathode surface. After full coverage of the cathode surface, further power increase results in increased voltage and current. This area is called

“abnormal glow discharge”. This is the typical area of operation in sputter deposition techniques.

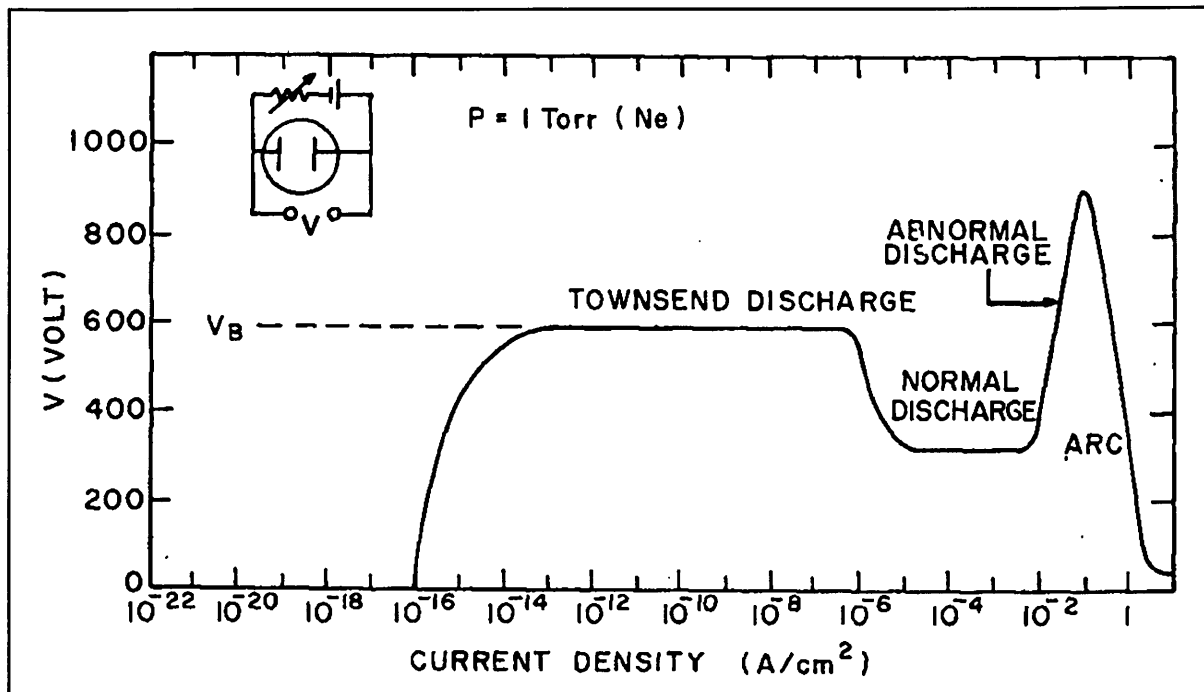


Figure 1.2. Current-Voltage characteristic of a glow discharge

The number of ejected target atoms is typically increased by applying a magnetic field in front of the target surface, so called magnetron sputtering. Entrapped secondary electrons are confining the plasma in front of the target and herewith enhancing the degree of ionisation therefore increasing the number of incident ion and consequently sputtering rate [26,27]. For a planar magnetron the basic design is shown in figure 1.3. The magnetic field strength just above the target characterises the ionisation efficiency of the sputter gas. The magnetic field strength close to the products can also increase locally the plasma density, creating additional ion bombardment onto the growing film [28].

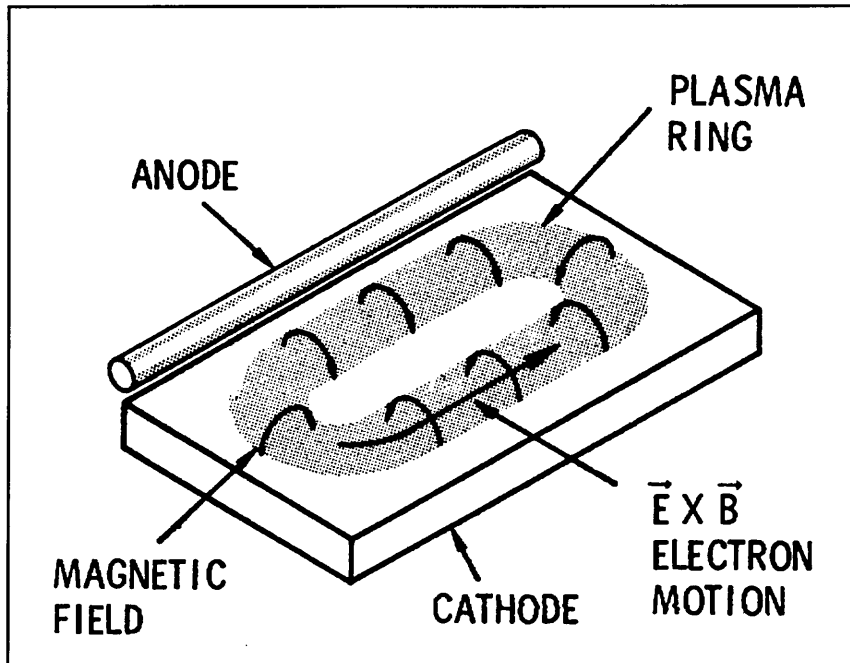


Figure 1.3. Schematic of a planar magnetron sputtering cathode

The “balanced” magnetrons (conventional magnetron), having the same magnetic field strength for the inner and outer pole, are most efficient in ionization of the sputter gas. Consequently high sputter rates can be achieved. As the magnetic field strength near the products is low, ion bombardment of the products is relatively low. Therefore the “balanced” magnetron system is suitable for deposition with a low energy flux onto the substrates (low temperature deposition). This can result in under dense coating structures for materials with high melting points [29]. The distribution of the magnetic field can be modified using a weak inner pole and a strong outer pole, resulting in an “unbalanced” magnetron. Within the PVD industry this magnetic field arrangement is used mostly, as it contributes to an enhanced ratio between ions and condensing target atoms on the substrate. This type of unbalanced magnetron has also been used in the experiments described in this thesis. In multi-cathode coating equipment increase in the substrate ion current density is possible with a closed field unbalanced magnetron configuration, where the magnetic field lines of individual cathodes are linked in order to enhance further electron entrapment [30].

Vaporised target material will condense on surfaces present. It is preferably collected on products in the centre of the vacuum chamber, because of high material transfer efficiency and low equipment contamination. Before condensation there will be an

interaction of vaporised target material with the species present in the vacuum chamber resulting in energy exchanges (ionisation, recombination, excitation energy transfer by collisions), reactions with reactive process gases and residual gases, and change of motion direction (scattering). Especially the intrinsic energy level of the ions and neutral atoms (kinetic and electrical) plays a dominant role within the growth of PVD films.

Besides the chemical composition, the coating properties are strongly influenced by the film microstructure. For vacuum deposited coatings structure models were developed by Movchan and Demchishin in 1969 [31] and refined for the sputtering technology by Thornton in 1977 [32] and Messier in 1984 [33]. They show a classification in either “zone i” (tapered crystallites separated by voids), “zone T” coatings (densely packed fibrous grains), “zone ii” (columnar grains) or “zone iii” (recrystallised grains). Within the PVD cycle the deposition pressure, deposition temperature and the ion bombardment determine the mode of film growth for the different types of coatings. Ion bombardment is achieved by applying a negative electrical potential to the parts, so called “bias voltage”. Film growth under ion bombardment is called “ion plating”. All the mentioned control parameters together set the energy level of the condensing flux and influence the adatom mobility. Increased adatom mobility results in larger grain sizes and less grain boundary surface area [34]. The Thornton model is shown in figure 1.4.

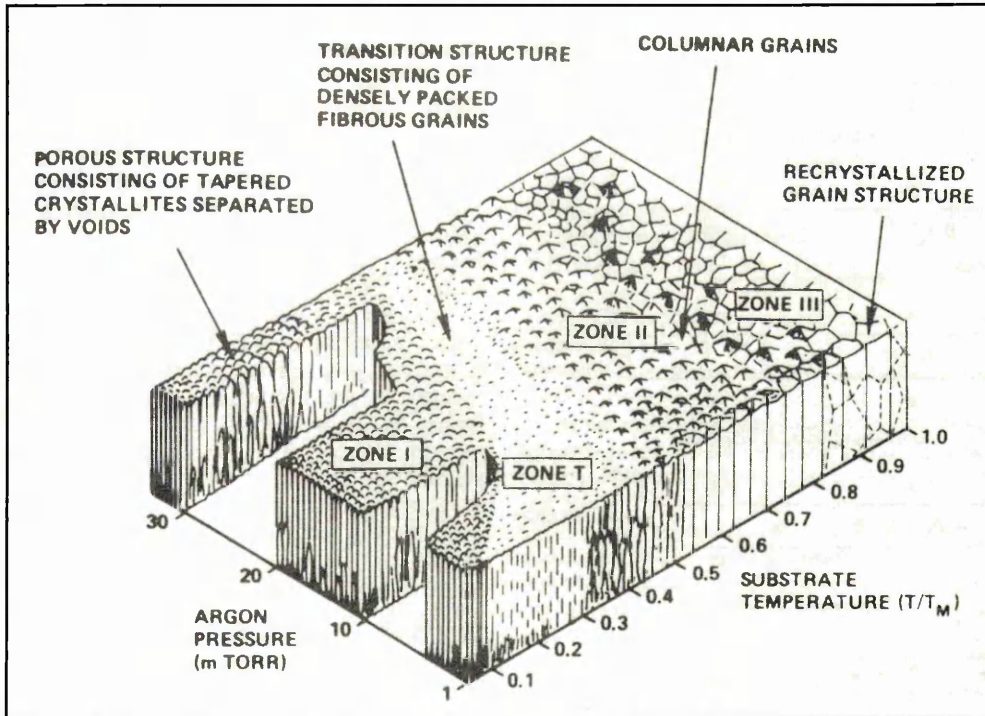


Figure 1.4. Thornton's structure zone model of sputter deposited films [32]

Sputter deposits exist in three different solid conditions:

- 1) single crystalline.
- 2) polycrystalline.
- 3) non-crystalline or amorphous.

Or combinations of amorphous and crystalline.

The CrN_x coatings as deposited in this work are polycrystalline materials.

Besides the growing structures the hard coating properties are strongly dependent on the bonding status and can be either metallic, covalent or ionic (also known as heteropolar). In 1990 Holleck [35] has presented an overview for several ceramic layers, figure 1.5.

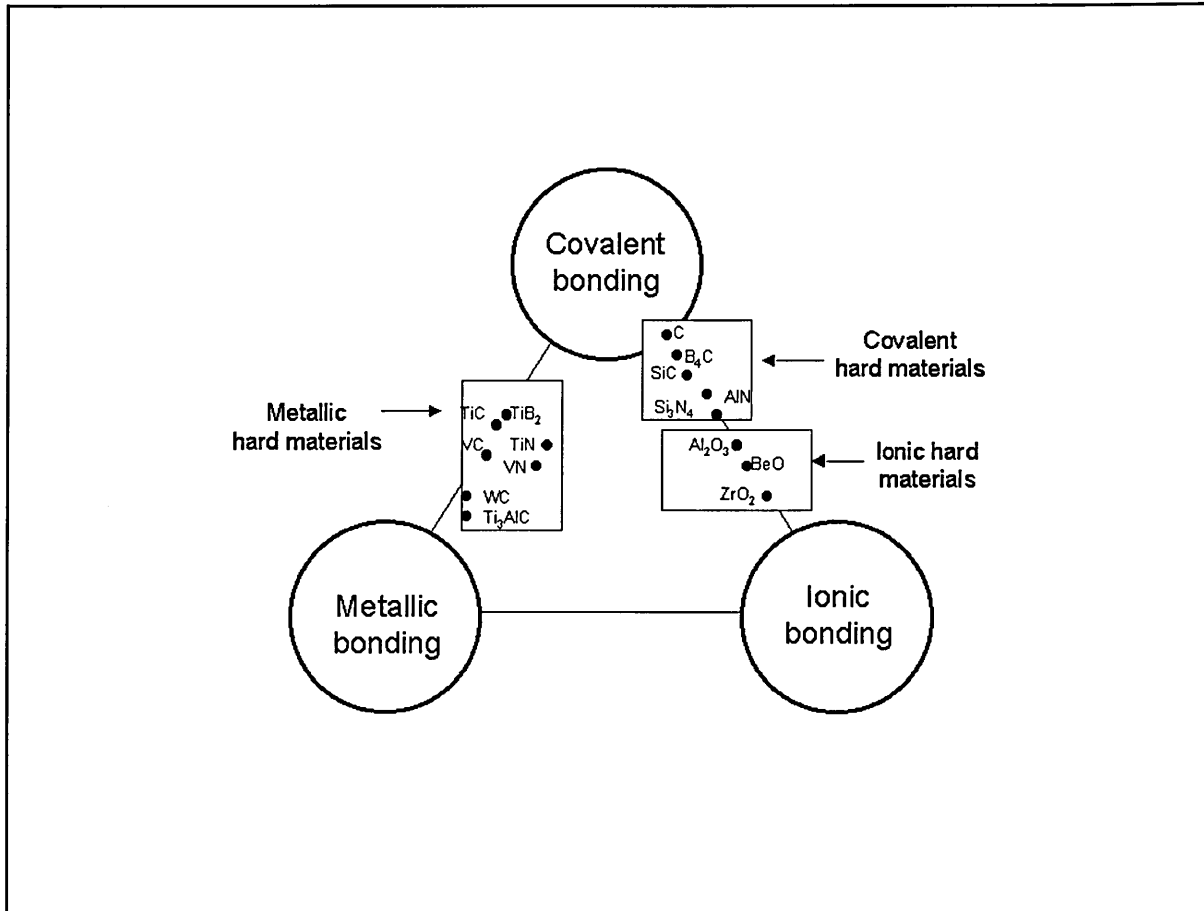


Figure 1.5. Groups of “ceramic” materials and typical structures as a function of different types of bonding [35]

Metallic hard coatings:

Metallic hard materials (positive ions in a gas of negative electrons) manufactured by vapour deposition processes are typically the carbides, nitrides, silicides and borides of the transition metals in groups IIIA, IVA, VA, VIA, VIIA and VIIIA. The free electrons impart high electrical and thermal conductivity. Compared to the covalent and ionic bonded hard materials metallic hard coatings are more ductile and therefore less susceptible to cracking and delamination when the coefficient of thermal expansion is significantly different for coating and substrate.

Covalent hard coatings:

The covalent bonded hard materials (sharing of electrons between neighbour atoms) are interesting coating materials for abrasive wear resistance, because of their typical high hardness. In general they also show high temperature resistance. With covalent

hard materials it is difficult to achieve good coating adhesion to metallic substrates and in general they have low electrical conductivity.

Ionic hard coatings:

Ionic bonded hard materials (transfer of electrons between atoms) within the thin film technology are typically the oxides. They show extreme low interaction with metallic counter parts. These hard materials tend to be brittle and show a high electrical resistivity. In most cases it is necessary to apply a metallic interlayer in order to achieve adhesion of an ionic hard coating to a metallic substrate.

Tables 1.2, 1.3, and 1.4 [36] show examples of properties of several ceramics out of the three different bonding groups:

Phase	Density [g/cm ³]	Melting point [°C]	Hardness [HV]	Young's Modulus [kN/mm ²]	Sp. Electr. Resistivity [μΩ cm]	Therm. Exp. Coefficient [10 ⁻⁶ /K]
TiB ₂	4.50	3225	3000	560	7	7.8
TiC	4.93	3067	2800	470	52	8.0-8.6
TiN	5.40	2950	2100	590	25	9.4
ZrB ₂	6.11	3245	2300	540	6	5.9
ZrC	6.63	3445	2560	400	42	7.0-7.4
ZrN	7.32	2982	1600	510	21	7.2
VB ₂	5.05	2747	2150	510	13	7.6
VC	5.41	2648	2900	430	59	7.3
VN	6.11	2177	1560	460	85	9.2
NbB ₂	6.98	3036	2600	630	12	8.0
NbC	7.78	3613	1800	580	19	7.2
NbN	8.43	2204(dec)	1400	480	58	10.1
TaB ₂	12.58	3037	2100	680	14	8.2
TaC	14.48	3985	1550	560	15	7.1
CrB ₂	5.58	2188	2250	540	18	10.5
Cr ₃ C ₂	6.68	1810	2150	400	75	11.7
CrN	6.12	1050	1100	400	640	(2.3)
Mo ₂ B ₅	7.45	2140	2350	670	18	8.6
Mo ₂ C	9.18	2517	1660	540	57	7.8-9.3
W ₂ B ₅	13.03	2365	2700	770	19	7.8
WC	15.72	2776	2350	720	17	3.8-3.9
LaB ₆	4.73	2770	2530	(400)	15	6.4

Table 1.2. Properties of several metallic hard materials [36]

Phase	Density [g/cm ³]	Melting point [°C]	Hardness [HV]	Young's Modulus [kN/mm ²]	Sp. Electr. Resistivity [μΩ cm]	Therm. Exp. Coefficient [10 ⁻⁶ /K]
B ₄ C	2.52	2450	3-4000	441	0.5 x 10 ⁶	4.5 (5.6)
BN cubic	3.48	2730	~ 5000	660	10 ¹⁸	--
C (diamond)	3.52	3800	~ 8000	910	10 ²⁰	1.0
B	2.34	2100	2700	490	10 ¹²	8.3
AlB ₁₂	2.58	2150 (dec)	2600	430	2 x 10 ¹²	--
SiC	3.22	2760 (dec)	2600	480	10 ⁵	5.3
SiB ₆	2.43	1900	2300	330	10 ⁷	5.4
Si ₃ N ₄	3.19	1900	1720	210	10 ¹⁸	2.5
AlN	3.26	2250 (dec)	1230	350	10 ¹⁵	5.7

Table 1.3. Properties of several covalent hard materials [36].

Phase	Density [g/cm ³]	Melting point [°C]	Hardness [HV]	Young's Modulus [kN/mm ²]	Sp. Electr. Resistivity [μΩ cm]	Therm. Exp. Coefficient [10 ⁻⁶ /K]
Al ₂ O ₃	3.98	2047	2100	400	10 ²⁰	8.4
Al ₂ TiO ₅	3.68	1894	--	13	10 ¹⁶	0.8
TiO ₂	4.25	1867	1100	205	--	9.0
ZrO ₂	5.76	2677	1200	190	10 ¹⁶	11 (7.6)
HfO ₂	10.2	2900	780	--	--	6.5
ThO ₂	10.2	3300	950	240	10 ¹⁶	9.3
BeO	3.03	2550	1500	390	10 ²³	9.0
MgO	3.77	2827	750	320	10 ¹²	13.0

Table 1.4. Properties of several heteropolar hard materials [36].

1.3 Why CrN by PVD?

Electroplated hard chromium is the most widely used approach to protect engineering components from wear and corrosion. The main advantage is a reasonably high hardness (HV1000 range) and thick coatings (up to 20 μm) at a low deposition temperature. In this way they offer a high “wear volume”. However, electroplated hard chromium coatings are micro-cracked, but offer the ability to retain lubrication fluids. Today this coating is still very competitive when compared with PVD hard coatings. Hard chromium by electroplating represents well-understood technology, which has reached its ultimate state of development with its obvious specific limitations. The micro-cracks set a maximum level of corrosion resistance, especially when adhesive layers like copper are used. For the layer thickness there seems to be a maximum of approximately 20 μm above which defect free coatings

cannot be produced. Another limitation is that Cr based alloy deposits cannot be easily processed by electroplating. On the other hand Cr alloy deposits are ideal candidates for corrosion and wear applications. Finally the pollution issues of electroplating will make the process more expensive and less competitive together with severe legal restrictions.

The PVD technique is a high quality, almost pollution free surface coating process. Amongst the known PVD coatings, CrN is reported frequently as a candidate for partly replacement of electroplated hard chromium. It can be deposited up to a fairly large thickness (up to 40 μm), reasonably hard (appr. HV2000) and very dense even when deposited at moderate substrate temperatures (below 250 °C). Compared to electroplated hard chromium it can be deposited as an alloy with excellent adhesion on a wide variety of substrate materials. It is also a "safe" processing technology, i.e. there is no risk of hydrogen embrittlement of the steel substrates. For large scale industrial use the deposition of CrN on 100Cr6 steel substrates is interesting. However, this material loses the heat treatment properties when PVD processing occurs above 180 °C ("tempering"). At such low deposition temperatures the energy flux should remain low, which affects the coating growth rate and herewith the economics of applying PVD coatings.

For the use of CrN coatings within tribological applications it will be an advantage to deposit smooth coatings. For that reason the work in this thesis will mainly concentrate on the deposition of CrN_x by the unbalanced magnetron technology. It avoids a polishing step, which might be required for the cathodic arc evaporation technology.

The aim of this research is to gain a better understanding of the dominant deposition parameters and resulting film properties of magnetron sputtered CrN coatings at 250 °C deposition temperature. Similar to TiN the expectation is that stoichiometry and ion bombardment will play an important role. The results will be used in order to produce CrN coatings, which are technically competitive with electroplated hard chromium. However, the economical competitiveness will depend on the required coating thickness, which may change from case to case and the environmental pressure on reducing pollution.

Chapter 2-Literature Review: Chromium (Cr) and chromiumnitride (CrN_x) deposited by PVD

2.1. Cr and CrN_x standards

Cr belongs to the VI-B group of elements in the periodic table of the elements together with Mo and W. The phase-diagram for the Cr-N system is shown in figure 2.1 [37]. For comparison the Ti-N phase diagram is also shown [38].

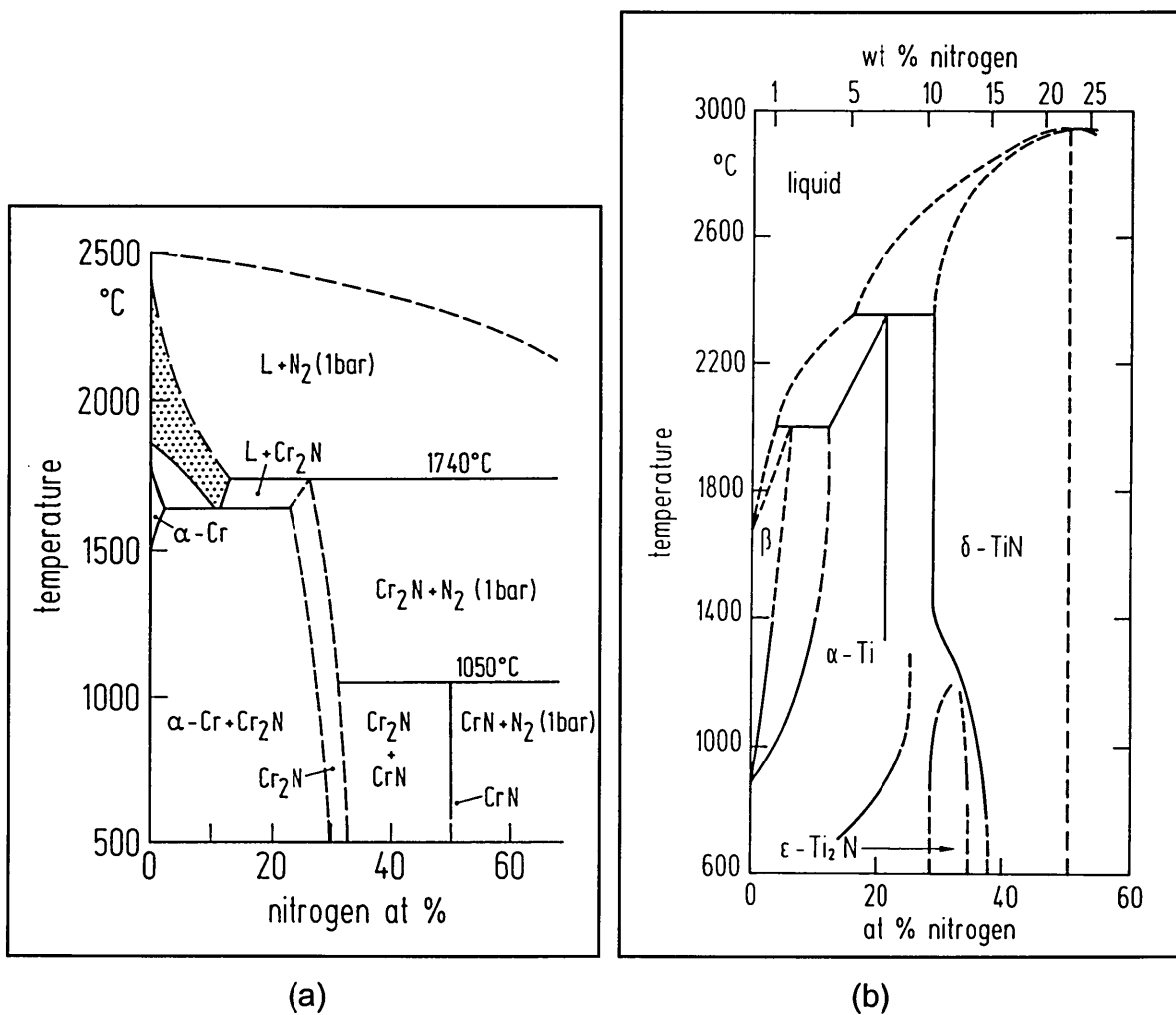


Figure 2.1. Phase-diagram for the (a) Cr-N [37] and (b) Ti-N system [38].

The diagram shows the existence of bcc-Cr, hcp-Cr₂N, fcc-CrN and mixed phases. It is clear from the equilibrium diagram that the thermal stability is higher for Cr₂N than for CrN. According to the equilibrium diagram CrN forms over a limited composition range and over-stoichiometric CrN is not present whereas TiN has a broader composition range and also shows over-stoichiometric TiN, figure 2.1 [38].

An overview of main physical properties and crystal structures according to JCPDS standards of Cr, Cr₂N and CrN are presented in tables 2.1 and 2.2:

	Cr	Cr ₂ N	CrN
Crystallographic Structure	bcc	hcp	fcc
JCPDS Lattice parameter [Å]	a ₀ = 2.8839	a = 4.8113 c = 4.4841	a ₀ = 4.1465
Molecular weight [g/mol]	51.996	118.03	66.02
Melting point [°C]	1863	1590	> 1500
Density [g/cm ³]	7.15	6.51	6.14
Coefficient of thermal expansion [10 ⁻⁶ /K]	4.9	9.41	2.3 (20-800 °C) 7.5 (850-1040 °C)
References 39, 40, 41			

Table 2.1. Physical properties of Cr, Cr₂N, and CrN.

	hkl	d-spacing [Å]	2 θ -reflection	rel. intensity [%]
Cr	110	2.0400	44.37	100
	200	1.4419	64.59	16
	211	1.1774	81.73	30
	220	1.0195	98.15	18
	310	0.9120	115.30	20
Cr ₂ N	101	3.0520	29.24	4
	110	2.4057	37.35	15
	002	2.2419	40.19	21
	111	2.1200	42.61	100
	200	2.0832	43.40	1
	201	1.8888	48.14	1
	112	1.6405	56.01	19
	211	1.4862	62.44	<1
	300	1.3892	67.35	15
	113	1.2696	74.71	13
	220	1.2030	79.63	<1
	302	1.1808	81.44	10
	221	1.1619	83.05	10
	004	1.1209	86.82	2
	222	1.0600	93.22	3
	114	1.0162	98.58	2
	223	0.9371	110.6	4
	313	0.9142	114.8	<1
410	0.9092	115.8	<1	
411	0.8910	119.66	8	
CrN	111	2.394	37.54	80
	200	2.068	43.74	100
	220	1.463	63.54	80
	311	1.249	76.16	60
	222	1.197	80.11	30
	400	1.034	96.30	30
	331	0.9496	108.4	50
	420	0.9260	112.6	60

JCPDS standard; CuK α with $\lambda=1.5405$

Table 2.2. Crystallographic X-Ray data of Cr, Cr₂N and CrN according to JCPDS standard [41]

Within the NaCl-type lattice of CrN the closed packed plane {111} is consisting of only Cr atoms. The {222} plane is a plane consisting of N atoms only. All other planes are mixtures of Cr and N atoms. This is illustrated in figure 2.3 for the {111}, {222}, {110}, and {100} planes.

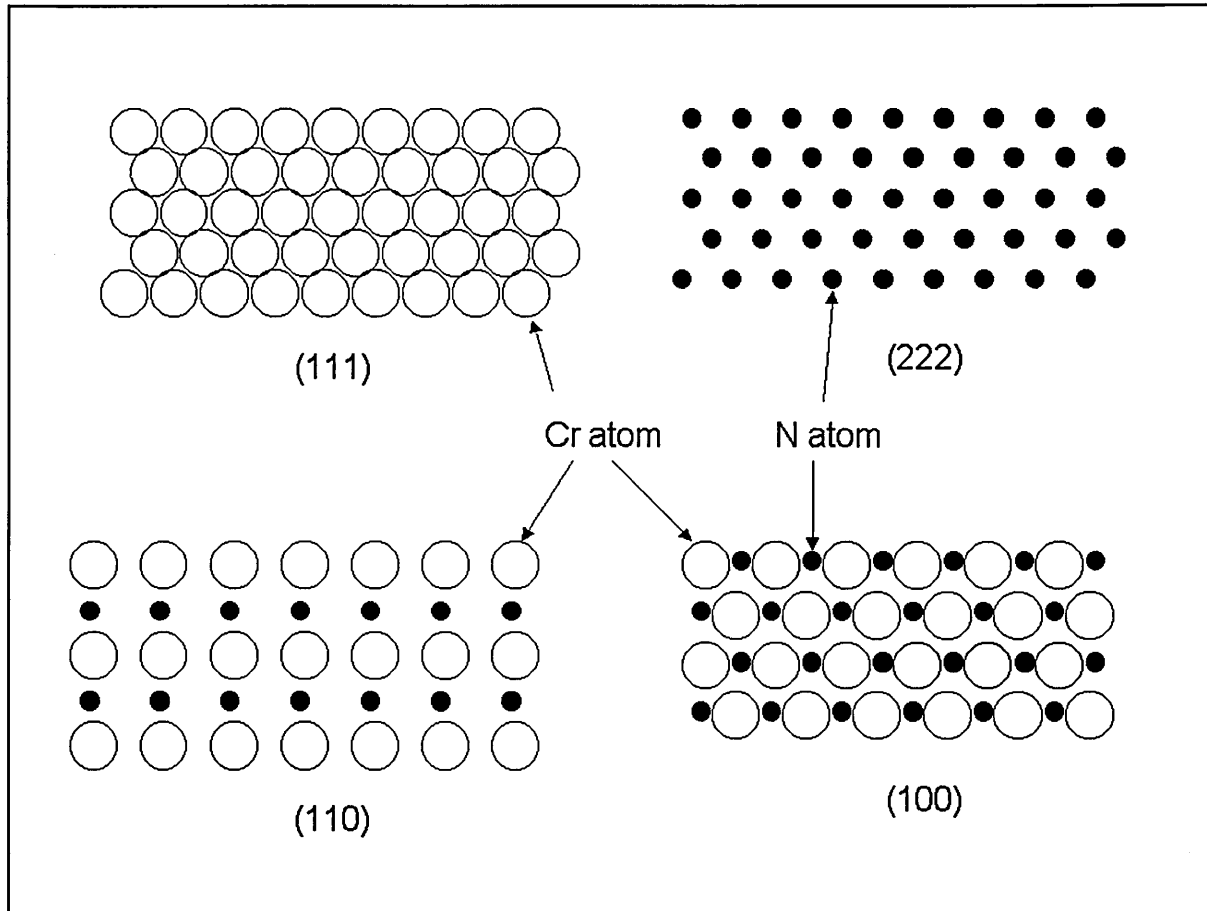


Figure 2.3. Schematic cross-section of the most important planes within the fcc-CrN lattice.

2.2. CrN_x by different PVD methods

In 1983 PVD CrN_x has been introduced for the first time [42]. It was the most discussed candidate to replace electroplated hard chromium. The basic properties of hard chromium are [43,44]:

- 1) it can be deposited up to large thickness (20 μm range)
- 2) deposition temperature up to 60 °C
- 3) HV=800-1100
- 4) micro-cracked structure
- 5) stripping and re-coating are possible
- 6) Correction of dimensions is possible by polishing
- 7) low coefficient of friction possible by PTFE (Teflon) incorporation

Applications are found within equipment building, aeroplanes, hydraulics, automotive-, plastics-, paper-, textile-, packaging-, food-, chemical-, nuclear-, medical-, and printing-industry.

CrN is an interesting candidate to replace hard chromium, because it is a PVD coating that can be deposited also at relatively low temperatures and with low internal stresses. The low stress level opens up the possibility to grow thick coatings (up to appr. 40 μm). The higher hardness can give similar wear properties at lower coating thickness compared with hard chromium. The corrosion behaviour of hard chromium is mainly set by the micro-cracked structure. The "open" structure avoids pitting corrosion. Pitting corrosion is known for PVD coatings with distinct pin-holes [45,46].

Successful introduction of PVD CrN coatings is reported in the field of forming, moulding, aluminium die casting, deep drawing, cutting (Cu, Ni and Ti), decorative, automotive, and electronics [47-59]. Mainly the cathodic arc evaporation technique and some magnetron sputtering are used. Besides these two methods, also CrN_x by electron beam evaporation has been reported [60-64]. CrN_x is also possible by chemical vapour deposition (CVD) at deposition temperatures between 350 and 550 $^\circ\text{C}$ [64]. The reaction is between Bis(benzene)chromium (BBS) and NH_3 or N_2H_4 within a low pressure hot wall chemical vapour deposition reactor. All the CVD produced CrN_x coatings contained low amounts of carbon.

Important to notice is that CrN_x coatings are very often combined with other surface modification techniques ("duplex treatment"). Electroless nickel [62,63] and (carbo-) nitrided [65,66,155] pre-treatments show improved corrosion and wear resistance compared to the PVD treatment only.

Following the knowledge of incorporation of elements into the TiN matrix, also work is carried out to incorporate Al [67,68], Ti [69-71], C [72,73], Ta [74], W [71], Mo [71], Nb [71] and O [75,76] into the CrN matrix.

CrN has also been used as one of the alternating layers within a superlattice structure with NbN [77] and TiAlN [78-80].

It is difficult to generate general conclusions on CrN_x based coatings, because there is a wide range and in many cases an incomplete description of the deposition conditions. The technology (RF, DC, pulsed-DC), the deposition temperature, the deposition speed, the ions-to-neutrals arrival ratio, the partial pressures, the total gas pressure, the background pressure, the cathode-substrate distance, and the substrate rotation are the main parameters influencing film growth and should be addressed.

As far as possible trends are reported in sections 2.3 and 2.4 for sputtered and arc evaporated CrN_x coatings.

2.3. CrN_x by sputtering

The literature overview on sputtered CrN_x is split in three main sections; bcc-Cr, hcp-Cr₂N and fcc-CrN. Mixed phases of the mentioned three main phases do exist.

2.3.1. bcc-Cr by sputtering

In the few cases found in the literature referring to the properties of bcc-Cr it was found that it either grows in a {110} or {211} preferred orientation, depending on the temperature. At relatively low deposition temperatures (up to 200 °C) the {110} orientation dominates [40,74,81-83]. At higher temperatures however, (480 °C) the development of a {211} preferred orientation is reported [84]. This is similar to increased bias voltage of –200 Volt at room temperature (specimens on heat sink) [83]. The hardness of PVD deposited metallic Cr ranges from HV600 to HV1050 [84, 76,74,85,86]. Atzor [40] reported on the effect of the deposition temperature on the lattice parameter and the crystallite size. At 400 °C the lattice parameter was 0.2881 nm and a crystal size of 21 nm whereas at 600 °C the values for the lattice parameter and crystallite size increased to 0.2886 nm and 32 nm respectively.

Within the Cr matrix it is possible to desolve up to 10 at.% N [73]. The hardness increases immediately with the incorporation of small amounts of nitrogen. Peak

broadening (XRD) and a preferred orientation change towards {100} is observed [76,82].

It is interesting to note the wide spread in values mentioned for the coefficient of thermal expansion: $4.9 \times 10^{-6}/\text{K}$ [39], $6.61 \times 10^{-6}/\text{K}$ [86,87], and $8.5 \times 10^{-6}/\text{K}$ [88].

In most papers Cr is used as a base layer for CrN_x coatings. It is reported to improve the adhesion and the corrosion resistance [89-92]. Also alternating layers of Cr and CrN_x are used [81,93].

2.3.2. hcp- Cr_2N by sputtering

The situation for hcp- Cr_2N is more complex than for bcc-Cr. This is mainly because of the possibility of mixtures of Cr_2N with either Cr or CrN phases. The impression is that many authors do not examine sufficiently carefully for the existence of multi-phases when reporting on Cr_2N .

The crystallographic preferred orientation is in the most cases {11.1} for the hexagonal Cr_2N coatings at deposition temperatures in the range of 200 °C [74,82, 83,85,94]. Kacsich [95] shows that at 300 K the preferred orientation is {11.0} and at 830 K {11.1} or {11.0} depending on the layer thickness (< 250 nm and > 250 nm respectively.).

In majority of the literature it is reported that the Cr_2N phase is the hardest phase within the Cr-N system [86,88,89,91,93,94,96]. On the other hand there are a few papers indicating that the highest hardness occurs at maximum N incorporation in to the Cr matrix [73] or at N content levels below 33 at.% [81-83].

The reported crystallite size is in the range of 4 till 40 nm [76,85,94,96] depending mainly on the deposition temperature; with the smaller crystallite size at lower deposition temperatures.

2.3.3. fcc-CrN by sputtering

fcc-CrN has been deposited under many different conditions. The resulting film properties vary within a wide range. The main data are collected in table 2.3.

The effect of deposition conditions on the resulting film properties is not obvious. Typically the crystallite size is reported in the range of 15 till 50 nm, the hardness between 15 and 30 GPa (with different measuring techniques), residual stress levels of -2 GPa but occasionally up to -4 GPa.

The preferred orientation of the fcc-CrN is affected by the deposition temperature, bias voltage and Ar/N₂ flow ratio, however there are no precise relationships between process conditions and coating properties.

The results on the film composition vary quite markedly. In general under-stoichiometric [40,71,81,88,90,95,98,107] and few over-stoichiometric CrN_x [82,86,107] coatings are reported. The composition seems to be strongly influenced by the deposition temperature and the energy of the impacting particles during film growth.

The effect of bias voltages (pulsed-DC) and Ar/N₂ flow ratios on the growth of CrN_x at a substrate temperatures below 100 °C is reported by He [107]. Figures 2.4 and 2.5 show the effect of these two parameters on composition, film density, hardness as measured by nano-indentation, and residual stress.

Ref.	Dep. Temp. [°C]	U _{bias} [-V]	Technology	Argon	Nitrogen	Preferred cryst. orient.	Hardness	Composition	Grainsize [nm]	Internal stress	E-modulus [GPa]	Remark
81	<200	50	DC	?	14.9 sccm	{200}	?	CrN0.93	?	?	?	
97	<400	100	DC	0.08 Pa	0.07 Pa	{220}+{200}	<15 GPa	?	?	?	220	
97	>400	100	DC	0.08 Pa	0.07 Pa	{111}	?	?	?	?	220	
97	400	<75	DC	0.08 Pa	0.07 Pa	{220}	appr. 15 GPa	?	55	?	220	
97	400	>75	DC	0.08 Pa	0.07 Pa	{220}	appr. 15 GPa	?	20	higher	220	
82	200	100	DC	0.2 Pa	0.27 Pa	{200}	HV2500	N/Cr=1.2	?	?	?	
98	500	0	DC	?	?	?	?	50 at% N	?	?	?	
99	?	?	RF	?	"high"	{111}	?	?	?	?	?	
100	?	?	DC	?	?	?	1900	?	?	?	?	
98	?	?	DC	?	?	{111}	HV1800-2040	Cr:N=1.1 to 1.3	15 to 40	-8 to -14.5 GPa (100nm)	?	
101	?	100	DC	?	?	?	HV2000-2200	Cr 58 at% N 42 at%	?	?	?	
101	?	250	DC	?	?	?	HV2000-2200	Cr 57 at% N 43 at%	?	?	?	
101	?	295	DC	?	?	?	HV2000-2200	Cr 59 at% N 41 at%	?	?	?	
86	453K	ground	RF	14 sccm	6 sccm	?	HV1100	53 at% N	?	?	?	
102	200	?	"sputron"	?	5x10 ⁻² Pa	{111}	HV2100-2280	50:50=Cr:N	20-40	P _{N2} <4.5X10 ⁻² Pa low tensile P _{N2} >4.5X10 ⁻² Pa low compressive	?	
83	90	65	DC	Σ 0.18 Pa	50%	{200}	HK1802	?	?	?	?	
88	250	40	RF	0	1.5 Pa	{200}	HU 34 GPa	N=43.8 at%	?	-3.3 GPa	400	
90	160 to 230	40	DC	?	?	?	HV1950-2100	Cr:N=55:45 at%	?	?	?	
91	170	20	RF	85	30	{220}	HU 30 GPa H _{tri} 23.2 GPa	?	?	-2.2 GPa	?	
95	300K	?	RF	27 sccm	21 sccm	{111}	?	Cr=50 to 53 at%	20	?	?	
95	830K	?	RF	27 sccm	21 sccm	{200}	?	Cr=50 to 53 at%	35	?	?	
71	670K	ground	RF	?	0.33 Pa	{200}	1800	CrN0.92	23	?	?	
103	?	?	RF	?	?	{111}	HU3530 H _{tri} 8900	?	?	?	?	
76	200	150	DC	?	30 %	{200}	2280	?	40	?	?	oxidation 4h at 450°C -> gr.size 100 nm 700°C -> 400 nm

84	480	60	DC	$\Sigma 6 \times 10^{-2}$ Torr	3%	{200}	2550	?	?	?	?	?	800C -> 650 nm "200" higher density than {111}
84	480	60	DC	$\Sigma 6 \times 10^{-2}$ Torr	9.5%	{111}	550	?	?	?	?	?	
85	200	?	RF	$\Sigma 0.67$ Pa	15.7 vol. %	{200}	1100	?	?	8.2	?	?	
85	400	?	RF	$\Sigma 0.67$ Pa	22.1 vol. %	{111}	flaking	?	?	52	?	?	
85	400	?	RF	$\Sigma 0.67$ Pa	15.7 vol. %	{200}	flaking	?	?	?	?	?	
104	300	0	DC	$\Sigma 0.45$ Pa	40 %	{111}	?	?	?	40	-1.5	?	
104	300	50	DC	$\Sigma 0.45$ Pa	40 %	{111}	?	?	?	12	-4.4	?	
104	300	50	RF	$\Sigma 0.45$ Pa	40 %	{111}	?	?	?	13.4	-3.7	?	
96	670 K	?	RF	$\Sigma 0.66$ Pa	?	?	17 GPa	50:50	?	20	?	?	
82	?	125	DC	$\Sigma 8$ mTorr	1 to 2 mTorr	?	1400	?	?	?	?	?	
105	?	300	DC	$\Sigma 3.34$ Pa	?	?	?	?	?	?	-7.2	400 assumed	E-modulus affects stress level
106	250	100	DC	?	?	{220}	HK2100	?	?	?	-2.0	?	
107	<100	250 pulsed	DC	$\Sigma 0.26$ Pa	N ₂ /Ar = 2	{220}	31 GPa nano-ind.	Cr/N=1.0	?	?	-4.0	?	
107	<100	250 pulsed	DC	$\Sigma 0.26$ Pa	N ₂ /Ar = 4	{220}	27 GPa nano-ind.	Cr/N=0.7	?	?	-3.0	?	
107	<100	550 pulsed	DC	$\Sigma 0.26$ Pa	N ₂ /Ar = 2	{200}	25 GPa nano-ind.	Cr/N=1.2	?	?	-3.0	?	
107	<100	50 pulsed	DC	$\Sigma 0.26$ Pa	N ₂ /Ar = 2	?	28 GPa nano-ind.	Cr/N=0.98	?	?	-3.4	?	
40	200	60	DC/RF	$\Sigma 8 \times 10^{-3}$ mbar	P _{N₂} /P _{Ar} =0.3	{200}	1900	42 at.% N	?	?	?	?	

Table 2.3. Reported deposition conditions and film properties of sputtered fcc-CrN

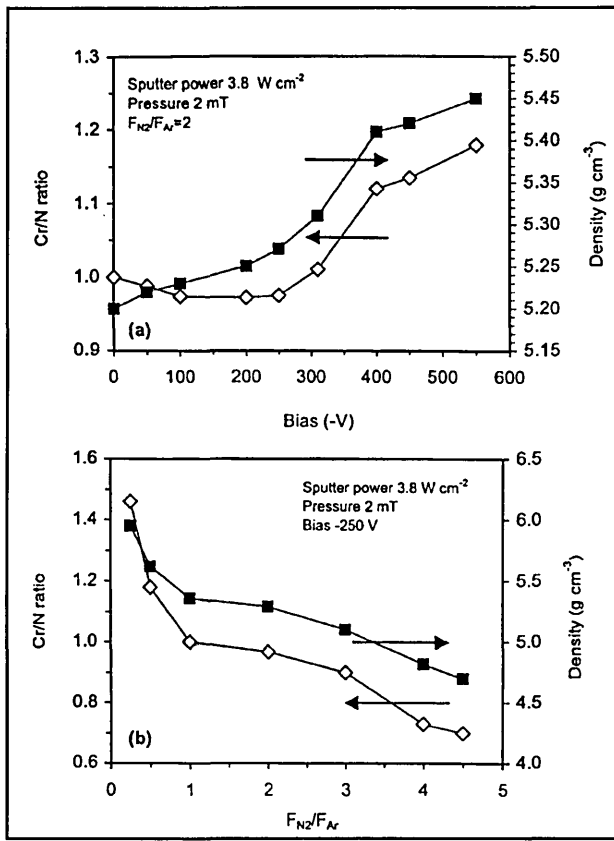


Figure 2.4. Effect of Bias voltage and N₂/Ar flow ratio on composition and density of CrN_x [107].

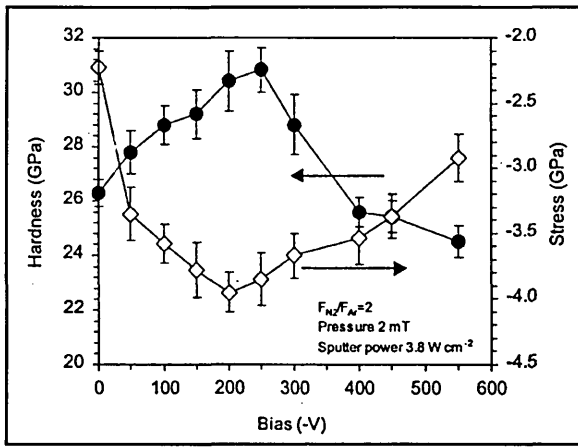


Figure 2.5. Effect of Bias voltage on hardness and residual stress [107].

2.4. CrN_x by cathodic arc evaporation

For CrN_x deposited by cathodic arc researchers reported mixed phases of Cr, Cr₂N, and CrN [108-112,65]. For example at a substrate bias voltage of –100 V and a deposition temperature of 400 °C the following phase dependency on the nitrogen partial pressure is reported [108]:

$P_{N_2} < 0.35 \text{ Pa}$:	Cr and Cr ₂ N
$0.35 \text{ Pa} < P_{N_2} < 1.3 \text{ Pa}$:	Cr ₂ N and CrN
$P_{N_2} > 1.3 \text{ Pa}$:	CrN

The mentioned pressure ranges are system specific, but give a clear indication of the phases to be expected.

2.4.1. bcc-Cr by cathodic arc evaporation

Some work on Cr by cathodic arc is reported by Grant et al. [111] and Ehrlich et al. [112]. The hardness of this single phase is reported to be 12.3 GPa at a substrate bias voltage of -150 V [111]. At a deposition temperature of 380 °C and a bias voltage of –100 V it was found that the preferred orientation is {100} with a mean grain size of 58 nm.

2.4.2. hcp-Cr₂N by cathodic arc evaporation

Ehrlich et al. [112] describes the existence of a pure Cr₂N phase, which is predominant {30.0} oriented and consists of 34 at.% N. At the stoichiometric composition the lattice constants reach their equilibrium values. Most probably mixed phases of hexagonal-Cr₂N with either bcc-Cr or fcc-CrN are present over a wide range of deposition parameters. Cr₂N was present at a concentration as low as 2 at.% of N in the matrix. The reported grain size is 20 nm [112]. Knotek et al. [109] reports a hardness value of roughly 2500 HV_{0.05} for {20.0} oriented Cr₂N coatings (softer than the CrN phase; 2600 to 3200 HV_{0.05}).

2.4.3. fcc-CrN by cathodic arc evaporation

In a similar manner to magnetron sputtered fcc-CrN coatings a considerable variation in the results is reported. At 400 °C an excellent overview of the phases deposited and preferred orientation dependence on substrate bias voltage and nitrogen partial pressure is given in Chiba et al. [110]. Figures 2.6 and 2.7 are from this report:

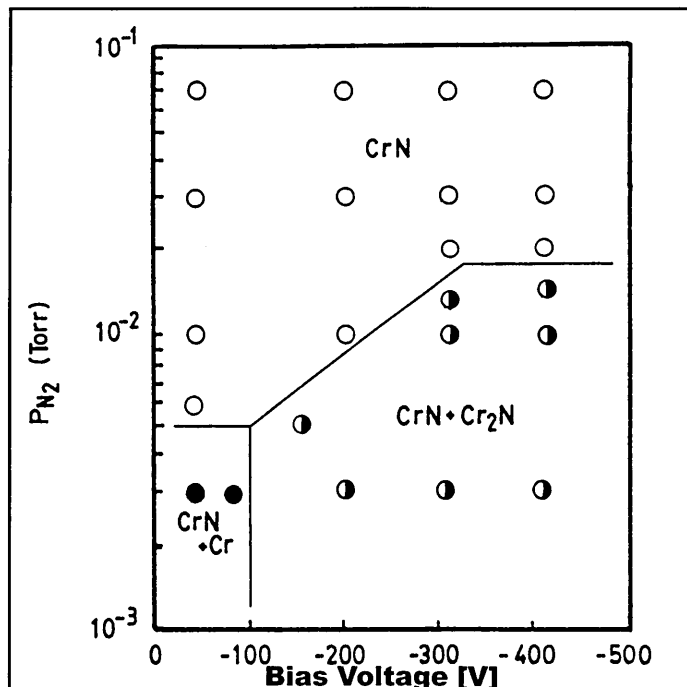


Figure 2.6. Overview of phase formation of Cr-N by cathodic arc deposition, dependent on bias voltage and nitrogen partial pressure [110].

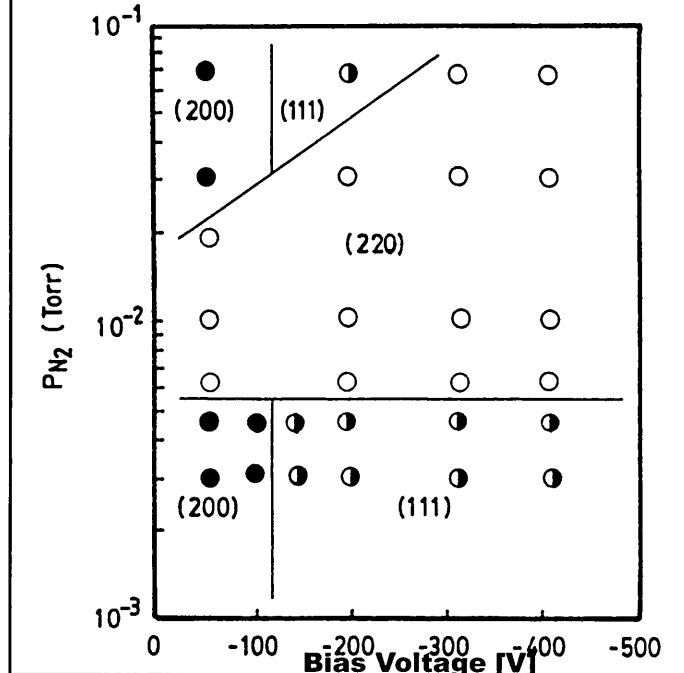


Figure 2.7. Preferred crystallographic orientation of Cr-N by cathodic arc deposition, dependent on bias voltage and nitrogen partial pressure [110].

Within the classical range of cathodic arc deposition the {110} preferred orientation is observed for fcc-CrN. In order to produce CrN coatings without a {110} preferred orientation the deposition should be performed at either low or high partial pressures of nitrogen and preferably at a substrate bias voltage between floating potential and – 200 V. Reported results from other groups [65,67,108,111,113-115] fit reasonably well in the mentioned crystallographic matrix.

According to Piot et al. [108] the texture changes from {110} to preferred {111} when the deposition temperature is increased from below 350 °C to 500 °C, while still maintaining a constant nitrogen pressure and substrate bias voltage of 1.6 Pa and – 100 V respectively. In parallel the crystallite size is increased from 6 to 9 nm which results in a hardness value of about 30 GPa. This relative small crystallite size is also reported by Sue et al. [115], who measured 3.9 to 7.5 nm at a deposition temperature of 200 °C. Within this paper there is a description how to calculate the Young's modulus (220 to 232 GPa) by using different substrate materials. Later Sue [114] reported a crystallite size of 17.3 nm at a deposition temperature of 450 till 500 °C. The coating was dense and featureless and had a hardness value of HV1685.

At lower deposition temperatures (range < 250 °C) Ganin [116] reported a hardness value of 1830 HV0.1 with a compressive stress level of -3.7 GPa. The main deposition parameters were -100 V for the substrate bias voltage and a nitrogen partial pressure of 2 Pa.

Most researchers reported under-stoichiometric CrN [111,112,117]. Lin et al. [117] measured only 40 at.% Cr when depositing at 5 Pa nitrogen and a substrate bias voltage of -120V. This result is either speculative or doubtful on the measuring technique (which was not mentioned).

Chapter 3 - Experimental

3.1. PVD deposition

3.1.1. HTC-625 deposition equipment

All the samples have been deposited in the same Hauzer Techno Coating HTC-625 system [118]. The vacuum chamber of this specific coater is equipped with one Arc Bond Sputtering cathode, ABS™ [2,21], and one cathodic arc cathode. The ABS cathode is equipped with an electromagnetic coil. The cathodic arc position is also equipped with an electromagnetic coil, but with a reversed polarity in order to create a closed field magnetic configuration for enhanced ionisation. A schematic plan view and the system are represented in figures 3.1 and 3.2:

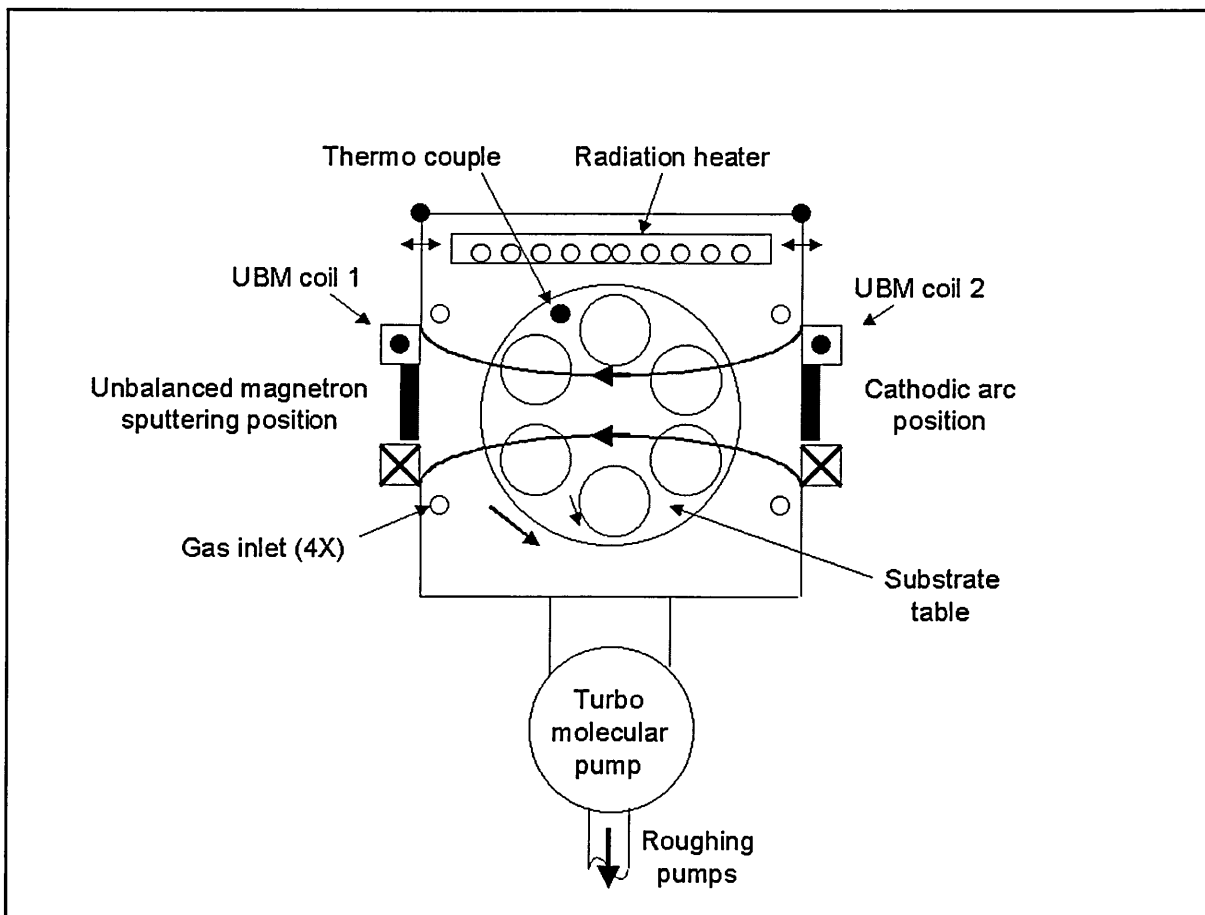


Figure 3.1. Schematic top view of the experimental HTC-625 deposition equipment.

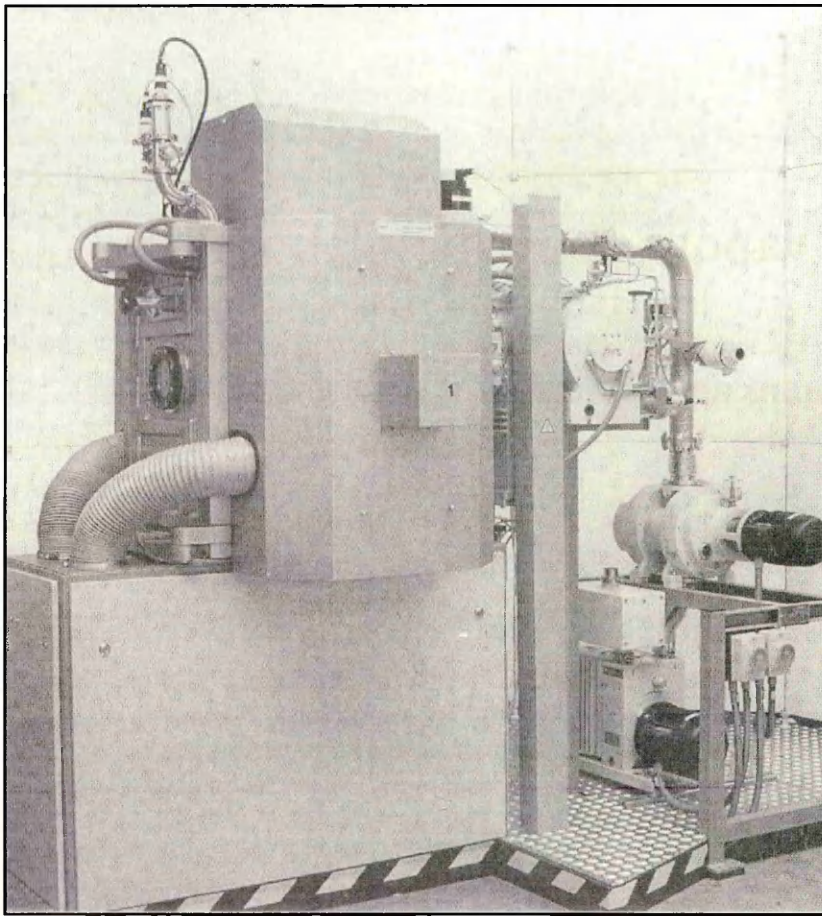


Figure 3.2. Experimental HTC-625 deposition equipment.

The ABS cathode has been used in the unbalanced magnetron-sputtering mode during the depositions. The cathodic arc cathode has been used to generate the metallic ions for the low energy metal ion bombardment (pre-treatment prior to deposition). Different target materials for the pre-treatment and the coating step have been used.

The substrate table, dimension ϕ 380 x 400 mm, carries 6 rotating spindles. The spindles can take samples or products for deposition using either two-fold or three-fold planetary rotation. The depositions were performed at a rotation speed of 9.5 rev/min for the main table motion, i.e. one-fold rotation. The distance from target surface to outer substrate table diameter is 130 mm. All the samples within the experiments were deposited under a two-fold planetary motion. As the deposition temperature is a key deposition parameter, the table is equipped with a biased

rotating thermocouple. The deposition temperature is regulated by controlled radiation heating power, with the thermocouple read-out as the input parameter. The power supplies are connected to the cathodes and substrate table (bias) and are straight DC driven. The chamber wall is the anode.

3.1.2. Targets

The target dimensions are 400 x 125 x 12 mm for height, width and thickness respectively. Basic properties of the used Cr and Ta targets are summarised in table 3.1:

	Cr	Ta
Purity	99.94 %	99.9 %
Maximum main impurities	Al 200 ppm C 100 ppm Fe 500 ppm S 100 ppm Si 100 ppm N 150 ppm O 300 ppm	C 100 ppm Fe 100 ppm Hf 100 ppm Nb 1000 ppm Re 300 ppm Ti 100 ppm W 300 ppm H 100 ppm N 100 ppm O 500 ppm
Production method	hot isostatic pressing	electron beam melting forging rolling
Theoretical density	7.19 g/cm ³	16.6 g/cm ³
Atomic weight	51.995	180.984
Melting point	1890 °C	2996 °C
Boiling point	2482 °C	5425 °C
Young's modulus	190 Gpa	183 GPa
Heat of vaporisation	76.635 Kcal/mol	180 Kcal/mol

Table 3.1. Purity and properties of the Cr and Ta target materials

3.1.3. Sample preparation prior to PVD

3.1.3.1. Substrates

For the different coating evaluations, different substrate materials were used. An overview is presented in table 3.2:

Analysis	Substrate Material	Substrate Shape	Surface Roughness Ra/Rtm [μm]
Hardness Vickers	HSS	\varnothing 30 x 6 mm	0.015 / 0.11
Critical Load	HSS	\varnothing 30 x 6 mm	0.015 / 0.11
HRc-DB adhesion	HSS	\varnothing 30 x 6 mm	0.015 / 0.11
Roughness	HSS	\varnothing 30 x 6 mm	0.015 / 0.11
Colour	HSS	\varnothing 30 x 6 mm	0.015 / 0.11
Pin-on-disc	HSS	\varnothing 30 x 6 mm	0.015 / 0.11
Cross section SEM	HSS drill blank	\varnothing 4.2 x 74 mm	-----
XRD	Ferritic Stainless Steel	50 x 20 x 0.1 mm	Parallel to polishing: 0.04 / 0.3 Perpendicular to polishing: 0.07 / 0.7
TEM	Austenitic Stainless Steel 304	50 x 20 x 1.5 mm	Parallel to polishing: 0.04 / 0.3 Perpendicular to polishing: 0.07 / 0.7
Corrosion	Austenitic Stainless Steel 304 SHU	\varnothing 30 x 5 mm	0.02/0.2
Stress (bending)	Ferritic Stainless Steel	\varnothing 30 x 0.5 mm	Parallel to polishing: 0.06 / 0.4 Perpendicular to polishing: 0.10 / 0.8
SNMS	Ferritic Stainless Steel	55 x 20 x 1.5 mm	Parallel to polishing: 0.06 / 0.4 Perpendicular to polishing: 0.10 / 0.8

Table 3.2. Overview of substrates.

3.1.3.2. Chemical cleaning of substrates

All samples were chemically cleaned by the following sequence:

- Alkaline “Turbo Cleaner SD-15 Extra” from Turco Produkten BV, Ede, NL; ultrasonic activation, 60 °C, 30 seconds, Ph = 13
- Rinsing 1; city water, 10 seconds
- Rinsing 2; city water, 10 seconds
- Rinsing 3; methanol, 10 seconds
- Rinsing 4; methanol, 10 seconds
- Drying; dried compressed air (oil free)

3.1.4. PVD process sequence

The process sequence and the individual process steps are put in an overview, table 3.3.

Process Step	Step parameter	Value
Pumping + Heating		Always used
	Temperature	220 °C
	End pressure Heating time	< 3x10 ⁻³ Pa > 2 hours
Argon glow discharge		Optional
	Temperature	240 °C
	Argon pressure	1 Pa
	Bias Voltage	-800 V
	UBM coils Cathode Voltage Time	100 A -150 V 20 min.
Metal ion etching		Optional
	Temperature	250 °C
	Target material	Cr or Ta
	Argon pressure	1x10 ⁻² Pa
	Bias Voltage Cathode current time	-800 V 150 A 5 min. (1 min. on / 1 min. off)
Arc interlayer		Optional
	Temperature	250 °C
	Target material	Cr or Ta
	Argon pressure	1 Pa
	Bias Voltage Cathode current time	-50 V 150 A 20 min.
UBM interlayer CrN _x		Optional
	Temperature	250 °C
	Argon flow	varied
	Nitrogen flow	varied
	Bias Voltage	50 V
	UBM coils Cathode power Cr Time	20 A 5 kW 25 min.
UBM deposition CrN _x		Always used
	Temperature	250 °C
	Argon flow	160 sccm
	Nitrogen flow	parameter (0-300 sccm)
	Bias Voltage	parameter (0-300 V)
	UBM coils Cathode power Cr Time	parameter (0-40 A) 5 kW parameter (goal 3 μm)
Cooling		Always used
	Temperature	< 100 °C
Venting		Always used

Remark: Rotation speed during all steps = 9.5 rev./min for the main table basis.

Table 3.3. PVD process sequence with parameter overview.

Pump down and heating:

In order to deposit coatings with low levels of impurities it is necessary to evacuate the process chamber to a relatively low pressure of $3 \cdot 10^{-3}$ Pa. After a roughing stage to 15 Pa the turbomolecular pump with a nominal pumping speed of 2200 l/s reduces the pressure into the high vacuum level range. In parallel radiation heating enhances water desorption from the process chamber and the substrate table, i.e. "outgassing".

Argon glow discharge:

Substrate surface contaminants can be removed by low energy ion bombardment (sputter cleaning at 0.1 to 1 keV). An abnormal DC glow discharge is initiated between the substrate table (cathode potential) and the process chamber wall (anode potential). Argon is used as the noble gas. Ionisation enhancement is achieved by applying -150 Volts to the UBM cathode and switching on the UBM coils in a closed field configuration. Running the UBM cathode in the range of or below the threshold for target sputtering, extra electrons and herewith-extra argon ions will be generated, without removal of serious number of target atoms from the target. High rates of sputtering would result in contamination of the substrate surface. The resulting bias current density was approximately 0.15 mA/cm^2 .

Metal ion etching:

Metal ions, generated in a cathodic arc discharge, are accelerated to the substrates by applying a negative electrical potential to the substrate table. The energetic species are bombarding the substrate surface and sputter cleaning occurs. In this way contamination is removed and at high energy levels implantation is reported. For steel substrates that have been treated with a Ti ion bombardment at an accelerating voltage of -1200 V radiation enhanced Ti diffusion was found to a depth of ~ 100 nm together with grain refinement in parallel in the same region [119].

Arc interlayer:

Within the experiments the cathodic arc was not only used as a cleaning step, prior to the deposition of the CrN_x coatings. In some runs metallic Cr and Ta were deposited as an interlayer (maximum thickness of 0.5 μm). The expectation was to improve the level of adhesion. The preferred crystallographic orientation of the latter deposited CrN_x can be dependent on the preferred orientation of the base layer.

UBM interlayer:

In a similar manner to the deposition of an arc interlayer, in some cases the UBM sputtering technique has been applied to form an interlayer with different properties from the bulk coating. In some cases it is useful to deposit a low stress coating before depositing a highly stressed one. In this way sufficient adhesion between coating and substrate is achievable even for highly stressed coatings.

UBM deposition:

The CrN_x properties studied are based on the film growth by reactive unbalanced magnetron sputtering from the metallic Cr target in an argon/nitrogen atmosphere. The influence of gas composition and the ion bombardment (number and energy) are the main parameters in the study of the resulting film properties. All depositions were performed at a substrate temperature of 250 °C.

3.1.5. Deposition rate estimation for Cr

The dynamic deposition rate in 2-fold motion at 5 kW cathode power and a substrate bias voltage of –100 V was measured to be 1.8 μm/h.

The expected Cr flux from the target at 5 kW and 500 V can be calculated:

Ion current to target surface = $(5000/500)/(1.6 \times 10^{-19}) = 6.25 \times 10^{19}$ ions/s

Sputter yield of Cr at 500 eV Ar = 1.2 [27,120]

Cr flux from target = 7.5×10^{19} atoms/s.

density ρ of Cr = 7.20 g/cm³ [39]

Mol. weight M of Cr = 51.9961 [39]

Cr density = $(7.20/51.9961) \times 6.022 \times 10^{23} \times 10^6 = 8.31 \times 10^{28}$ atoms/m³

Assumptions:

- 35 % flux losses next to the table (geometrically).
- No Cr deposition through the table.
- Flux to the table is parallel, i.e. only normal to the target surface.
- Target height is equal to table height.

Known are:

- Target dimensions: height 40 cm and width 12.5 cm.
- Table diameter: 38 cm.
- Satellite diameter: 12.5 cm (only 6 sample holders, rod shaped).

Figure 3.3 gives an overview of the situation.

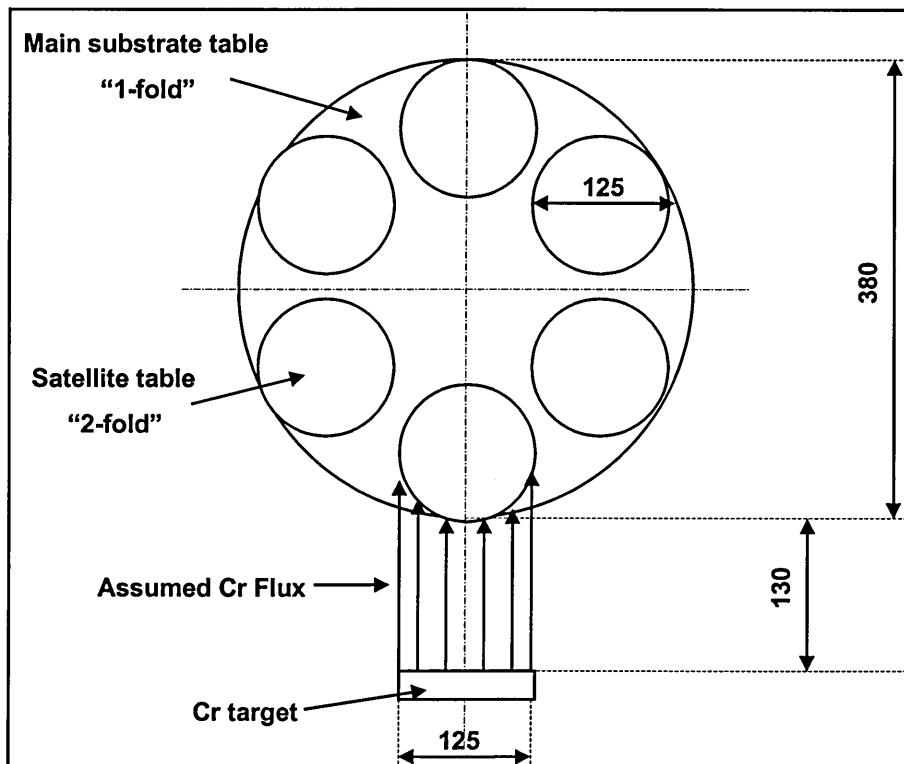


Figure 3.3. Overview of the assumed deposition situation.

Growth rate stationary:

$$\text{Rate } a_{\text{stat}} = (0,65 \times 7,5 \times 10^{19}) / (8.31 \times 10^{22}) / (12.5 \times 40) \times (1 \times 10^4) \times 3600 = 42.2 \text{ } \mu\text{m/h}$$

Growth rate 1-fold rotation:

$$\text{Rate } a_{1\text{-fold}} = (a_{\text{stat}} \times 12,5) / (\pi \times 38) = 4.4 \text{ } \mu\text{m/h}$$

Growth rate 2-fold rotation:

$$\text{Rate } a_{2\text{-fold}} = a_{1\text{-fold}} \times 38 / (6 \times 12.5) = 2.2 \text{ } \mu\text{m/h}$$

The difference between estimated and measured deposition rate of Cr is appr. 22 %, which seems to be reasonable with the assumptions made.

3.2. Characterisation techniques

3.2.1. X-Ray Diffraction (XRD):

Crystallographic texture, lattice parameters, stress status and phases can be determined by X-ray diffraction. A collimated X-ray beam from a x-ray tube, typically CuK_α -radiation, strikes the sample. Beam reflection will occur on crystallographic planes and intensity reinforcement takes place under Bragg's law conditions [121]:

$$n.\lambda = 2.d.\sin\theta$$

λ = wavelength of X-ray beam

n = order of diffraction, integral number

d = interplanar spacing

θ = Bragg angle

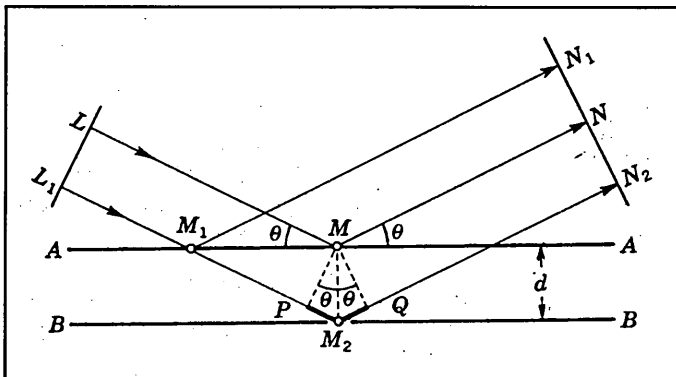


Figure 3.4. Bragg's law of reflection from planes of atoms in a crystal.

The specimens were examined by x-ray diffraction using both Bragg-Brentano and glancing angle parallel beam geometries.

3.2.1.1. Bragg-Brentano

This geometry was used for phase identification, lattice parameter determination, texture measurements, and peak broadening. In the hexagonal coatings with the Cr₂N phase the residual stress was also determined using asymmetric Bragg-Brentano geometry (omega tilting).

Phase identification:

Phase identification was carried by comparing the peak positions obtained from the coated specimens with that of standard data from the JCPDS file [41].

Lattice parameter:

Lattice parameter measurement is an indirect one. The lattice parameter of a substance is proportional to its interplanar spacing d . The value of d may be determined from Bragg's law

$$n.\lambda = 2.d.\sin\theta$$

hence from this a can be calculated. For a cubic crystal " a " is given by:

$$a = d\sqrt{(h^2 + k^2 + l^2)}$$

The precision of " d " and hence " a " depends on the precision of $\sin\theta$, not that of the measured quantity. An accurate value of $\sin\theta$ may be determined from a measure of θ , which itself is not precise, provided that θ is close to 90°. Although the error is zero at $2\theta = 180^\circ$, one cannot observe a reflected beam at this angle. Hence true value is obtained when 2θ is 180°, therefore a plot of " a " against 2θ and extrapolating to 180° should give a true value of lattice parameter " a ". In this work the lattice parameters, a_0 were plotted versus the Cohen-Wagner function [122,123] ($\cos\theta.\cot\theta$) in order to eliminate systematic errors. An extrapolation to $\cos\theta.\cot\theta = 0$ gives the lattice parameter a_0 .

Texture:

Texture, $T^*_{\{hkl\}}$ was determined in accordance with the Harris inverse pole figure technique [124,125]. Inverse pole figures offer a convenient method of depicting the

proportions of grains with various orientations referred to an unique axis. In coatings this is taken as the normal to the surface of the deposit. Under standard Bragg-Brentano conditions diffraction, using a diffractometer, takes place only from planes parallel to the surface of the sample, when surface and counter are inclined at θ and 2θ respectively to the X-ray beam, therefore the poles to each plane or plane normals are parallel to the normal to the surface of the deposit. In a powder material the $\{hkl\}$ Bragg reflections are oriented at random and the relative intensity of each reflection is characteristic of the phase. Inverse pole figures are represented in terms of T^* values, which are a measure of the statistical chance of any plane, $\{hkl\}$, lying in the plane parallel to the surface. For a particular plane, $\{hkl\}$, $T^*_{\{hkl\}}$ is evaluated as follows:

$$T^*_{hkl} = \frac{\frac{I_{(hkl)}}{R_{(hkl)}}}{\frac{1}{n} \sum_0^n \frac{I_{(hkl)}}{R_{(hkl)}}}$$

Where ' $I_{\{hkl\}}$ ' is the integrated intensity of the $\{hkl\}$ reflections from the textured specimen. These were determined by peak de-convolution using the Pearson fitting routine. ' $R_{\{hkl\}}$ ' is the intensity corresponding to a random sample, and 'n' is the number of reflections considered. Thus a ' T^* ' value of one signifies a random orientation, while for values greater than one, the plane is considered to have preferred orientation.

The value of ' $R_{\{hkl\}}$ ' was determined from:

$$R_{hkl} = QSI_o \cos ec\theta \left(\frac{1}{2 \frac{\mu}{\rho} \rho \cos ec\theta} \right) \left[1 - e^{-2 \frac{\mu}{\rho} \rho t \cos ec\theta} \right]$$

Where 'S' is the cross-sectional area of the beam, θ is the Bragg angle, 't' is the thickness of the coating, ' I_o ' is the intensity of the incident beam, ' μ/ρ ' is the mass absorption coefficient, ' ρ ' is the density, and 'Q' is given by the following expression:

$$Q = \frac{1}{v^2} [F^2 M(LP)]$$

Where 'F' is the structure factor and 'M' is the multiplicity factor, which allows for the contribution of equivalent planes to the reflection. LP is the Lorentz-Polarisation and factor v is the volume of the unit cell. Remark: $\text{Cosec } \theta = 1/\text{Sin } \theta$.

Peak Broadening:

Measuring the full width at half maximum (FWHM) of the x-ray diffraction peaks using a Pearson fitting routine were carried out to determine peak broadening. The contribution due to instrumental broadening was subtracted.

Residual Stress:

Residual stresses in the Cr₂N coatings were determined using a omega diffractometer. This method uses asymmetric Bragg-Brentano geometry i.e. $\theta/2\theta$ scans at different angles of tilt (i.e. omega angles). In this work the {41.1} Cr₂N peak was used for these measurements at omega tilt angles of 16, 24, 32, 40, 48 and 56 degrees. The peak position at each omega tilt position was determined using a Pearson peak fitting routine. The stress dependence of the interplanar spacing of the {41.1} plane, d_ψ is related by the equation [126]:

$$d_\psi = \sigma d_0 \left\{ \left[\frac{(1+\nu)}{E} \right] \sin^2 \psi - \frac{2\nu}{E} \right\} + d_0$$

where d_0 is the unstressed lattice parameter, E is the elastic modulus and ν is the Poisson's ratio. For the Poisson's ratio, a value of 0.3 corresponding to that of TiN was used. The omega tilt angle was used for the ψ angle. The stress can thus be determined from the slope of the least-squares fit of the plot of d_ψ versus $\sin^2 \psi$ [126,127]:

$$\sigma = \frac{\text{Slope } E}{a_0(1+\nu)}$$

3.2.1.2. Glancing Angle Parallel Beam Geometry

Residual stresses on the coatings which had a fcc-CrN structure were determined using glancing angle parallel beam [128]. For cubic structures the lattice parameters, $a_{hkl}(\psi)$ can be calculated for each diffraction peak where ψ is the angle between the

diffraction vector of plane {hkl} and the normal to the film surface, such that $\psi = \theta - \gamma$ where θ is the Bragg angle and γ is the angle of incidence of the x-ray beam relative to the specimen surface. The peak positions were determined using a Pearson fitting routine. For a thin film in a state of equi-biaxial stress the equation describing the stress dependence of the lattice parameter, a_ψ is related by the equation [126]:

$$a_\psi = \sigma a_0 \left\{ \left[\frac{(1 + \nu)}{E} \right] \sin^2 \psi - \frac{2\nu}{E} \right\} + a_0$$

where a_0 is the unstressed lattice parameter, E is the elastic modulus and ν is the Poisson's ratio. For the Poisson's ratio, a value of 0.3 corresponding to that of TiN was used. For the elastic modulus 250 GPa was taken. The stress can be determined from the slope of the least-squares fit of the plot of a_ψ versus $\sin^2 \psi$ [127,156]:

$$\sigma = \frac{\text{Slope } E}{a_0(1 + \nu)}$$

In addition the value for which $a_\psi = a_0$ is defined by the ratio:

$$\sin^2 \psi = \frac{2\nu}{1 + \nu}$$

In glancing angle geometry the penetration depth is defined as the distance, x_e from the surface that the diffracting planes in the specimen contribute to the whole diffracted intensity by the ratio 1/e [156]:

$$x_e = \frac{\sin \gamma \sin(2\theta - \gamma)}{\mu (\sin \gamma + \sin(2\theta - \gamma))}$$

3.2.2. Scanning Electron Microscopy (SEM)

Within the work the scanning electron microscope, type JEOL 840, has been used to study surface topography and fractured cross-sections of deposited coatings. The SEM uses a focussed primary electron beam typically 40 Å to 1 μm, which scans the sample surface. The excitation of the surface results in Auger electrons (typical escape depth 40 Å), secondary electrons (typical escape depth 100 Å), reflected primary electrons (typical escape depth 0.3 μm) and X-rays (typical escape depth 1 to 2 μm). The secondary emitted electrons from the sample are collected, amplified

and represented in an oscilloscopic picture. This means that the resolution is in the range of 40 Å. Qualitative elemental analysis is possible by measuring the specific energy levels of elements of the resulting X-rays (EDX). EDX has a spatial resolution in the range of 1 to 2 μm depending on the material and kV and detection of elements with atomic numbers greater than 4 can be achieved. As an alternative the X-rays can be collected on a wavelength dispersive detector (WDX) [129].

3.2.3. Transmission Electron Microscopy (TEM)

Thin materials become transparent to the electron beam. Typical specimen thickness in the range of 50 to 500 nm are used for electron microscopy (beam diameter approximately 1 μm) at acceleration potentials of 200 keV. The objective lens forms the diffraction pattern and the initial magnified image of the specimen. The final image is obtained by the magnification system (intermediate and projector lenses) and can be observed in bright or dark field mode on a fluorescent screen (figure 3.5.a).

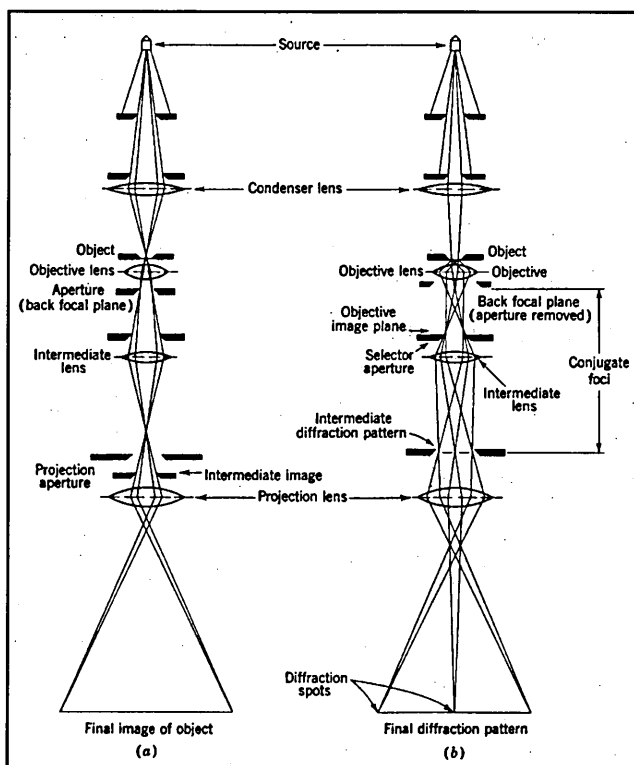


Figure 3.5. Arrangements of lenses and diaphragms in the TEM. (a) Transmission electron microscope and b) Selected Area Diffraction Pattern [130].

The images (500 to 1,000,000 times magnification) show information of grain shape, grain size and growth defects like dislocations, voids and gas inclusions.

Preferred growth directions of grains can be obtained from Selected Area Diffraction Patterns (SADP, figure 3.5.b). Diffraction of the electron beam on the crystal planes approximately parallel to the electron beam results in either diffraction spots for single crystals and circles for a large number of randomly oriented grains. The distance between the spots formed from the same plane $\{hkl\}$ or the diameter of an individual Debye ring is specific for a set of planes in a material.

3.2.4. Sputtered Neutral Mass Spectrometry (SNMS)

For elemental analysis and depth profiling the SNMS technique has been used. The sample is placed in an ultra high vacuum chamber ($\sim 10^{-10}$ mbar) and is bombarded by using a special designed ion gun. The sputtered neutrals are post-ionised and analysed by mass spectrometry (time of flight or quadrupole).

The instrument used within the current work uses a Ga-ion-source at an acceleration voltage of 16 kV. The sputtered flux from the sample consists of a mixture of neutrals and ions. Mainly neutrals are formed and the ratio between neutrals and ions is dependent on the elemental species. Therefore the flux is ionised within an electron beam (emission from a hot filament and about 300 eV acceleration). The ionised flux is accelerated through a series of filters and detected with a quadrupole mass spectrometer.

3.2.5. Hardness measurement

Classical Vickers and Knoop hardness measurements have been used within the work. As a general rule the indentation depth of the indenter should not exceed 10% of the coating thickness in order to avoid influences from the substrate.

So called nano-indentation methods overcome substrate influences, but at very low loads applied, the surface inhomogeneities of the coatings (oxide films), inhomogeneous film properties (macroparticles) and system hardware (including imperfect tip shape) become dominant. By dynamic loading and unloading of normal

forces on the indenter and measuring in parallel the indentation depth it is possible to separate elastic and plastic properties of the coating. The slope of the unloading curve (dF/dh) is equal to the Young's modulus E :

$$dF/dh = (2/\sqrt{\pi}) \cdot \beta \cdot \sqrt{A \cdot E_r}$$

F = Normal load

h = Indentation depth

β = Indenter shape factor

A = Projected contact area under maximum load

E_r = Effective elastic modulus, including small deformation of indenter

The universal hardness is taken at the maximum indentation depth. The intercept of the slope of the unloading curve with the indentation depth axis represents the plastic hardness value and correlates to the classical hardness measurements.

3.2.6. Scratchtest

A well-established method of measuring the coating to substrate adhesion quality is the scratchtest, also called the Revetest. Within the test a Rockwell diamond tip is moved over the coating surface and the normal load to the tip is increased continuously. The load at which first failure occurs is defined as the critical load L_c . Adhesion failures can be detected by monitoring acoustic emission during scratching or by optical measurements after scratching. In practice there are about 12 failure mechanisms [131], which can be either cohesive (adhesion failure inside the coating) or adhesive (separation of coating and substrate) in nature. Within this work mainly the "sideward lateral flaking" is reported. The measured values depend strongly on substrate material, substrate hardness, substrate roughness and coating thickness.

3.2.7. Rockwell indentation test

The classical Rockwell C hardness test is frequently used within the PVD field. It shows possible softening of the substrate materials due to annealing during the PVD cycle. It is also used to judge coating to substrate adhesion. The indentation is evaluated optically and cohesive and adhesive failures are classified, ranging from 1 to 6, representing very good to bad adhesion levels respectively [132].

3.2.8. Ball-cratering thickness test

The coating thickness of the samples within this work are determined using the ball cratering technique [132]. A rotating steel ball, diameter 20 mm, with a diamond slurry (particle size 1 μm) wears a crater through the coating, so-called calotte. Optical measurement of the calotte inner and outer diameter reveals the coating thickness:

$$h = (D^2 - d^2) / 8R$$

h = Coating thickness

R = Radius of ball

D = Outer diameter of calotte

d = Inner diameter of calotte

In addition to the coating thickness the calotte provides information about colour uniformity, particle inclusions and interface irregularities.

3.2.9. Surface roughness profiling

Macro-particles inclusions, etching methods and film growth contribute to the surface topography of deposited PVD coatings [133]. Surface roughness affects the film properties within certain applications, especially tribological contacts. Within the work

the roughness of the deposited coatings is measured by scanning the coating surface with a diamond tip. Two roughness values are reported:

* Roughness R_a , which is the arithmetic mean value of the departures of the roughness profile from the mean line, according to NEN 3632 [134].

* Roughness R_z , which is the average height of the profile irregularities in ten points, according to ISO/R 468 [134].

Although R_a is mostly recognised within the technical field, R_z is more critical in many applications of coatings. Peaks are of more influence in rolling and sliding contacts than valleys. It is important that the valleys do not extend to the coating substrate interface.

3.2.10. Stress measurement by the deflection method

Laser cut thin stainless steel discs ($\varnothing 30 \times 0.5$ mm) are deposited on one side. The disc deflection is measured before and after coating [120]. The total stress of the coating can be calculated:

$$\sigma_t = \{4 \cdot E_s \cdot d_s^2 \cdot (s_b - s_a)\} / \{3 \cdot (1 - \nu_s) \cdot d_c \cdot D_s^2\}$$

σ_t = total stress [GPa]

E_s = Young's modulus of the substrate [GPa]

d_s = thickness of substrate [mm]

s_b = height of sample before coating [mm]

s_a = height of sample after coating [mm]

ν_s = poisson's ratio of the substrate [-]

d_c = coating thickness [μm]

D_s = substrate diameter [mm]

The intrinsic growing stress and the thermal stress, the latter is induced by the difference in thermal expansion between substrate and coating (elevated deposition temperatures) sets the total stress.

$$\sigma_{th} = \{(\alpha_c - \alpha_s) * (T_d - T_r) * E_c\} / (1 - \nu_c)$$

σ_{th} = thermal induced stress [GPa]

α_c = coefficient of thermal expansion of the coating

α_s = coefficient of thermal expansion of the substrate

T_d = deposition temperature

T_r = temperature of stress measurement = room temperature

E_c = Young's modulus of the coating [GPa]

ν_c = poisson's ratio of the coating [-]

Typically the intrinsic growing stress divided by the layer thickness [GPa/ μm] is reported within the work.

3.2.11 Pin-on-disc

With the pin-on-disc test some tribological properties of coatings against different counter materials can be measured. Mainly the coefficient of friction μ (COF) and the wear fraction of the coating and the counter material (ball within the work) are observed.

The classical definition of the coefficient of friction is:

$$\mu = F_t / F_N$$

F_t = sliding force

F_N = normal force

Within the pin-on-disc test a coated cylindrical test coupon is rotated under a stationary ball, loaded with a pre-set normal force. The sliding force is monitored.

The resulting wear of this sliding test is typically abrasive or adhesive (also called galling and scuffing). Rolling contacts suffer also from fatigue wear [1].

Other possible wear mechanisms are fretting, corrosion, electrical arcing and erosion.

The wear rate of the coating k can be quantified by the Archard equation:

$$k = V / (F_N * d)$$

V = Worn off volume [m^3]

F_N = normal force [N]

d = sliding distance [m]

3.2.12. Corrosion testing

Corrosion testing was limited to electrochemical behaviour in 3 % NaCl solutions. Within an electrochemical cell the polarisation was observed under anodic potentiodynamic conditions, according to ASTM G59-91; Scanning voltage from – 1000mV till +1200 mV at a scanrate of 0.5 mV/sec. The working potential is measured against a saturated calomel electrode in a KCl solution through a salt bridge. The polarisation current is measured over a pair of auxiliary electrodes.

CrN coatings are noble compared to steel based substrates. Any coating defect which extends from the coating/steel substrate interface to the coating surface (pinhole) will lead to increased galvanic corrosion attack at these sites, because the exposed substrate surface area (anode) is small compared to the coated area (cathode) [135]. CrN coatings show initially passivation of Cr by the formation of protective oxides. Relative low anodic currents are observed. At a critical polarisation voltage E_{pit} the chloride ions present break down the passive behaviour and severe pitting occurs. The anodic current increases rapidly.

3.2.13. Colourimetry

The coating composition and structure correspond to very reproducible light reflections. With a spectrophotometer the light reflection of a coating can be quantified by colour co-ordinates [136-138]. Within the the colour co-ordinates L^* , a^* , b^* are reported, responding to:

$0 < L^* < 100$; Lightness changing from black to white

$-60 < a^* < +60$; Chromaticity changing from green to red

$-60 < b^* < +60$; Chromaticity changing from blue to yellow.

Basically a flat sample is illuminated by a diffuse light source. Reflected light, under an angle of 8° normal to the specimen surface, is transmitted to a spectral sensor by an optical fibre. The light is split by wavelength in 10 nm pitch, within the range from 400 to 700 nm. The different light intensities are converted to electrical currents by silicon photodiode array and recalculated to the specific colour co-ordinate systems.

Chapter 4 – Results

This chapter is divided into 5 segments. The first 3 sections describe the effect of nitrogen flow rate, substrate bias voltage and magnetic field strength (controlling ion bombardment) on the growth, structure and properties of CrN_x films. Within chapter 4.4 there is attention for the effect of different etching species prior to deposition and thin arc deposited interlayers on subsequently sputter deposited CrN_x. The last section shows mechanical and corrosion data of CrN_x under specific deposition conditions.

4.1. Influence of nitrogen flow rate on unbalanced magnetron sputtered CrN_x

4.1.1. Overview of the experiments

During the different stages of the research the amount of nitrogen was varied in very narrow steps applying 3 different substrate bias voltage levels, namely -75 V, -100 V and -200 V. The process sequence was according to table 3.3. In the etching process an argon glow discharge only was used without interlayers. During the deposition the two UBM coils were each set at 20 A.

At -100 V substrate bias the bcc-Cr and hcp-Cr₂N phase fields were studied at smaller increments of nitrogen flow rate.

An overview of the range of nitrogen variations in the experiments is presented in table 4.1:

Substrate Bias [V]	Nitrogen flow rate [sccm]																		
	0	15	25	30	35	40	45	50	55	60	65	75	100	125	150	200	250	300	500
-75								X					X	X		X			
-100	X	X	X	X	X	X	X	X	X	X	X	X	X		X	X			
-200													X			X	X	X	X

Table 4.1. Experiments with nitrogen flow rate variation.

4.1.2. Influence of the nitrogen flow rate on the deposition parameters

Within reactive magnetron sputtering of Cr targets in an argon/nitrogen atmosphere nitriding activity at the target surface occurs. As there is only marginal sputtering adjacent to the racetrack, nitrogen compounds are formed (“poisoning”). Formation of compounds inside the racetrack affects the sputter yield, because the target surface behaves as a compound material with a reduced sputtering yield. Thus, the amount of reactive gas necessary to form identical stoichiometry is less. If the reactive gas flow is maintained at a constant level then an increase in pressure will occur [139]. Reducing the amount of nitrogen gas will not always immediately lower the pressure of the reactive gas, as re-sputtered nitrogen becomes available from the racetrack. After sputter cleaning the racetrack, the total pressure will drop to the initial level. This behaviour is known as hysteresis of reactive sputtering. The hysteresis can be substantially reduced if an effective pumping speed higher than the critical pumping speed is employed [140].

This critical pumping speed is material dependent and is related to the total target surface area in sputtering mode. Strong hysteresis behaviour makes reactive gas control very difficult to deposit stoichiometric coatings [139,141,142]. Figure 4.1 shows the “hysteresis” behaviour of Cr with nitrogen for the used experimental sputtering equipment, with obviously high pumping speed (2200 l/s, turbo molecular pump). Further deposition conditions are: sputtering power 5 kW DC, argon flow 160 sccm, target surface area 400 x 125 mm, bias voltage –100 V, unbalanced magnetron coils at 20 A and at 250 °C substrate temperature.

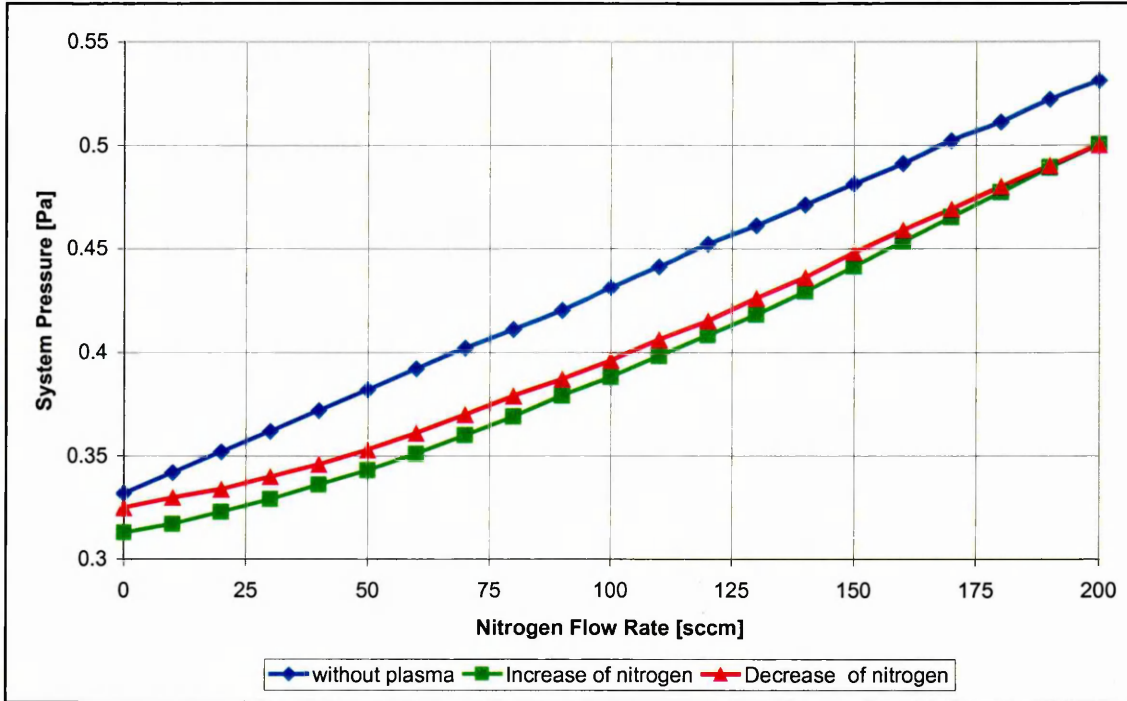


Figure 4.1. Cr-N Hysteresis characteristics of experimental sputtering system; total pressure.

It shows that the sputtering occurs beyond the critical pumping speed. The almost linear increase of the total pressure with increased nitrogen flow rate indicates little or no target poisoning. This makes it very easy to control the discharge precisely and to investigate the effect of very small increments of nitrogen flow rate on the film properties. This is not the case for systems with pronounced hysteresis effects. In parallel the target voltage has been monitored and is shown in figure 4.2:

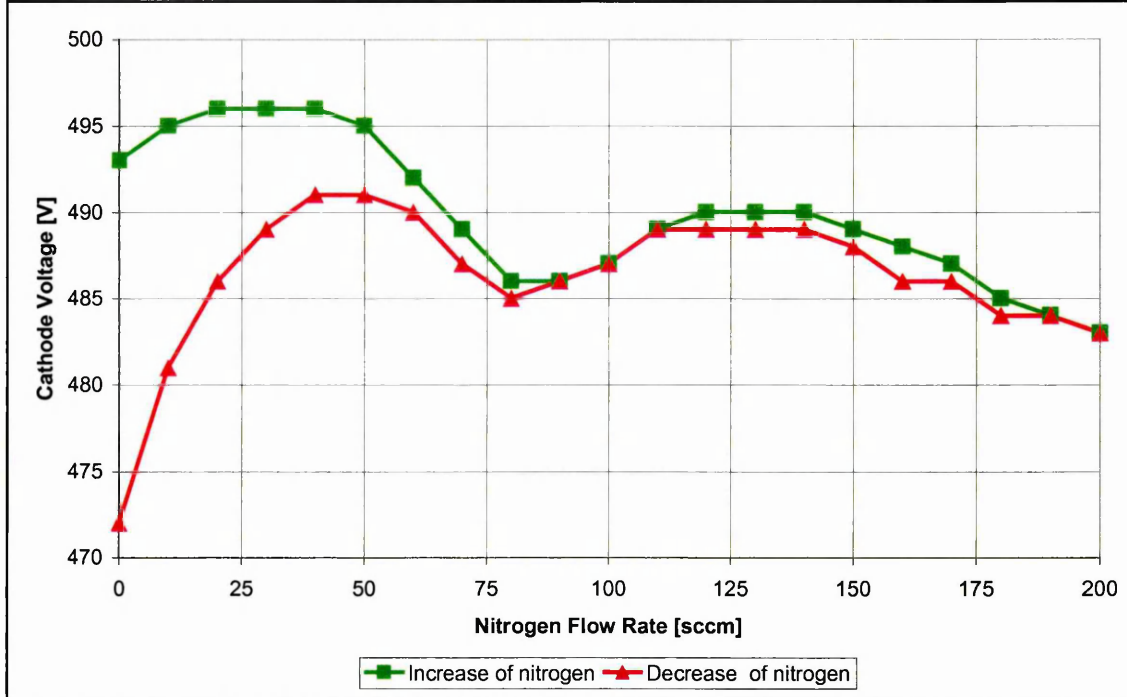


Figure 4.2. Cr-N Hysteresis characteristics of experimental sputtering system; cathode voltage.

There are two voltage maxima. The first at approximately 40 sccm and the second at around 130 sccm nitrogen flow rate respectively. Identical behaviour was reported by Kuruppu et al. [81], and could be correlated to the deposition of hcp-Cr₂N and fcc-CrN respectively. In general the target voltage stays within a narrow band-width of approximately 25 V up to 0.18 Pa of nitrogen partial pressure. Sproul et al. [143] reported a voltage change of 60 Volts for Ti at a nitrogen partial pressure of 0.07 Pa.

As pointed out previously the deposition rate is in general decreasing with increasing amount of nitrogen flow rate because of the lower sputter yield as shown in figure 4.3. It can be assumed that the sputter rate is linearly dependent on the target power density.

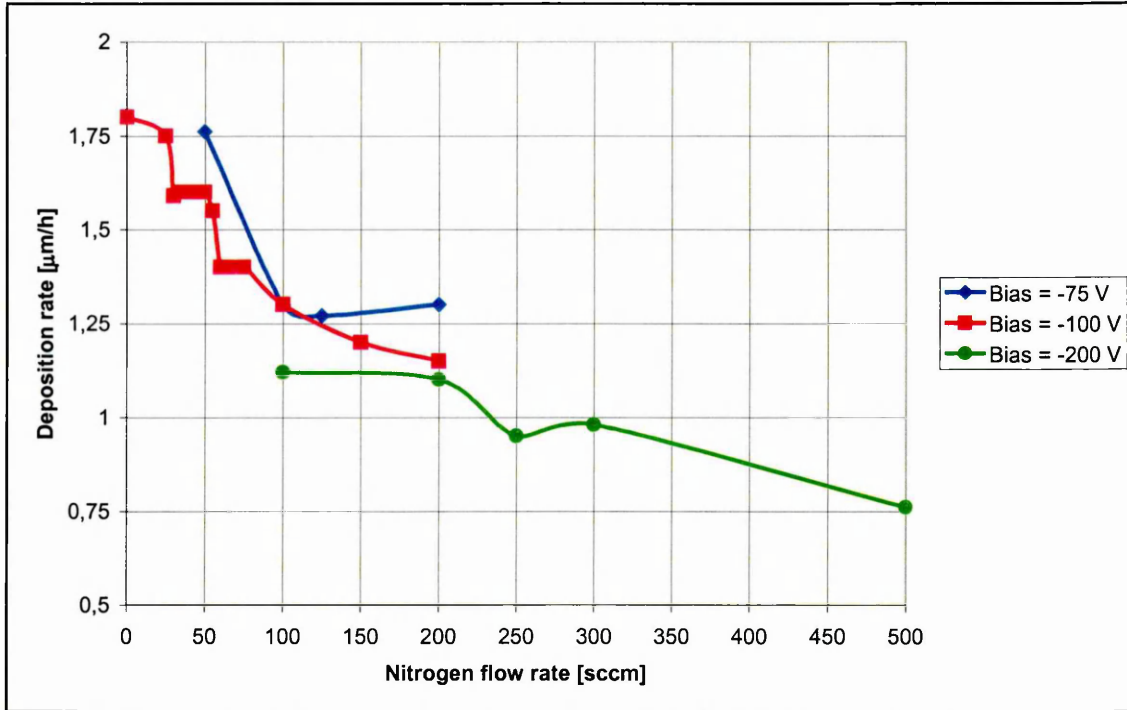


Figure 4.3. Deposition rate dependent on the nitrogen flow rate.

Despite limitations in the accuracy of the calo-test, which was used for the measurement of the layer thickness, it is clear that the deposition rate decreases with increasing substrate bias voltage. This results from the increased energy of impinging ions and hence higher re-sputtering rates of the growing coating.

For the experimental conditions used the deposition rate decreases by approximately 30 % when the nitrogen flow rate is increased to the same level of the argon flow rate (i.e. 160 sccm). Compared with Ti, Cr exhibits indeed a very low target poisoning effect. Sproul et al. [143] reported for reactive magnetron sputtering of TiN from Ti targets a loss of the deposition rate of 69 % at a nitrogen partial pressure of 0.07 Pa compared to the non-reactive deposition of Ti.

In addition to the reduction in sputtering rate due to target poisoning, a further reduction in deposition rate can be expected, because of the increased number of nitrogen ions (N_2^+ .28, N^+ .14) relative to the number of Ar ions (Ar^+ .40). Any reduction of the rate can be expected, since nitrogen is replacing partly the argon in the total target current. This lighter element sputters at a lower yield.

4.1.3. X-Ray diffraction (Bragg Brentano high angle scan)

4.1.3.1. Phase development

The different phases in the Cr-N system were identified using X-ray diffraction, with the JCPDS standards file used as the reference. The figures 4.4 to 4.12 show the following phase development at a substrate bias voltage of -100 V:

$f_{N_2} = 0$ sccm	bcc-Cr
0 sccm $< f_{N_2} < 25$ sccm	expanded bcc-Cr-N
25 sccm $< f_{N_2} < 35$ sccm	mixed bcc-Cr-N and hcp-Cr ₂ N
35 sccm $< f_{N_2} < 55$ sccm	hcp-Cr ₂ N
55 sccm $< f_{N_2} < 75$ sccm	mixed hcp-Cr ₂ N and fcc-CrN
$f_{N_2} > 75$ sccm	fcc-CrN

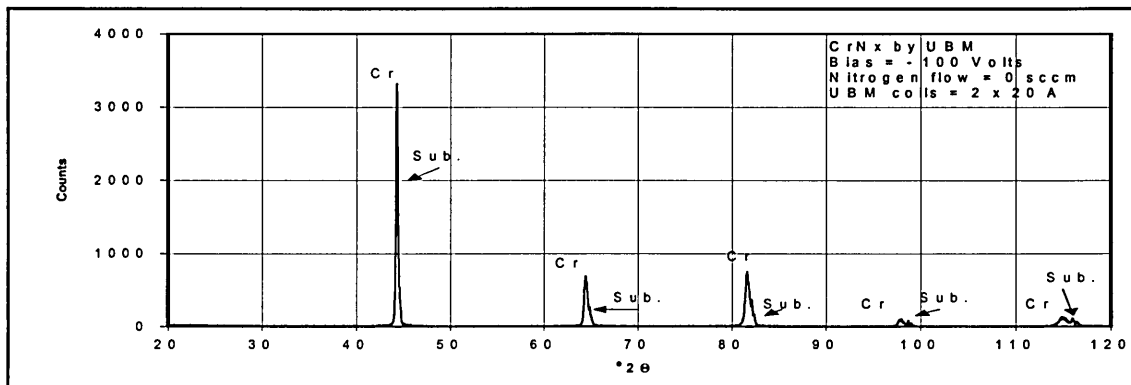


Figure 4.4. X-Ray diffraction pattern of bcc-Cr at -100 V bias and 0 sccm nitrogen flow rate.

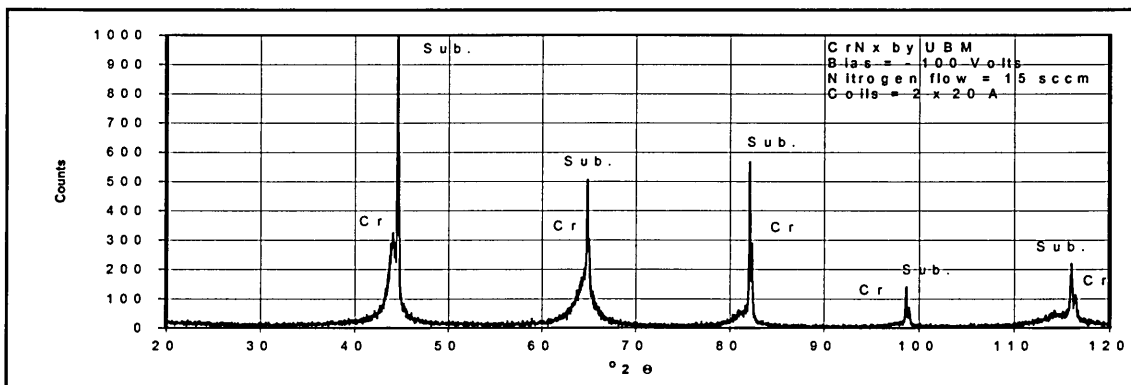


Figure 4.5. X-Ray diffraction pattern of bcc-Cr-N at -100 V bias and 15 sccm nitrogen flow rate.

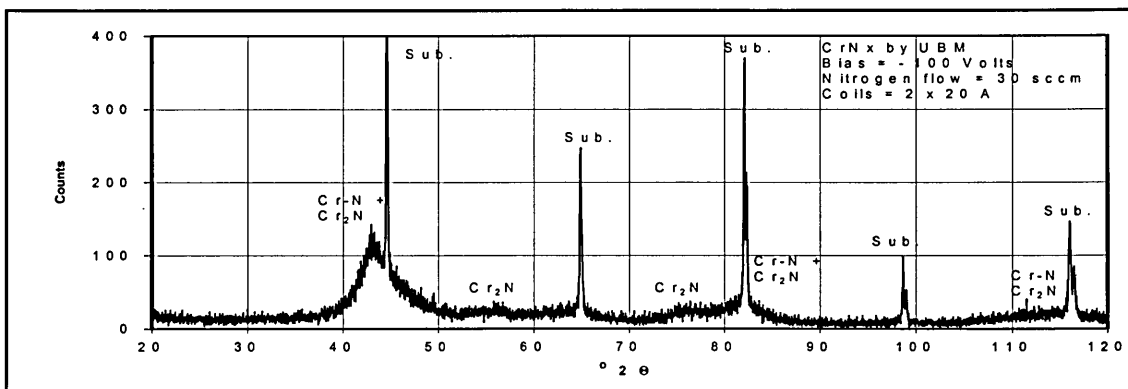


Figure 4.6. X-Ray diffraction pattern of CrN_x at -100 V bias and 30 sccm nitrogen flow rate (mixed phases bcc-Cr-N and hcp- Cr_2N).

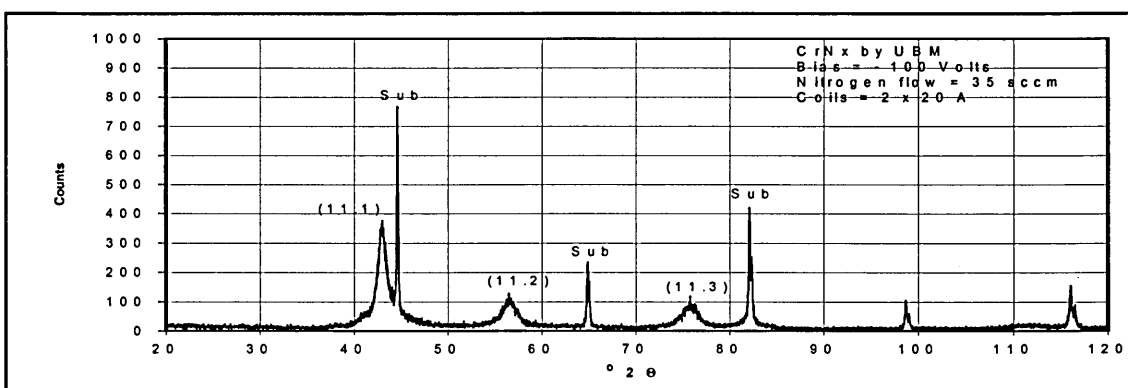


Figure 4.7. X-Ray diffraction pattern of hcp- CrN_x at -100 V bias and 35 sccm nitrogen flow rate.

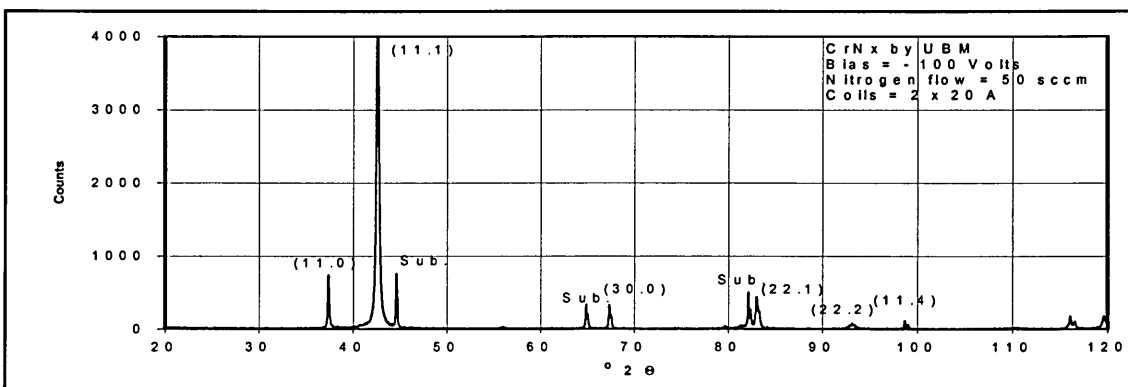


Figure 4.8. X-Ray diffraction pattern of hcp- CrN_x at -100 V bias and 50 sccm nitrogen flow rate.

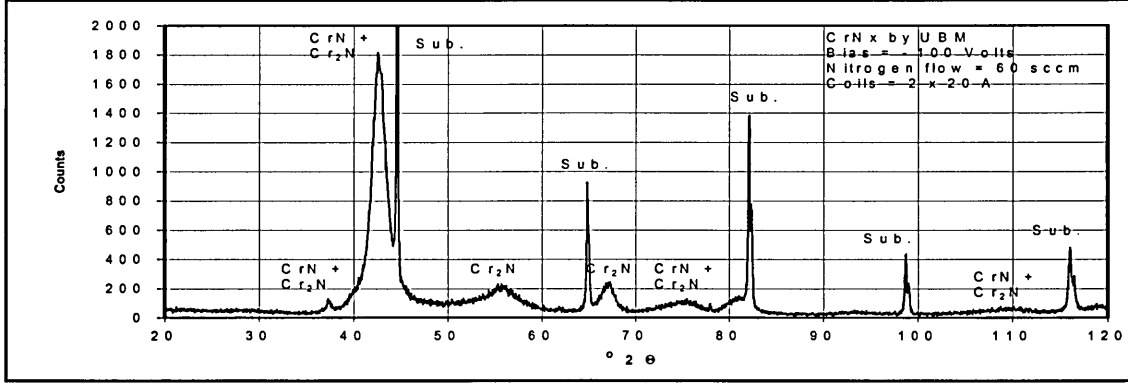


Figure 4.9. X-Ray diffraction pattern of CrN_x at -100 V bias and 60 sccm nitrogen flow rate (mixed phases hcp- Cr_2N and fcc- CrN)

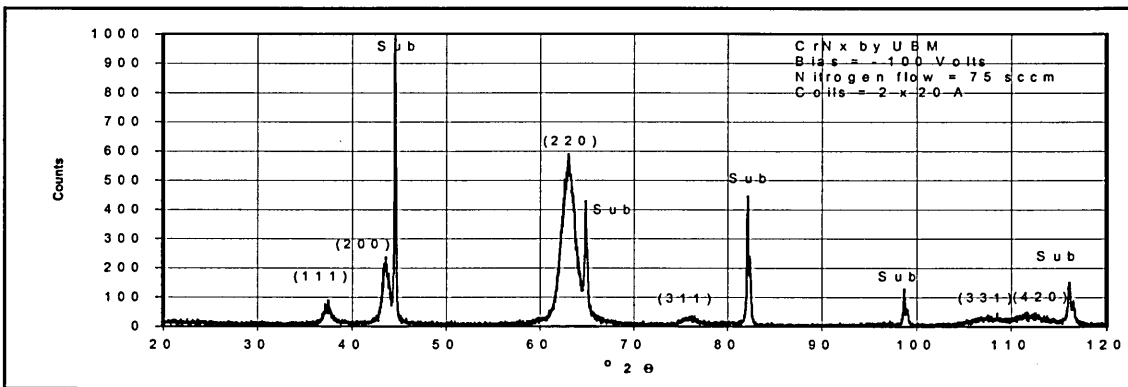


Figure 4.10. X-Ray diffraction pattern of fcc- CrN_x at -100 V bias and 75 sccm nitrogen flow rate.

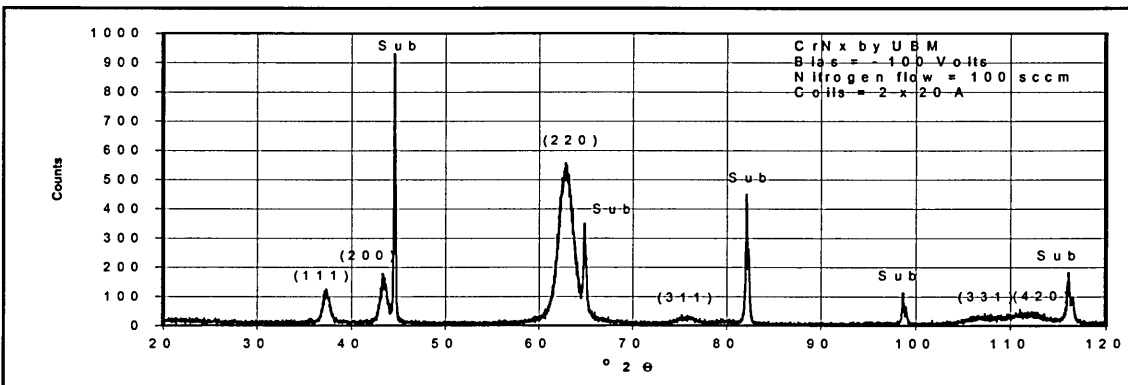


Figure 4.11. X-Ray diffraction pattern of fcc- CrN_x at -100 V bias and 100 sccm nitrogen flow rate (fcc- CrN).

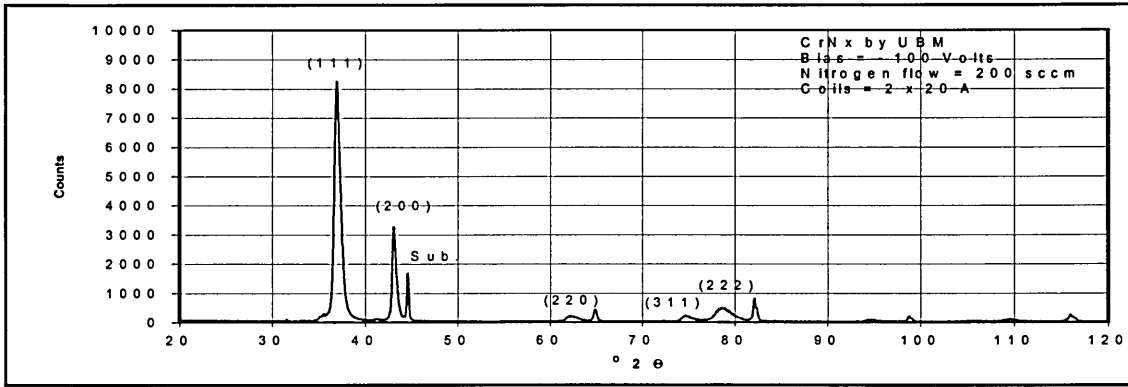


Figure 4.12. X-Ray diffraction pattern of fcc-CrN_x at -100 V bias and 200 sccm nitrogen flow rate (fcc-CrN).

For the fcc-CrN phase scans the influence of the nitrogen flow rate at a substrate bias voltage of -75 V and -200 V are presented in figures 4.13 to 4.15 and 4.16 to 4.19 respectively. All the Bragg-Brentano scans show clearly a fcc-CrN phase.

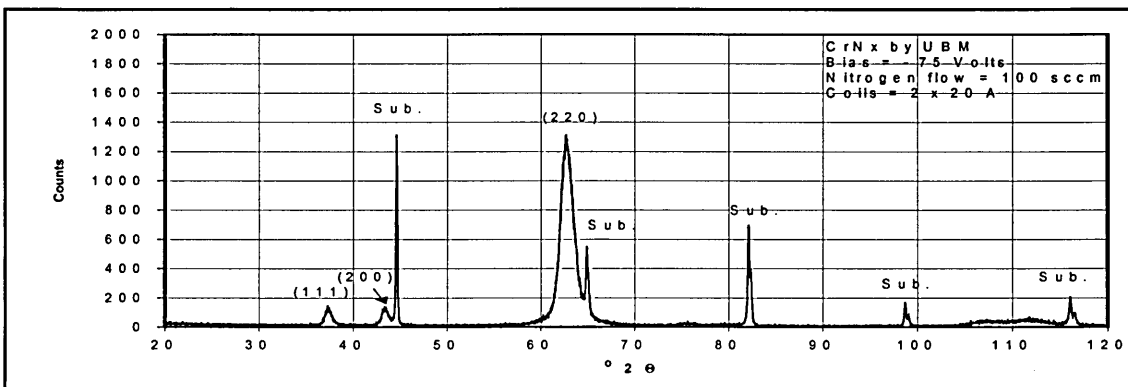


Figure 4.13. X-Ray diffraction pattern of fcc-CrN_x at -75 V bias and 100 sccm nitrogen flow rate.

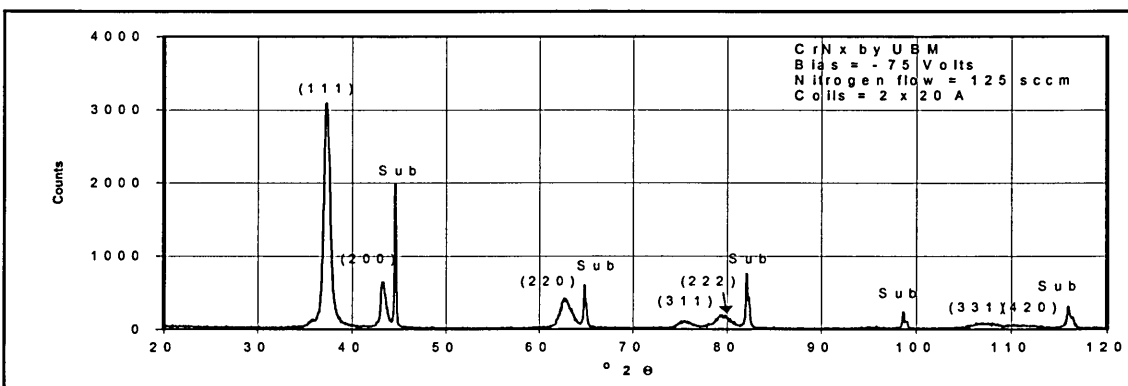


Figure 4.14. X-Ray diffraction pattern of fcc-CrN_x at -75 V bias and 125 sccm nitrogen flow rate.

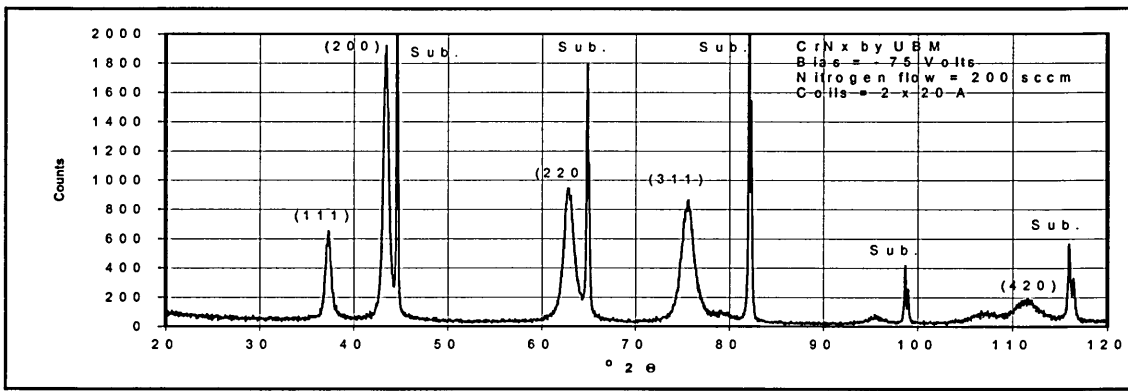


Figure 4.15. X-Ray diffraction pattern of fcc-CrN_x at -75 V bias and 200 sccm nitrogen flow rate.

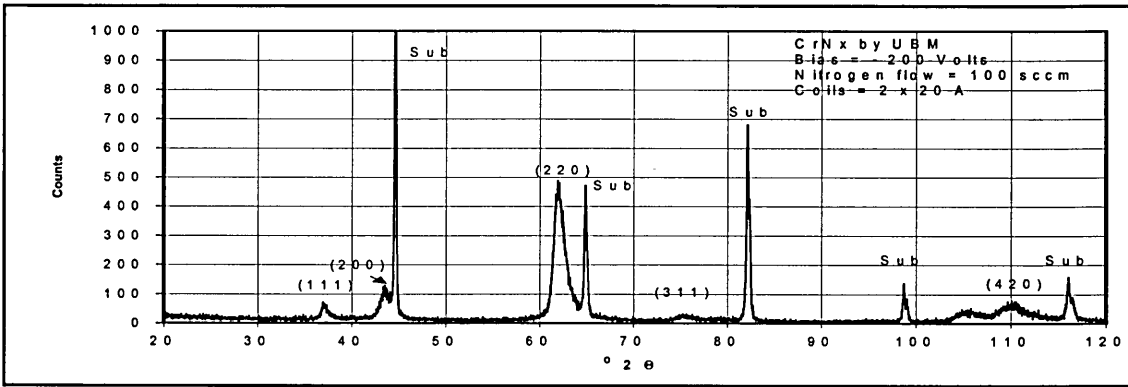


Figure 4.16. X-Ray diffraction pattern of fcc-CrN_x at -200 V bias and 100 sccm nitrogen flow rate.

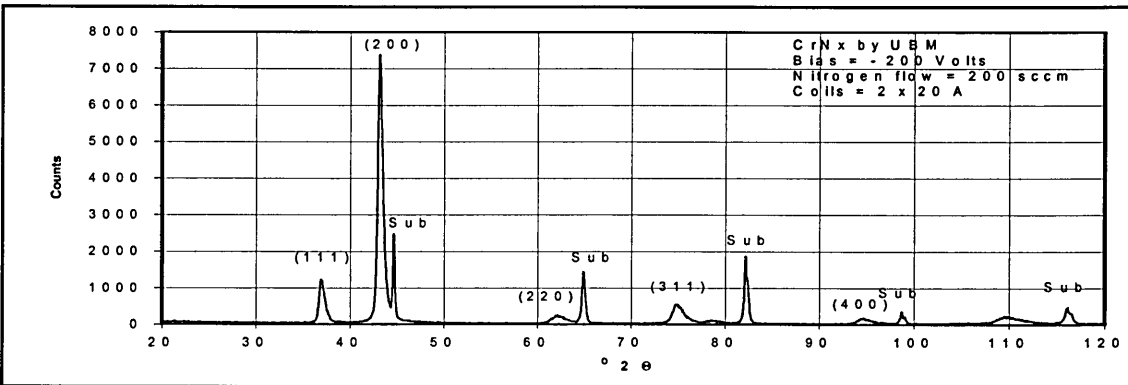


Figure 4.17. X-Ray diffraction pattern of fcc-CrN_x at -200 V bias and 200 sccm nitrogen flow rate.

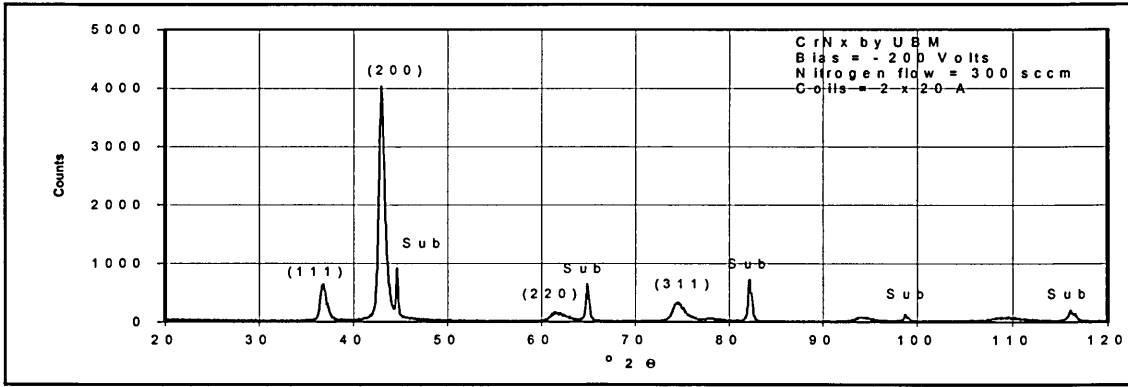


Figure 4.18. X-Ray diffraction pattern of fcc-CrN_x at -200 V bias and 300 sccm nitrogen flow rate.

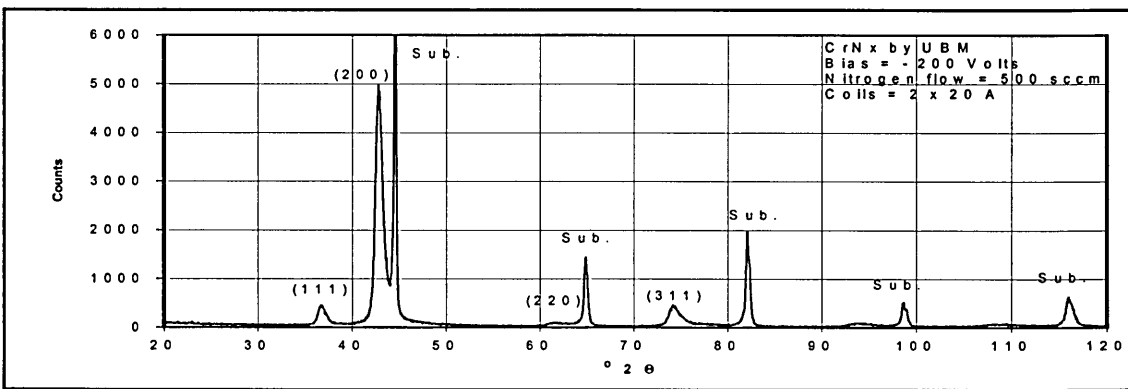


Figure 4.19. X-Ray diffraction pattern of fcc-CrN_x at -200 V bias and 500 sccm nitrogen flow rate.

4.1.3.2. Texture

The texture of the deposited films depends on the deposition parameters (paragraph 4.1.2 and tables 4.2, 4.3 and 4.4).

F _{N2} [sccm]	Texture parameter T* [%] for Cr-N			
	{110}	{200}	{211}	{310}
0	17	37	32	15
15	11	65	11	12
25	18	37	30	17

Table 4.2. Texture parameter T* for bcc-Cr-N as a function of nitrogen flow rate at U_B=-100V.

F_{N_2} [sccm]	Texture parameter T^* [%] for Cr_2N					
	{11.0}	{11.1}	{22.1}	{22.3}	{31.3}	{41.1}
35	0	4	0	10	61	0
40	2	16	3	51	0	20
50	15	27	18	6	0	20

Table 4.3. Texture parameter T^* for hcp- Cr_2N as a function of nitrogen flow rate at $U_B = -100V$.

F_{N_2} [sccm]	Texture parameter T^* [%] for CrN		
	{111}	{100}	{110}
75	7	8	79
100	4	10	67
150	61	5	4
200	70	15	3

Table 4.4. Texture parameter T^* for fcc-CrN as a function of nitrogen flow rate at $U_B = -100V$.

The pure Cr and solid solution Cr-N exhibit a {100} preferred orientation. The β - Cr_2N rich coatings tend to change from strongly preferred {31.3} orientation to a much weaker preferred {11.1} orientation as the nitrogen flow rate is increased from 35 sccm to 50 sccm.

The effect of nitrogen flow rate on the texture development in fcc-CrN coatings deposited at a substrate bias voltages of $-100 V$ is represented in figure 4.20. At this bias voltage level the preferred orientation changes from a strong {110} to a strong {111} texture when the nitrogen flow rate is increased from 75 to 200 sccm. In contrast at a bias voltage level of $-200V$ the {100} orientation becomes dominant as high nitrogen flow rate is increased from 100 to 500 sccm (table 4.5 and figure 4.21). Summarising the change over from {110} preferred orientation to either {111} or {100} can be clearly correlated to the ratio of the nitrogen to argon flow rate (f_{N_2}/f_{Ar}). If $f_{N_2}/f_{Ar} < 1$ and the substrate bias voltage is between $-75V$ and $-200V$, which is typical for

most of the published literature in reactive magnetron sputtering, than the preferred {110} orientation is developed.

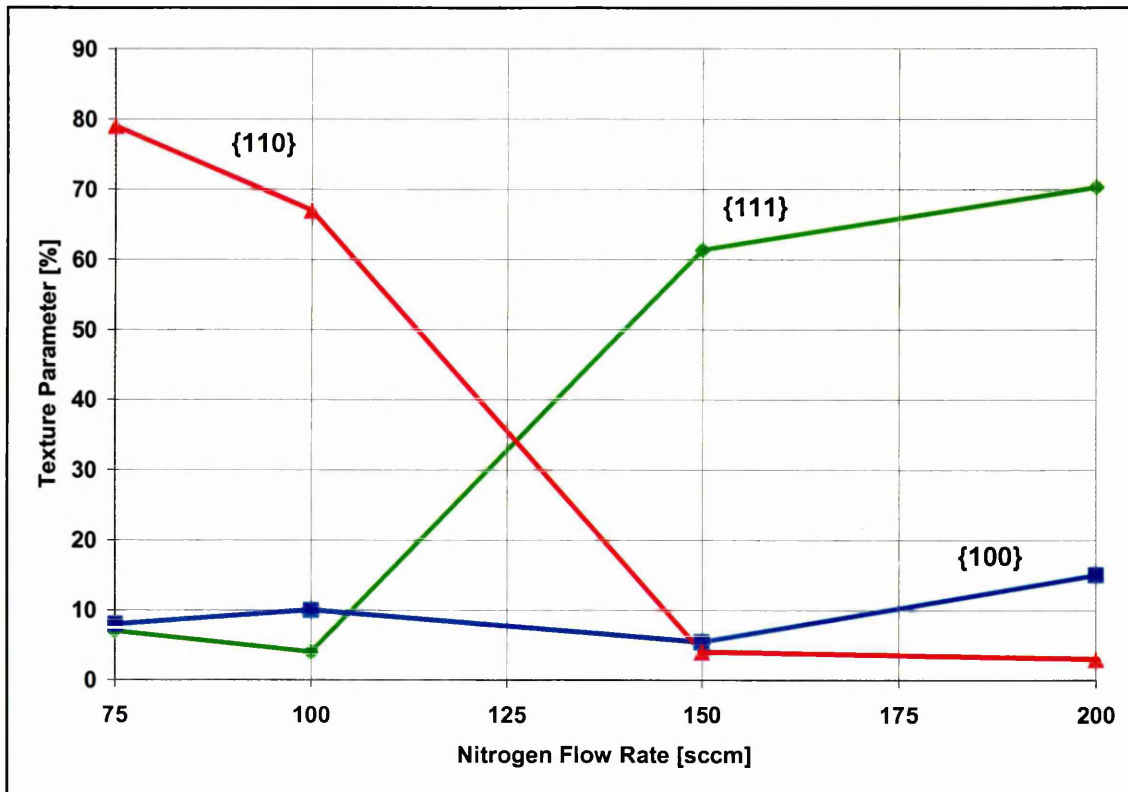


Figure 4.20. Effect of nitrogen flow rate on texture development of fcc-CrN_x at -100 V bias.

F _{N2} [sccm]	Texture parameter T* [%] for CrN		
	{111}	{100}	{110}
100	3	3	80
200	11	55	5
250	8	57	1
300	10	56	7
500	5	60	3

Table 4.5. Texture parameter T* for fcc-CrN as a function of nitrogen flow rate at U_B=-200V.

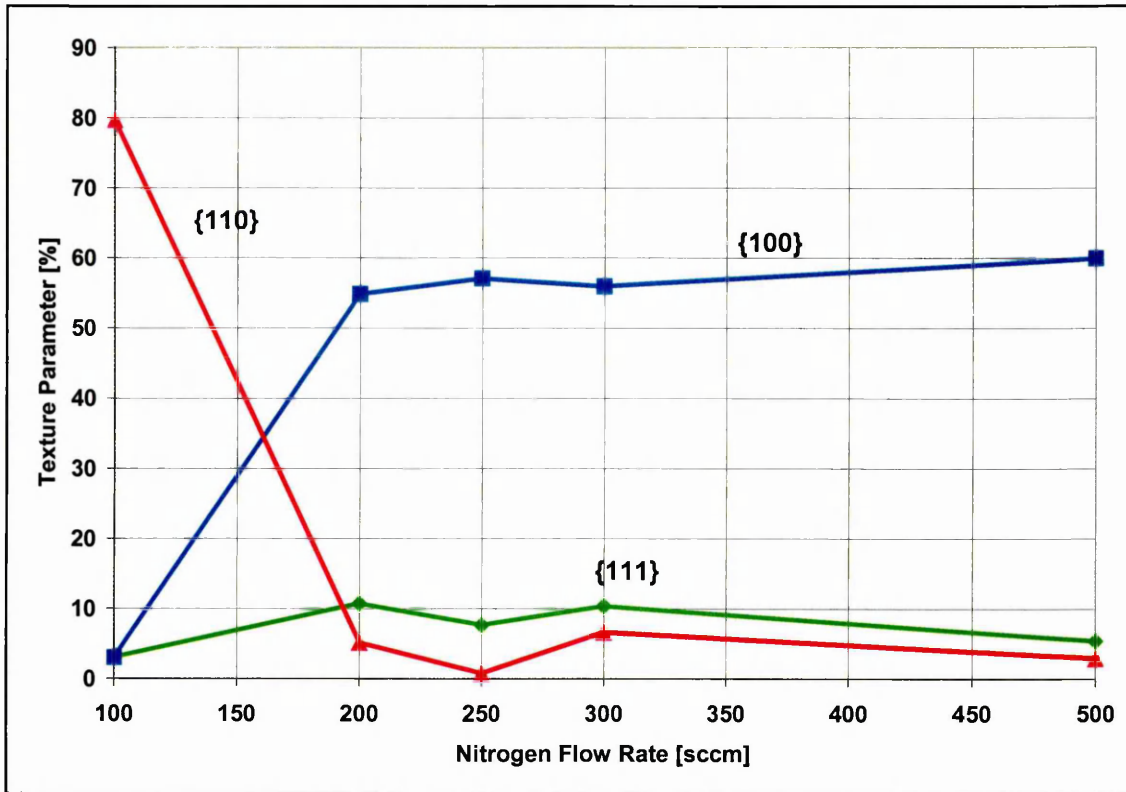


Figure 4.21. Effect of nitrogen flow rate on texture development of fcc-CrN_x at -200 V bias.

4.1.3.3. Interplanar spacing and peak broadening

The change in interplanar spacing and peak broadening as a function of different nitrogen flow levels is shown in tables 4.6 to 4.10. At a bias voltage of -100 V the peak positions of the pure bcc-Cr ($f_{N_2}=0$ sccm) is almost identical to the JCPDS standard. The lack of stress is reflected by the sharp peaks and by the low values of peak broadening. The solid solution of nitrogen into the Cr lattice results in a larger interplanar spacing and an increase of the peak broadening. The same effect is reported by Rebholz et al. [144].

The X-ray diffraction patterns of the hcp-Cr₂N coatings change over from broad to sharp peaks when the nitrogen flow level is increased from 35 to 50 sccm. In parallel the interplanar spacing changes from less than bulk values to those of the bulk values. This indicates that a significant residual stress was present in the Cr₂N coatings deposited at the lower nitrogen flow rate level of $f_{N_2}=35$ sccm.

F _{N2} [sccm]	Interplanar Spacing [Å] Relative to JCPDS [%]			Peak Broadening FWHM [°2θ]		
	{110}	{200}	{211}	{110}	{200}	{211}
JCPDS	2.040	1.442	1.177	-	-	-
0	2.040 0	1.443 0.076	1.178 0.085	0.07	0.19	0.31
15	2.054 0.69	1.444 0.15	1.181 0.34	1.47	2.39	2.29
25	2.081 2.01	1.449 0.49	1.184 0.59	4.02	4.07	6.09

Table 4.6. Interplanar spacing and peak broadening (FWHM) for bcc-Cr-N at U_B=-100V

F _{N2} [sccm]	Interplanar Spacing [Å] Relative to JCPDS [%]			Peak Broadening FWHM [°2θ]		
	{11.1}	{11.2}	{22.2}	{11.1}	{11.2}	{22.2}
JCPDS	2.120	1.641	1.060	-	-	-
35	2.100 -0.94	1.628 -0.80	1.054 -0.57	1.48	1.84	3.84
40	2.105 -0.71	1.632 -0.25	1.053 -0.66	0.29	0.80	0.81
50	2.120 0	1.641 0	1.061 0.09	0.28	0.46	0.69

Table 4.7. Interplanar spacing and peak broadening (FWHM) for hcp-Cr₂N at U_B=-100V

Evaluation of the X-ray diffraction data of fcc-CrN coatings shows that the peak broadening tends to decrease at moderate bias voltage levels (-75 V to -100 V) and to increase at a higher bias voltage level (-200 V) as the nitrogen content increases. The interplanar spacing increases with increasing flow rates for all 3 bias voltage

levels. The large increase in both the interplanar spacing and the peak broadening in the coatings deposited at the high bias voltage and high nitrogen flow rate indicates the development of very high internal stress levels, as will be shown later.

F _{N2} [sccm]	Interplanar Spacing [Å] Relative to JCPDS [%]			Peak Broadening FWHM [°2θ]		
	{111}	{200}	{220}	{111}	{200}	{220}
JCPDS	2.394	2.068	1.463	-	-	-
100	2.406 0.51	2.083 0.72	1.482 1.29	0.59	0.68	1.03
125	2.411 0.71	2.093 1.21	1.482 1.27	0.51	0.55	0.89
200	2.412 0.77	2.084 0.78	1.479 1.06	0.50	0.50	0.88

Table 4.8. Interplanar spacing and peak broadening (FWHM) for fcc-CrN at U_B=-75V

F _{N2} [sccm]	Interplanar Spacing [Å] Relative to JCPDS [%]			Peak Broadening FWHM [°2θ]		
	{111}	{200}	{220}	{111}	{200}	{220}
JCPDS	2.394	2.068	1.463	-	-	-
75	2.400 0.25	2.074 0.29	1.470 0.47	0.84	0.75	1.53
100	2.407 0.54	2.082 0.68	1.477 0.96	0.71	0.77	1.66
150	2.421 1.13	2.096 1.35	1.483 1.37	0.54	0.36	0.83
200	2.433 1.63	2.100 1.55	1.488 1.71	0.57	0.34	0.79

Table 4.9. Interplanar spacing and peak broadening (FWHM) for fcc-CrN at U_B=-100V

F _{N2} [sccm]	Interplanar Spacing [Å] Relative to JCPDS [%]			Peak Broadening FWHM [°2θ]		
	{111}	{200}	{220}	{111}	{200}	{220}
JCPDS	2.394	2.068	1.463	-	-	-
100	2.421 1.13	2.075 0.34	1.499 2.46	0.51	0.76	0.99
200	2.435 1.71	2.097 1.40	1.494 2.12	0.54	0.44	1.16
250	2.452 2.42	2.110 2.03	1.504 2.80	0.47	0.38	0.64
300	2.449 2.30	2.106 1.84	1.507 3.01	0.58	0.51	1.39
500	2.450 2.34	2.113 2.18	1.511 3.28	0.72	0.61	2.69

Table 4.10. Interplanar spacing and peak broadening (FWHM) for fcc-CrN at U_B=-200V

For the CrN coatings deposited at U_B=-100 V and U_B=-200 V the lattice parameter a₀ vs nitrogen flow rate is plotted in figure 4.22. A lattice parameter increase up to 4.258 Å was measured at f_{N2}=500 sccm, compared to the unstressed JCPDS value of 4.1465 Å. This indicates high internal compressive stress for these modified coatings which are deposited at high nitrogen flow (>200 sccm) and high bias voltage levels (-200 V).

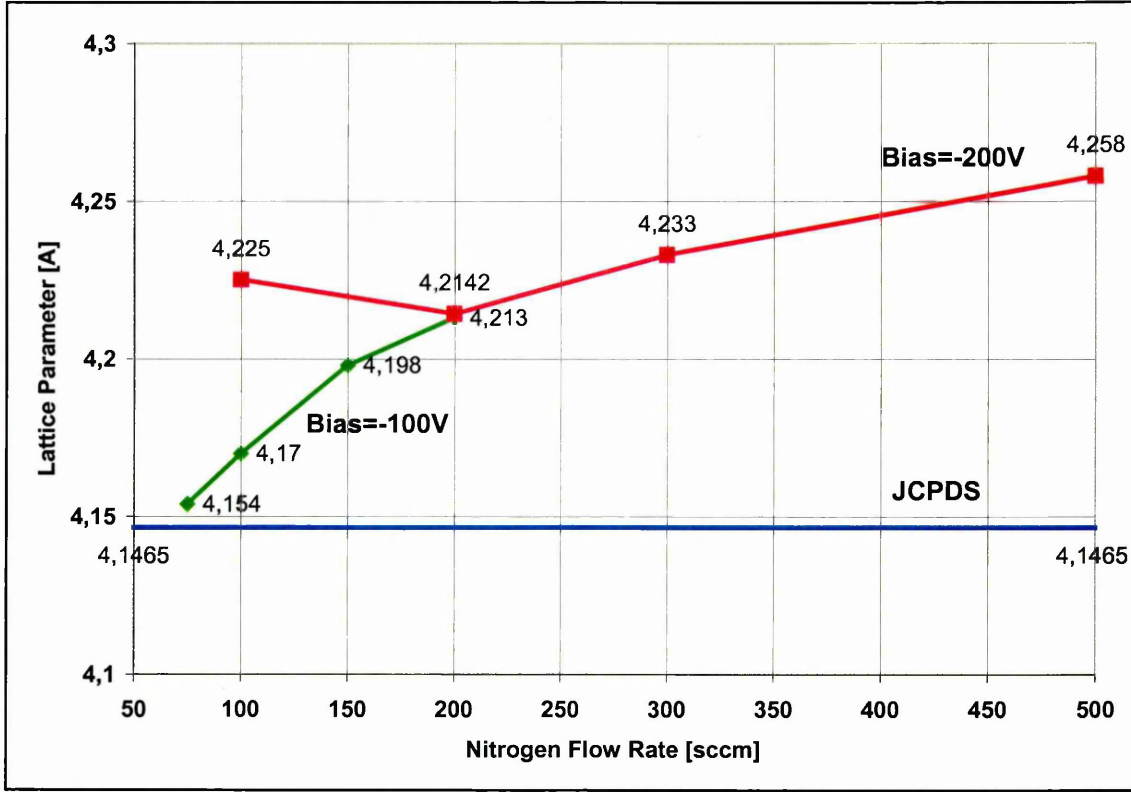
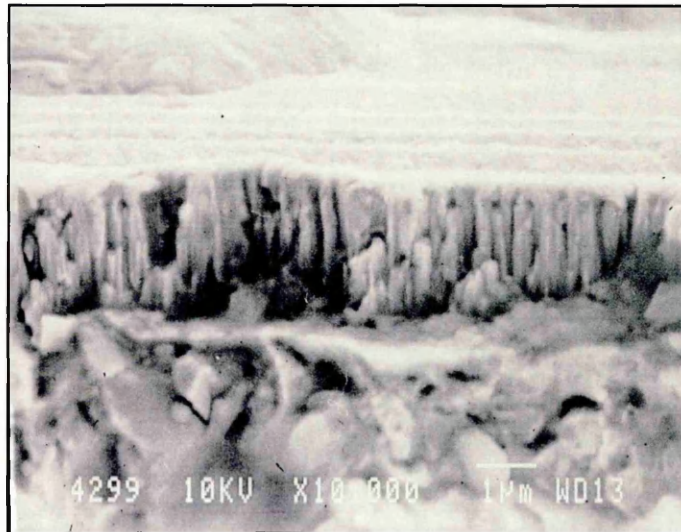


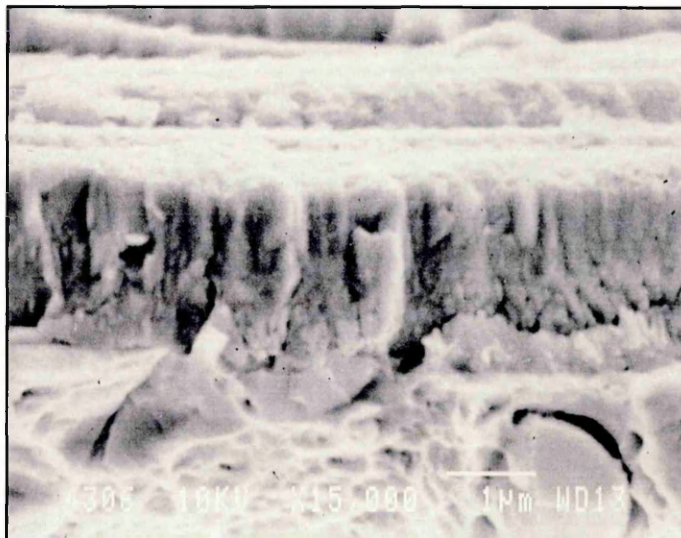
Figure 4.22. Effect of nitrogen flow rate on lattice parameter at $U_B = -100$ and -200 V

4.1.4. SEM cross sections

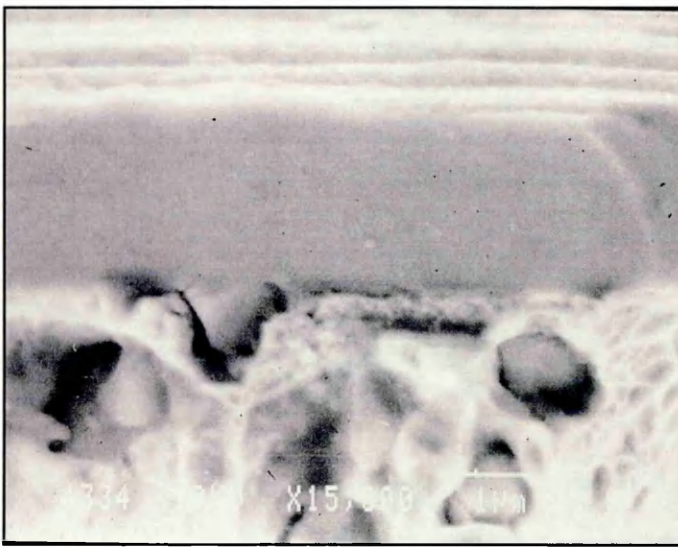
A selection of SEM fracture cross sections identifying the effects of nitrogen flow rate on the structure of CrN_x coatings grown at a bias voltage level of -100 V in figure 4.23:



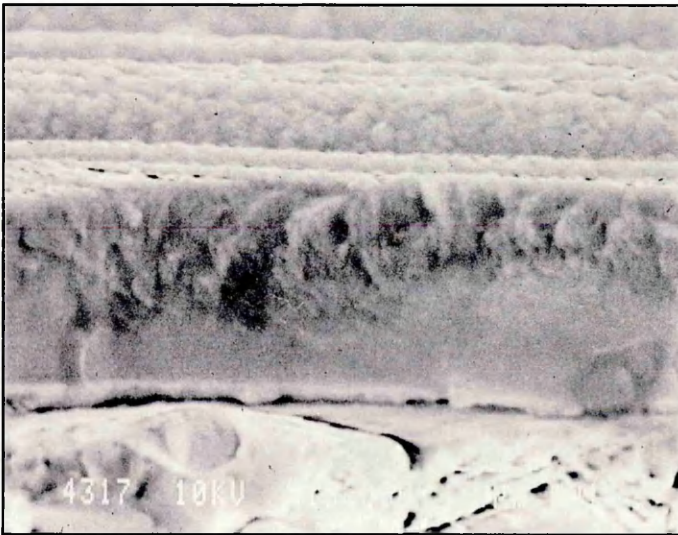
(a) Nitrogen flow = 0 sccm



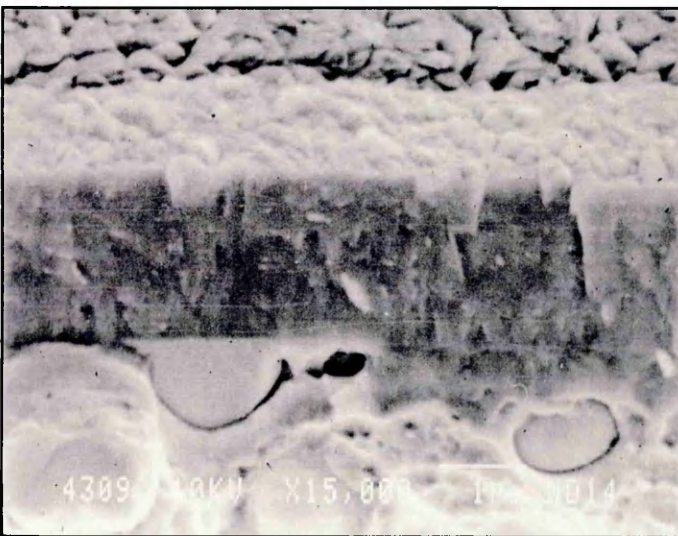
(b) Nitrogen flow = 15 sccm



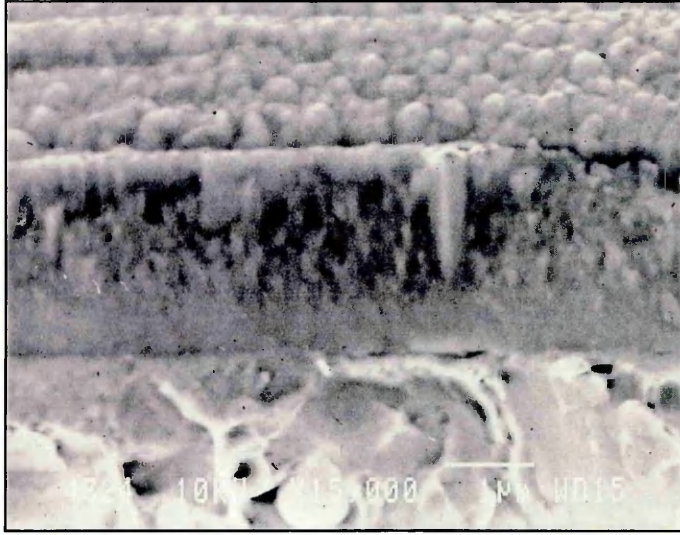
(c) Nitrogen flow = 25 sccm



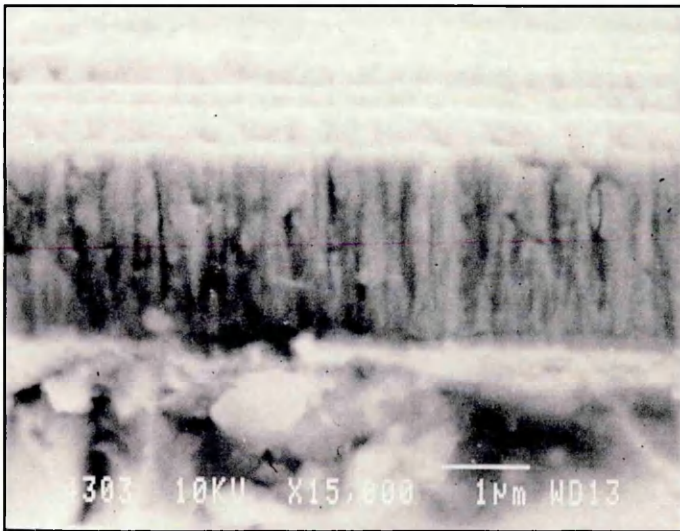
(d) Nitrogen flow = 35 sccm



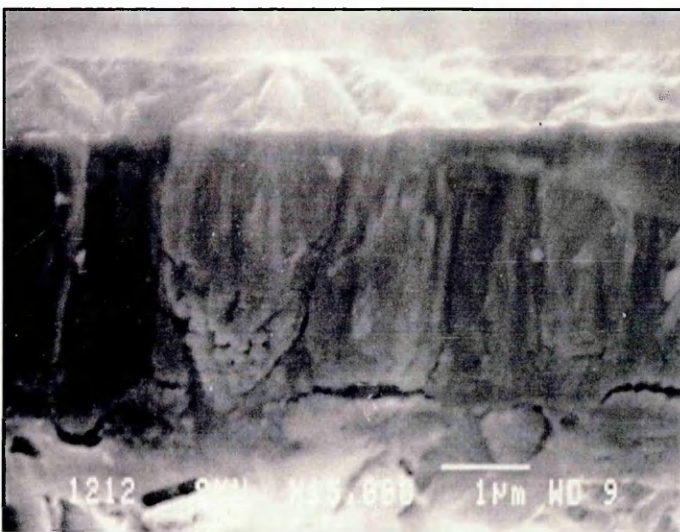
(e) Nitrogen flow = 50 sccm



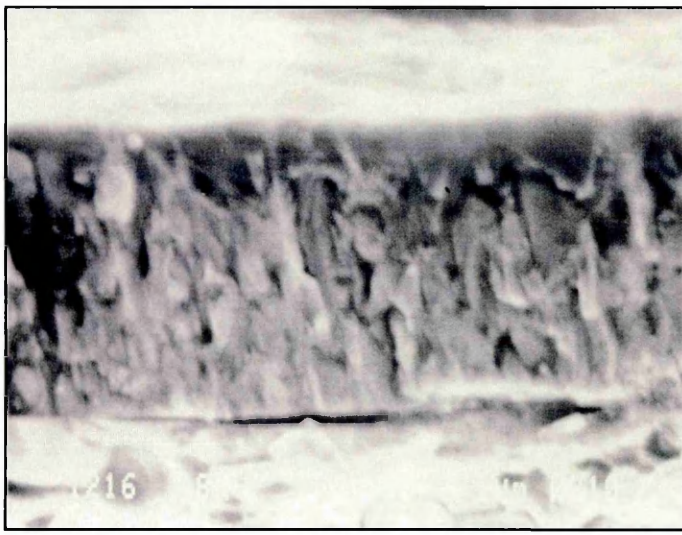
(f) Nitrogen flow = 75 sccm



(g) Nitrogen flow = 100 sccm



(h) Nitrogen flow = 150 sccm



(i) Nitrogen flow = 200 sccm

Figure 4.23. SEM cross sections at different nitrogen flow rate levels at $U_B = -100$ V.

With the increase of nitrogen content the morphology of the fracture cross sections of the coatings changes rapidly. For the low flow levels of $f_{N_2} = 0$ and 15 sccm the coatings are distinctly columnar. With further increase in interstitial nitrogen in the Cr matrix the image of the fracture cross section becomes featureless ($f_{N_2} = 25$ sccm). This effect which indicates densification was also reported by Rebholz et al. [144]. In the coating deposited at $f_{N_2} = 35$ sccm the featureless appearance is still present near the coating/substrate interface where as close to the surface the morphology is columnar. The fracture cross section of the Cr_2N coating ($f_{N_2} = 50$ sccm) appears rather featureless and shows a fine-grained microstructure. The first pure fcc-CrN film, $f_{N_2} = 75$ sccm, shows a similar duplex fracture morphology as the under-stoichiometric Cr_2N coating ($f_{N_2} = 35$ sccm). With further increases in the nitrogen flow rate ($f_{N_2} = 100$ sccm) a distinct columnar morphology becomes visible. At $f_{N_2} = 150$ sccm an apparent densification in the coating microstructure can be observed. At a flow rate of 200 sccm the grain size seems to be reduced and the growth direction becomes less clear. This effect is fortified if the flow rate is increased to 250 sccm and the bias voltage increased to -200 V (Figure 4.24).

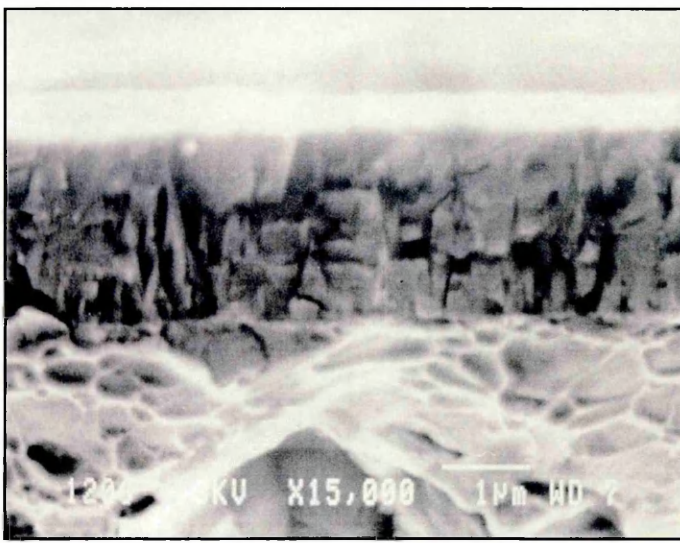


Figure 4.24. SEM cross sections at a nitrogen flow rate level of 250 sccm and at $U_B = -200$ V.

4.1.5. Cross section Transmission Microscopy (TEM)

In addition to the fracture cross sections evaluated by SEM the TEM has been applied to examine the microstructure on selected specimens. Micrograph 4.25 shows the bright and dark field image of a hcp-Cr₂N coating, deposited at $U_B = -100$ V and $f_{N_2} = 50$ sccm.

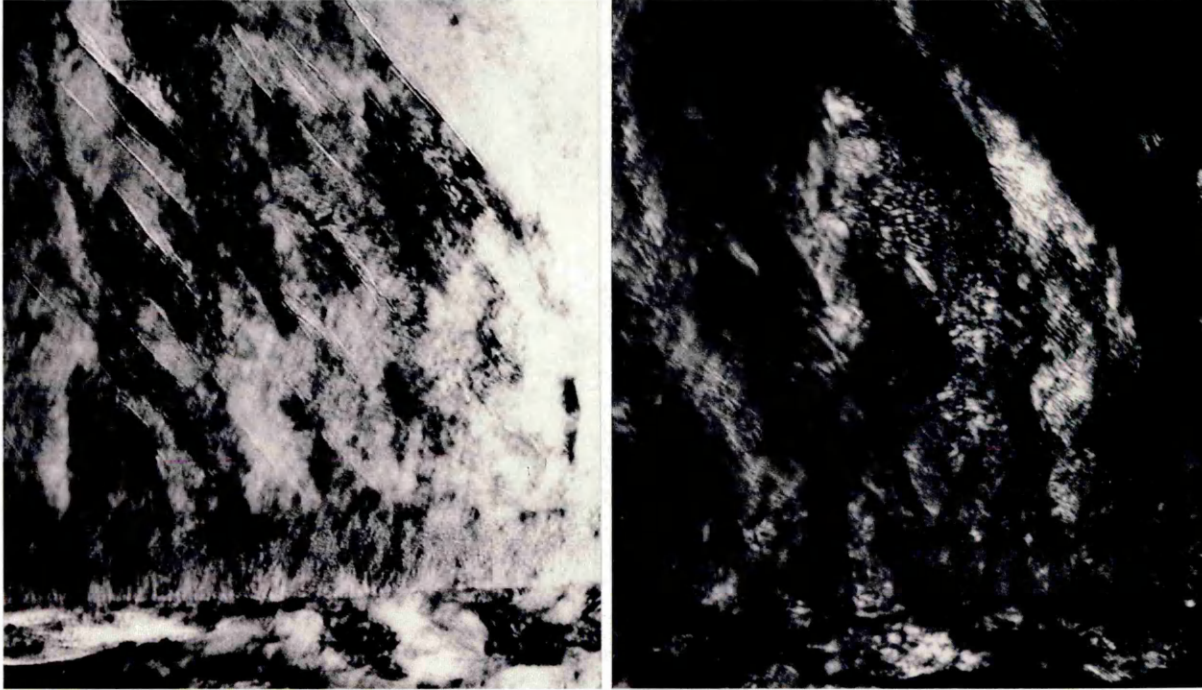


Figure 4.25. Cross-section TEM, bright field left and dark field right, of hcp-Cr₂N deposited at $U_B = -100$ V and $f_{N_2} = 50$ sccm (magnification 140,000 X).

The micrograph shows initial competitive film growth extending approximately 75 nm from the coating/substrate interface. The main body of the film is highly cracked at approximately 45° to the growth direction. Increasing the nitrogen flow rate to 100 or 150 sccm results in the formation of fcc-CrN coatings with the well known columnar growth morphology, as shown in figures 4.26 and 4.27.



Figure 4.26. Cross-section TEM and SADP pattern of fcc-CrN deposited at at $U_B = -100$ V and $f_{N_2} = 100$ sccm (magnification 220,000 X).

Micrograph 4.26 shows the existence of intergranular voids. The diameter of the grains is estimated to be approximately 50 nm. The selected area diffraction pattern (SADP) shows a $\langle 110 \rangle$ growth direction thus confirming the $\{110\}$ texture as described previously in the section on XRD analysis. The distinct arcing in the associated electron diffraction pattern is consistent with the rather fine grain structure.



Figure 4.27. Cross-section TEM and SADP pattern of fcc-CrN deposited at at $U_B = -100$ V and $f_{N_2} = 150$ sccm (magnification 45,000 X).

At $U_B = -100$ V and $f_{N_2} = 150$ sccm competitive grain growth is observed at the interface extending approximately $0.5 \mu\text{m}$. In the body of the coating the column is estimated to be in the 100 nm range. The numbers of intergranular voids is reduced, but are still evident. In the selected area diffraction patterns $\langle 111 \rangle$ and $\langle 100 \rangle$ growth directions could be identified indicating the presence of both $\{111\}$ and $\{100\}$ textures within the film. The presence of discrete spots rather than the arcs as in the SADP taken from the coating deposited at $f_{N_2} = 150$ sccm is consistent with the larger column diameter. It is clear from the micrographs that many of the tips to the columns at the coating

surface are tapered. Hultman et al. [145] correlated tapered TiN columns with the preferred {111} orientation, whereas the {100} oriented columns showed plane ends parallel to the coating surface.

At the even higher bias voltage of -200 V and further increased nitrogen flow rate, i.e. 200 sccm, the coating appears absolutely void free with a columnar microstructure and smooth surface, with a column diameter in the range of 150 nm. The selected area diffraction patterns obtained exhibited $\langle 100 \rangle$ growth directions, thus indicating the presence of a {100} texture, which is again in agreement with that measured by XRD. The smooth surface at the scale of the grain diameter together with a {100} preferred orientation were also reported for magnetron sputtered TiN films [119]. This is shown in figure 4.28.

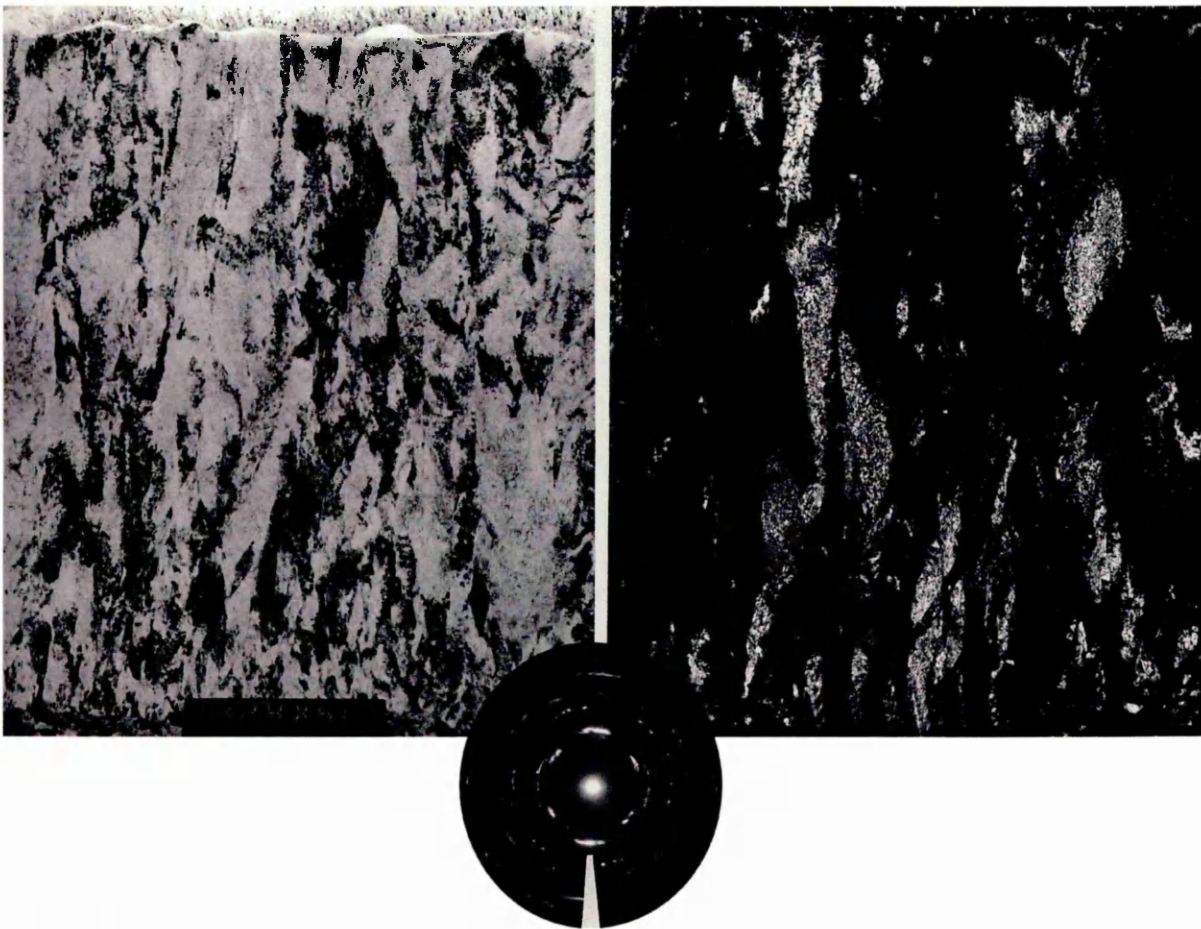


Figure 4.28. Cross-section TEM, left bright field and right dark field, and SADP pattern of fcc-CrN deposited at at $U_B = -200$ V and $f_{N_2} = 200$ sccm (magnification 27,500 X).

4.1.6. Composition

The composition has been determined by SNMS. The SNMS measurements have been calibrated on two samples by Rutherford Back Scattering. The first calibration sample had been deposited at $U_B = -100$ V and $f_{N_2} = 50$ sccm, which showed a pure Cr_2N pattern in the XRD scans. It confirmed indeed a stoichiometric Cr_2N coating. The second calibration sample had been taken from experiments undertaken in the high nitrogen flow range, namely deposited at $U_B = -200$ V and $f_{N_2} = 300$ sccm resulting in an understoichiometric Cr:N ratio of $1:0.90 \pm 0.045$. The amount of oxygen, argon and carbon contamination was always below 2 atomic %. This is shown in the depth profile of the Cr_2N sample, figure 4.29. The profile indicates also the completely uniform incorporation of nitrogen throughout the coating thickness confirming the poison-free sputtering condition. Based on 15 separate SNMS depth profiles analysis the composition of the coatings was evaluated as a function of nitrogen flow rate, figure 4.30. Up to a flow rate of $f_{N_2} = 75$ sccm an almost linear dependence of nitrogen incorporation versus nitrogen flow rate was found. Above $f_{N_2} = 75$ sccm the amount of nitrogen incorporation approaches stoichiometry asymptotically but never reaching complete stoichiometric composition.

Even at 200 sccm of nitrogen flow rate and $U_B = -100$ V the coatings are still slightly under-stoichiometric. In order to reach a similar composition at $U_B = -200$ V a nitrogen flow rate of 250 sccm is required, figure 4.31. This effect can be explained by preferred resputtering of the light nitrogen atoms during the growth of the coating, which is typical for the weak binding characteristics of Cr with nitrogen.

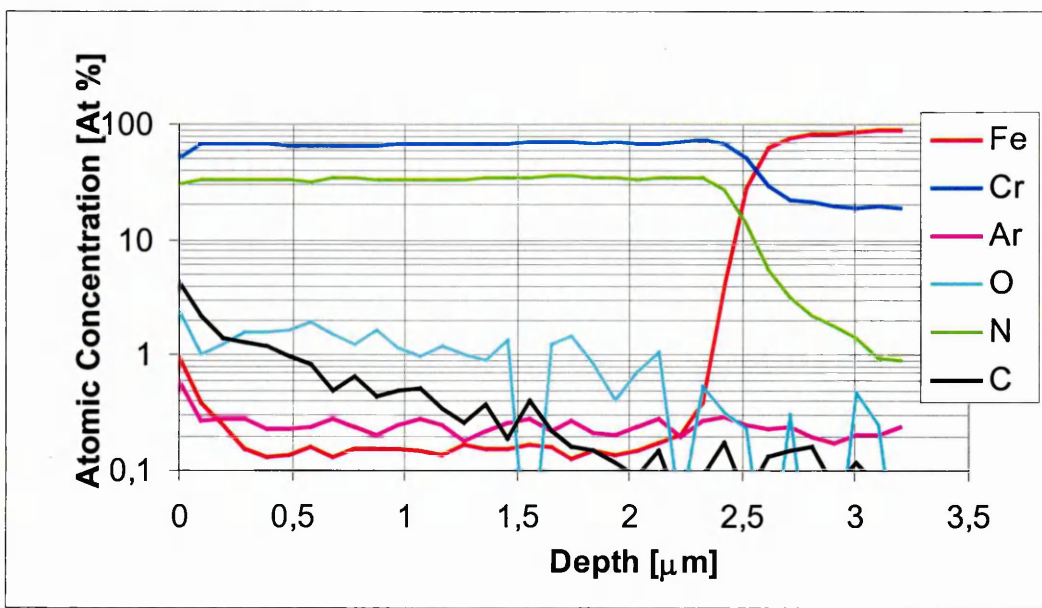


Figure 4.29. Compositional depth profile of a hcp-Cr₂N sample deposited at U_B=-100 V and f_{N₂}=50 sccm.

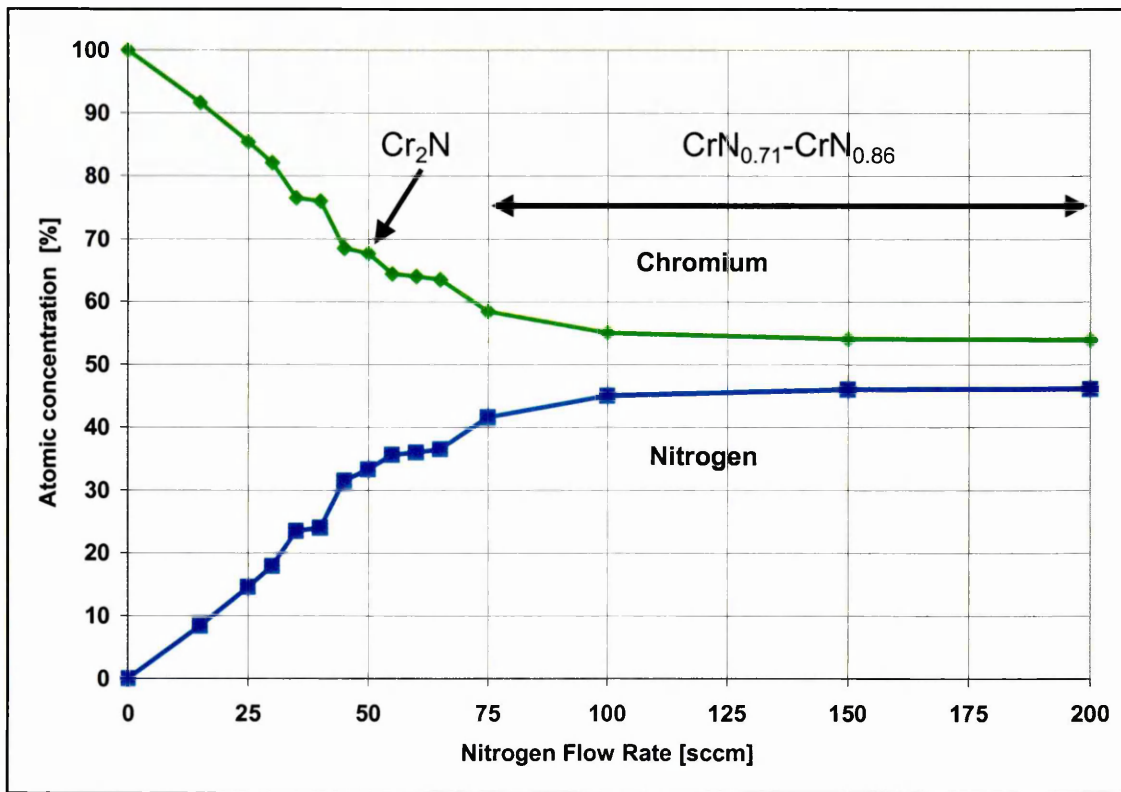


Figure 4.30. Effect of nitrogen flow rate on composition at U_B=-100 V.

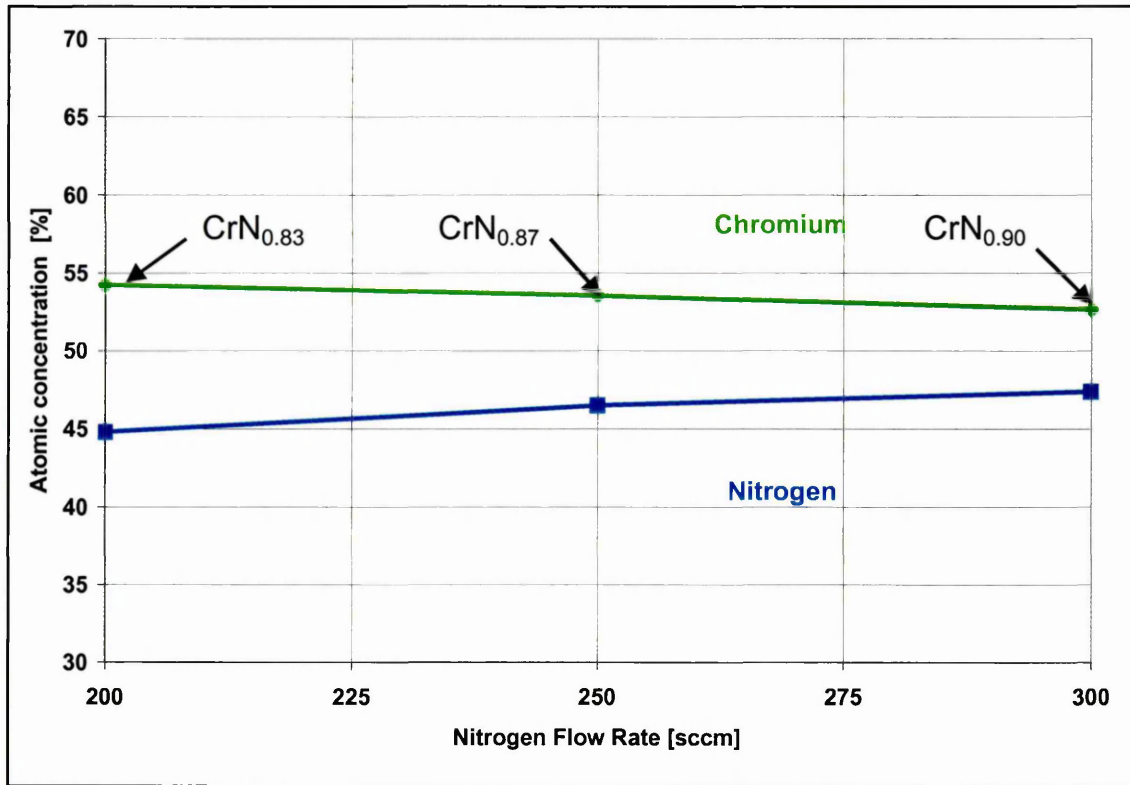


Figure 4.31. Effect of high nitrogen flow rate on composition at $U_B = -200$ V.

4.1.7. Hardness and Young's modulus

The effect of nitrogen flow rate on the hardness $HV_{0.025}$ at $U_B = -75$, -100 and -200 V is presented in figure 4.32. At a moderate bias voltage level of -100 V there is an interesting development of the hardness of the coating with increased nitrogen content. For the pure chromium and solid solution Cr-N there is a steep increase in hardness with increased amount of interstitial nitrogen. For pure chromium and for $CrN_{0.22}$ (maximum concentration of dissolved nitrogen in bcc-Cr) a hardness value of 7.8 and 18.0 GPa was measured respectively. The relative low hardness of the chromium has been reported before [40] and in conjunction with pure metals in general. Increased hardness values by interstitial nitrogen are in the line of expectations, as it will dilate the Cr-lattice and result in compressive stresses. The maximum hardness measured at $U_B = -100$ V is 22 GPa for the sub-stoichiometric hcp- $CrN_{0.31}$, deposited at $f_{N_2} = 35$ sccm. The hardness of the pure hcp- Cr_2N phase is only 16 GPa. Many scientific papers [86,88,89,91,93,94,96] report a maximum hardness for stoichiometric hcp- Cr_2N . However, because of the excellent hysteresis control it was possible to allow nitrogen increments sufficiently small to produce

precisely the pure hcp-Cr₂N phase, which exists in a narrow parameter window around $f_{N_2}=50$ sccm. This result is in agreement with what is known for the magnetron sputtered hcp-Ti₂N phase [146]. Increasing the nitrogen flow above $f_{N_2}=50$ sccm results in a fcc-CrN coating and an asymptotic increase of the hardness to a value of approximately 18.9 GPa for $f_{N_2}=200$ sccm (CrN_{0.86}). This value of ~20 GPa confirms the typical hardness value reported for CrN coatings in the literature [40,83,98,100,101,106]. The CrN depositions at $U_B=-75$ V show a rather constant hardness value of 17 GPa for nitrogen flow rates between 50 and 200 sccm. Extending the parameter window beyond the typical values known for unbalanced magnetron sputtering, for the deposition of TiN, extreme hardness values of over 30 GPa are recorded for fcc-CrN. Two criteria have to be fulfilled in parallel in order to produce fcc-CrN coatings with hardness in excess of 25 GPa: the substrate bias voltage must be at least -200 V and the nitrogen flow rate must be over 200 sccm. The latter value correlates strictly to the PVD system used in this research project, the ratio of reactive gas and inert gas f_{N_2}/f_{Ar} now exceeds the value of 1. At $f_{N_2}/f_{Ar} = 3.2$ and $U_B=-200$ V the measured hardness is 31.8 GPa. It is known for TiN and TiAlN coatings that the hardness increases with increased negative bias voltage [119]. For Ti based nitrides an increase in the lattice parameter, an increase of the FWHM in the XRD peaks, a decrease of the grain size, a decrease of the void density and an increase of the dislocation density was observed in parallel. For the hard fcc-CrN coatings there is also a significant increase the lattice parameter, an increase in the FWHM in the XRD scans and a lower voids density. A decrease in the grainsize however, was not found.

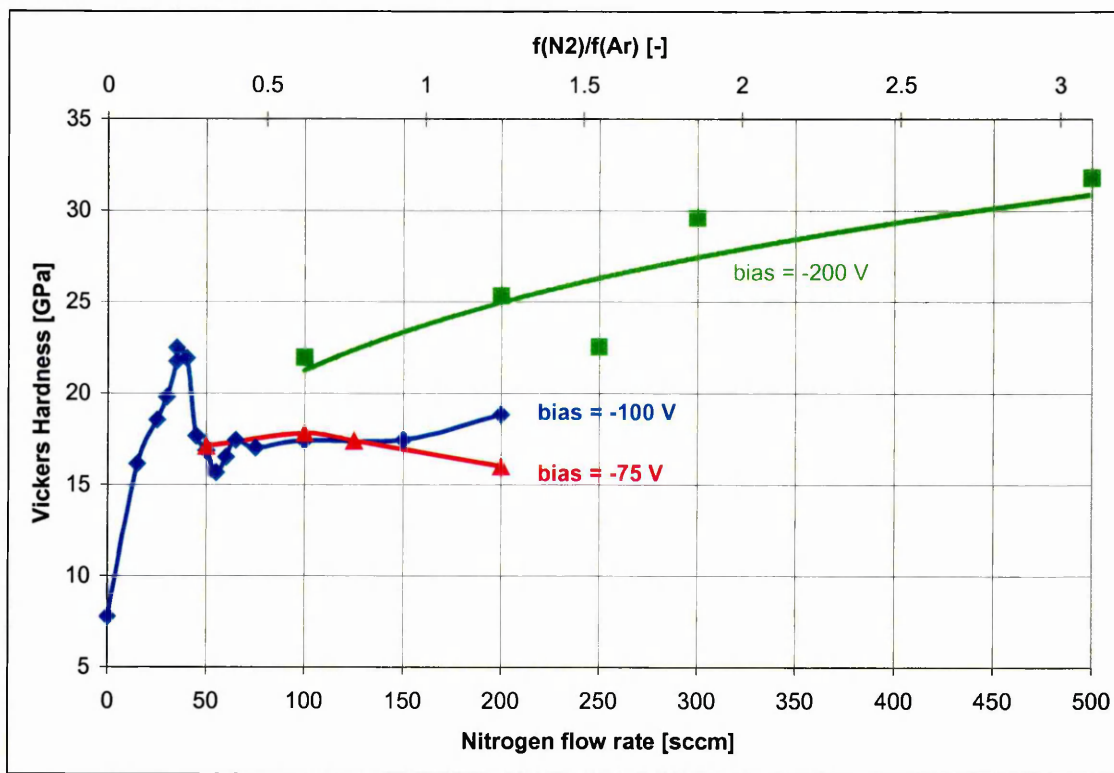


Figure 4.32. The effect of nitrogen flow rate on the hardness $HV_{0.025}$ at $U_B = -75, -100$ and -200 V.

For a set of samples the E-modulus was determined by nano-indentation. The results are shown in table 4.11.

	Solid Solution bcc-Cr-N	Sub- stoichiometric hcp-Cr ₂ N	Stoichiometric hcp-Cr ₂ N	fcc-CrN {110} texture	fcc-CrN {100} texture
E-Modulus [GPa±10 GPa]	150	195	165	195	380

Table 4.11. Young's modulus for the different phases of CrN.

Except for the high hardness fcc-CrN with a {100} preferred orientation the coatings show a low E-modulus for a metalnitride.

The E-modulus for the high hardness fcc-CrN, {100} texture, approaches the typical reported E-modulus between 450 and 600 GPa as known for other metal nitrides [36].

4.1.8. Residual stress

The growing stress as measured by the mechanical deflection method for the samples deposited at $U_B = -75$ V and $U_B = -100$ V show growing stress values below 0.4 GPa/ μ m over the full range of nitrogen flow rates. At these low values precise trends are difficult to derive, as the measurements of the layer thickness by calotest and evaluation of the deflection value are not accurate enough for values in the order of tenth's of GPa/ μ m to be used in narrow tolerances.

Table 4.12 shows for the samples coated at $U_B = -200$ V the residual stress values derived from both the deflection method and XRD (Glancing angle parallel beam geometry).

Nitrogen Flow [sccm]	Bias=-75V (mechanical)	Bias=-100V (mechanical)	Bias=-200V (mechanical)	Bias=-200V (XRD)
35	--	-0.25	--	--
40	--	-0.28	--	--
45	--	-0.07	--	--
50	0.0	-0.11	--	--
55	--	-0.16	--	--
60	--	-0.21	--	--
65	--	-0.28	--	--
100	-0.22	-0.24	-1.0	-0.78
150	--	-0.25	--	--
200	-0.02	-0.38	-0.86	-0.85
300	--	--	-0.97	-1.21
500	--	--	-1.0	-1.28

Table 4.12. Effect of nitrogen flow rate on the intrinsic growing stress [GPa/ μ m] at $U_B = -75$, -100 and -200 V.

The coatings deposited at the higher bias level of -200 V show clearly a higher state of compressive growing stress with values over 1 GPa/ μ m. Similar or even higher values are typically obtained for TiN. In general the trends in growing stress fit very well with the hardness trends as described in 4.1.7. Although being a simple test, the

results from the mechanical bending test show a reasonable correlation with the data from the x-ray $\sin^2\psi$ measurements.

4.1.9. Surface roughness

There was no clear tendency of surface roughness depending on the nitrogen flow level as measured with the profilometer. The R_a values were in the range of 0.02 to 0.04 μm and the R_z varied in the range of 0.1 to 0.8 μm .

4.1.10. Colour

The a^* and b^* values showed random scattering within the following window:
 $-1 < a^* < 2$ and $0.5 < b^* < 6$.

More interesting is the effect of the nitrogen flow rate on the L^* values. Figure 4.33 shows this dependency for the three bias voltage levels.

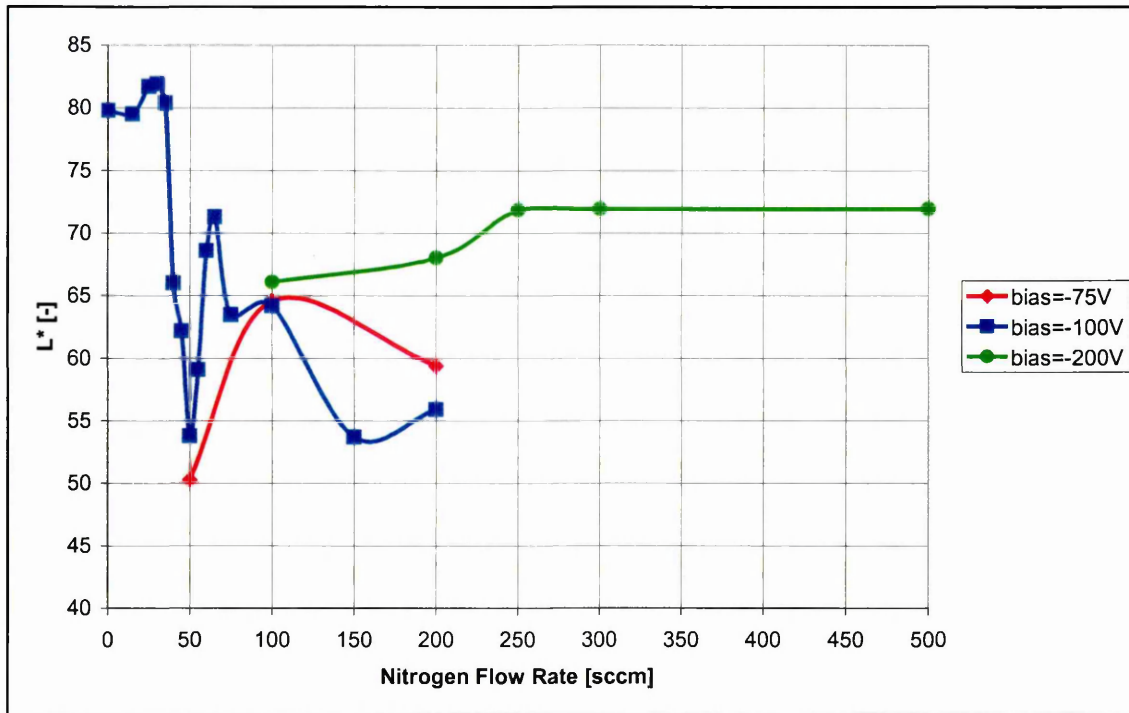


Figure 4.33. Effect of nitrogen flow rate on colour co-ordinate L^* .

The figure shows that pure hcp- Cr_2N coatings have low reflection values. The hard sub-stoichiometric hcp- Cr_2N and the hard CrN show much higher L^* values. If the

bias voltage during deposition is moderate the L^* value drops in the high nitrogen area. In general it shows a high similarity with the tendency as shown for the effect of nitrogen flow rate on the coating hardness.

4.2. Influence of substrate bias voltage on unbalanced magnetron sputtered CrN_x

4.2.1. Overview of the experiments

The substrate bias potential represents one of the most important deposition parameters as it defines the energy of the ions bombarding the growing film. It influences not only the mobility of the ad-atoms but it also causes defects (dislocations and vacancies). The applied bias voltage level minus the floating potential of the plasma gives the effective energy level during the sputtering operation. The typical floating potential is -20 V. The substrate bias voltage was varied for hcp-Cr₂N ($f_{N_2}=55$ sccm) and for fcc-CrN at $f_{N_2}=100$ sccm and $f_{N_2}=200$ sccm. The combinations of nitrogen flow rate and substrate bias voltage are listed in table 4.13.

Prior to deposition etching was performed using an argon glow discharge. During the deposition process steps the magnetic field of the UBM were kept constant by keeping the electromagnetic coils around the cathodes at a value of 20 A. The two opposing cathodes and electromagnets were operated in a closed field configuration. All other parameters are as shown in table 3.3.

f_{N_2} [sccm]	Substrate bias voltage [V]									
	0	20	40	50	75	100	125	150	200	300
55			X	X	X	X				
100	X	X		X	X	X	X	X	X	X
200				X	X	X		X	X	

Table 4.13. Range of experiments with substrate bias voltage variation.

4.2.2. Influence of the substrate bias voltage on the deposition parameters

Figure 4.34 shows the dependence of total bias current as a function of bias voltage potential. After exceeding the floating potential (approximately -20 V) the current drawn by the substrates, the substrate fittings and the turntable increase gradually up to a bias voltage of -200 V. Beyond this value saturation of the bias current is

reached with 1.15 A representing a bias current density of 3.6 mA/cm^2 . This means that as the bias voltage is increasing the number of bombarding ions will also increase in parallel to the increase in ion energy.

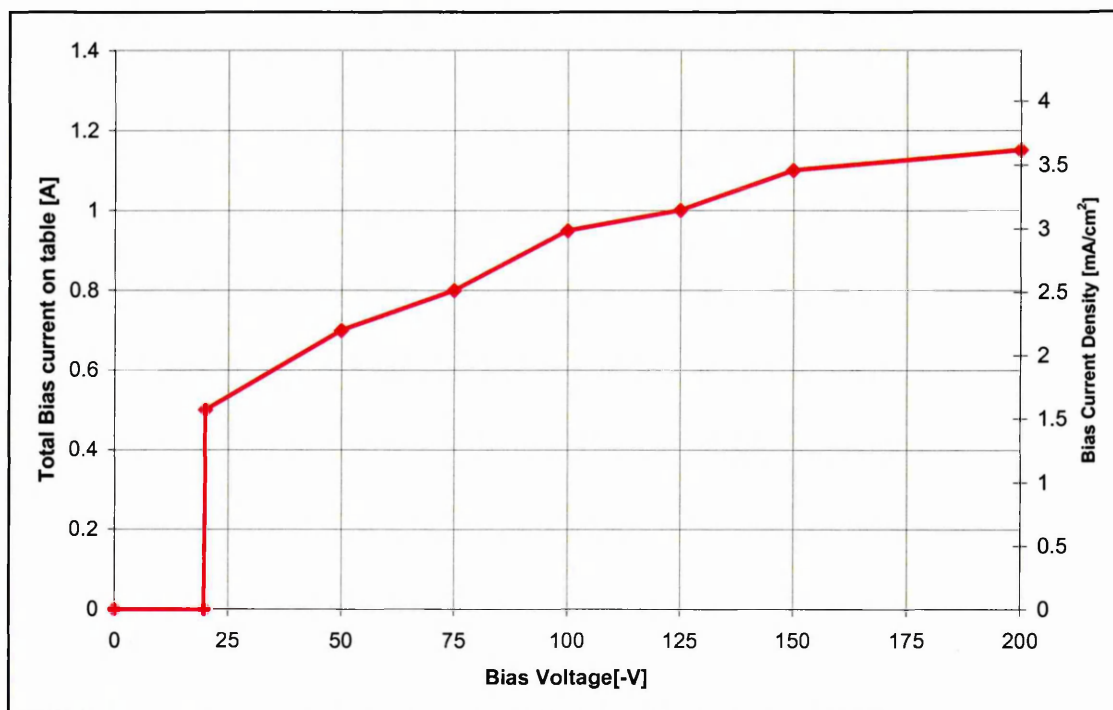


Figure 4.34. Effect of substrate bias voltage on the total substrate bias current at $f_{N_2}=100 \text{ sccm}$ and UBM electromagnetic coils at 20 A.

The effect of the substrate bias voltage on the deposition rate is shown in figure 4.35.

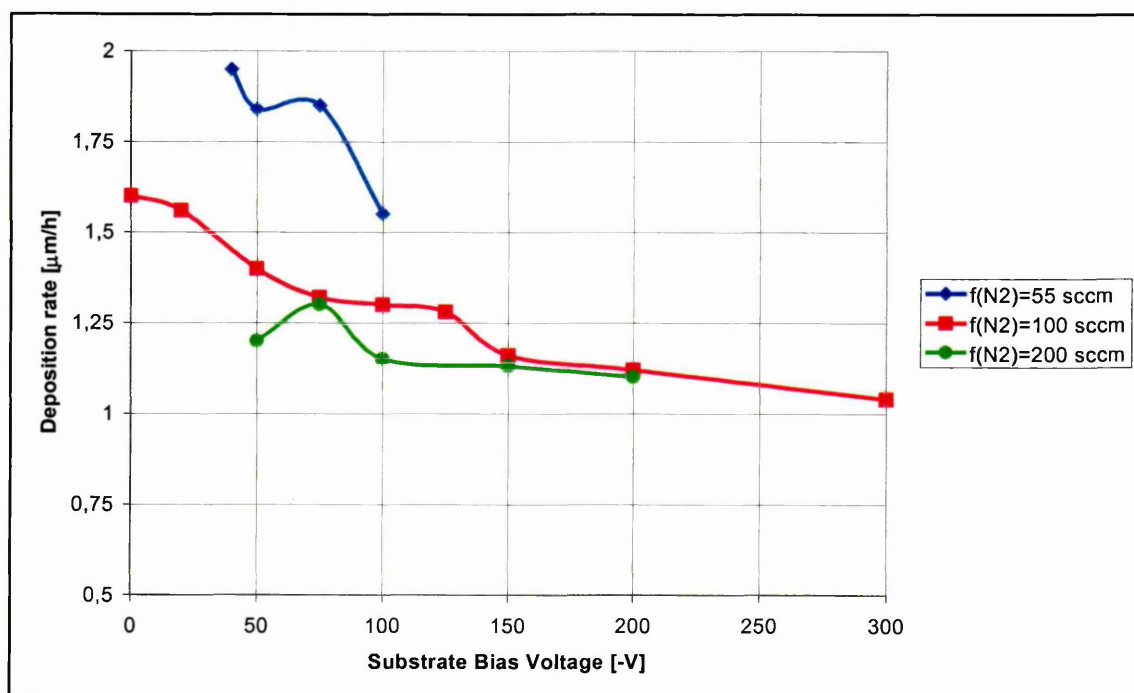


Figure 4.35. Effect of substrate bias voltage on deposition rate.

As expected the deposition rate decreased with increasing bias voltage and availability of nitrogen. The latter effect may be explained by a reduction in sputter yield resulting from increased poisoning of the chromium target at higher nitrogen flow rates. The effect of the substrate bias voltage on the deposition rate is quite marked particularly at low nitrogen flow rates. The average deposition rate decreased by 35% when the substrate bias voltage is increased from 0 to -300 V. The decrease in deposition rate can be explained by the increased re-sputtering activity with increasing energy mainly of the impinging Ar^+ ions. At higher flow rates a less pronounced dependency of the deposition rate is observed. At nitrogen flow rates of 200 sccm the decay in the deposition rate is only 15% over the entire range of substrate bias voltage. This effect is basically due to the reduced re-sputtering rate in the presence of higher N_2 concentrations and increased availability of the highly energetic N_2 ions to form a stable nitride, which is a similar effect to that occurring on the target during poisoning.

4.2.3. X-Ray diffraction (Bragg Brentano high angle scan)

4.2.3.1. Phase development

At $f_{\text{N}_2} = 55$ sccm, the Bragg Brentano scans show a hcp- Cr_2N structure for all four samples, and all look very similar to the scan presented in figure 4.12. However, the preferred orientation changes from $\{22.1\}$ for $U_B = -40$ V and -50 V to $\{11.1\}$ at $U_B = -75$ V, -100 V.

For the $f_{\text{N}_2} = 100$ sccm series the coatings are clearly fcc-CrN if deposited at $U_B = -20$ V (figure 4.36), -50 V, -75 V, -100 V (figure 4.11), and -200 V (figure 4.37). The coatings change from $\{111\}$ orientation when deposited just above the floating potential towards a preferred $\{110\}$ orientation when deposited at a substrate bias voltage in the range of -50 to -200 V. At $U_B = -300$ V peaks of hcp- Cr_2N appear next to the fcc-CrN due to re-sputtering of light nitrogen atoms out of the growing film, figure 4.38.

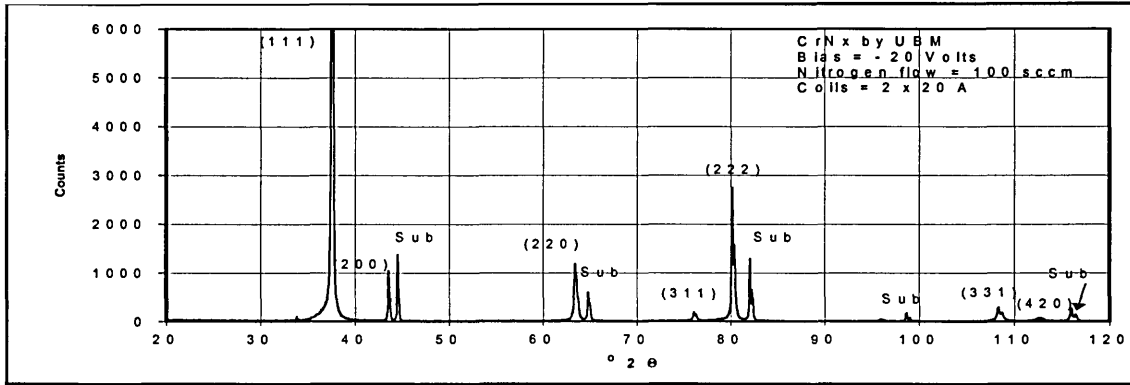


Figure 4.36. X-Ray diffraction pattern of CrNx at -20 V bias and 100 sccm nitrogen flow rate.

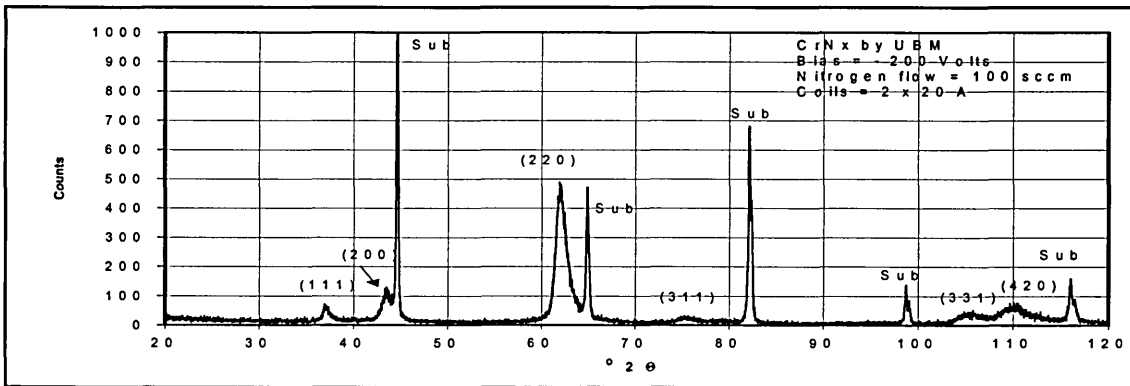


Figure 4.37. X-Ray diffraction pattern of CrNx at -200 V bias and 100 sccm nitrogen flow rate.

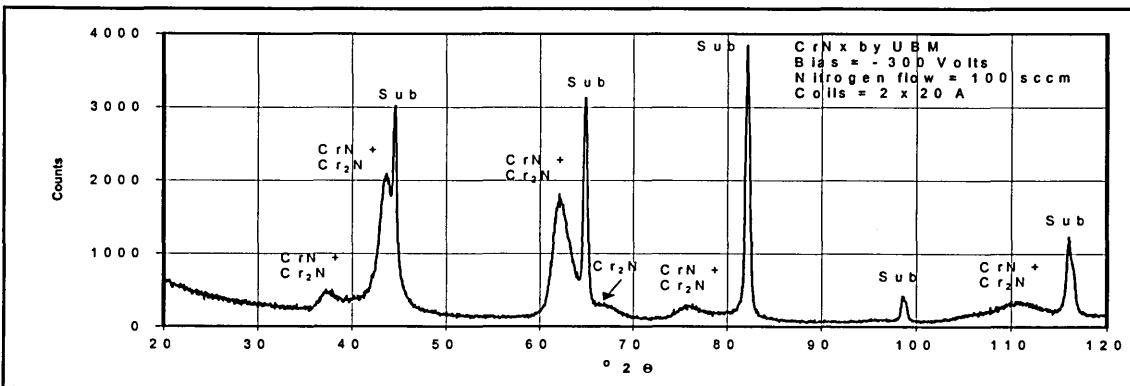


Figure 4.38. X-Ray diffraction pattern of CrNx at -300 V bias and 100 sccm nitrogen flow rate.

At $f_{N_2}=200$ sccm the scans show a strong dependency of the crystallographic orientation on the substrate bias voltage. The results for $U_B=-50$ V, -75 V, -150 V and -200 V are presented in figures 4.39, 4.40, 4.41 en 4.17 respectively. At low bias voltage levels the $\{110\}$ planes are dominant, changing to a preferred $\{111\}$ orientation at $U_B=-150$ V. At $U_B=-200$ V the main reflections are on the $\{100\}$ planes. All the samples show a fcc-CrN identity.

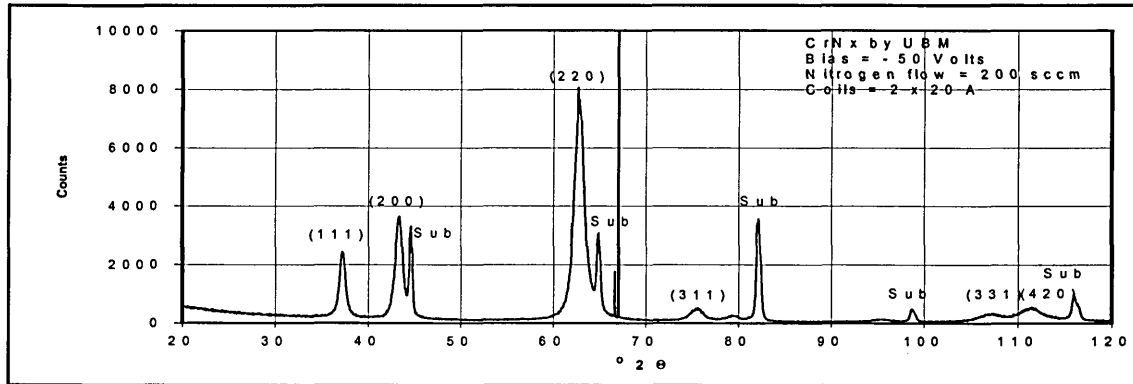


Figure 4.39. X-Ray diffraction pattern of CrNx at -50 V bias and 200 sccm nitrogen flow rate.

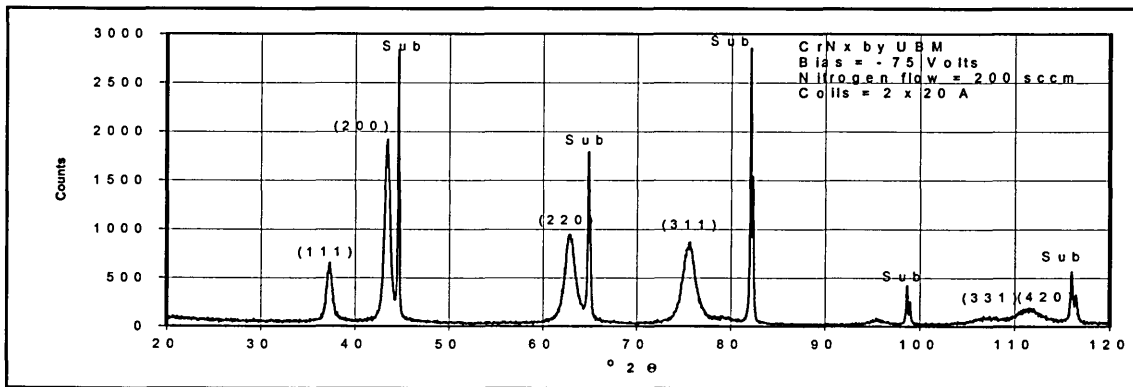


Figure 4.40. X-Ray diffraction pattern of CrNx at -75 V bias and 200 sccm nitrogen flow rate.

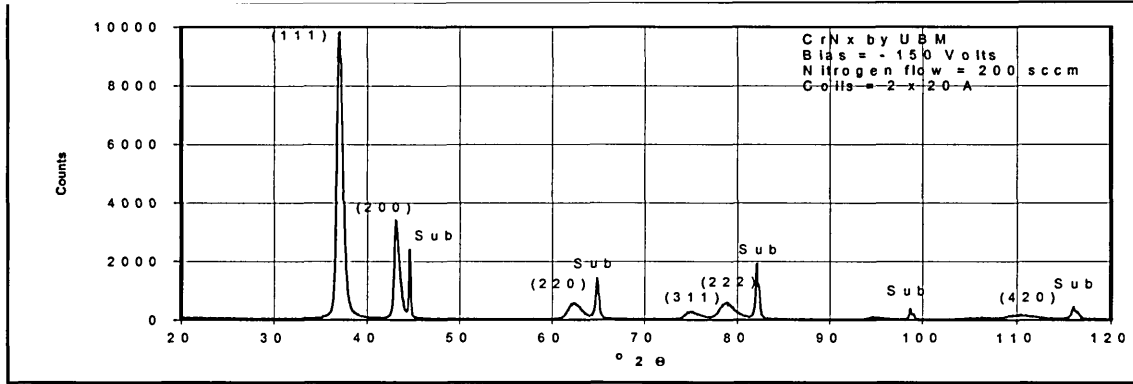


Figure 4.41. X-Ray diffraction pattern of CrNx at -150 V bias and 200 sccm nitrogen flow rate.

4.2.3.2. Texture

The texture development for the hcp-Cr₂N (f_{N_2} =55 sccm) and fcc-CrN (f_{N_2} =100 and 200 sccm) is presented in tables 4.14, 4.15 and 4.16.

U _{Bias} [-V]	Texture Parameter T* [%] for hcp Cr ₂ N								
	{11.0}	{00.2}	{11.1}	{11.2}	{30.0}	{30.2}	{11.3}	{22.1}	{22.3}
40.	33.6	0	12.0	2.7	15.5	0.0	0.7	31.5	3.9
50	0.9	5.4	11.9	7.8	14.7	0.0	8.9	38.6	11.8
75	7.5	0.0	30.9	5.3	10.3	11.7	0.0	13.5	20.8
100	16.5	0	26.4	9.5	17.8	3.8	0	18.3	7.7

Table 4.14. Texture parameter T* for hcp-Cr₂N as a function of the bias voltage at f_{N_2} =55 sccm.

U _{Bias} [-V]	Texture parameter T* [%] for fcc-CrN		
	{111}	{100}	{110}
0	96	1	2
20	79	2	8
50	13	8	55
75	3	3	80
100	3	4	80
125	6	15	42
150	6	12	29
200	3	3	80
300	—	—	—

Table 4.15. Texture parameter T* for fcc-CrN as a function of the bias voltage at $f_{N_2}=100$ sccm.

U _{Bias} [-V]	Texture parameter T* [%] for fcc-CrN		
	{111}	{100}	{110}
50	9	14	57
75	6	16	21
100	52	11	12
150	60	15	9
200	11	55	5

Table 4.16. Texture parameter T* for fcc-CrN as a function of the bias voltage at $f_{N_2}=200$ sccm.

The texture development over the full range of bias voltage levels at $f_{N_2}=200$ sccm is also shown in figure 4.42.

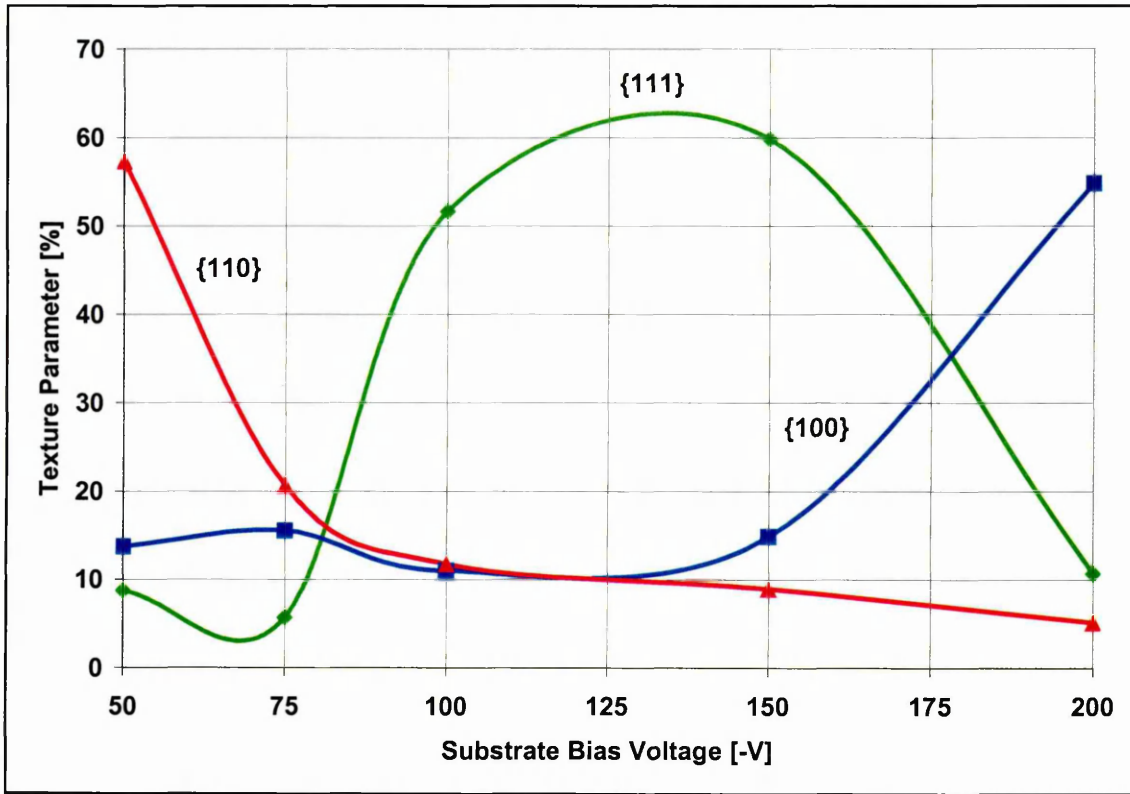


Figure 4.42. Effect of substrate bias voltage on texture development of fcc-CrN_x at f_{N2}=200 sccm.

4.2.3.3. Interplanar spacing and peak broadening

Tables 4.17, 4.18 and 4.19 show the tabulated values for the interplanar spacing and peak broadening.

U _{Bias} [-V]	Interplanar Spacing [Å] Relative to JCPDS [%]			Peak Broadening FWHM [°2θ]		
	{11.1}	{11.2}	{22.2}	{11.1}	{11.2}	{22.2}
JCPDS	2.120	1.641	1.060	-	-	-
40	2.115 -0.23	1.635 -0.37	1.0578 -0.21	0.05	0.35	0.22
50	2.099 -0.99	1.6225 -1.13	1.0496 -0.98	0.23	0.65	0.54
75	2.1217 0.08	1.6424 0.09	1.0604 0.04	0.04	0.46	0.15
100	2.125 0.24	1.6611* 1.22	1.0617 0.16	0.49	2.82*	1.04

* Poor Statistics; weak reflection

Table 4.17. Interplanar spacing and peak broadening (FWHM) for hcp-Cr₂N at F_{N2}=55 sccm.

In the case of the hcp-Cr₂N phase the interplanar spacing shows a change in stress status from a residual tensile stress at U_B = -40 V and -50 V to a compressive stress at U_B = -75 V and -100 V. In parallel an increase in peak broadening was observed with increasing bias voltage indicating a decreasing grain size and an increasing lattice strain by an increase in defect density originating from bombardment of the growing film by highly energetic argon ions.

U _{Bias} [-V]	Interplanar Spacing [Å] Relative to JCPDS [%]			Peak Broadening FWHM [°2θ]		
	{111}	{200}	{220}	{111}	{200}	{220}
JCPDS	2.394	2.068	1.463	-	-	-
0	2.377 -0.72	2.064 -0.22	1.463 0	0.13	0.27	0.34
20	2.393 -0.03	2.076 0.38	1.465 0.12	0.10	0.13	0.26
50	2.41 0.65	2.088 0.90	1.478 1.0	0.49	0.17	1.64
75	2.406 0.51	2.083 0.72	1.482 1.29	0.79	0.93	1.83
100	2.428 1.41	2.068 0.90	1.492 1.95	1.07	1.06	1.91
125	2.430 1.49	2.088 0.99	1.496 2.23	0.97	1.03	1.36
150	2.424 1.25	2.085 0.8	1.497 2.28	0.81	0.96	1.11
200	2.421 1.13	2.075 0.34	1.499 2.46	0.82	1.26	1.77
300	--	--	--	--	--	--

Table 4.18. Interplanar spacing and peak broadening (FWHM) for fcc-CrN at F_{N2}=100 sccm

A similar behaviour of the interplanar spacing was observed when CrN crystallises in a fcc lattice at a flow of f_{N2} =100 sccm. Again tensile behaviour and very sharp diffraction peaks are observed at low bias voltages (U_B = 0 V to -20 V). Increasing the bias voltage leads to the development of a residual compressive stress with increasing broadening of the diffraction peaks caused by identical reasons as discussed previously for Cr₂N.

U _{Bias} [-V]	Interplanar Spacing [Å] Relative to JCPDS [%]			Peak Broadening FWHM [°2θ]		
	{111}	{200}	{220}	{111}	{200}	{220}
JCPDS	2.394	2.068	1.463	-	-	-
50	2.4145 0.86	2.0881 0.97	1.4794 1.12	0.39	0.49	0.61
75	2.4124 0.77	2.0842 0.78	1.4785 1.06	0.36	0.34	0.67
100	2.433 1.63	2.100 1.55	1.488 1.71	0.57	0.34	0.79
150	2.4304 1.52	2.0992 1.51	1.4896 1.82	0.47	0.47	1.05
200	2.435 1.71	2.097 1.40	1.494 2.13	0.54	0.44	1.16

Table 4.19. Interplanar spacing and peak broadening (FWHM) for fcc-CrN at $f_{N_2}=200$ sccm

In the bias voltage range as applied at $f_{N_2}=200$ sccm, only compressive residual stresses are observed. The peak broadening is not as marked as coatings deposited at $f_{N_2}=100$ sccm. Only for the {220} diffraction peak there was a pronounced increase in peak width with increased bias voltage at a nitrogen flow rate of 200 sccm.

Figure 4.43 summarises the results for the lattice parameter determined for CrN_x coatings deposited at $f_{N_2}=100$ sccm and 200 sccm. The results mirror the results utilised for the interplanar spacings. The graphical representation confirms the gradual increases in lattice spacings as caused by highly energetic ion bombardment of the growing film.

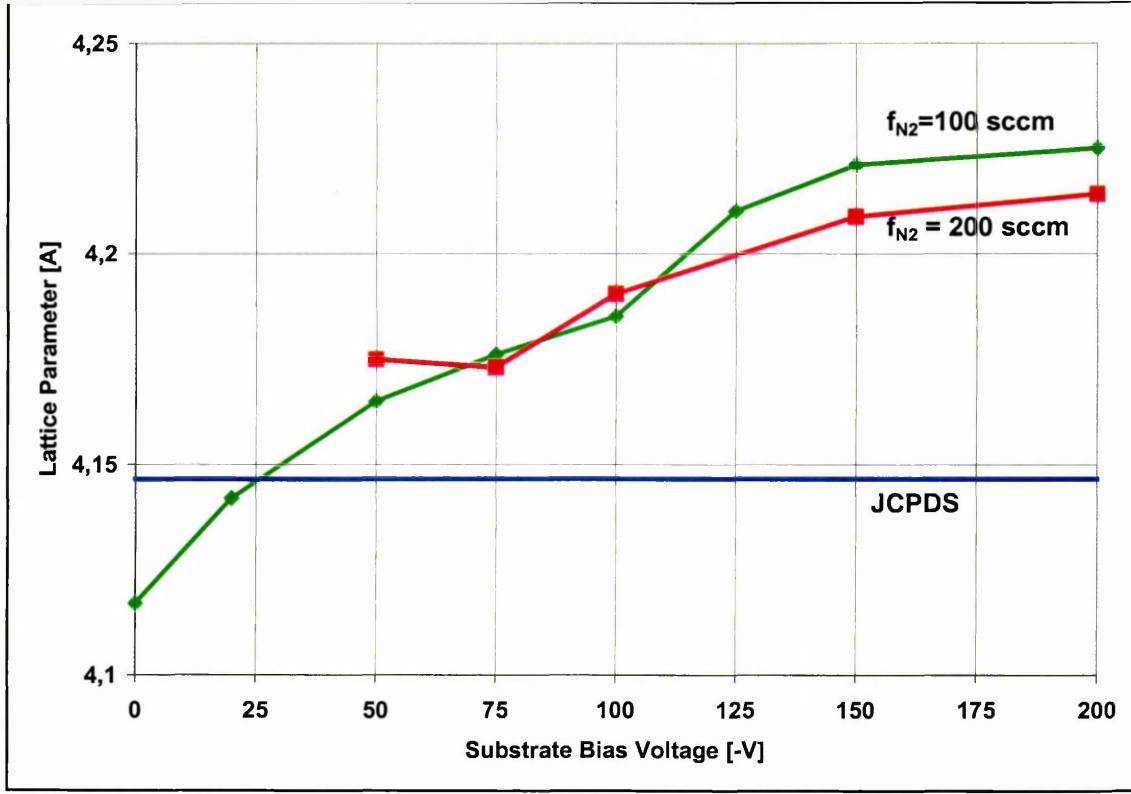
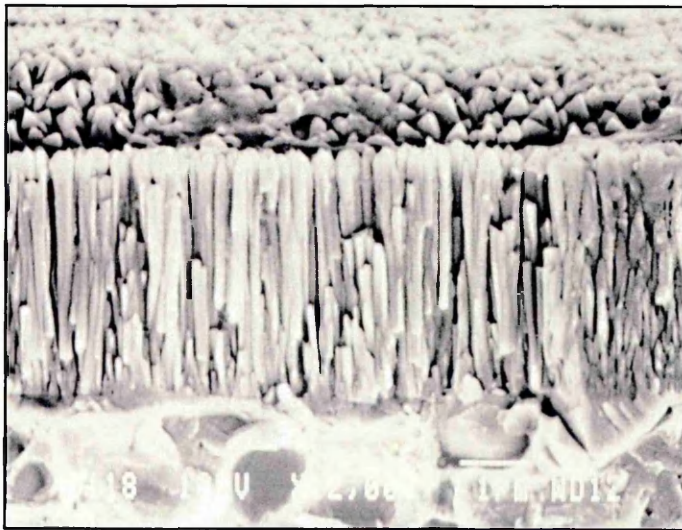


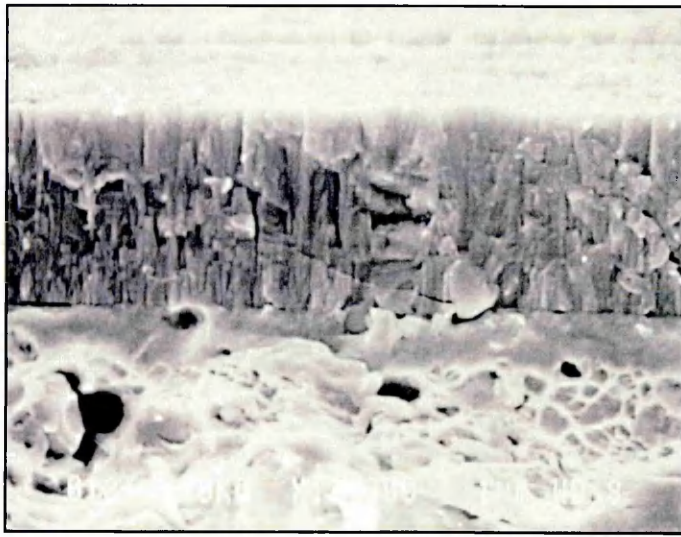
Figure 4.43. Effect of bias voltage on CrN lattice parameter at $f_{N_2}=100$ and 200 sccm.

4.2.4. SEM cross sections

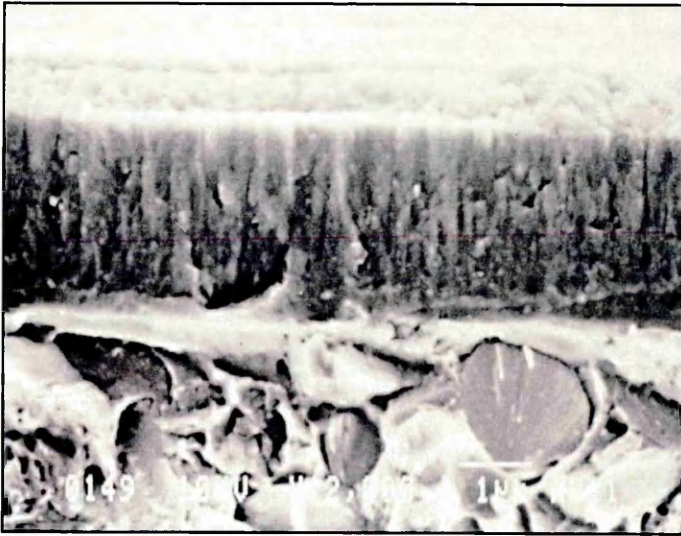
The SEM fracture cross section micrographs in figure 4.44 show the typical open structure at low or no ion bombardment energy levels as expected from the tensile stress behaviour. At higher bias voltage levels the structure becomes denser, even featureless, and the surface appears to be smoother.



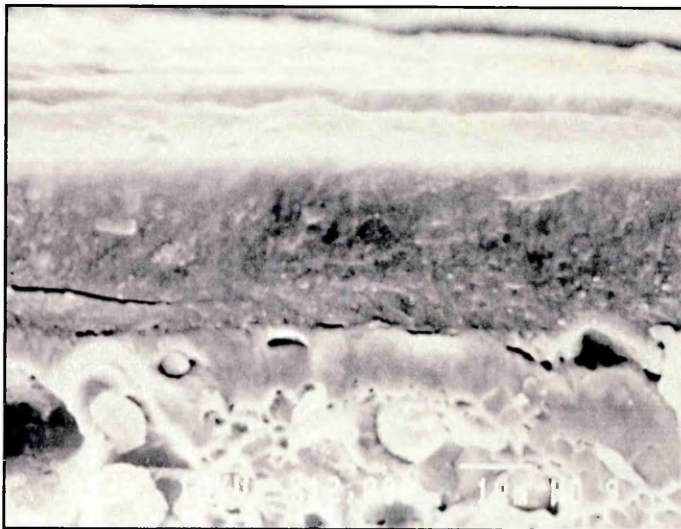
(a) Bias Voltage = 0 V



(b) Bias Voltage = -50 V



(c) Bias Voltage = -100 V



(d) Bias Voltage = -200 V

Figure 4.44. SEM cross sections at different bias voltage levels at $f_{N_2}=100$ sccm.

4.2.5. Cross section TEM

The bright field image in figure 4.45 confirms impressively the columnar film growth for the CrN coating deposited at $U_B=0$ V and $f_{N_2}=100$ sccm. The individual columns show practically no cohesion. The column diameter is in the range of 150 to 250 nm. The SADP indicates a $\langle 111 \rangle$ growth direction, thus confirming the $\{111\}$ texture observed from the XRD data. The grain morphology, i.e. pyramidal tips to the columns, is consistent with $\langle 111 \rangle$ preferred crystal growth.



Figure 4.45. Cross-section TEM and SADP pattern of CrN deposited at $U_B=0$ V and $f_{N_2}=100$ sccm (magnification 62,000 X).

4.2.6. Composition

Figure 4.46 summarises the results of 8 SNMS depth profiles analyses. Using a nitrogen flow rate of 100 sccm in no case was stoichiometry observed. It is interesting to note that the nitrogen content of the coating decreases almost linearly with increasing bias voltage. At a bias voltage $U_B = -200$ V a composition of $CrN_{0.76}$ has been evaluated.

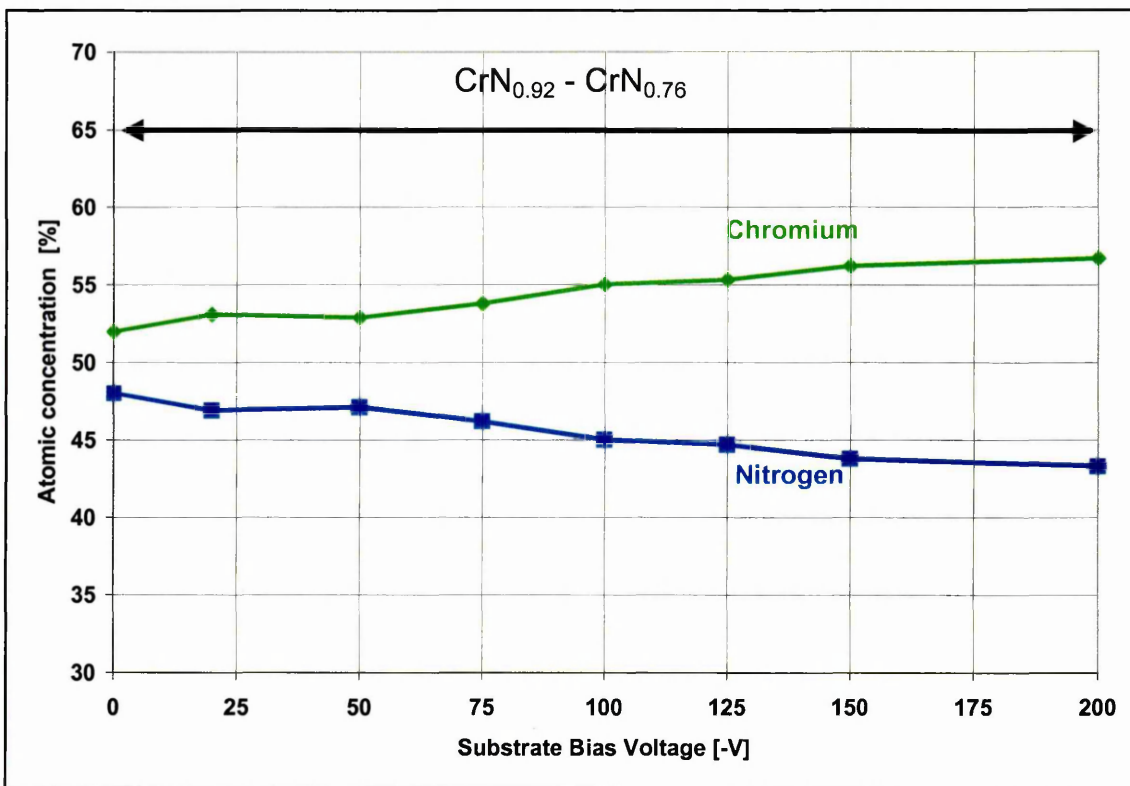


Figure 4.46. Effect of bias voltage on composition of CrN_x at $f_{\text{N}_2}=100$ sccm.

4.2.7. Hardness and Young's modulus

The hardness is again strongly influenced by the substrate bias voltage, as shown in figure 4.47. For $f_{\text{N}_2}=100$ sccm there is a maximum hardness of 22 GPa at $U_B=-150$ V which decreases to 20 GPa at $U_B=-300$ V. This decrease in hardness is not observed for $f_{\text{N}_2}=200$ sccm for bias voltages up to $U_B=-200$ V. Unfortunately no data are available for bias voltages above $U_B=-200$ V.

The Cr_2N coatings deposited at $f_{\text{N}_2}=55$ sccm show in the observed bias range a linear increase of hardness between $U_B=-40$ V and $U_B=-100$ V.

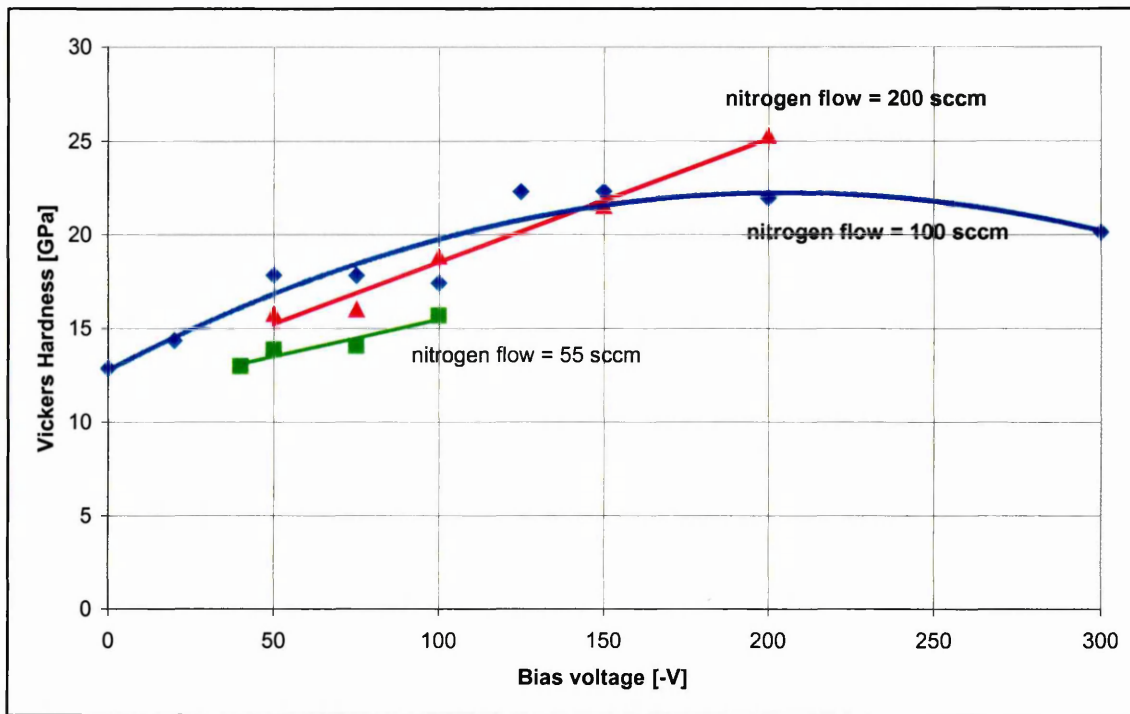


Figure 4.47. Effect of substrate bias voltage on the hardness $HV_{0.025}$ at $f_{N_2} = 55, 100$ and 200 sccm.

The E-modulus of the CrN_x coatings deposited without bias is reduced to 122 ± 10 GPa, compared to the typical 195 ± 10 GPa for the biased films.

4.2.8. Residual stress

As expected the residual compressive stress for the CrN_x coatings ($f_{N_2} = 100$ and 200 sccm) is increasing with increasing substrate bias potential, figure 4.48. It was not possible to measure the residual stress of the coating deposited at $f_{N_2} = 100$ sccm and $U_B = -300$ V since there was too much peak overlap between reflections from fcc- CrN and hcp- Cr_2N phases.

For the hcp- Cr_2N coatings a residual tensile stress was observed which increased from 0.2 GPa/ μm for $U_B = -40$ to 0.3 GPa/ μm for $U_B = -75$ indicating total stress below 1 GPa for all Cr_2N coatings. In contrast the residual compressive stress of fcc- CrN_x at $U_B = -200$ V reaches a value of typically 0.8 GPa/ μm .

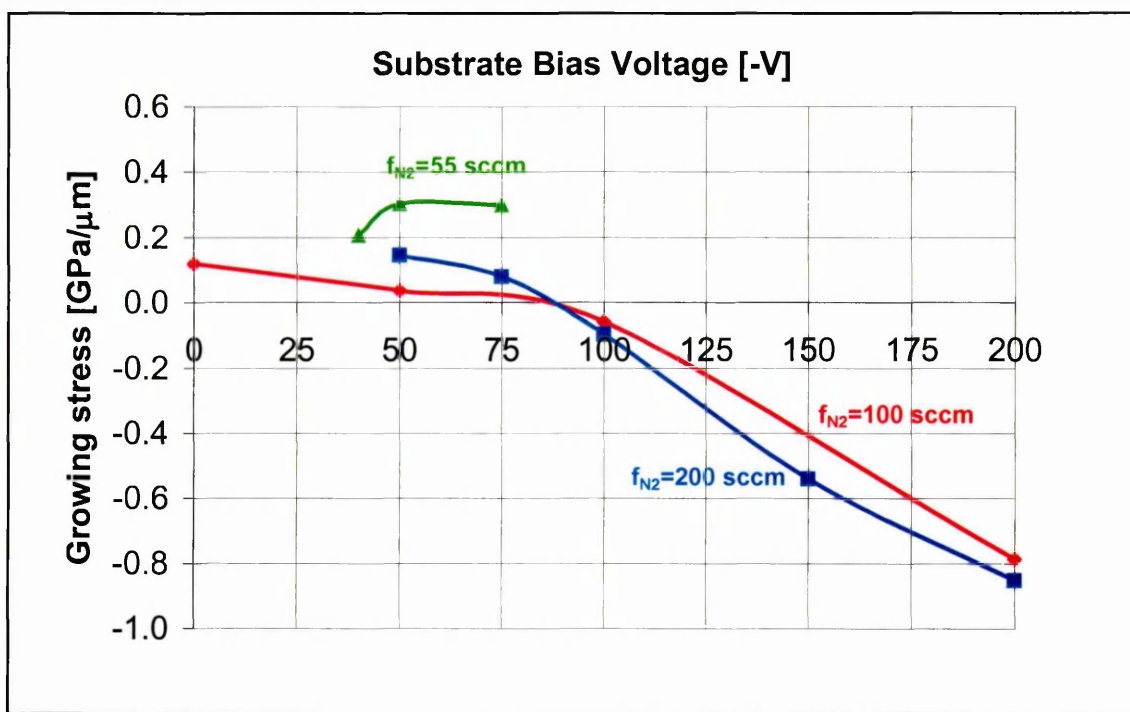


Figure 4.48. Effect of substrate bias voltage on the growing stress at $f_{N_2}=55$, 100, and 200 sccm.

4.2.9. Surface roughness

The hcp-Cr₂N coatings as deposited at $f_{N_2}=55$ sccm show a roughness R_a ranging from 0.04 to 0.07 μm . The corresponding R_z value is in the range from 0.5 to 1.1 μm . At a nitrogen flow level of 100 sccm the fcc-CrN coatings appear to be smoother and their R_a value is in the range of 0.01 to 0.03 μm . The R_z value measures between 0.07 and 0.3 μm . The surface roughness is slightly higher for the fcc-CrN coatings deposited at $f_{N_2}=200$ sccm. The R_a value is then between 0.02 and 0.05 μm . In parallel the R_z value is in the range from 0.3 to 0.8 μm .

It seems that the hcp-Cr₂N grow somewhat rougher than the fcc-CrN coatings. The increased surface roughness of fcc-CrN deposited at higher nitrogen flow rates might be caused by increased micro-arcing on the target surface as an effect of increased target poisoning. The level of micro-arcing was not monitored during the deposition cycles.

4.2.10. Colour

Within the bias voltage variation there was a low variation of the a^* value, between 0 and 2.1. The b^* value occurred to be random between 0 and 5. The L^* value shows a tendency similar to that for the hardness, figure 4.49.

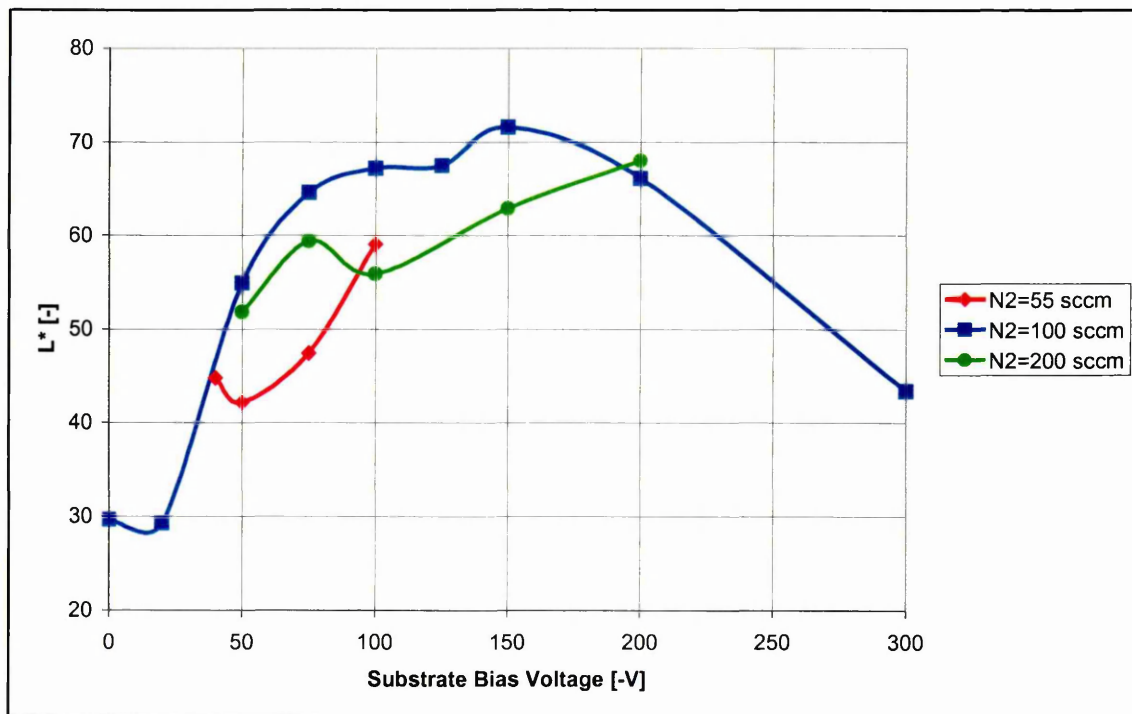


Figure 4.49. Effect of substrate bias voltage on colour co-ordinate L^* .

4.3. Influence of the substrate bias current density on unbalanced magnetron sputtered CrN_x

4.3.1. Overview of the experiments

Similar to the nitrogen flow rate and substrate bias voltage variation the substrate bias current density has been varied at 4 different levels. This was done by changing the current through the 2 electromagnetic coils, which surround the two cathode bodies. The 2 electromagnetic coils are in a closed field configuration and were operated at the same set-point of current, namely 0, 5, 20, or 40 A. The process sequence was in accordance to table 3.3 with the argon glow discharge as the substrate cleaning step. During the deposition the substrate bias voltage was set to –100 V and the nitrogen flow rate to 100 sccm.

4.3.2. Influence of the substrate bias current density on the deposition parameters

The increased magnetic field strength in a closed field configuration increases the ion current density on the growing films, as shown in figure 4.50. The measurement was done at a bias voltage of –100 V, an argon pressure of 0.3 Pa and a sputtering power of 5 kW for chromium. Within the measured range there is a linear relationship between the magnetic field strength (as represented by the coil current) and the substrate bias current density.

Figure 4.51 shows the effect of the substrate bias current density on the deposition rate at $U_B = -100$ V. Within the measured range of substrate bias current density settings there is a very limited change of the resulting deposition speed with increased level of impinging ions at this specific substrate bias voltage level. The energy level (substrate bias voltage) of the ions seems to affect the deposition rate more than the number of bombarding ions (figure 4.19). The lesser effect of the number of bombarding ions when compared with the effect of ion energy can be explained by the preferred ionisation of N₂ and N over Ar (ionisation potential of 15.58, 14.53 and 15.76 eV respectively). The increased bias current density might

produce an increased number of N_2^+ and N^+ ions. The sputter effect of these lighter ions will be less than for Ar^+ ions. Furthermore, the reactivity with Cr will also be increased by the higher availability of N_2^+ and N^+ ions.

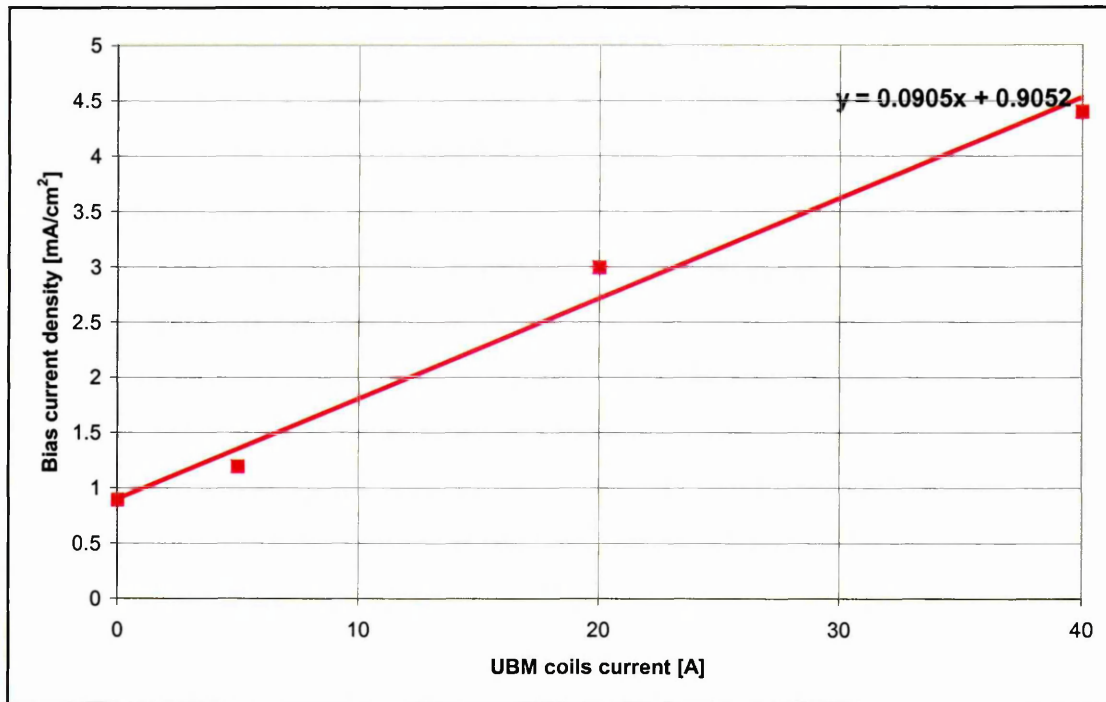


Figure 4.50. The effect of the grade of unbalancing the magnet field strength on the substrate bias current density.

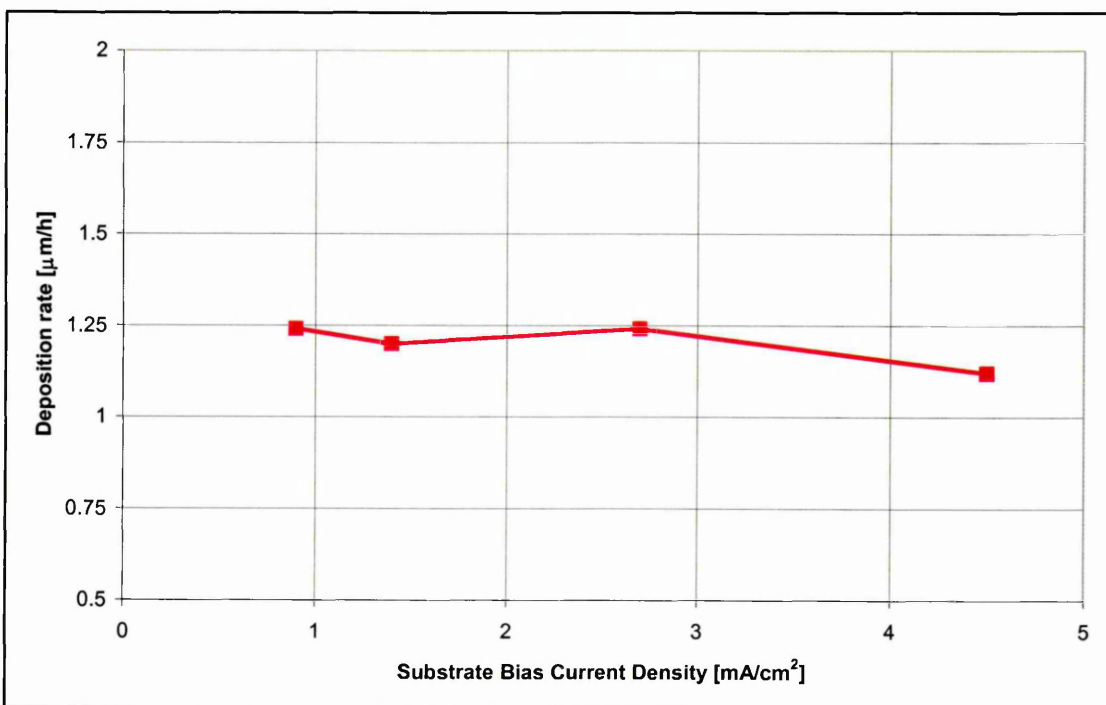


Figure 4.51. Effect of the substrate bias current density on the deposition rate.

4.3.3. X-Ray diffraction (Bragg Brentano high angle scan)

4.3.3.1. Phase development

The effect of the increased ion bombardment level on the high angle X-ray diffraction patterns is presented in figures 4.52, 4.53, 4.11, and 4.54 for substrate bias current densities of 0.9, 1.4, 2.7 and 4.5 mA/cm² respectively.

All the coatings exhibited the NaCl fcc-CrN phase.

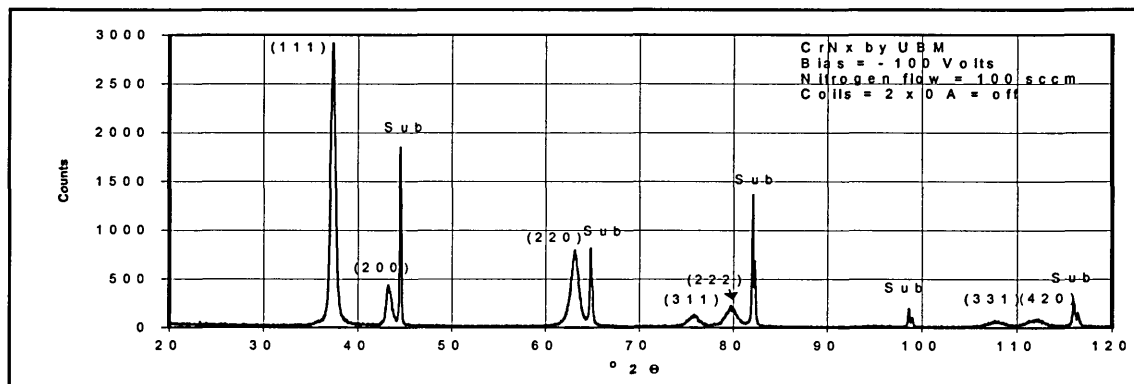


Figure 4.52. X-Ray diffraction pattern of fcc-CrN_x at $i_s = 0.9$ mA/cm²

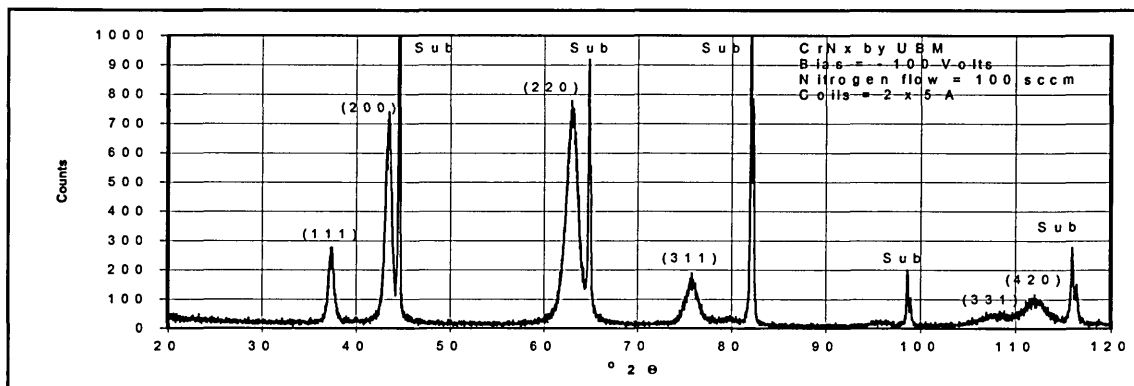


Figure 4.53. X-Ray diffraction pattern of fcc-CrN_x at $i_s = 1.4$ mA/cm²

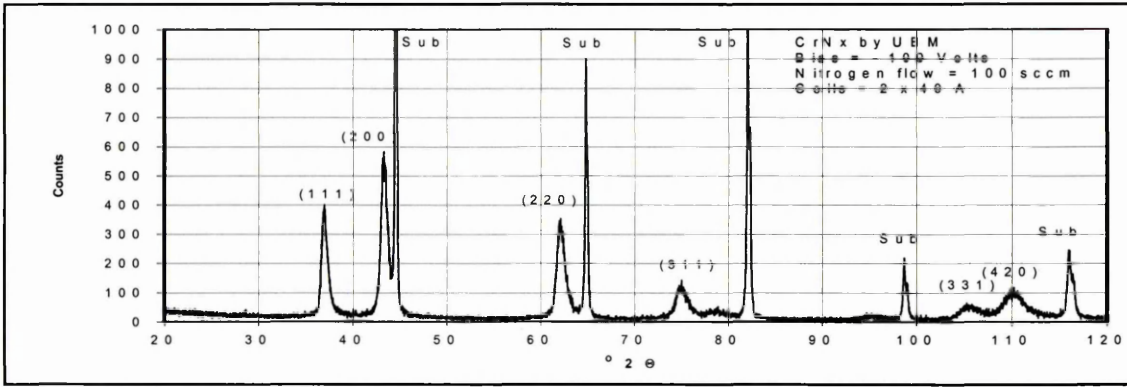


Figure 4.54. X-Ray diffraction pattern of fcc-CrN_x at $i_s = 4.5 \text{ mA/cm}^2$

4.3.3.2. Texture

Figure 4.55 shows that the preferred orientation is {111} for the coating deposited at $i_s = 0.9 \text{ mA/cm}^2$. With increased ion bombardment, $i_s = 1.4$ to 2.7 mA/cm^2 , the preferred orientation changes towards {110}. At $i_s = 4.5 \text{ mA/cm}^2$ the texture appears to be more random and the intensity of the {100} orientation increases.

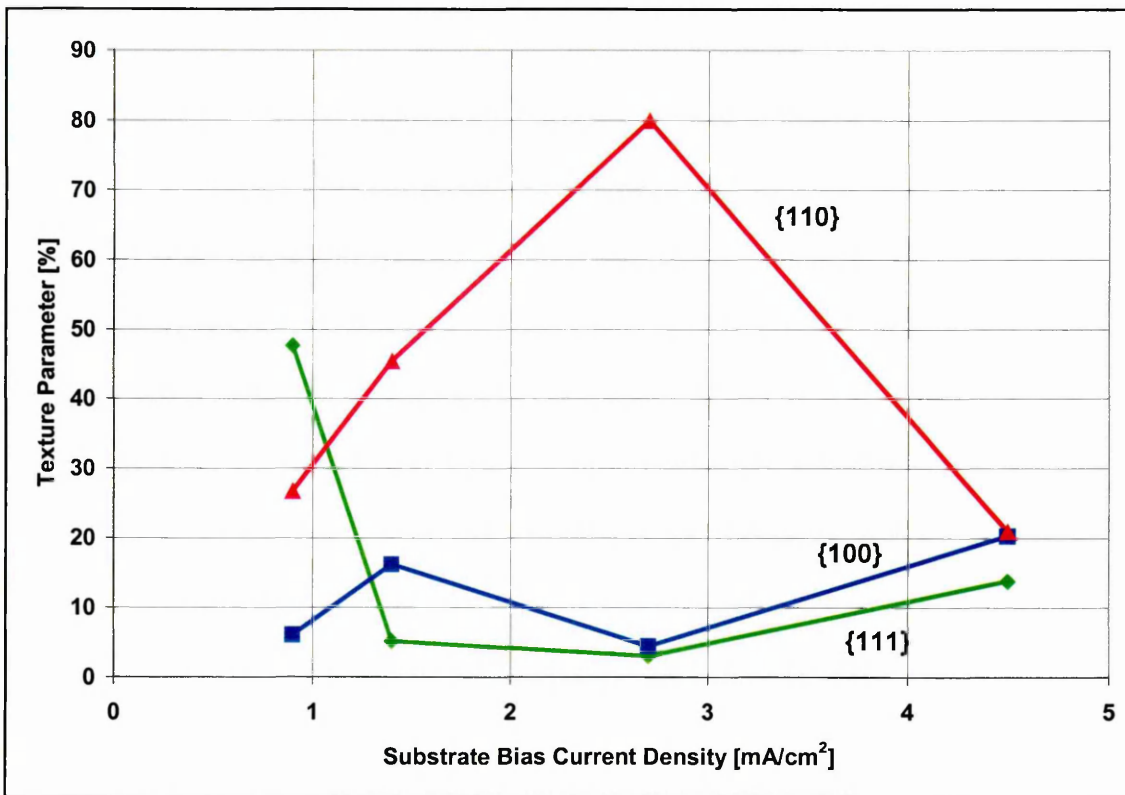


Figure 4.55. Effect of the substrate bias current density on texture development of fcc-CrN_x.

4.3.3.3. Interplanar spacing and peak broadening

The interplanar spacing and peak broadening dependencies on the substrate bias current density are in table 4.20. The interplanar spacing is increased by enhanced ion bombardment at $U_B = -100$ V.

i_s [mA/cm ²]	Interplanar Spacing [Å] Relative to JCPDS [%]			Peak Broadening FWHM [°2θ]		
	{111}	{200}	{220}	{111}	{200}	{220}
JCPDS	2.394	2.068	1.463	-	-	-
0.9	2.407 0.53	2.089 0.99	1.473 0.66	0.54	0.65	0.92
1.4	2.406 0.52	2.083 0.72	1.475 0.81	0.64	0.75	1.42
2.7	2.428 1.41	2.068 0.90	1.492 1.95	1.07	1.06	1.91
4.5	2.435 1.73	2.091 1.10	1.495 2.19	0.86	0.98	1.18

Table 4.20. Interplanar spacing and peak broadening (FWHM) for fcc-CrN at different substrate bias current density levels

Increased ion bombardment results in an increased lattice parameter a_0 in the range of $i_s = 0.9$ to 4.5 mA/cm², figure 4.56. The increase of the lattice parameter with increased ion bombardment indicates higher compressive stress.

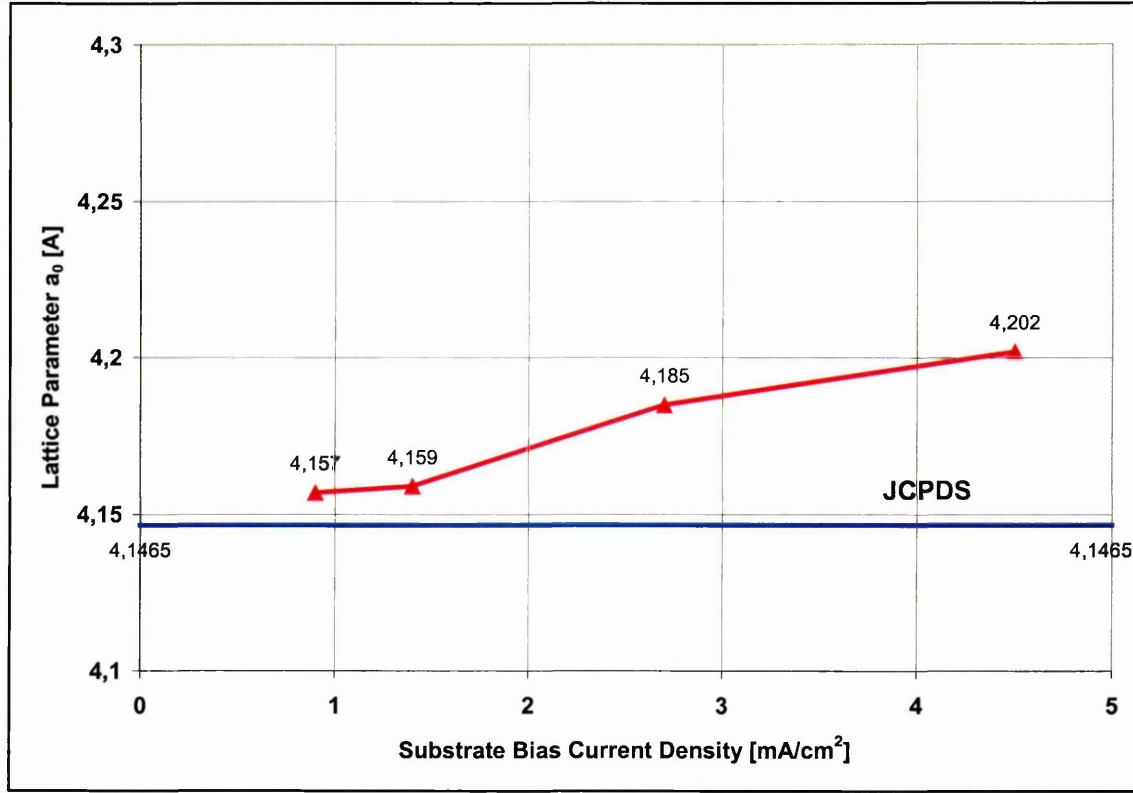


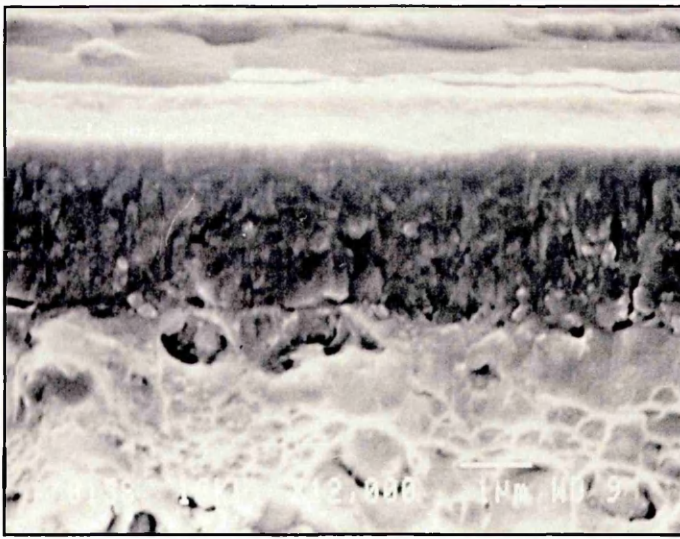
Figure 4.56. Effect of substrate bias current density on the lattice parameter a_0 of CrN_x .

4.3.4. SEM cross sections

The fracture cross-section SEM micrographs of the 2 extreme settings, i.e. $i_s = 0.9$ and 4.5 mA/cm^2 , are presented in figure 4.57.



(a) $i_s = 0.9 \text{ mA/cm}^2$



(b) $i_s = 4.5 \text{ mA/cm}^2$

Figure 4.57. SEM fracture cross sections at a bias current density i_s of 0.9 and 4.5 mA/cm^2 .

The micrographs indicate that the morphology becomes less columnar and the surface roughness decreases with increased ion bombardment. This was also shown for sputtered TiN [145].

This is in accordance with Messier's structure zone model [33].

4.3.5 Composition

At the substrate bias voltage level of -100 V the composition of the coatings remained unchanged with variation in the ion current density. The Cr concentration was $54.2 \pm 0.2 \text{ at.}\%$ and the N concentration remained at $45.8 \pm 0.2 \text{ at.}\%$.

4.3.6 Hardness and Young's modulus

Increased ion bombardment resulted in increased coating hardness values up to 24.5 GPa at a substrate bias current density of 4.5 mA/cm^2 , figure 4.58. In parallel the Young's modulus increased from 170 GPa at $i_s=0.9 \text{ mA/cm}^2$ to 200 GPa at $i_s=4.5 \text{ mA/cm}^2$.

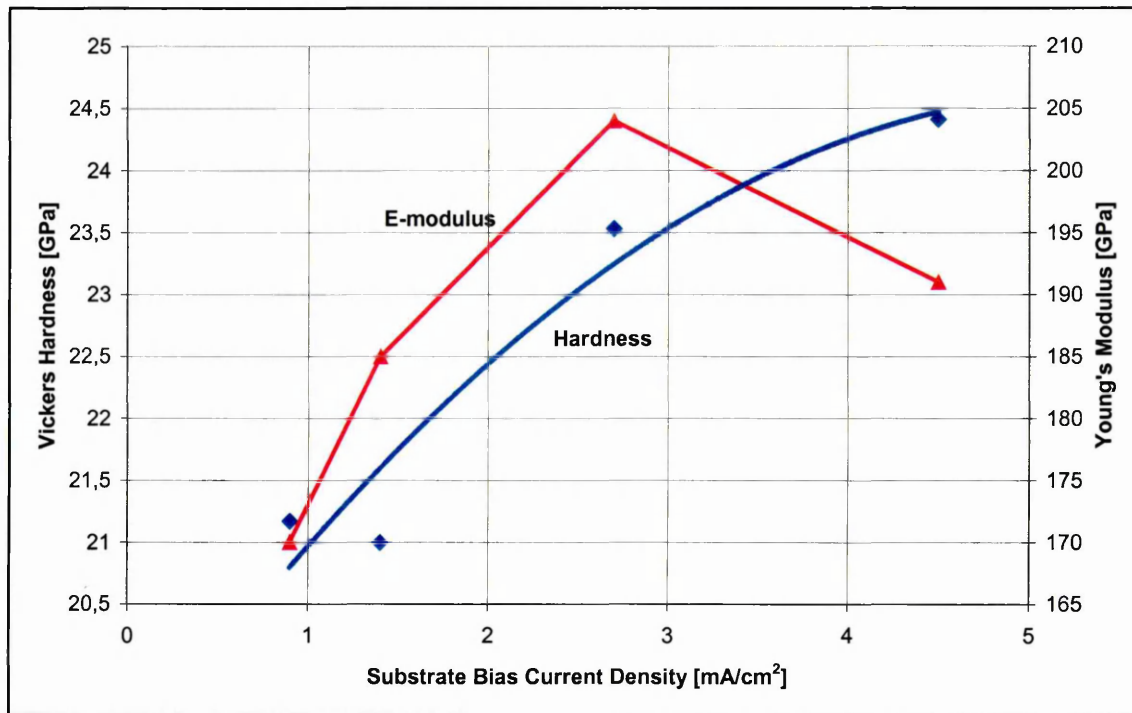


Figure 4.58. Effect of substrate bias current density on hardness and Young's modulus.

4.3.7. Residual stress

The residual stress measurements by the deflection method correspond well with the hardness and lattice parameter developments. With increased ion bombardment the compressive growing stress is increased (figure 4.59). The measurements substrate bias current densities of 0.9 and 1.4 mA/cm² indicate a tensile stress development. This data is not fully reliable since the samples are not fully free to bend in the tensile direction. The stress development is in accordance with the hardness development.

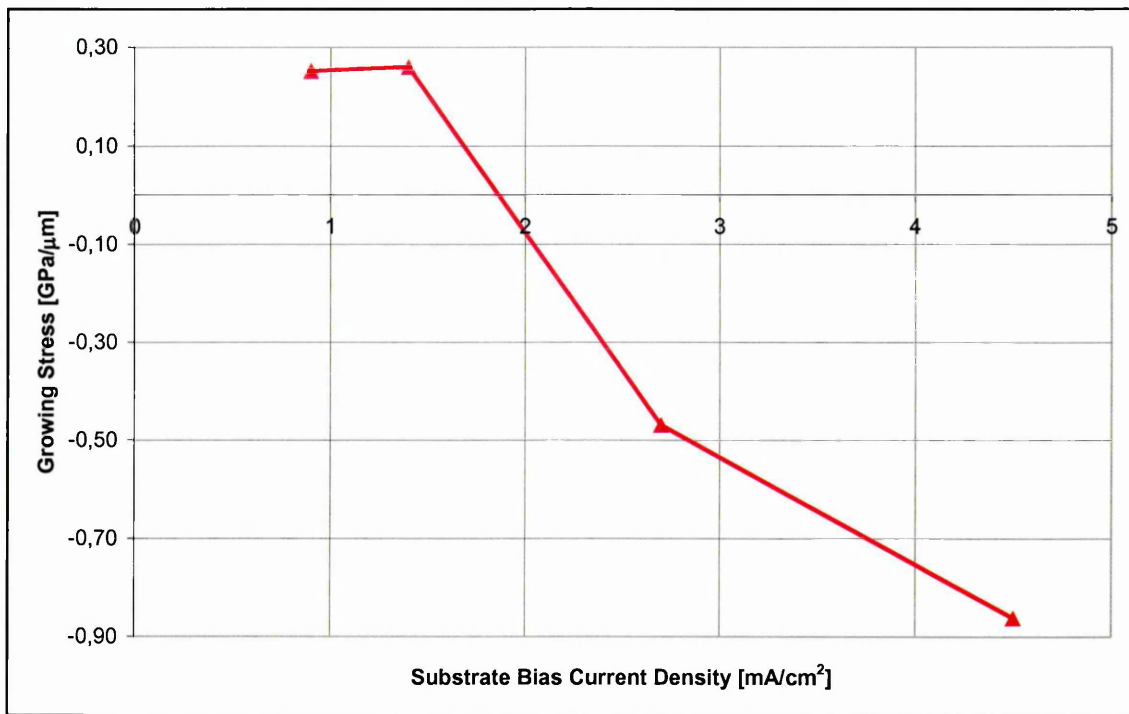


Figure 4.59. Effect of substrate bias current density on the growing stress.

4.3.8. Surface roughness

Figure 4.60 shows the tendency of the surface roughness to be decreasing with increased ion bombardment. The measured surface roughness at $i_s=2.7$ and 4.5 mA/cm² is in the range of the surface roughness of the substrate prior to coating. From the SEM fracture cross section micrographs there was also an indication of smoothing of the coating at enhanced ion bombardment.

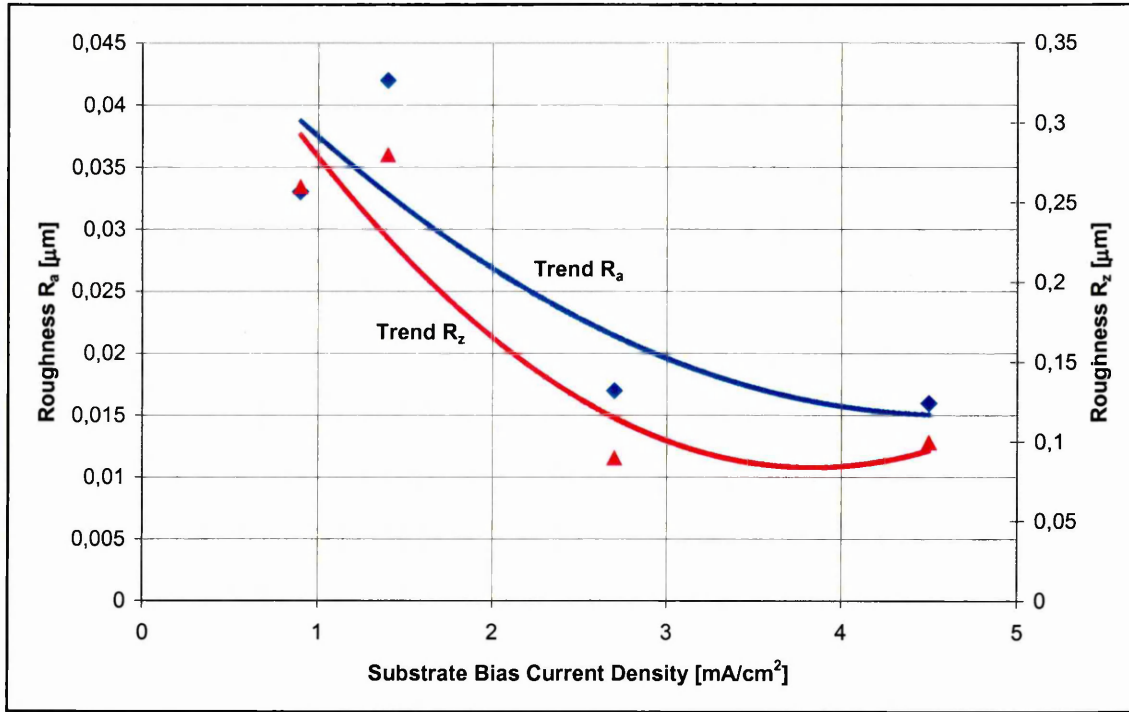


Figure 4.60. Effect of substrate bias current density on the surface roughness.

4.3.9. Colour

The value of L^* shows the same behaviour as the hardness value dependent on bias current density. This correlation was also observed for the influence of the nitrogen flow rate and the substrate bias voltage during the deposition. At the highest hardness value the L^* value is 75.2. The a^* and b^* values vary randomly within a small band width: $0.3 < a^* < 0.8$ and $1 < b^* < 3.1$. Figure 4.61 shows the dependency of L^* on the substrate bias current density i_s .

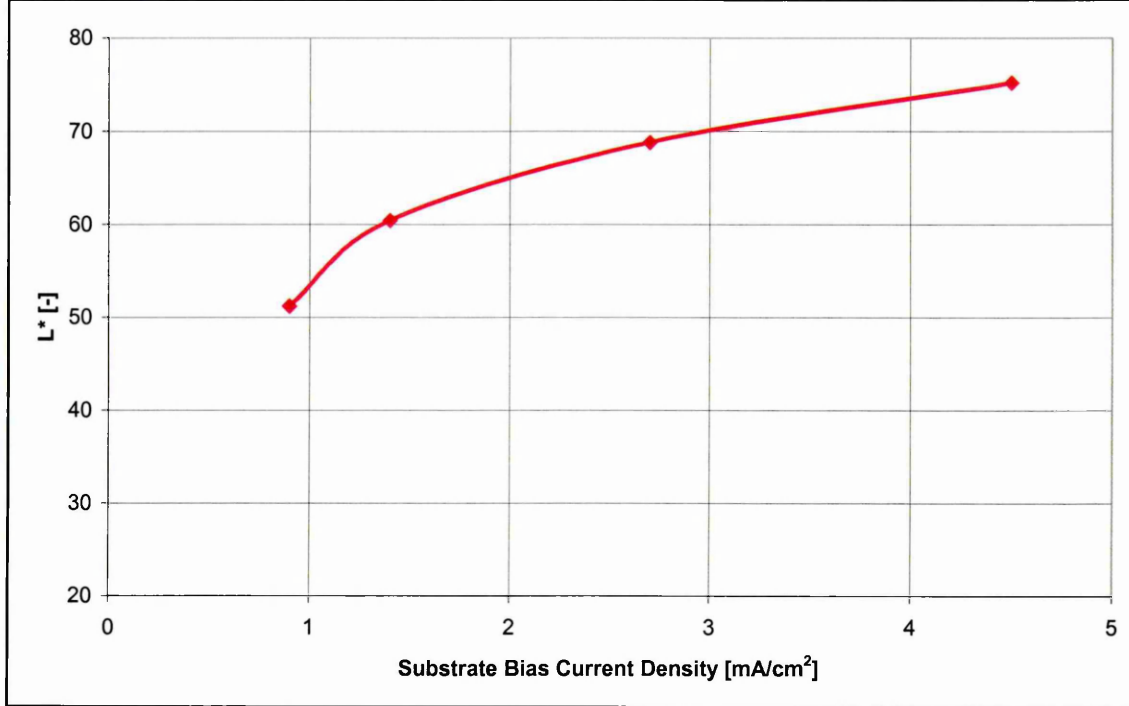


Figure 4.61. Effect of substrate bias current density on the colour co-ordinate L^* .

4.3.10 Adhesion

As expected the adhesion level reduces with an increase in the compressive stress as induced by increased ion bombardment. Figure 4.62 shows that the critical load L_c is 100 N at a substrate bias current density of 0.9 to 1.4 mA/cm² and is reduced to 75 N when depositing at a substrate bias current density of 2.7 to 4.5 mA/cm². The adhesion measurement by the Rockwell C indentation test resulted in all cases in a quality level "1", indicating no adhesion failures.

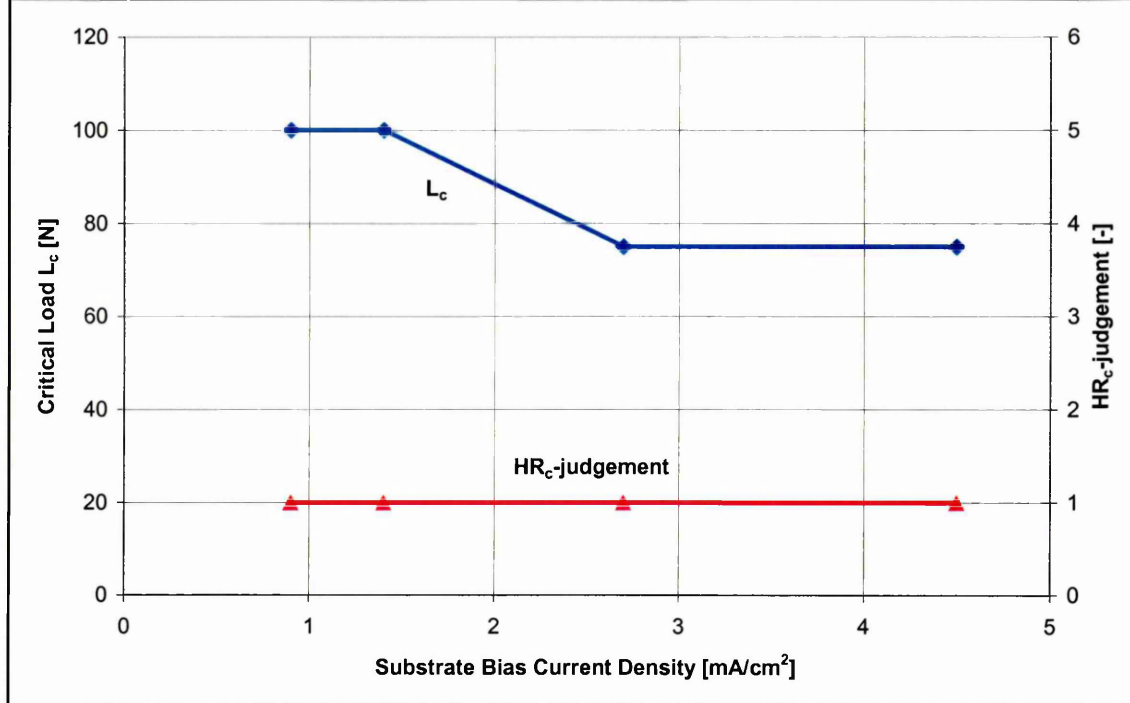


Figure 4.62. Effect of substrate bias current density on the coating adhesion.

4.4. Influence of type of ion etching on unbalanced magnetron sputtered CrN_x

4.4.1. Overview of the experiments

The possibility to investigate different ion treatments prior to PVD has been used for fcc-CrN deposited at $U_B = -75$ V and $f_{N_2} = 125$ sccm. In addition to argon ion bombardment chromium and tantalum ions, generated by the cathodic arc technology, have also been applied. Finally thin cathodic arc inter-layers of either chromium or tantalum were deposited in two experiments.

The cathodic arc ions bombardment was performed with the following set of parameters: Bias voltage = -800 V, cathodic arc current = 150 A, argon pressure $5 \cdot 10^{-2}$ Pa and an effective etching time of 5 minutes. The etching process was interrupted in order to maintain the substrate temperature below 300 °C.

The cathodic arc inter-layers were deposited under the following conditions: substrate bias voltage = -50 V, cathodic arc current = 150 A, argon pressure 1 Pa, coating time 20 minutes at a substrate temperature of 250 °C.

One CrN_x coating was deposited with cathodic arc only, after a chromium ion bombardment. This coating was deposited at Bias voltage = -50 V, cathodic arc current = 150 A, nitrogen flow rate of 600 sccm (resulting in a total pressure of 0.74 Pa with the turbo molecular pump at 80% of total pumping capacity), coating time 150 minutes and substrate temperature 250 °C.

The effect of metal ion pre-treatment at an acceleration voltage of -800 V can be particularly influential because of the high average ionisation-state of Cr and Ta, in a cathodic arc discharge namely 2.1 and 2.9 respectively [147], table 4.21.

Element	Atomic number	Q=+1	Q=+2	Q=+3	Q=+4	Q=+5	Q=+6	Q _{average}
Cr	24	10%	68%	21%	1%			2.1
Ta	73	2%	33%	38%	24%	3%		2.9

Table 4.21. Ionisation state of Cr and Ta within a cathodic arc discharge [147].

Besides the different degree of ionisation there is a strong difference in atomic weight for the three elements Ar, Cr and Ta (39.94, 52.01 and 180.95 respectively).

4.4.2. X-Ray diffraction (Bragg Brentano high angle scan)

4.4.2.1. Phase development

All the magnetron sputtered CrN_x coatings in this set of experiments show a preferred $\{111\}$ orientation in the fcc lattice, figures 4.63, 4.64, 4.65 and are similar to the coatings deposited with $U_B = -100$ V at $f_{N_2} = 150$ sccm (table 4.4). However, coatings pre-treated with Ta ions exhibit an even stronger $\{111\}$ preferred orientation. The cathodic arc deposited coating shows a typical $\{110\}$ preferred texture, figure 4.66.

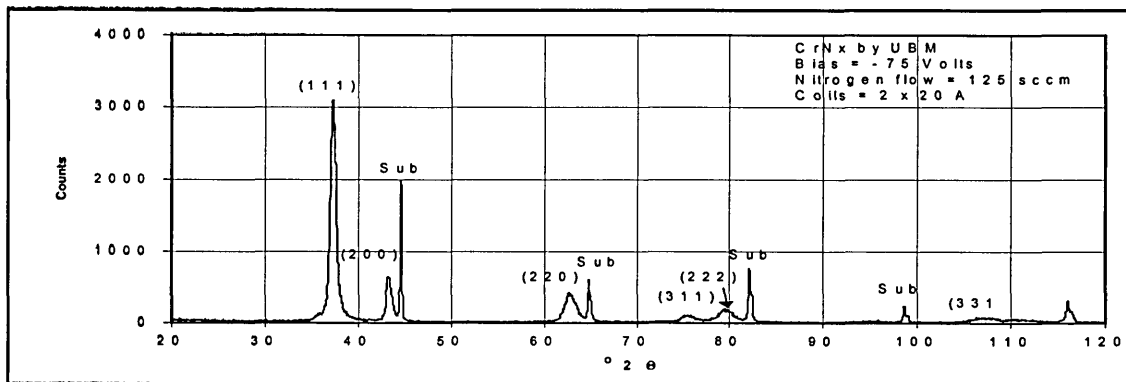


Figure 4.63. X-Ray diffraction pattern of magnetron sputtered CrN_x at $U_B = -75$ V and $f_{N_2} = 125$ sccm; argon ions pre-treatment.

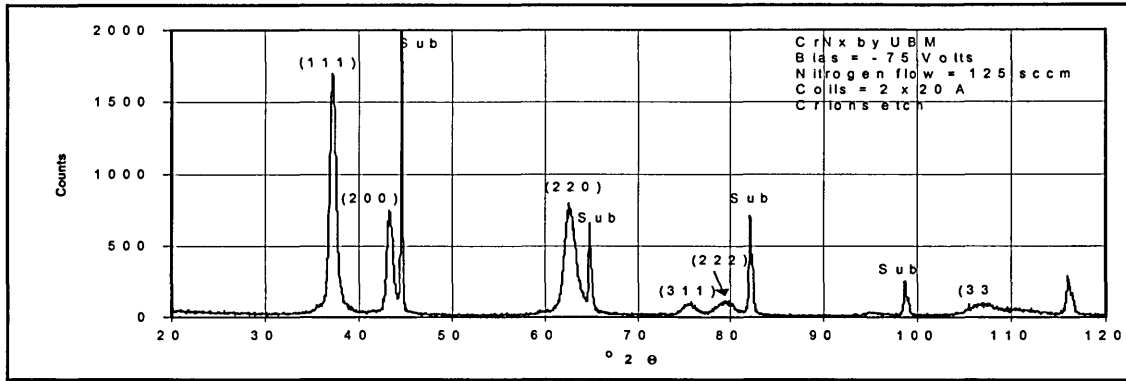


Figure 4.64. X-Ray diffraction pattern of magnetron sputtered CrN_x at $U_B=-75$ V and $f_{N_2}=125$ sccm; chromium ions pre-treatment.

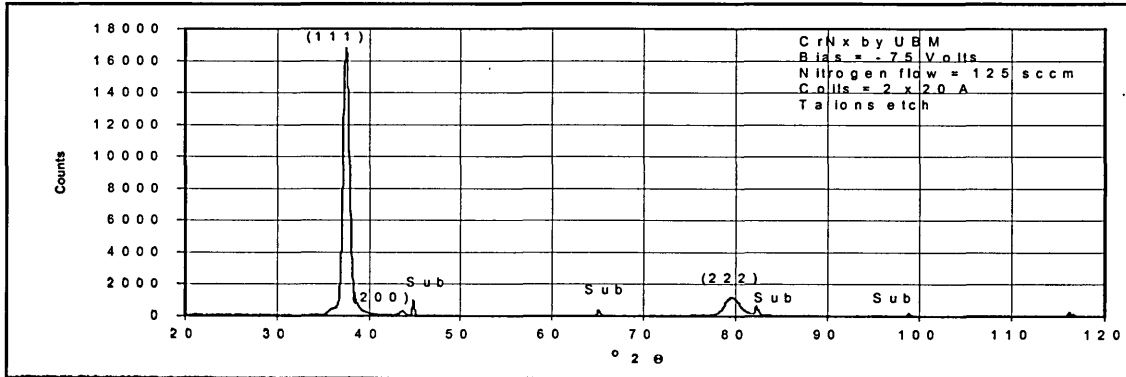


Figure 4.65. X-Ray diffraction pattern of magnetron sputtered CrN_x at $U_B=-75$ V and $f_{N_2}=125$ sccm; tantalum ions pre-treatment.

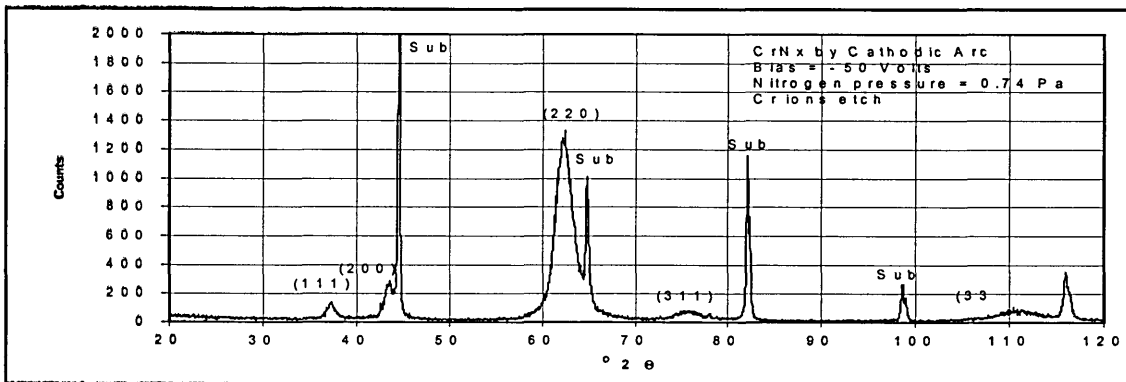


Figure 4.66. X-Ray diffraction pattern of cathodic arc CrN_x at $U_B=-50$ V and $p_{N_2}=0.74$ Pa; chromium ions pretreatment.

4.4.2.2. Texture

The sputtered fcc-CrN_x coatings, as deposited at U_B=-75 V and f_{N₂}=125 sccm, show a {111} preferred texture independent on the type of ions used during the pre-treatment step, table 4.22. However, the {111} preferred orientation is more pronounced for the coatings pre-treated with Ta ions. It is expected that there is already some Ta deposited during the pre-treatment step with Ta ions at an acceleration voltage of -800 V. A similar behaviour was reported for Nb ions at a bias voltage of -800 V [148].

The CrN coating deposited by the cathodic arc shows a typical {110} preferred orientation, and the result fits in the crystallographic model as presented in figure 2.6.

Technology			Texture parameter T* [%]		
Etching	Interlayer	Coating	{111}	{100}	{110}
Ar-glow discharge	----	CrN-sputter	52	10	15
Cr-Arc	----	CrN-sputter	31	10	29
Ta-Arc	----	CrN-sputter	93	3	2
Cr-Arc	Cr-Arc	CrN-sputter	48	7	23
Ta-Arc	Ta-Arc	CrN-sputter	98	2	0
Cr-Arc	----	CrN-Arc	2	3	73

Table 4.22. Texture parameter T* for fcc-CrN for different etching and deposition technologies.

4.4.2.3. Interplanar spacing and peak broadening

The interplanar spacing, peak broadening, and lattice parameter for the different etching and deposition conditions are summarised in tables 4.23, 4.24, and 4.25. The different pre-treatment steps hardly influence the interplanar spacing, peak broadening and lattice parameter of the sputtered fcc-CrN_x coatings. The arc deposited CrN_x coating shows higher values for the interplanar spacing, peak broadening, and lattice parameter. This indicates a higher compressive stress state compared to the sputtered fcc-CrN_x coatings.

Technology			Interplanar Spacing [Å] Relative to JCPDS [%]		
Etching	Interlayer	Coating	{111}	{200}	{220}
Ar-glow discharge	----	CrN-sputter	2.411 0.71	2.093 1.21	1.482 1.30
Cr-Arc	----	CrN-sputter	2.414 0.83	2.089 1.02	1.483 1.37
Ta-Arc	----	CrN-sputter	2.414 0.83	2.085 0.82	1.478 1.03
Cr-Arc	Cr-Arc	CrN-sputter	2.411 0.71	2.078 0.48	1.480 1.16
Ta-Arc	Ta-Arc	CrN-sputter	2.412 0.75	2.083 0.73	no significant peak
Cr-Arc	----	CrN-Arc	2.412 0.75	2.083 0.73	1.489 1.78

Table 4.23. Interplanar spacing for fcc-CrN for different etching and deposition technologies.

Technology			Peak Broadening FWHM [$^{\circ}2\theta$]		
Etching	Interlayer	Coating	{111}	{200}	{220}
Ar-glow discharge	----	CrN-sputter	0.71	0.64	1.33
Cr-Arc	----	CrN-sputter	0.74	0.71	1.34
Ta-Arc	----	CrN-sputter	0.77	0.77	1.36
Cr-Arc	Cr-Arc	CrN-sputter	0.68	0.61	1.37
Ta-Arc	Ta-Arc	CrN-sputter	0.70	0.65	no peak
Cr-Arc	----	CrN-Arc	1.02	1.05	2.13

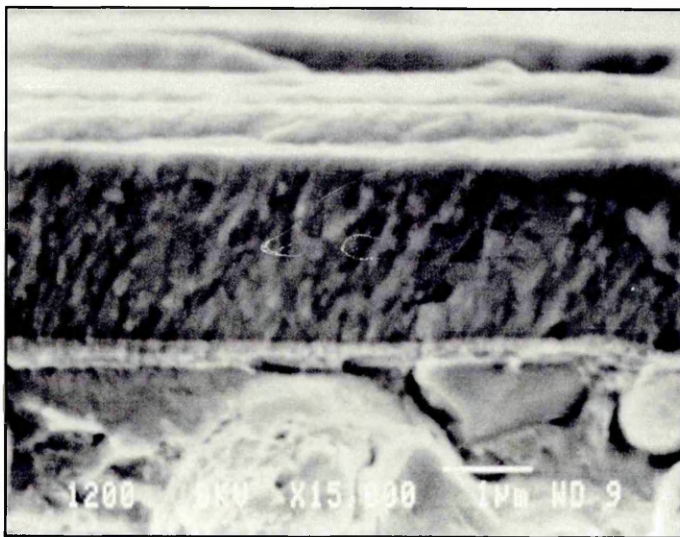
Table 4.24. Peak broadening (FWHM) for fcc-CrN for different etching and deposition technologies

Technology			Lattice parameter [\AA]
Etching	Interlayer	Coating	
Ar-glow discharge	----	CrN-sputter	4.177
Cr-Arc	----	CrN-sputter	4.180
Ta-Arc	----	CrN-sputter	4.178
Cr-Arc	Cr-Arc	CrN-sputter	4.169
Ta-Arc	Ta-Arc	CrN-sputter	4.175
Cr-Arc	----	CrN-Arc	4.186

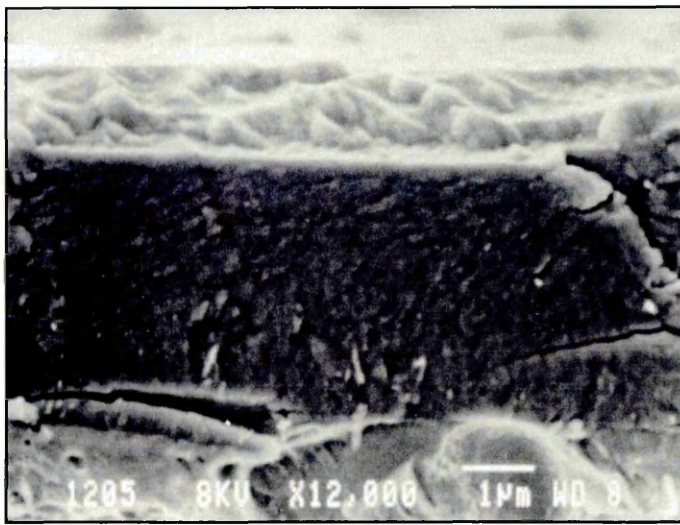
Table 4.25. Lattice parameter for different etching and deposition technologies.

4.4.3. SEM cross sections

The fracture cross section micrographs of the sputtered fcc-CrN_x with a Ta interlayer and the cathodic arc deposited fcc-CrN_x are shown in figure 4.67.



(a)



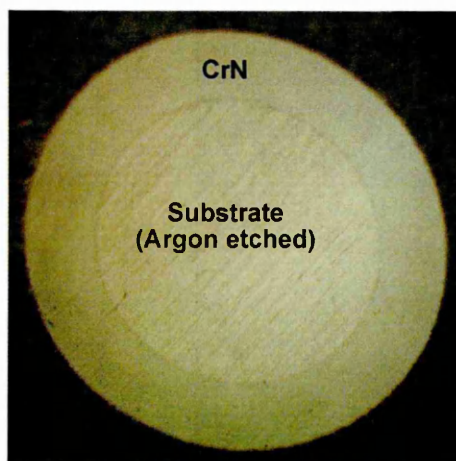
(b)

Figure 4.67. SEM cross section for a) sputtered and b) cathodic arc fcc-CrN_x.

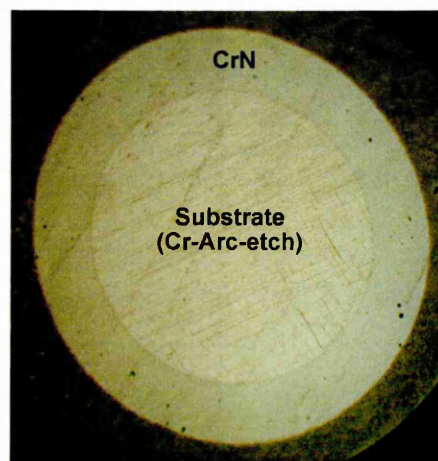
Both SEM cross section micrographs show a rather dense morphology without a clear growth direction, the most pronounced for the cathodic arc deposited fcc-CrN_x coating. In contrast the surface roughness is higher for the cathodic arc coating, as a result of the droplets.

4.4.4. Kalotest

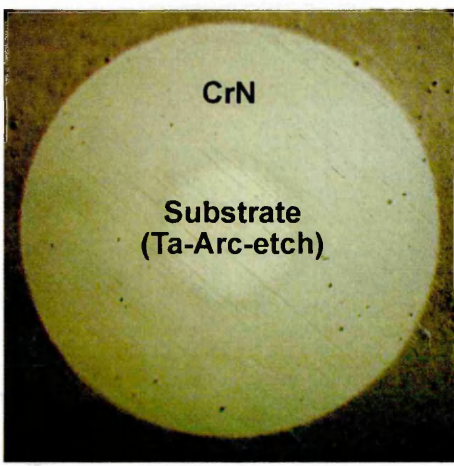
The kalo tests on the fcc-CrN_x coatings with the different pre-treatments steps are presented in figure 4.68. The versions with the metallic inter-layers are presented in figure 4.69. For the comparison the kalo of the cathodic arc coating is shown in figure 4.70.



a) Ar-ion-etch (3.8 μm)

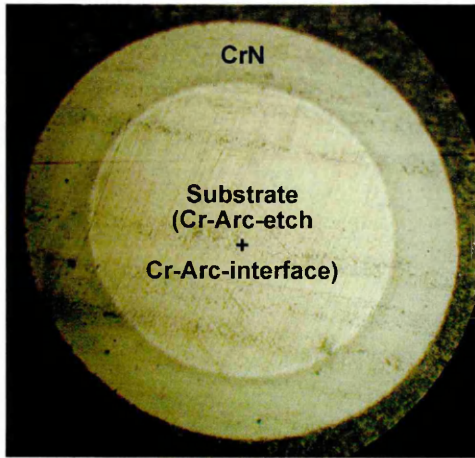


b) Cr-ion-etch (3.8 μm)

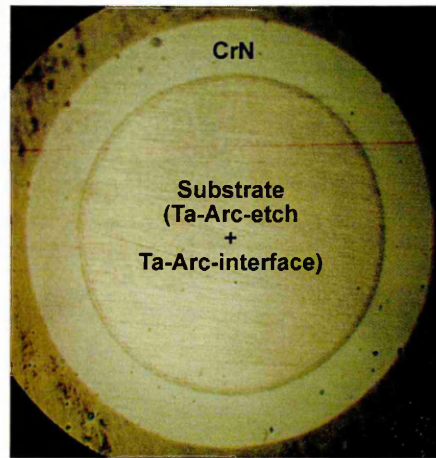


c) Ta-ion-etch ($3.8 \mu\text{m}$)

Figure 4.68. Kalo tests of a) argon etched, b) chromium and c) tantalum etched substrate and sputter coated CrN_x substrates.



a) $0.4 \mu\text{m}$ Cr + $3.8 \mu\text{m}$ CrN



b) $0.4 \mu\text{m}$ Ta + $3.6 \mu\text{m}$ CrN

Figure 4.69. Kalo tests of a) Cr cathodic arc inter-layer and b) Ta cathodic arc inter-layer with sputter deposited CrN_x on top.

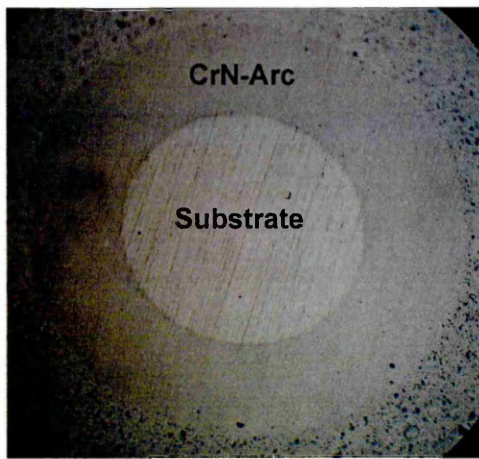


Figure 4.70. Kalo test of Cr cathodic arc etched substrate and cathodic arc deposited CrN_x ($4.3 \mu\text{m}$).

4.4.5. Hardness

The hardness of the sputtered CrN_x coatings within this set of experiments were within a hardness range of 20.1 ± 0.6 GPa, except for the argon etched sample, which showed a hardness value of 17.4 GPa. The CrN_x sample as deposited by cathodic arc evaporation showed a hardness value of 25.1 GPa. The higher hardness value correlates to the larger interplanar spacing and increased lattice parameter as discussed previously.

4.4.6. Surface roughness

The cathodic arc is known to be generating micro-particles, so called droplets. This is especially true in the case of random arc or low magnetic steering. The arc cathode as used within the experiments is in the category of low arc steering. As a result the coatings deposited with metal ion etch prior to coating or arc deposition deposited solely with the arc deposition process show a higher surface roughness than the one without the cathodic arc technology, table 4.26.

Technology			Surface roughness	
Etching	Interlayer	Coating	R _a [μm]	R _z [μm]
Ar-glow discharge	----	CrN-sputter	0.04	0.48
Cr-Arc	----	CrN-sputter	0.11	1.1
Ta-Arc	----	CrN-sputter	0.06	1.2
Cr-Arc	Cr-Arc	CrN-sputter	0.20	1.9
Ta-Arc	Ta-Arc	CrN-sputter	0.11	1.9
Cr-Arc	----	CrN-Arc	0.19	2.0

Table 4.26. Surface roughness overview for different etching and deposition technologies.

The higher melting temperature of tantalum reduces the resulting surface roughness when compared with the lower melting point chromium [149,150].

4.4.7. Adhesion

For the individual test runs the micrographs of the scratch test and Rockwell indentation test are presented in figures 4.71 to 4.76. The interpretation of the pictures is presented in table 4.27.

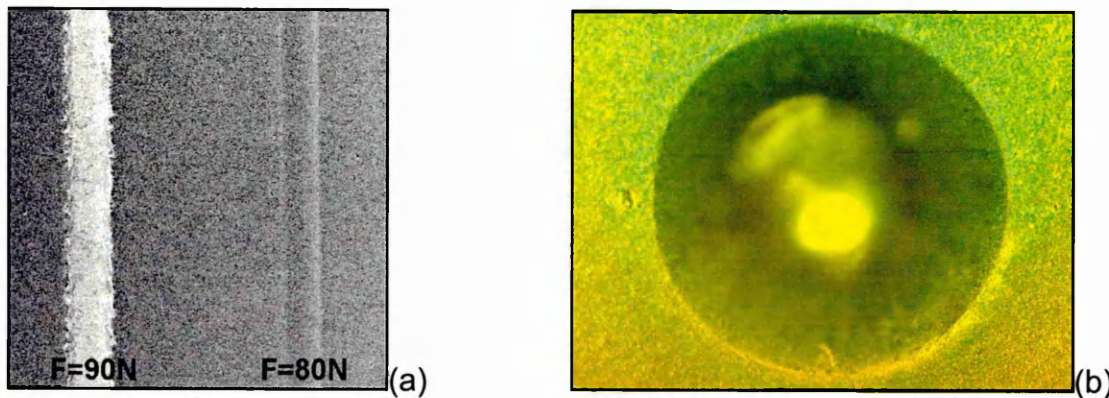
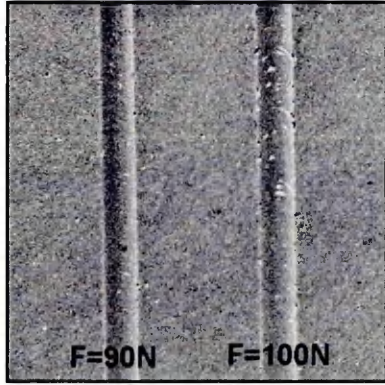
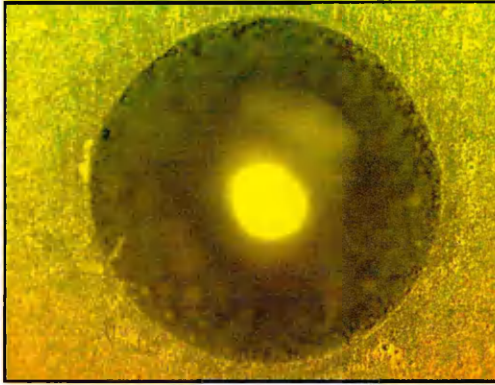


Figure 4.71. Adhesion test of Ar-etched and sputtered CrN_x; a) scratch test and b) HRc-test.

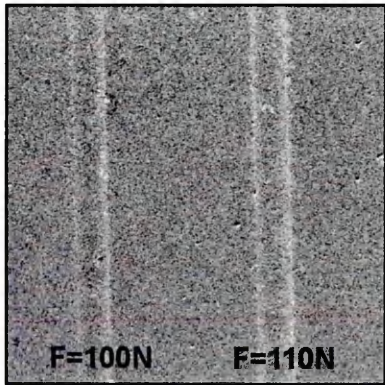


(a)

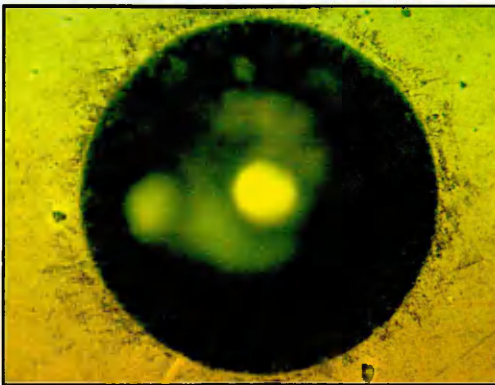


(b)

Figure 4.72. Adhesion test of Cr-etched and sputtered CrN_x ; a) scratch test and b) HRC-test.

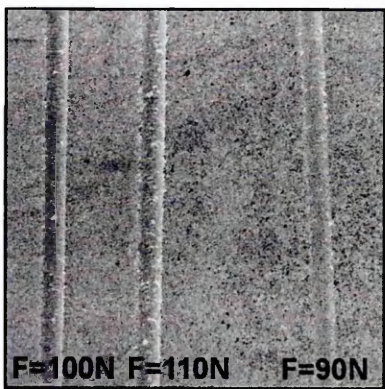


(a)

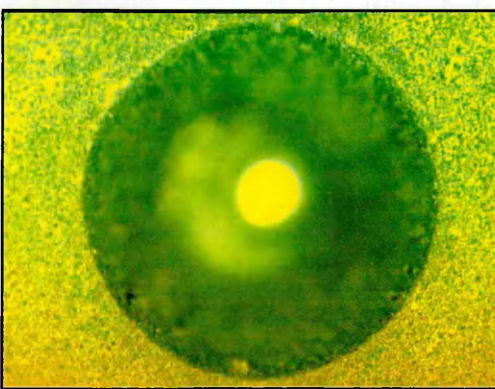


(b)

Figure 4.73. Adhesion test of Ta-etched and sputtered CrN_x ; a) scratch test and b) HRC-test.



(a)



(b)

Figure 4.74. Adhesion test of Cr-etched, Cr-interlayer and sputtered CrN_x ; a) scratch test and b) HRC-test.

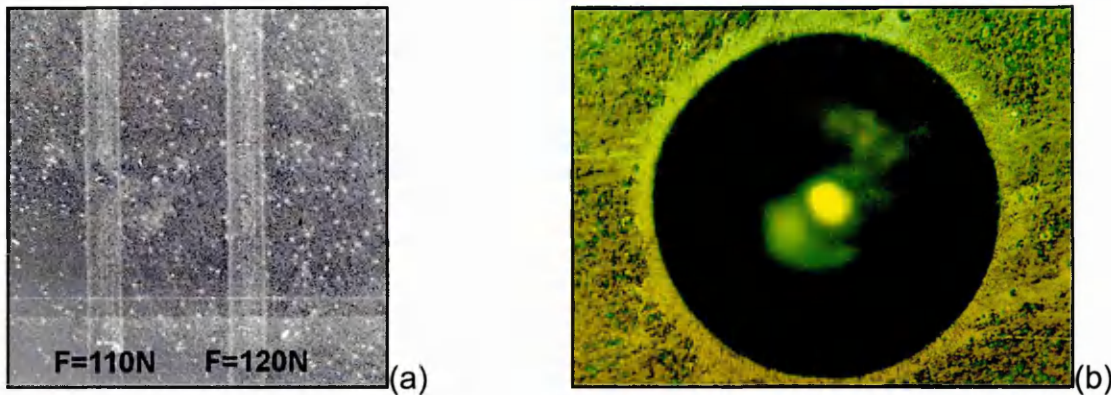


Figure 4.75. Adhesion test of Ta-etched, Ta-interlayer and sputtered CrN_x; a) scratch test and b) HRc-test.

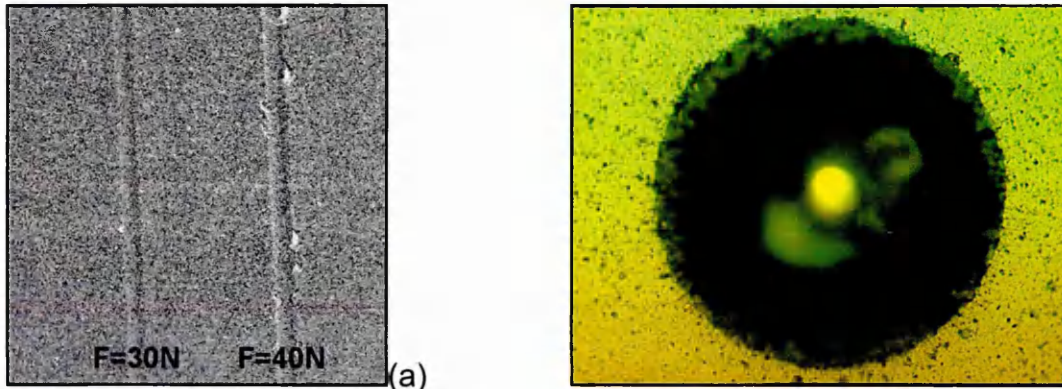


Figure 4.76. Adhesion test of Cr-etched and arc CrN_x; a) scratch test and b) HRc-test.

Technology			Adhesion		
Etching	Interlayer	Coating	L _c = OK [N]	L _c = Not OK [N]	HRc-judgement
Ar-glow discharge	----	CrN-sputter	80	90	1
Cr-Arc	----	CrN-sputter	90	100	1
Ta-Arc	----	CrN-sputter	100	110	1
Cr-Arc	Cr-Arc	CrN-sputter	100	110	1
Ta-Arc	Ta-Arc	CrN-sputter	110	120	1
Cr-Arc	----	CrN-Arc	30	40	2

Table 4.27. Adhesion overview for different etching and deposition technologies.

The deposition parameters for the sputtered CrN_x coatings were selected in a low internal stress regime ($U_B < -100$ V), which in general resulted in high critical load and low HR_C classification values. Etching with metallic ions showed an improved adhesion level as measured by critical load in the scratch test when compared with substrate cleaning with argon ions only. The adhesion performance is further

improved for Ta ion pre-treatment than for the Cr ion pre-treatment. The higher average ionisation state and the higher atomic weight of the Ta ions might be explained by the more energetic ion bombardment and penetration of these atoms into the substrate surface [151].

Thin metallic inter-layers further improve the adhesion of the sputtered CrN_x coating. In this case the softer materials act as a stress relieve zone between the hard ceramic coating and the softer substrate material, M2 HSS in this case.

The coating as deposited by the cathodic arc shows surprisingly a lower adhesion value than the lower hardness UBM deposited coatings. However, a hardness of 25.1 GPa indicates higher internal compressive stress which lead to a reduced adhesion at the substrate/coating interface.

4.5. Engineered properties of hard sputtered CrN_x

4.5.1. Overview of the experiments

In this chapter corrosion and pin-on-disc tests of several single layers and engineered dual-layers are studied. An overview of the deposition conditions is given in table 4.28.

Sample	Etch (Arc)	Inter-layer			Coating		
		Technology	Bias [-V]	N2-flow [sccm]	Technology	Bias [-V]	N2-flow [sccm]
1	Cr	--	--	--	Arc	50	600* ¹
2	Ar	--	--	--	UBM	75	100
3	Ar	--	--	--	UBM	50	200
4	Cr	UBM	75	100	UBM	200	200
5	Ta	--	--	--	UBM	50	55
6	Cr	UBM	50	55	UBM	150	200
7	Cr	UBM	50	55	UBM	200	300
8	Ta	UBM	50	55	UBM	200	300
9* ²	Cr	UBM	75	100	UBM	200	30

*¹ Turbo molecular pump at 80% capacity, resulting in 0.74 Pa.

*² The steady state temperature for the set of deposition conditions was 390 °C.

table 4.28. Overview of the test samples for corrosion and wear tests

4.5.2. Film properties

The values for the layer thickness, adhesion, hardness, light reflection L*, surface roughness R_a, and texture are reported in table 4.29.

The majority of the properties are in line of expectations, which may be concluded from the results in sections 4.1, 4.2, 4.3, and 4.4. However, there exist some features, which need further discussion. Samples 2 and 3 show surprisingly high surface roughness for magnetron sputtered coatings with an argon ion bombardment as the pre-treatment. A possible explanation may be seen in severe micro-arcing at the target surface. Samples 7 and 8 were less hard than expected for. Although the

preferred {100} orientation, a high substrate bias voltage and high N₂ flow rates, directs towards high hardness values (figure 4.32). It might be assumed that the relatively soft hcp-Cr₂N inter-layer (12.5 GPa), stimulates crystal growth with a lower residual stress.

The high hardness of sample 9 seems to be a result of the two effects: a high substrate bias voltage of -200 V and a high steady state deposition temperature of 390 °C, caused by the high energetic ion bombardment (high substrate bias voltage and high substrate bias current density).

Sample	Thickness [μm]	Critical Load [N]	HR _c -DB [-]	HV _{0.025} [GPa]	R _a [μm]	L* [-]	Phases	Pref. Orient.
1	4.3	35	1	25.1	0.19	73.7	fcc-CrN	{110}
2	3.3	65	3	17.8	0.14	64.6	fcc-CrN	{110}
3	3.6	65	1	15.8	0.31	51.8	fcc-CrN	{110}
4	0.2+2.1	60	2	31.0	--	70.9	fcc-CrN	{100}
5	4.3	115	1	12.5	0.05	42.2	hcp-Cr ₂ N	{11.1}
6	0.5+2.9	105	1 to 2	20.5	0.14	58.8	fcc-CrN	{111}
7	0.5+2.8	95	2	21.4	0.17	68.2	fcc-CrN	{100}
8	0.6+2.7	95	2 to 3	24.6	0.07	71.9	fcc-CrN	{100}
9	0.2+3.3	60	2	30.0	0.06	83.1	bcc-Cr & hcp-Cr ₂ N	--

Table 4.29. Film properties of engineered CrN_x coatings.

4.5.3. Corrosion properties of unbalanced magnetron sputtered CrN_x coatings

The polarisation curves of the different coatings on stainless steel are plotted in figures 4.77 to 4.81. The polarisation curves of uncoated stainless steel and stainless steel with an 18 μm electroplated hard chromium are included as a reference. All experiments have been carried out using an aqueous electrolyte containing 3% NaCl. Under these conditions stainless steel and electroplated hard chromium exhibit at V_{corr} = 0 anodic corrosion current densities of typically 1. 10⁻⁶ A/cm². The pitting potential of stainless steel and hard chromium reached values of approximately + 0.2 V and + 0.7 V, respectively.

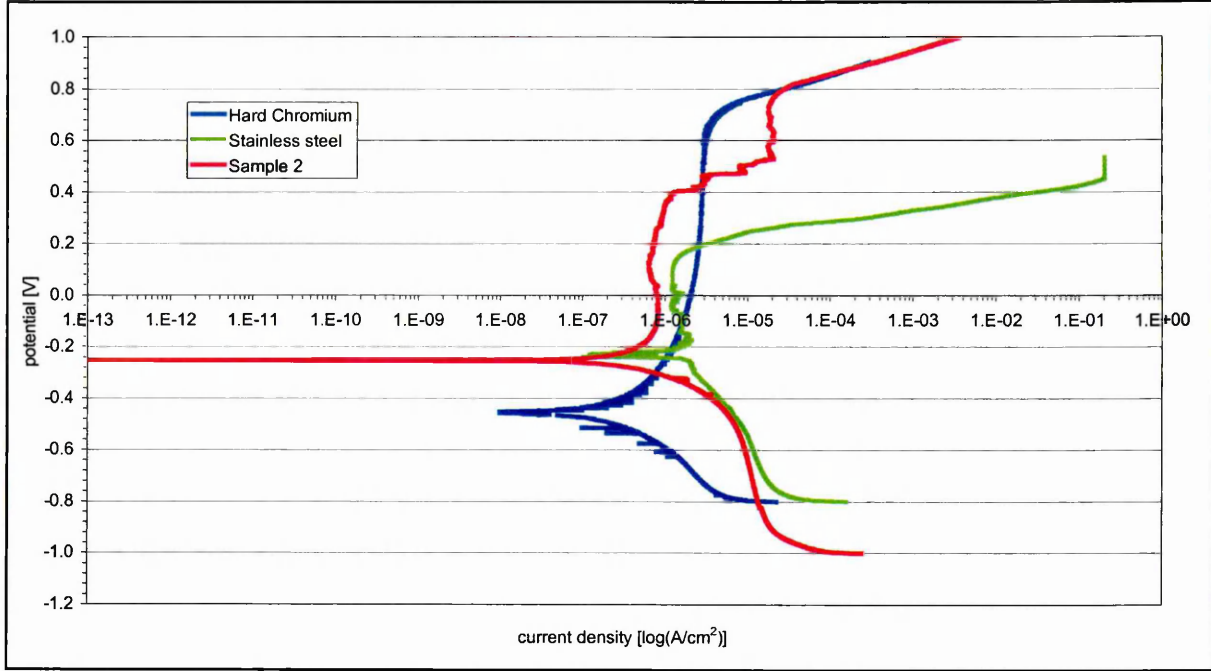


Figure 4.77. Potentiodynamic polarisation curve for sample 2.

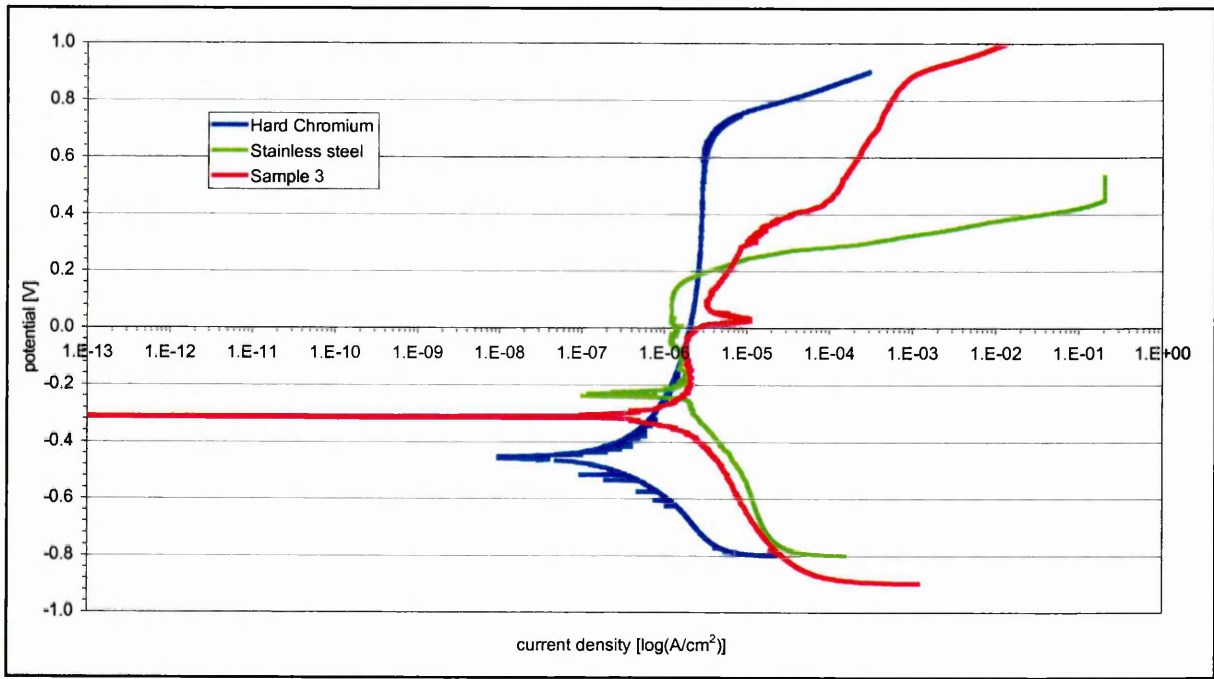


Figure 4.78. Potentiodynamic polarisation curve for sample 3.

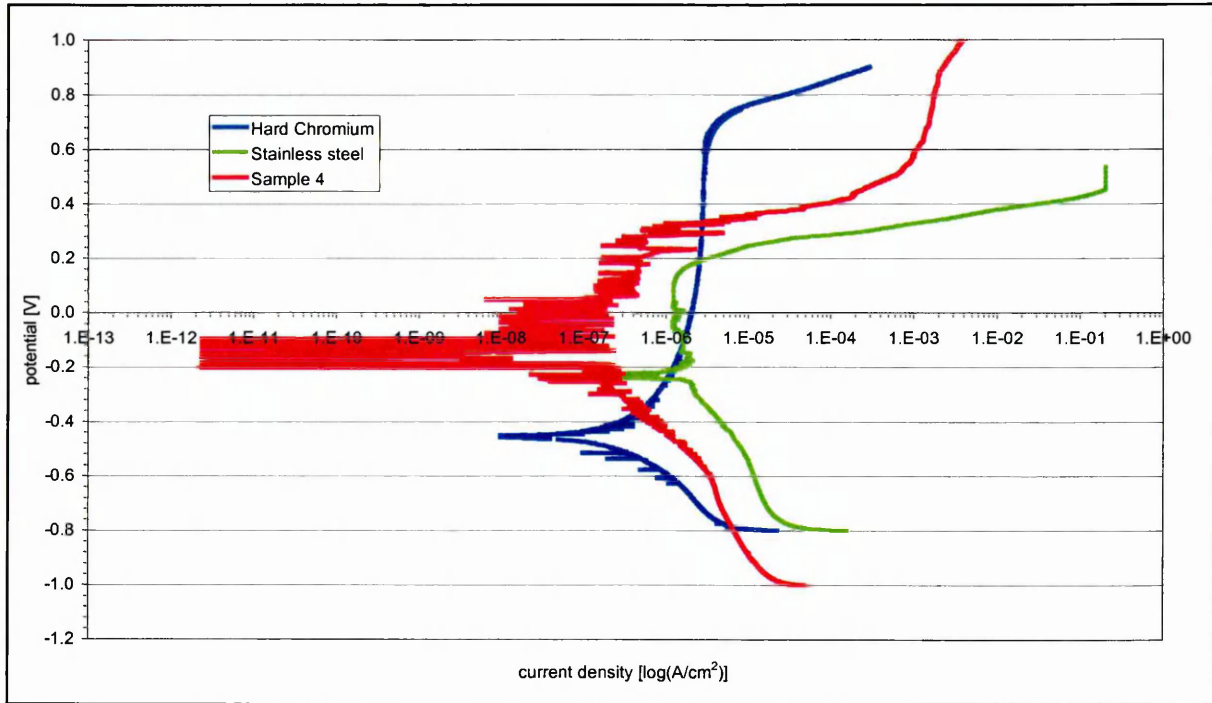


Figure 4.79. Potentiodynamic polarisation curve for sample 4.

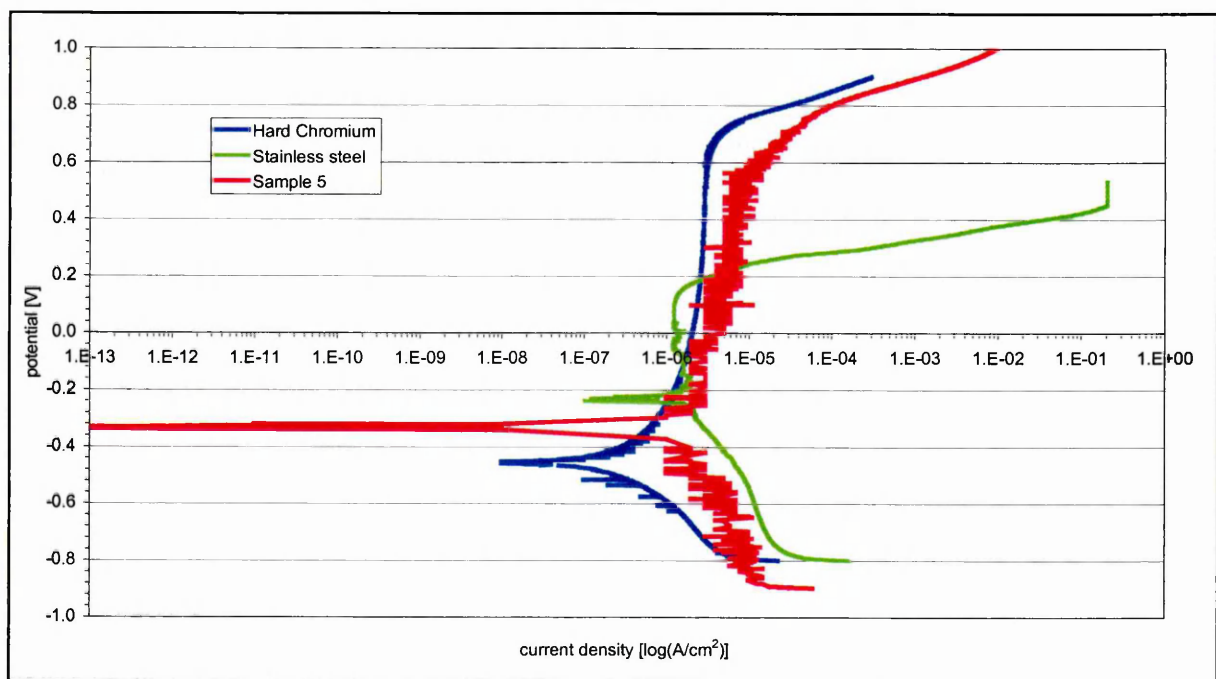


Figure 4.80. Potentiodynamic polarisation curve for sample 5.

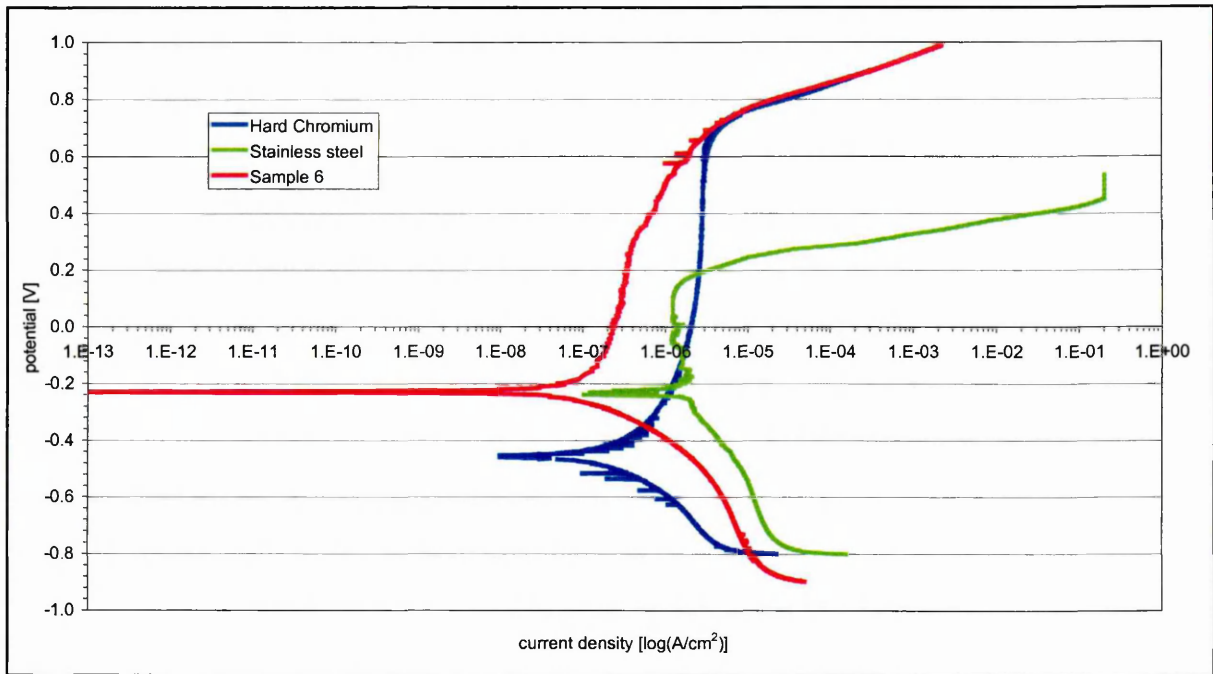


Figure 4.81. Potentiodynamic polarisation curve for sample 6.

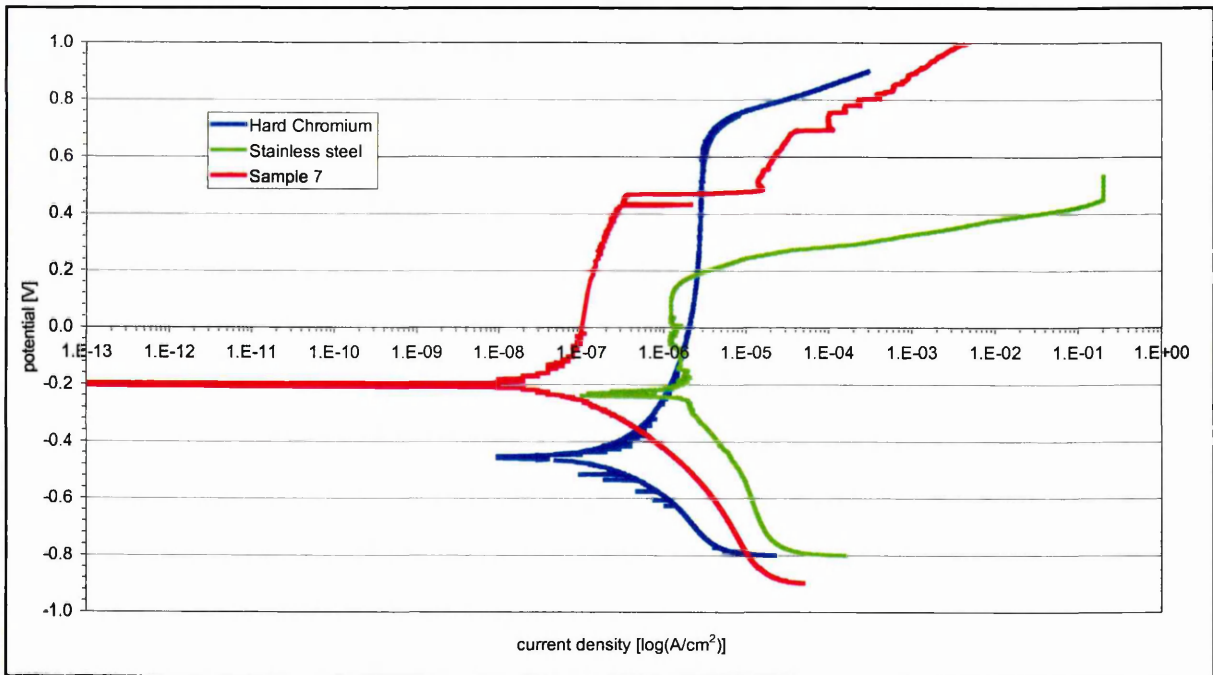


Figure 4.82. Potentiodynamic polarisation curve for sample 7.

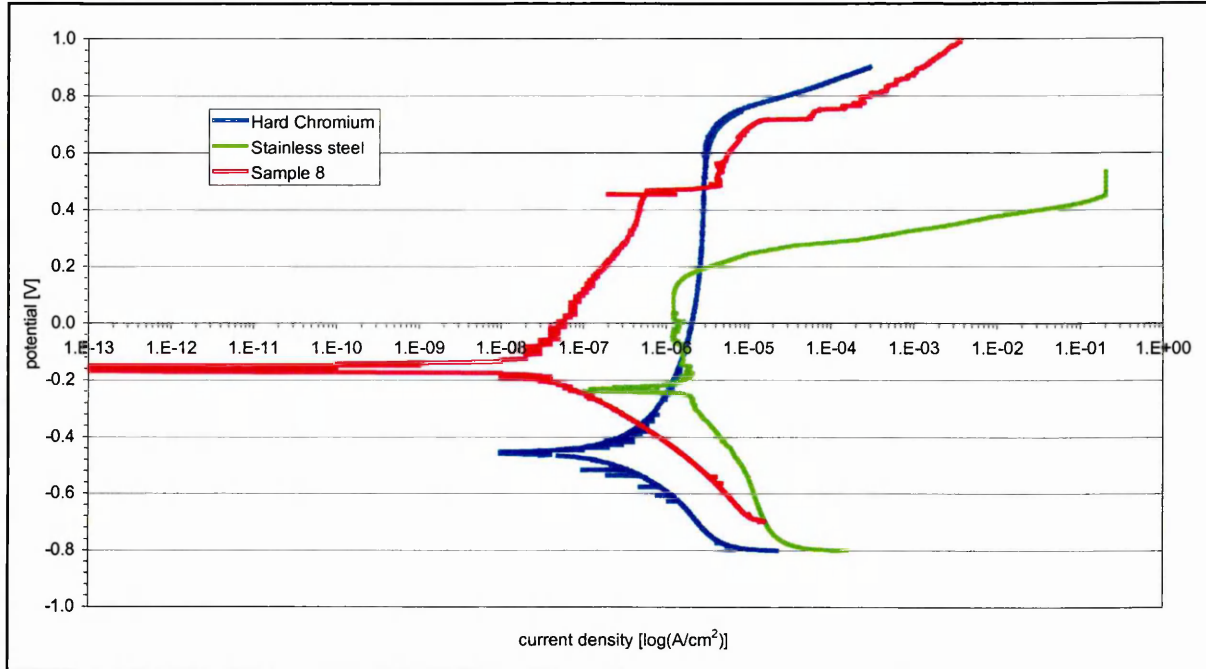


Figure 4.83. Potentiodynamic polarisation curve for sample 8.

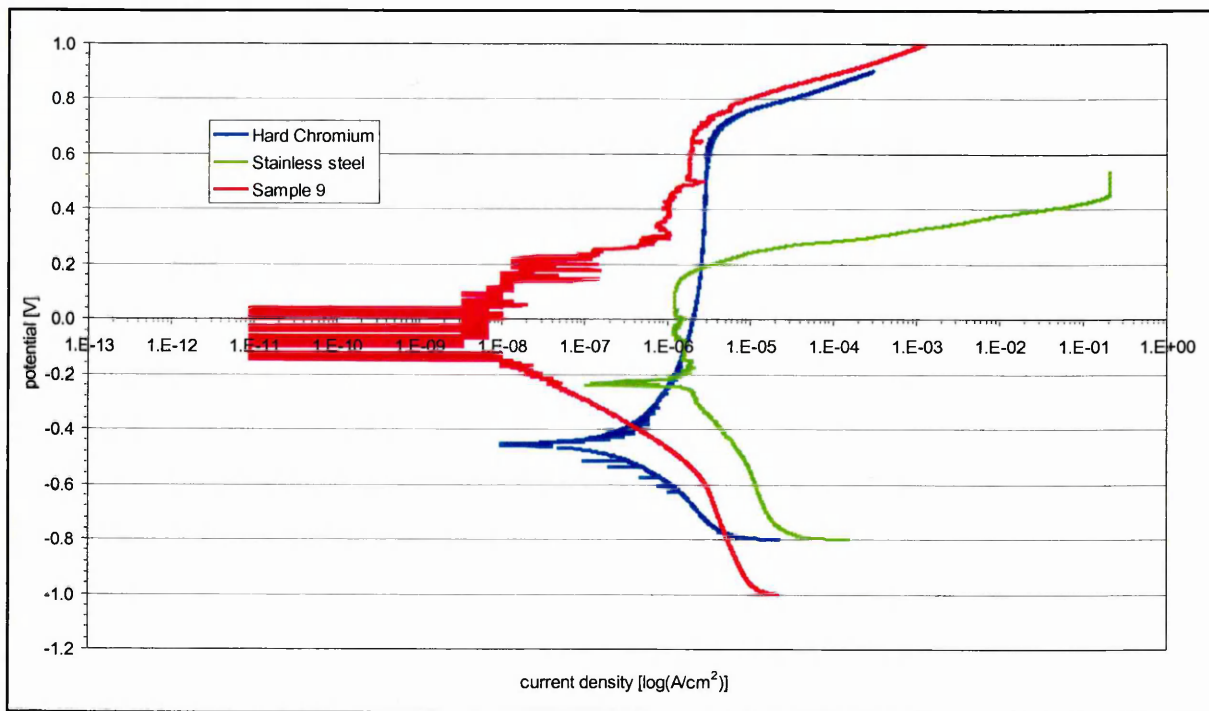


Figure 4.84. Potentiodynamic polarisation curve for sample 9.

In comparison with stainless steel and electroplated hard chromium samples 4,6,7, 8, and 9 showed a distinct improvement in corrosion behaviour. All these samples were deposited with a base layer and at fairly high substrate bias voltages ($U_B \geq -150$ V). All the coatings exhibited high critical load values and low HR_c -DB classifications

(except sample 8). In contrast coatings with Ar^+ pre-treatment (samples 2 and 3) and low N_2 flow rates (sample 5) exhibited corrosion currents similar to those of stainless steel and electroplated hard chromium. The latter three coatings were grown with rather low substrate bias voltages ($U_B \leq -75$), which indicates the existence of micro voids along column boundary, (figure 4.27) [33] in contrast to samples 4, 6, 7, 8, and 9 which were deposited at bias voltages ($U_B \geq -150$) and almost void free (figure 4.28) and indeed Figure 4.85 shows that there is a strong correlation between bias voltage and anodic current density in the polarisation tests.

The two samples with a hcp- Cr_2N inter-layer and coated at $U_B = -200$ V and high nitrogen flow rate ($f_{\text{N}_2} = 300$ sccm) showed a sudden increase in the current density at approximately +460 mV working potential. In both cases a local delamination of the coating is observed, like in figure 4.86. In order to achieve good adhesion of the highly stressed fcc- CrN a low stressed inter-layer was chosen. The choice of going for a hcp- Cr_2N was most probably not the best one, because of the mismatching crystal structures. Fcc- CrN conditions such as for sample 6 might be a better choice as the inter-layer.

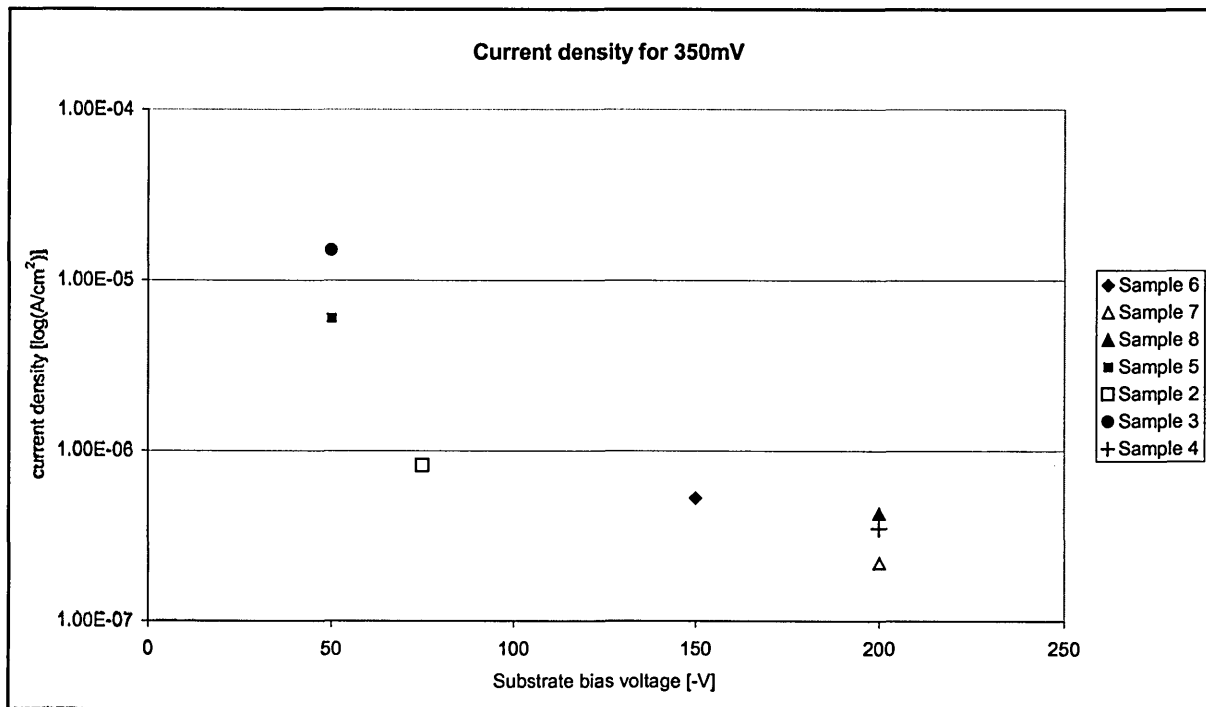


Figure 4.85. Anodic current density at a working potential of +350 mV dependent on the substrate bias voltage, coated at a substrate temperature of 250 °C.

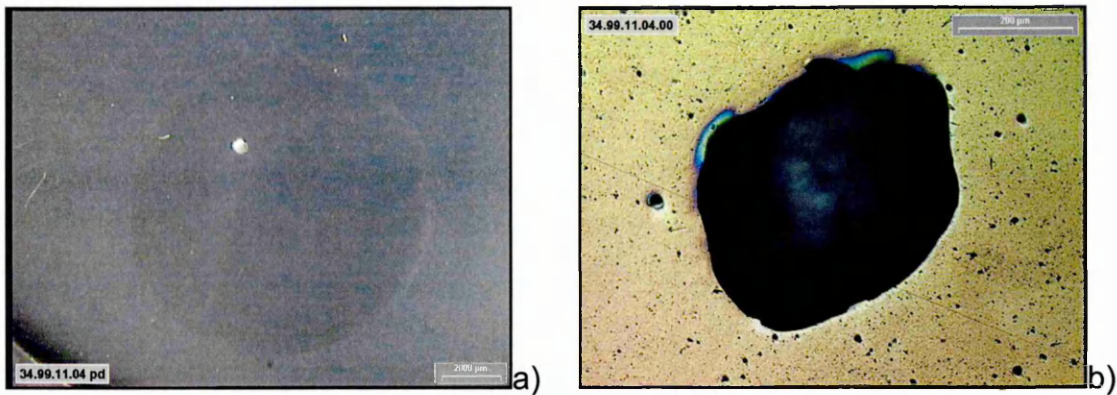


Figure 4.86. a) Corrosion test area of sample 8 and b) local defect at a higher magnification.

4.5.4. Pin-on-disc and wear test results of CrN_x coatings

With respect to the interest of CrN_x coatings it is also important to know the tribological behaviour. For this reason several single layer and dual layer coatings have been tested with the pin-on-disc test. Figures 4.87 shows the arc deposited coating “sample 1”.

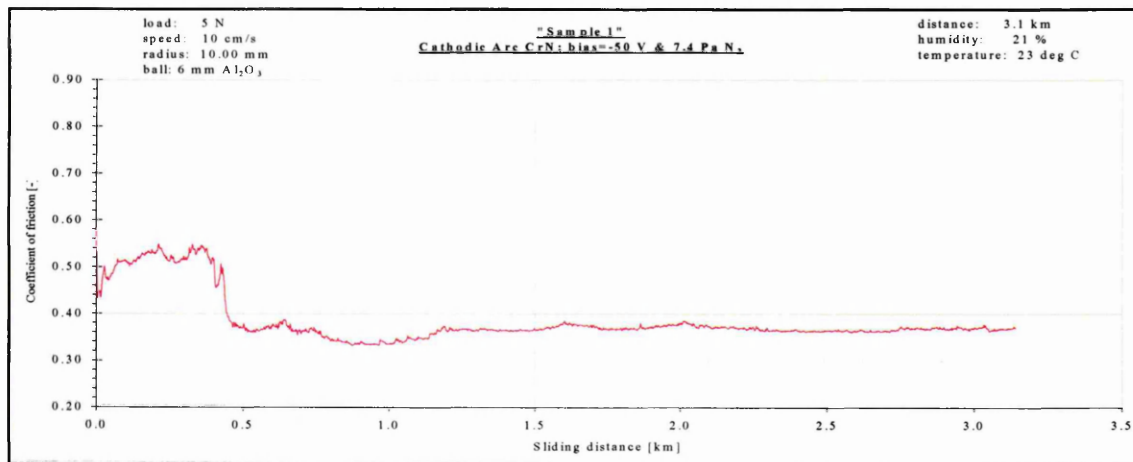


Figure 4.87. Pin-on-disc test of sample 1; Cathodic arc deposited fcc-CrN.

The steady state value for the coefficient of friction (“C.O.F.”) is 0.37 and is relatively low for a metal nitride coating. During the first 0.5 km sliding distance a C.O.F. of 0.54 is measured as a result of the surface roughness, caused by the droplets.

Within figures 4.88 to 4.5.92 it can be seen that the C.O.F. is reduced from 0.85 to 0.48 when increasing the bias voltage from -20 V to -300 V. The nitrogen flow rate for these samples remained the same at 100 sccm and they are etched with argon ions.

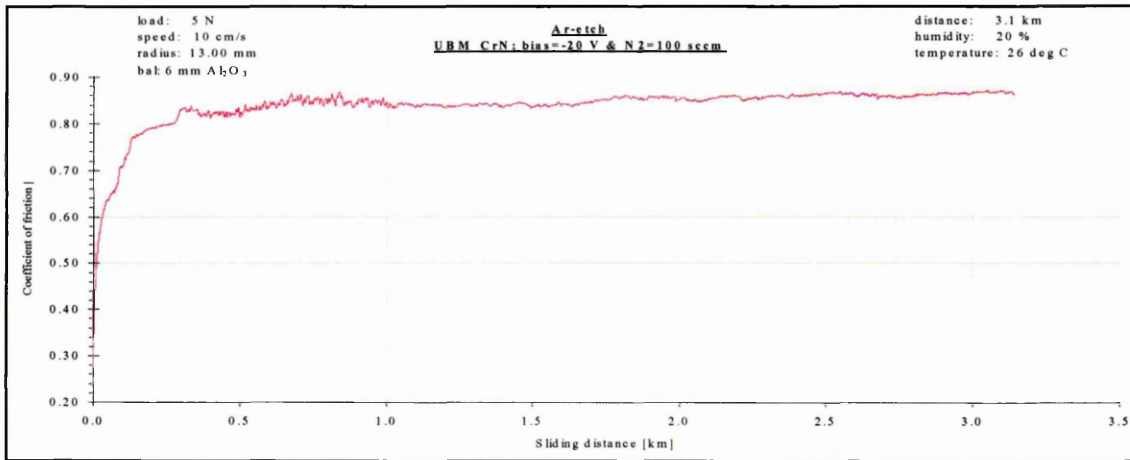


Figure 4.88. Pin-on-disc test of fcc-CrN_x; Ar etch and UBM at $U_B=-20$ V and $f_{N_2}=100$ sccm.

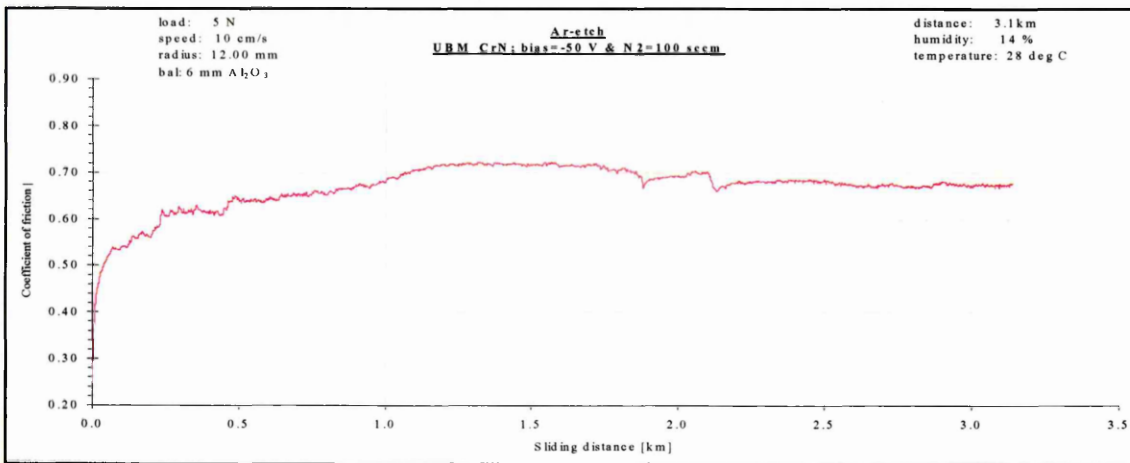


Figure 4.89. Pin-on-disc test of fcc-CrN_x; Ar etch and UBM at $U_B=-50$ V and $f_{N_2}=100$ sccm.

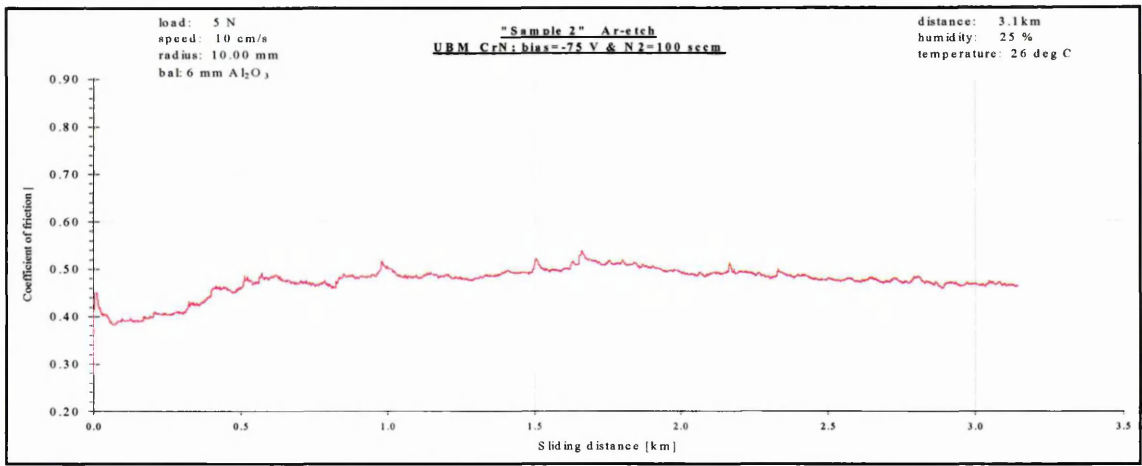


Figure 4.90. Pin-on-disc test of fcc-CrN_x; Ar etch and UBM at U_B=-75 V and f_{N2}=100 sccm.

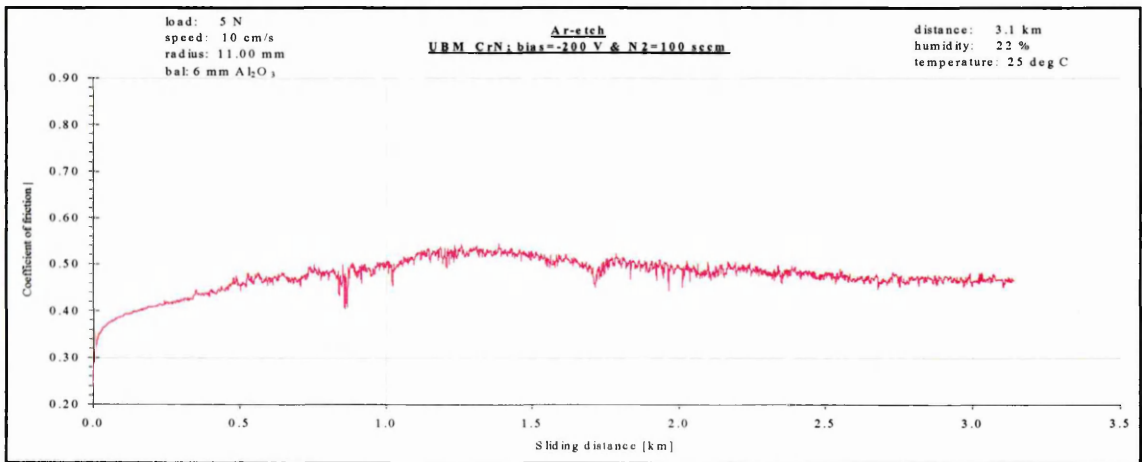


Figure 4.91. Pin-on-disc test of fcc-CrN_x; Ar etch and UBM at U_B=-200 V and f_{N2}=100 sccm.

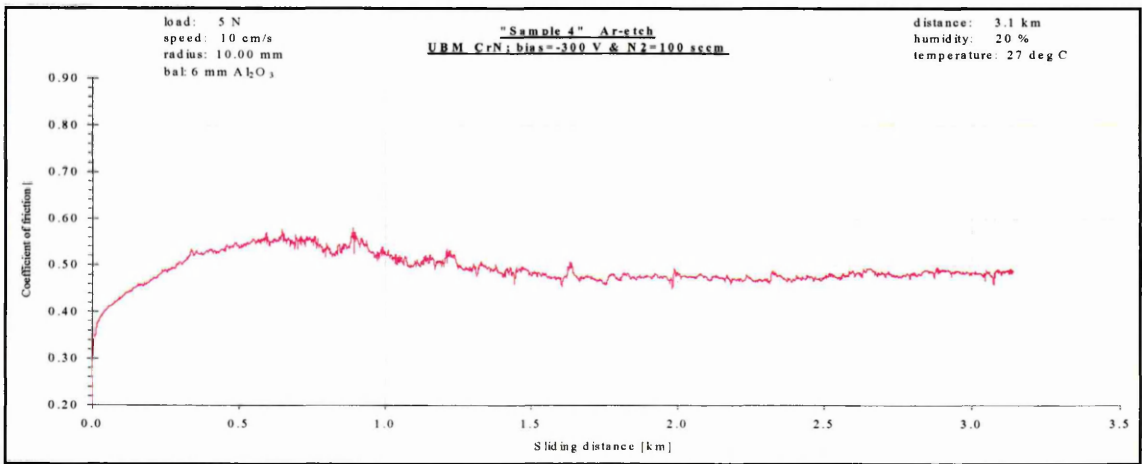


Figure 4.92. Pin-on-disc test of mixed fcc-CrN_x and hcp-Cr₂N; Ar etch and UBM at U_B=-300 V and f_{N2}=100 sccm.

Depositing CrN_x coatings by magnetron sputtering at a nitrogen flow level of 200 sccm does not significantly reduce the C.O.F. as can be seen in figures 4.93 to 4.95.

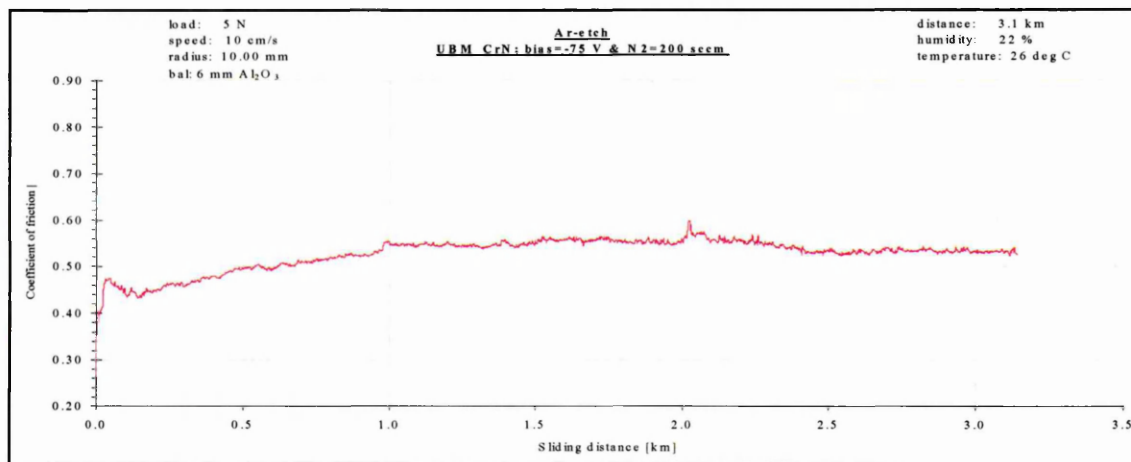


Figure 4.93. Pin-on-disc test of fcc-CrN_x; Ar etch and UBM at U_B=-75 V and f_{N2}=200 sccm.

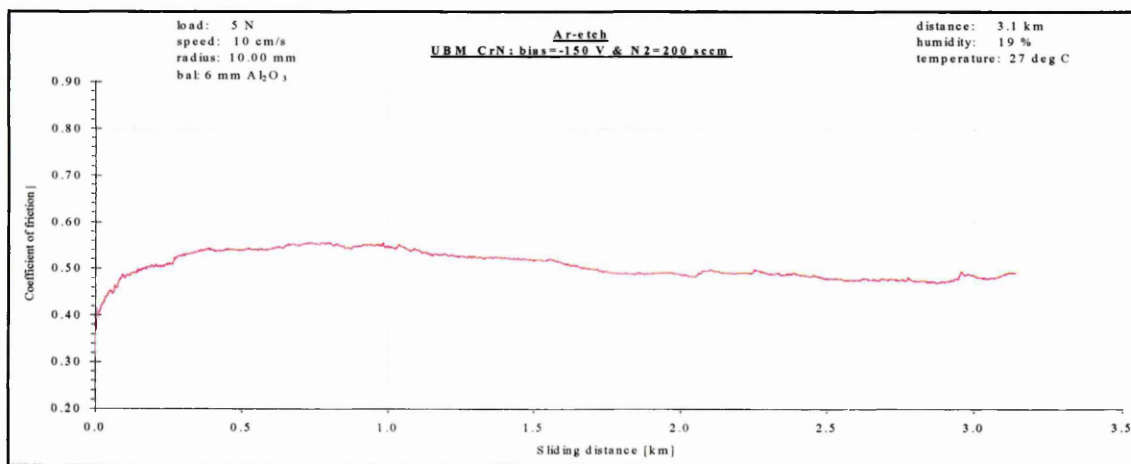


Figure 4.95. Pin-on-disc test of fcc-CrN_x; Ar etch and UBM at U_B=-150 V and f_{N2}=200 sccm.

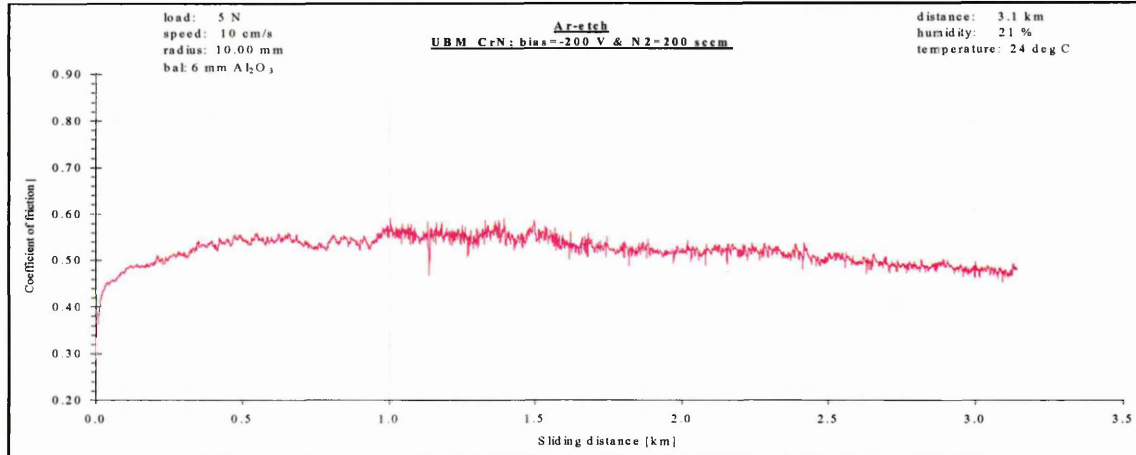


Figure 4.95. Pin-on-disc test of fcc-CrN_x; Ar etch and UBM at U_B=-200 V and f_{N2}=200 sccm.

Further increase of the nitrogen flow rate to 300 sccm and remaining a bias voltage level of -200 V, which result in {100} textured coatings, shows indications of a C.O.F. as low as 0.32, as shown in figures 4.96 to 4.98. The coatings with a metal ion etch as a pre-treatment and a 0.5 μm hcp-Cr₂N interlayer perform more stable than the coating with an argon ion pre-treatment. The irregular pattern for the argon-etched sample (figure 4.96) indicates adhesion failures of the coating to the substrate, as can be expected for these highly compressive stressed coatings (section 4.4). Probably larger particles break out of the coating, creating a three-body wear situation. It might be the case that loosened particles lift the ball and therefore reduce the C.O.F.

A Cr₂N inter-layer is probably not the best choice with respect to wear resistance. This coating as a single layer performs very bad in the pin-on-disc test, figure 4.99.

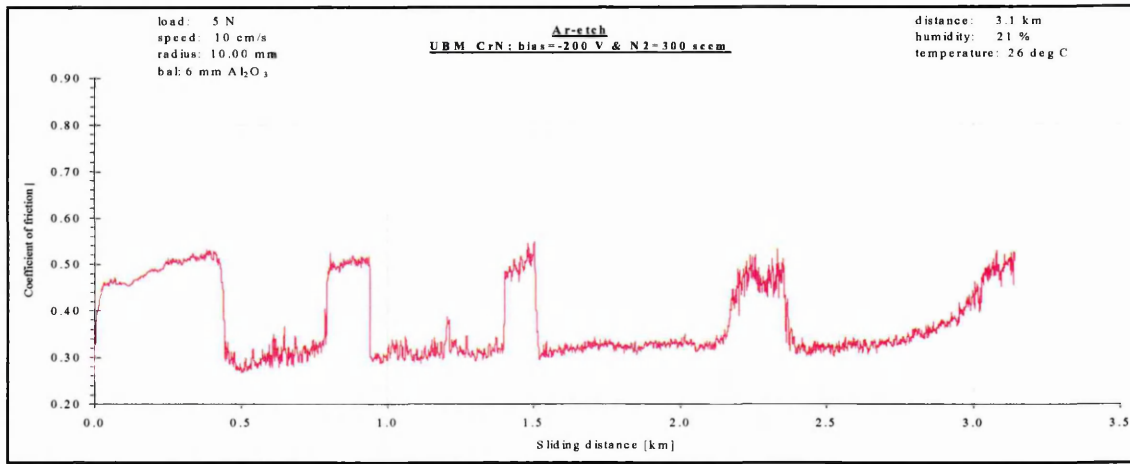


Figure 4.96. Pin-on-disc test of fcc-Cr_{Nx}; Ar etch and UBM at U_B=-200 V and f_{N2}=300 sccm.

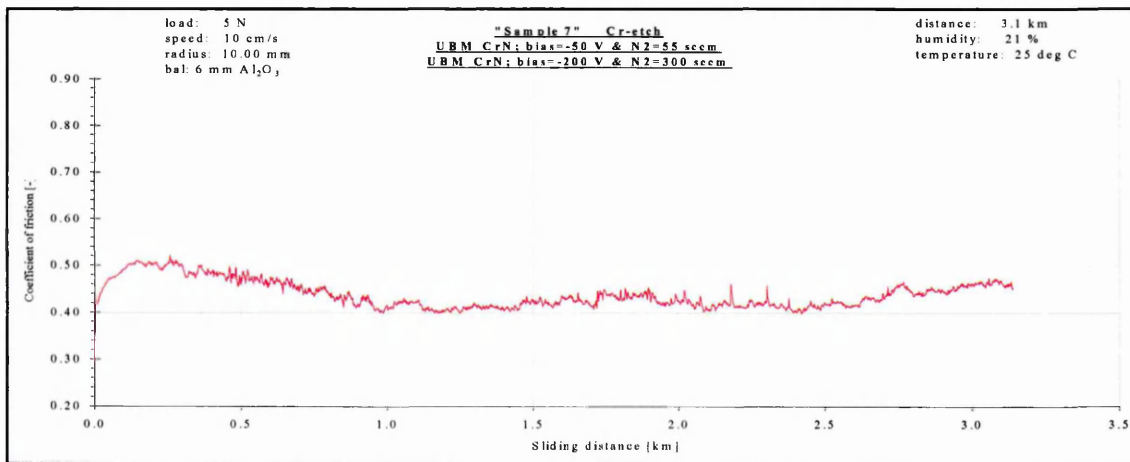


Figure 4.97. Pin-on-disc test of fcc-Cr_{Nx}; Cr etch and hcp-Cr₂N inter-layer at U_B=-50 V and f_{N2}=55 sccm and UBM at U_B=-200 V and f_{N2}=300 sccm.

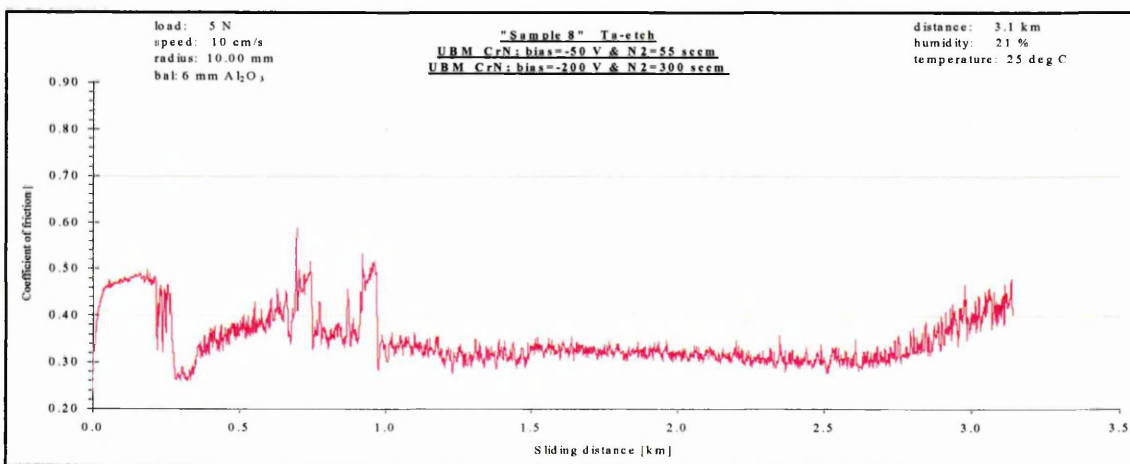


Figure 4.98. Pin-on-disc test of fcc-Cr_{Nx}; Ta etch and hcp-Cr₂N inter-layer at U_B=-50 V and f_{N2}=55 sccm and UBM at U_B=-200 V and f_{N2}=300 sccm.

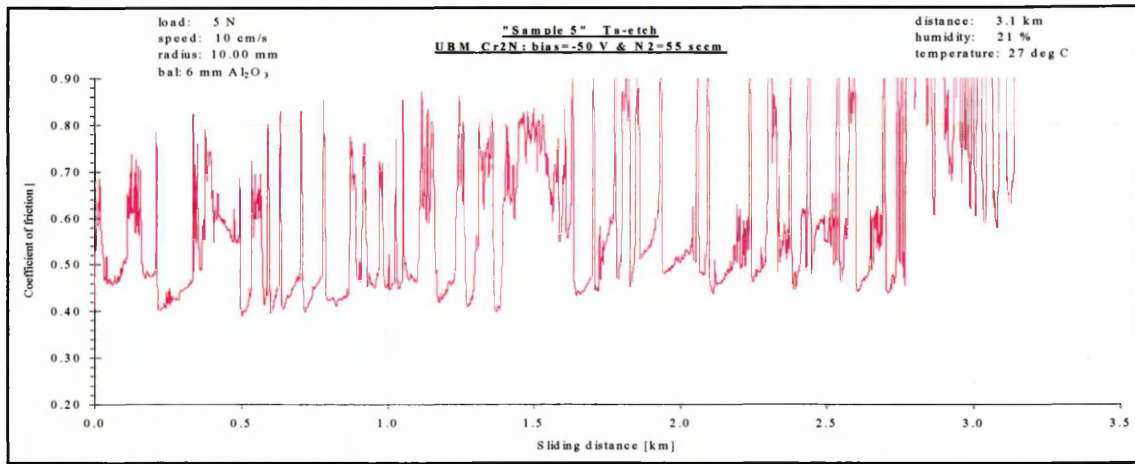


Figure 4.99. Pin-on-disc test of hcp-Cr₂N; Ar etch and UBM at $U_B=-50$ V and $f_{N_2}=55$ sccm.

Figure 4.100 shows the pin-on-disc results of a hard {100} textured fcc-CrN coating with a thin low stressed {110} oriented fcc-CrN inter-layer (adhesion promoter). The C.O.F. reaches a steady state value of ~ 0.44 . The running-in behaviour shows a gradually increase towards the steady state value, which is highly desirable in engineering applications. It seems that there is a better transfer of the high hardness properties by selecting a better matching lattice structure of the inter-layer, both fcc in this case.

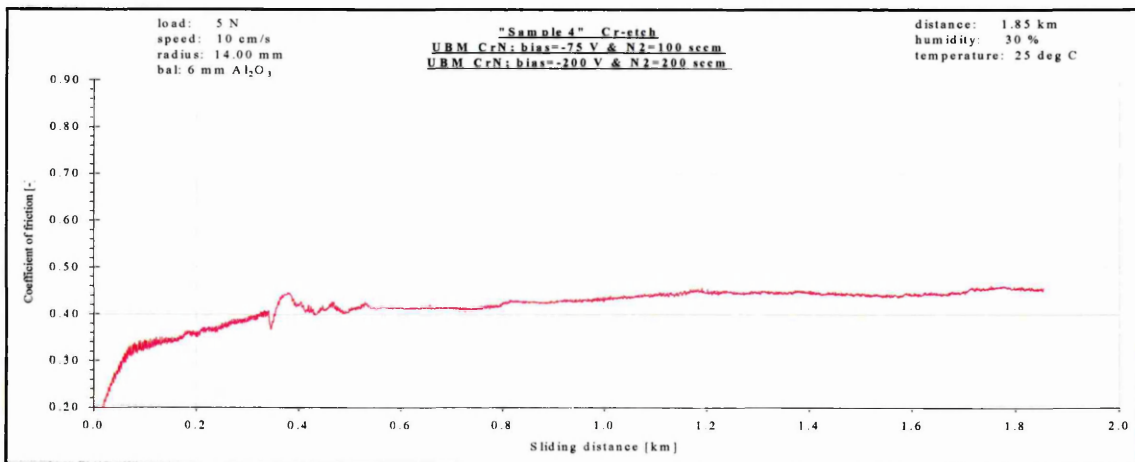


Figure 4.100. Pin-on-disc test of fcc-CrN_x; Cr etch and fcc-CrN inter-layer at $U_B=-75$ V and $f_{N_2}=100$ sccm and UBM at $U_B=-200$ V and $f_{N_2}=200$ sccm.

Because of the nice behaviour in the pin-on-disc test sample 4 has been evaluated on wear resistance. The wear resistance was measured after the pin-on-disc test

(sliding wear coefficient) and by the kalo-wear test (micro-abrasive wear factor K_c), table 4.30. Sample 9, which showed a high hardness value, was also tested. The test results are compared with coatings that are typically used in today's industry as protection against abrasive wear namely PVD TiN and electroplated hard chromium. Newly developed superlattice coatings are also included because they perform well under abrasive wear conditions [152].

Coating type	C.O.F.	Sliding wear coefficient [m ² /N]	Micro-abrasive wear K_c [m ² /N]
CrN/NbN superlattice -75 V [152]	0.70	2.1x10 ⁻¹⁵	6.1x10 ⁻¹³
CrN/NbN superlattice -120 V [152]	0.90	5x10 ⁻¹⁵	6.6x10 ⁻¹³
Sample 9	0.50	8.3x10 ⁻¹⁵	8.74x10 ⁻¹³
Sample 4	0.44	4.55x10 ⁻¹⁵	6.93x10 ⁻¹³
TiN [77]	0.85	7.7x10 ⁻¹⁵	8.4x10 ⁻¹³
Electroplated hard Cr [152]	0.72	5.8x10 ⁻¹⁴	8.8x10 ⁻¹³
CrN (Arc) [77]	0.50	8.9x10 ⁻¹⁵	7.7x10 ⁻¹³
TiAlN/VN superlattice [152]	0.45	1.26x10 ⁻¹⁷	2.2x10 ⁻¹³

Table 4.30. Wear resistance of industrial available coatings.

When comparing the coefficient of friction the hard CrN (sample 4) shows the lowest steady state value of 0.44 and is approximately the same as for TiAlN/VN, which is especially developed for low friction characteristics. TiN and electroplated hard chromium show much higher C.O.F. values of 0.85 and 0.72 respectively.

The lowest value for wear in the sliding test (dry testing conditions) is measured for TiAlN/VN and the highest for electroplated hard chromium. Sample 4 (hard CrN by PVD) performs at least as good as the high hardness CrN/NbN superlattice coating as deposited at -120 V bias. This is an astonishing result for a single layer configured coating and clearly better than that for TiN, which is known to be wear resistant.

The performance differences are less for the micro-abrasion test. TiAlN/VN outperforms all other coatings. In general the test results are directly correlated to the hardness of the coatings. The softer electroplated hard chromium, although clearly softer, performs as good as the typical PVD metal nitrides. This can be explained by the cracked structure of the electroplated chromium, which gives the coating the possibility to retain the test slurry and herewith extra lubrication and resistance against wear.

Chapter 5 – Discussion

The research project presented here outlines an extensive investigation into the influence of deposition parameters on the properties of reactively sputtered CrN_x coatings. The high flexibility of the unbalanced magnetron sputtering equipment used in this work allowed a comprehensive insight into the influence of nitrogen flow rate/partial pressure, bias voltage, current density, and the methods of substrate pre-treatment by inert Ar^+ etching or metal ion etching. Only the influence of deposition temperature has not been varied, although the necessary heater elements were incorporated in the deposition equipment. It is well known that thick CrN coatings can be deposited already at temperatures of 200°C [76] with excellent adhesion. CrN is therefore an ideal candidate for large scale coating of parts and components, which are manufactured from case hardened steels or electroplated brass. To meet these special requirements the deposition temperature has been restricted to 250°C in these experiments.

Three phase fields have been found to be characteristic of the sputtering process of Cr in a argon/nitrogen gas atmosphere. Figure 5.1 describes the stability ranges of Cr, Cr_2N and CrN as a function of nitrogen flow rate and substrate bias voltage. The most important result is the lack of influence of the substrate bias voltage up to $U_B = -200\text{ V}$. Only at bias voltages beyond this critical value, may the preferential re-sputtering of the light N atoms be expected. Therefore the stability range of Cr and Cr-N (solid solution of N in Cr lattice) is represented by a well-defined narrow band up to nitrogen flow rates of 25 sccm. Above this value and below $f_{\text{N}_2} < 75\text{ sccm}$ Cr + Cr_2N , Cr_2N and $\text{Cr}_2\text{N} + \text{CrN}$ phases exist. However, at $U_B = -300\text{ V}$ the upper critical value is increased quite markedly to $f_{\text{N}_2} = 100\text{ sccm}$.

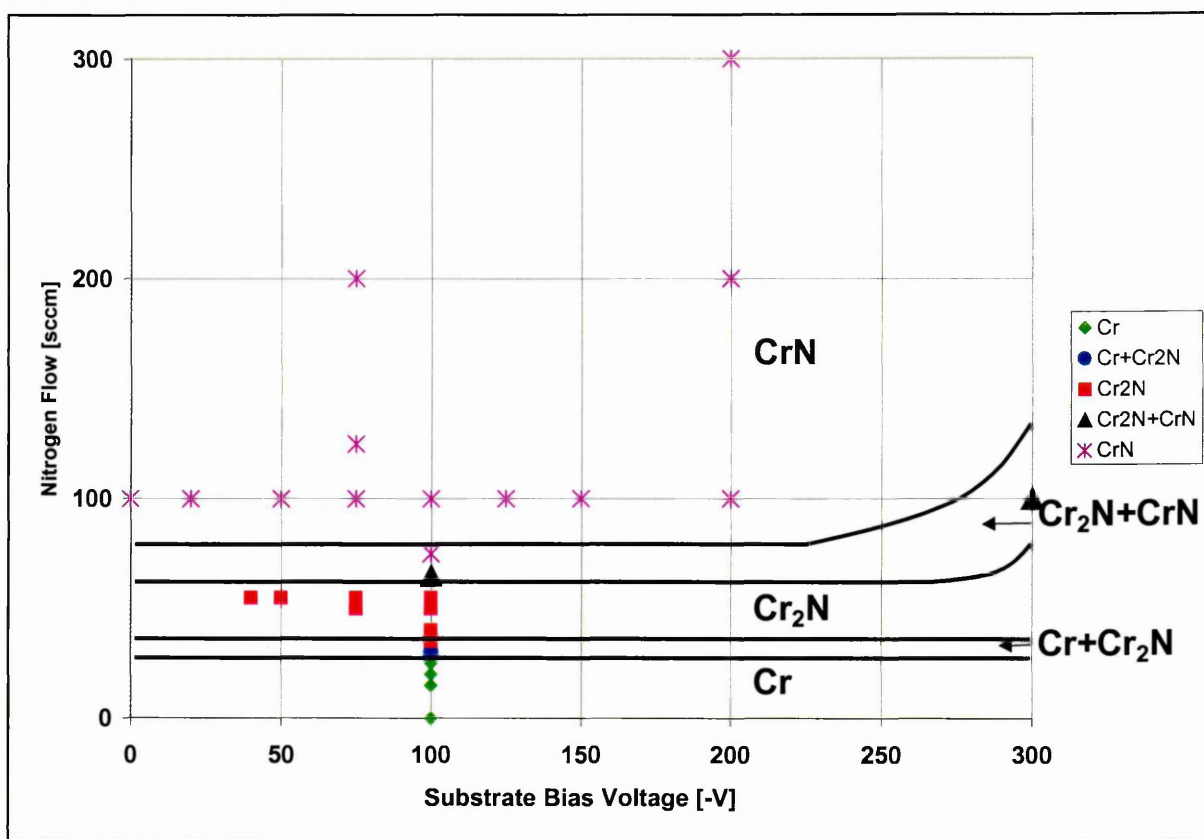


Figure 5.1. CrN_x phases dependent on substrate bias voltage and nitrogen flow.

5.1. (expanded) bcc-Cr

In the stability range of the Cr-N solid solution small amounts of incorporated nitrogen into the Cr lattice gives rise to a tremendous increase in the hardness of the material from 7.8 to 18.0 GPa. This maximum hardness is in the range of the typical hardness value as published for fcc-CrN [144]. At a bias voltage of -100 V a maximum of 18 at.% of interstitial nitrogen was measured. The solid solution hardening can be predicted from the measured increased interplanar spacing and increased peak broadening with increased amounts of nitrogen. Also the shape of the X-ray diffraction pattern, rather flat and wide peaks, indicate a fine crystalline structure. The cross-sectional SEM shows an extremely featureless and very smooth fracture surface.

The solid solution hardened material has a great potential in tribological applications. The smoothness and relative high hardness will contribute to reasonable abrasive wear resistance. The bcc structure makes an excellent match to bcc steel substrates, table 5.1. This contributes to extraordinary adhesion conditions for the coating.

JCPDS-data	Interplanar Spacing [Å]		
	{110}	{200}	{211}
Iron	2.027	1.433	1.170
Chromium	2.040 (+ 0.64%)	1.442 (+ 0.63%)	1.177 (+ 0.60%)

Table 5.1. JCPDS data on interplanar spacing of iron and chromium

With nitrogen incorporation the interplanar spacing is increased for chromium. The same is true for most iron substrates, because of nitriding steps prior to PVD deposition.

The relative high hardness, high density, and smoothness make the coating an excellent candidate for (injection) moulding applications. Particularly as replacement for the cathodic arc evaporated CrN coatings where expensive post-polishing treatments are needed. With a smooth sputtered film it is very well possible to eliminate this post-treatment step.

The low E-modulus makes the bcc-Cr-N coatings also a favourable candidate in applications where fatigue resistance is required, like roller bearings.

In the case of applications without any lubrication the carbon based coatings are typically used [153,154], because of the very low coefficient of friction (<0.2). Until now in most cases Cr is used as the adherent layer between the (hardened) steel substrates and the carbon based coating. With the current know-how on the expanded chromium coatings it makes this coating very suitable to replace the metallic nitrogen free chromium coatings. The advantages are given in the smoothness, excellent matching possibilities of the hardness of this interlayer with the hardness of hardened steel, higher shear strength, higher wear resistance, and in potential higher corrosion resistance.

5.2. hcp-Cr₂N

It is a particularly astonishing finding of this work that the Cr₂N phase could deposit as completely pure Cr₂N without any Cr or CrN components. This result originates

from the high pumping speed of the unthrottled turbomolecular pumps with 2200 l/s used in this rather small chamber (approximately 275 l). Any uncontrolled increase in the partial pressure of Δp_{N_2} due to target poisoning will be minimised. The sharp peaks in the XRD pattern for the hexagonal lattice (Figure 4.8) and the corresponding low values of peak broadening and interplanar spacings almost identical with those of JCPDS data further confirm this result. It has also been found that the hexagonal Cr_2N possess the lowest hardness value of 16 GPa compared with mixed phases of either $Cr+Cr_2N$ or $Cr_2N + CrN$. This result seems to contradict many publications [86,88,89,91,93,94,96] on coatings which were deposited under similar advantageous vacuum conditions. However, the result is similar to the lower hardness values reported for Ti_2N (HK2100) compared to TiN (HK2300) [157]. The sub-stoichiometric hcp- Cr_2N (~ 24 at.% N) revealed clearly higher hardness values in the range of 22 GPa.

5.3. fcc-CrN

Under the experimental conditions employed the fcc-CrN phase dominates the phase field beyond $f_{N_2} > 75$ sccm as outlined in figure 5.1. Four texture regimes have been found to exist depending on the nitrogen flow rate and substrate bias voltage, figure 5.2. The most familiar modification of {110} texture CrN coatings is found over the complete bias voltage range from -50 V to -200 V at a nitrogen flow rate of 100 sccm. Extremely surprising is the very wide extended window representing the stability of the {111} texture. This band extends between very low bias voltages, where dendritic columnar growth of the coating has been observed to completely dense coating modifications deposited at bias voltages up to $U_B = -150$ V. Even more surprising was the re-appearance of the {110} texture at high nitrogen flow rates (200 sccm) and moderate bias voltages (-50 V to -75 V). At extremely high bias voltages ($U_B = -200$ to -300 V) and high nitrogen flow rates ($f_{N_2} = 200$ to 500 sccm) a very hard {100} textured CrN modification (hardness HV 2700 to 3000) was found. This highly compressive stressed modification should be investigated with respect to technical applications. It represents so far the only known CrN coating with hardness values similar to TiN. In comparison to TiN and electroplated hard chromium this hard sputtered CrN outperforms them both in corrosion and tribological

testing. In sliding wear and abrasive wear tests the hard CrN shows results similar to CrN/NbN and TiAlN/VN superlattice coatings (section 4.5.4).

The performance in corrosion testing seems to be strongly dependent on the level of ion energy of impinging ions during film growth. CrN_x films deposited at a substrate bias voltage more negative than -100 V showed lower anodic corrosion current densities than coatings grown between floating potential and -75 V (figure 4.85). This phenomena can be explained by a distinct reduction of the micro-voids as can be observed in the TEM micrographs (figures 4.27, 4.28, and 4.45). Corrosive liquids can reach the substrate through such voids. In parallel it was observed that at approximately -75 V the intrinsic growing stress state changes from low residual tensile to compressive (figure 4.48). The compressive forces act to close the intergranular voids. In the same manner in the pin-on-disc test the coefficient of friction (COF) decreased with increased densification of the CrN_x coatings. The COF decreases from 0.95 to 0.44 as the substrate bias voltage is increased from floating potential to -200 V (COF of electroplated hard chromium is measured at 0.72). In addition to the benefits of a lower COF, the densification helps to reduce the sliding wear (up to 10 times lower than the wear value of electroplated hard chromium). In this test the densification results in a higher hardness, which produces a coating with higher wear resistance.

The nature of the stability ranges as shown in figure 5.2 cannot be explained at this time. Nothing comparative is known for the more stable TiN and ZrN coatings. It is however, very important to note that in the case of CrN stoichiometry is never achieved. In no single case was deterioration observed as a consequence of the high reactive gas flow rates used as can be observed for TiN when the golden colour turns brownish with the development of an open under dense film structure.

Extensive SNMS analyses have clearly demonstrated that stoichiometry is not reached even at N₂ flow rates up to 300 sccm. This work is in contradiction to the work of He [107]. According to He [107], a paper that was found relatively late in the research program, it is possible to achieve slightly over-stoichiometric and similar hard fcc-CrN in the case of a deposition at room temperature. This is achieved by water-cooled substrates.

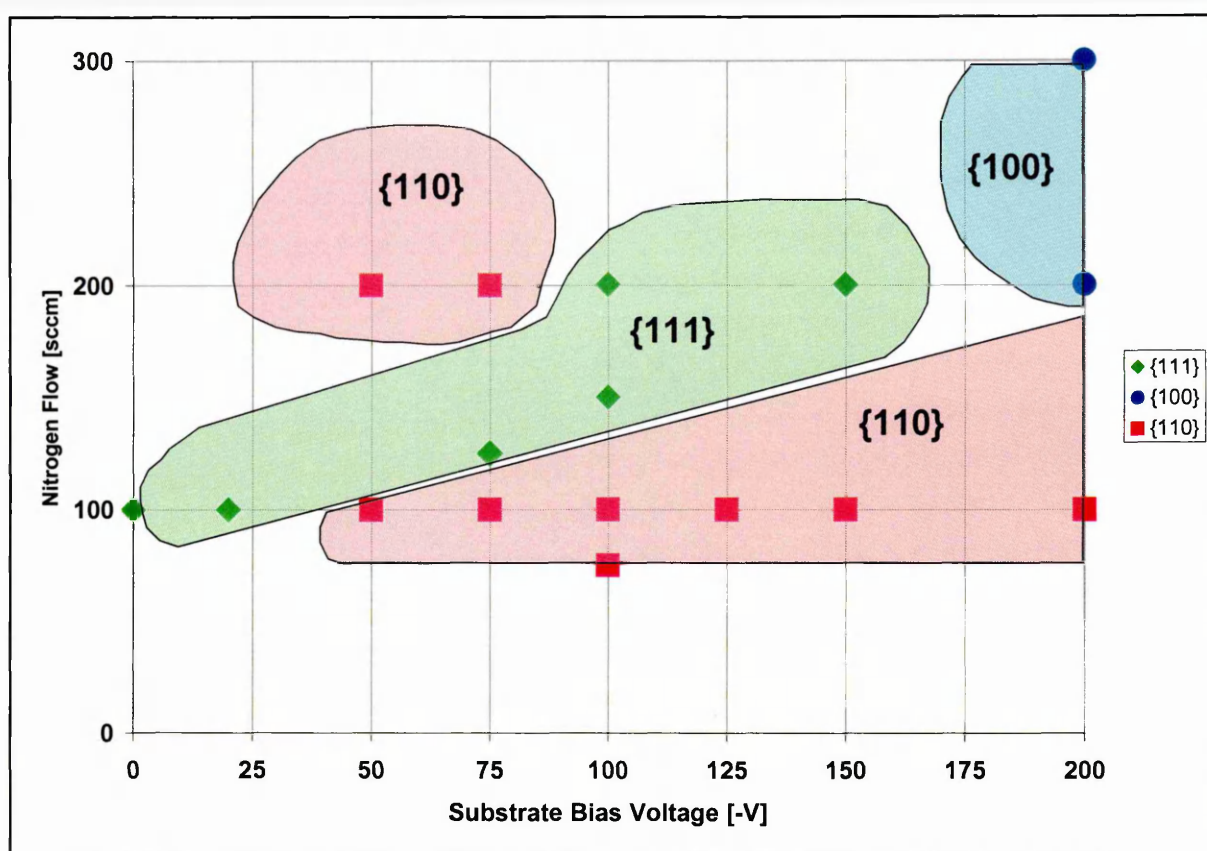


Figure 5.2. Preferred crystallographic orientation of fcc-CrN, dependent on substrate bias voltage and nitrogen flow rate.

It is interesting to note that high bias voltages cannot compensate for the lack of stoichiometry. Increasing the bias voltage does not lead to an increased incorporation of N^+ due to low energy implantation. In contrast a reduction of N incorporation is found with increasing bias voltage as can be seen in figure 4.46 indicating preferential re-sputtering of the lighter N atoms. No substantial influence of the number of bombarding ions has been found with respect to the composition of the deposited CrN_x coating (section 4.3.5). The same result is mirrored by the influence of the bias current density on the deposition rate of CrN_x . If the ion energy is low enough, the deposition rate is independent of the number of bombarding ions at the substrate (figure 4.51).

Whereas no substantial influence of ion bombardment on the composition of the deposited film was found. The well-known influence of ion energy on the microstructure, lattice parameter, peak broadening, residual stress, hardness and coating density (voids found by TEM) was found. Increasing the energy and number

of impinging ions also positively influenced surface roughness and corrosion resistance. All the results show that the coating properties seem to improve with increasing presence of reactive gas during the deposition process. This goes along with the fact that the target poisoning process is far less developed as in the case of TiN, ZrN and HfN. The lower stability of the CrN lattice seems to become relevant on both sites of ion bombardment, namely on the target as well as the substrate. This amazing result makes the CrN process much more robust in comparison with other commonly used reactive sputtering processes for hard nitride coatings.

Finally, within this work it is confirmed again that the coating to substrate adhesion is enhanced by a pre-treatment with metallic ions, compared to argon ions [151]. The metallic ions, Cr and Ta, were generated by the cathodic arc technique. The cathodic arc has not been optimised in this work and there are possibilities to use stronger arc steering in order to reduce the number and size of the droplets. The strength of the magnetic field (parallel component) was approximately 20 Gauss and should be increased to at least 50 Gauss. This will reduce the negative effect on the surface roughness, since the number of nucleation sites for growth defects are reduced for the sputtered coating. Especially in tribological and corrosive environments this is required.

Chapter 6 – Conclusions

Within this work there has been an extensive variation of major PVD coating parameters for unbalanced magnetron sputtered CrN_x coatings. All coatings have been reactively deposited at a substrate temperature of 250 °C in an argon/nitrogen atmosphere from a metallic Cr target.

Bcc-Cr:

- High nitrogen content metallic bcc-Cr with nitrogen in solid solution (up to 18 at. %) revealed a fine-grained microstructure, reasonable high hardness (HV18.0 GPa), low Young's modulus and smooth surface finish. This material is interesting to be applied on engineered components, either as a monolithically deposited coating or as an interface layer between (hardened) steel and carbon based tribological coatings. Especially applications that need to combine fatigue and wear resistance can benefit from this metallic coating.

Hcp-Cr₂N:

- The hcp-Cr₂N films were shown to be relatively hard (22 GPa) in their sub-stoichiometric range (~24 at.% N). The stoichiometric hcp-Cr₂N phase revealed low hardness values of 16 GPa with a tensile residual stress state. It was possible to deposit within a narrow composition window because of the high pumping speed in relation to the equipment size.

Fcc-CrN:

- Under the typical deposition conditions as known for other metal nitrides (bias voltage between -50 and -150 V and a nitrogen flow rate of 50 to 100 sccm) the {110} orientation was dominant, unlike TiN which develops a {111} orientation under similar deposition conditions. Dense {111} oriented fcc-CrN_x films grow when the bias voltage is between -75 and -150 V in parallel with a nitrogen flow rate between 100 and 200 sccm.
- A special hard fcc-CrN phase was found, which could only be observed under very specific and not common range of coating parameters. For metal nitrides the

deposition parameter window is at high partial pressures of nitrogen ($f_{N_2} > f_{Ar}$) in combination with a relatively high substrate bias voltage (> -200 V). These hard coatings show a strong {100} preferred crystallographic orientation and are very comparable to other hard coatings like TiN and TiAlN. For this material a patent application has been filed.

- At a deposition temperature of 250 °C stoichiometric fcc-CrN was never achieved, not even within the wide experimental window. The stoichiometry of the fcc-CrN coatings was strongly affected by the nitrogen flow rate and the substrate bias voltage. However, the effect of the ion current density on the stoichiometry was less pronounced.

Corrosion resistance:

- At a bias voltage more negative than -75 V the corrosion resistance of 3 μm CrN_x in the polarisation test was superior to that of 18 μm industrial electroplated hard chromium. This can be explained by the densification of the coatings with increased ion bombardment (confirmed by the reduction of inter-columnar voids in the cross-section TEM micrographs). In parallel the fcc-CrN coatings showed a transition from a low tensile growing stress ($+0.15$ GPa/ μm) to a compressive growing stress state (up to -0.9 GPa/ μm).

Tribological:

- An increase of the bias voltage from floating potential to -200 V on fcc-CrN showed a significant decrease in the coefficient of friction (COF) from 0.95 to 0.44 in the pin-on-disc test. The lower end values of the COF were substantial lower than that of electroplated hard chromium with a COF of typically 0.72.
- The dry sliding wear coefficient of the {100} textured fcc-CrN was approximately 10 times lower than that of electroplated hard chromium.

References

- [1] B. Bhushan, B. Gupta
Handbook of tribology materials, coatings and surface treatments
1991, McGraw-Hill, Inc.
ISBN 0-07-005249-2
- [2] W-D Münz, D. Schulze, F. Hauzer
Surf. & Coat. Technol., 50, 1992, 169
- [3] H. Holleck
Surf. & Coat. Technol., 36, 1988, 151-159
- [4] H. Holleck, H. Schulz
Surf. & Coat. Technol., 36, 1988, 707-714
- [5] H. Holleck, M. Lahres, P. Woll
Surf. & Coat. Technol., 41, 1990, 179-190
- [6] H. Holleck
Surf. Eng., 7 (2), 1991, 137-144
- [7] R. Fella, H. Holleck
Mat. Sci. Eng., A140, 1991, 676-681
- [8] V. Schier
Dissertation, Forschungszentrum Karlsruhe GmbH, 1995, Karlsruhe, Germany
- [9] U. Helmersson, S. Todorova, S. Barnett, J.E. Sundgren, L.C. Markent,
J.E. Greene
J. Applied Physics, 62, 1987, 481
- [10] N. Hirashita, J.E. Greene, U. Helmersson, J. Birch, J.E. Sundgren
J. Applied Physics, 70, 1991, 4963
- [11] J.E. Sundgren
Vacuum, 43 (1/2), 1992, 49
- [12] X. Chu, M. Wong, W. Sproul, S. Rohde, S. Barnett
J. Vac. Science Technol., A10, 1992, 1604
- [13] T. Hurkmans, T. Trinh, D.B. Lewis, J. Brooks, W-D Münz
Surf. & Coat Technol., 76-77, 1995, 159-166
- [14] L. Donohue, W-D Münz, D.B. Lewis, J. Cawley, T. Hurkmans, T. Trinh,
I. Petrov, J.E. Greene
Surf. & Coat. Technol., 93, 1997, 69-87
- [15] D. McIntyre, J. Greene, G. Håkansson, J.-E. Sundgren, W.-D. Münz
J. Appl. Phys., 67, 1990, 1542
- [16] O. Knotek, F. Löffler, G. Krämer
Surf. & Coat. Technol., 59, 1993, 14-20
- [17] W-D Münz
J. Vac. Sci. Technol., A4(6), 1986
- [18] S. Kadlec, J. Musil, J. Vyskocil
Surf & Coat Technol., 54/55, 1992, 287-296
- [19] H.J. Scheibe, P. Siemroth
IEEE Trans. Plasma Science, 18, 1990, 917
- [20] H.J. Scheibe, P. Siemroth, W. Pompe, B. Schoeneich
Surf. Coat. Technol., 47, 1991, 455
- [21] W-D Münz, D. Schulze, B. Buil
Surf. Coat. Technol., 49, 1991, 161

- [22] I. Smith, D. Gillibrand, J. Brooks, W-D Münz, S. Harvey, R. Goodwin
Surf. & Coat. Technol., 90, 1997, 164-171
- [23] R.L. Boxman, P. Martin, D.M. Sanders
Handbook of vacuum Arc Science and Technology, Noyes Publications
- [24] S. Ramalingam
International patent WO 85/03954, 1985
- [25] J. Vossen, W. Kern
Thin Film Processes
Academic Press, New York, NY, 1978, isbn 0-12-728250-5
- [26] K.L. Chopra
Thin film phenomena, 1969, McGraw-Hill Inc.
- [27] R.F. Bunshah et al.
Deposition Technologies for films and coatings, 1982, Noyes publications
- [28] B. Window, N. Savvides
J. Vac. Sci. Technol. A, Vol. 4, No. 2, 1986, 196-202
- [29] J. Musil, S. Kadlec, V. Valvoda, R. Kuzel, R. Cerny
Surf. & Coat. Technol., 43/44, 1990, 259-269
- [30] W-D Münz
Surf. & Coat. Technol., 48, 1991, 81-94
- [31] B.A. Movchan, A.V. Demchishin
Phys. Met. Metallogr., Vol. 28, 1969, 83
- [32] J. A. Thornton
Ann. Rev. Mater. Science, Vol. 7, 1977, 239-260
- [33] R. Messier, A.P. Giri, R.A. Roy,
J. Vac. Sci. Technol. A, Vol. 2, 1984, 500
- [34] J.E. Sundgren
Thin solid Films, 128, 1985, 21-44
- [35] H. Holleck
Surf. & Coat. Technol. 43/44, 1990, 245-258
- [36] O. Knotek, A. Schrey
Handbook of thin film process Technology Inst. of physics publishing Bristol
and Philadelphia
Part X1: "hard and Protective materials"
- [37] H. Holleck
Binäre and ternäre karbid-und nitridsysteme der Übergangsmetalle
1984, Stuttgart, Gebr. Bornträger
- [38] L. Wolf, G. Bastin, H. Heiligers
11th Plansee Seminar, Vol. 1, 1985, 465
- [39] D.R. Lide
Handbook of chemistry and physics
73rd edition, 1992-1993
- [40] M. Atzor
Dissertation, Aachen, 1989
- [41] JCPDS-ICDD Diffraction Data Database
International centre for Diffraction Data, 1993
- [42] A. Aubert, R. Gillet, A. Gaucher, J.P. Terrat
Thin Solid Films, 108, 1983, 165-172
- [43] Prospect "Funktionellere Oberflächen durch Hartchrom"
Galvano Technik, AGG, Düsseldorf, 1994

- [44] Prospect Arthur Henninger GmbH, Karlsruhe, Germany
- [45] A. Jehn, M. Baumgärtner
Surf. & Coat. Technol., 54/55, 1992, 108-114
- [46] P. Gelling
Introduction to corrosion prevention and control
Delft University press, 1985
- [47] P. Seserko, U. Kopacz, S. Schulz
Galvanotechnik, Nr. 12, 1989, 4274-4277
- [48] A. Kawana, H. Ichimura, Y. Iwata, S. Ono
Surf. & Coat. Technol., 86/87, 1996, 212-217
- [49] C. Friedrich, G. Berg, E. Broszeit, F. Rick, J. Holland
Surf. & Coat. Technol., 97, 1997, 661-668
- [50] B. Navinšek, P. Panjau, J. Krušič
Surf & Coat. Technol., 98, 1998, 809-815
- [51] B. Navinšek, P. Panjau, I. Milosev
Surf & Coat. Technol., 97, 1997, 182-191
- [52] O. Knotek, F. Löffler
Metall, 45 Jahrgang, Heft 3, 1991, 236-240
- [53] N. Matentzoglou, W. Dürholt
Metall, 45 Jahrgang, Heft 3, 1991, 241
- [54] H. Schulz
Maschinenmarkt, 25, 1992, 20-23
- [55] N. Sbrockey, S. Day, M. Walsh
Presented at ICMCTF 1995, San Diego, USA
- [56] B. McGarvey, J. Curran, R. Ford, I Gale, J. Hewett, M. Teobald
Accepted for publishing in Journal of Applied Physics, 1997.
- [57] Y. Su, J. Lin
Wear, 170, 1993, 45-53
- [58] P. Vencovsky, R. Sanchez, J. Branco, M. Galvano
Surf. & Coat. Technol., 108-109, 1998, 599-603
- [59] Y. Wang
Surf. & Coat. Technol., 94-95, 1997, 60-63
- [60] K. Kashiwagi, K. Kobayashi, A. Masuyama, Y. Murayama
J. Vac. Sci. Technol. A, 4(2), 1986, 210-214
- [61] H. Schulz, E. Bergmann
Surf. & Coat. Technol., 50, 1991, 53-56
- [62] A. Leyland, M. Bin-Sudin, A. James, M. Kalantary, P. Wells, A. Matthews,
J. Housden, B. Garside
Surf. & Coat. Technol., 60, 1993, 474-479
- [63] M. Bin-Sudin, A. Leyland, A. James, A. Matthews, J. Housden, B. Garside
Surf. & Coat. Technol., 81, 1996, 215-224
- [64] F. Schuster, F. Maury, J. Nowak, C. Bernard
Surf. & Coat. Technol., 46, 1991, 275-288
- [65] F. Lai, J. Wu
Surf. & Coat. Technol., 88, 1996, 183-189
- [66] S. Lee, W. Ho, W. Pao
Surf. Coat. Technol., 73, 1995, 34-38
- [67] J. Vetter, E. Lugscheider, S. Guerreiro
Surf & Coat Technol., 98, 1998, 1233-1239

- [68] F. Sanchette, T. Huu Loi, A. Billard, C. Frantz
Paper presented PSE, 1994, Garmisch-Partenkirchen, Germany
- [69] G. Ebersbach, D. Fabian, W. Wuttke, H. Jehn
Surf. & Coat. Technol., 59, 1993, 160-165
- [70] H. Jehn, F. Thiergarten, E. Ebersbach, D. Fabian
Surf. & Coat. Technol., 50, 1991, 45-52
- [71] P. Hones, R. Sanjines, F. Levy
Thin Solid Films, 332, 1998, 240-246
- [72] E. Lugscheider, O. Knotek, C. Barimani, S. Guerreiro, H. Zimmermann
Surf. & Coat. Technol., 94/95, 1997, 416-421
- [73] A. Aubert, J. Danroc, A. Gaucher, J. Terrat
Thin Solid Films, 126, 1985, 61-67
- [74] R. Saha, R. Inturi, J. Barnard
Surf. & Coat. Technol. 82, 1996, 42-47
- [75] C. Gautier, J. Machet
Surf. & Coat. Technol., 94/95, 1997, 422-427
- [76] B. Navinšek, P. Panjan
Surf. & Coat. Technol., 59, 1993, 244-248
- [77] Brite-Euram Project no. BE 96-3305
"NEWCHROME"
- [78] I. Wadsworth, I. Smith, L. Donohue, W-D Münz
Surf. & Coat. Technol. 94-95, 1997, 315-321
- [79] M. Lembke, D.B. Lewis, W-D Münz
Paper presented at ICMCTF2000, San Diego, USA
- [80] D.B. Lewis, I. Wadsworth, W.-D. Münz, R. Kuzel Jr., V. Valvoda
Surf. & Coat. Technol., 116/119, 1999, 284-291
- [81] Kuruppu, G. Negrea, I. Ivanov, S. Rohde
J. Vac. Sci. Technol. A, 16 (3), 1998, 1949-1955
- [82] J. Terrat, A. Gaucher, H. Hadj-Rabah, R. Fillit
Surf. & Coat Technol., 45, 1991, 59-65
- [83] Y. Chang, R. Warsop, N. Farb, R. Parsons
Surf. & Coat Technol., 68/69, 1994, 157-165
- [84] S. Bull, D. Rickerby
Surface & Coat. Technol., 43/44, 1990, 732-744
- [85] M. Pakala, R. Lin
Surf. & Coat. Technol. 81, 1996, 233-239
- [86] G. Bertrand, C. Savall, C. Meunier
Surf. & Coat. Technol., 96, 1997, 323-329
- [87] C. Friedrich, G. Berg, E. Broszeit, K. Kloos
Surf. & Coat. Technol., 74/75, 1995, 279
- [88] W. Herr, B. Matthes, E. Broszeit, M. Meyer, R. Suchentrunk
Surf. & Coat. Technol. 60, 1993, 428-433
- [89] K. Legg, M. Graham, P. Chang, F. Rastagar, A. Gonzales, B. Sartwell
Surf. & Coat. Technol., 81, 1996, 99-105
- [90] P. Ballhause, B. Hensel, A. Rost, H. Schüssler
Materials Science and Engineering, A163, 1993, 193-196
- [91] G. Berg, C. Friedrich, E. Broszeit, C. Berger
Surf. & Coat. Technol., 86/87, 184-191
- [92] L. Cunha, M. Andritschky, L. Rebouta, R. Silva
Thin Solid Films, 317, 1998, 351-355

- [93] W. Herr, E. Broszeit
Surf. & Coat. Technol., 97, 1997, 669-674
- [94] P. Hones, R. Sanjines, F. Levy
Surf. & Coat. Technol., 94/95, 1997, 398-402
- [95] T. Kacsich, M. Niederdrenk, P. Schaaf, K. Lieb, U. Geyer, O. Schulte
Surf. & Coat. Technol., 93, 1997, 32-36
- [96] R. Sanjines, P. Hones, F. Levy
Thin Solid Films, 332, 1998, 225-229
- [97] C. Gautier, H. Moussaoui, F. Elstner, J. Machet
Surf. & Coat. Technol., 86-87, 1996, 254-262
- [98] P. Fabis
Surf. & Coat. Technol., 52, 1992, 243-250
- [99] H. Jensen, U. Jensen, G. Pedersen, G. Sorensen
Surf. & Coat. Technol., 59, 1993, 135-139
- [100] D. Monaghan, D. Teer, K. Laing, I. Efeoglu, R. Arnell
Surf. & Coat. Technol., 59, 1993, 21-25
- [101] W.-D. Münz, J. Göbel
Surface Engineering, vol. 3, No. 1, 1987, 47-51
- [102] B. Navinsek, P. Panjau, A. Cvelbar
Surf. & Coat. Technol., 74/75, 1995, 155-161
- [103] G. Berg, C. Friedrich, E. Broszeit, C. Berger
Surf. & Coat. Technol., 97, 1997, 326-334
- [104] L. Cunha, M. Andritschky
Surf. & Coat. Technol., 111, 1999, 158-162
- [105] P. Fabis, R. Cooke, S. McDonough
J. Vac. Sci. Technol. A, 8(5), 1990, 3819-3826
- [106] W.-D. Münz, L. Donohue, P. Hovsepian
MRS conference, 1-4 June, 1999, Strasbourg, France
- [107] X. He, N. Baker, B. Kehler, K. Walter, M. Nastasi, Y. Nakamura
J. Vac. Sci. Technol. A, 18(1), 2000, 30-36
- [108] O. Piot, C. Gaiter, J. Machet
Surf. & Coat. Technol., 94/95, 1997, 409-415
- [109] O. Knotek, F. Löffler, H. Scholl
Surf. & Coat. Technol., 45, 1991, 53-58
- [110] Y. Chiba, T. Omura, H. Ichimura
J. Mater. Res., Vol. 8, no. 5, 1993, 1109-1115
- [111] W. Grant, C. Loomis, J. Moore, D. Olson, B. Mishra, A. Perry
Surf. & Coat. Technol., 86/87, 1996, 788-796
- [112] A. Ehrlich, M. Kühn, F. Richter, W. Hoyer
Surf. & Coat. Technol., 76/77, 1995, 280-286
- [113] R. Aharonov, B. Coll, R. Fontana
Surf. & Coat. Technol., 61, 1993, 223-226
- [114] J. Sue, T. Chang
Paper presented at ICMCTF1995, San Diego, Ca, USA
- [115] J. Sue, A. Perry, J. Vetter
Surf. & Coat. Technol., 68/69, 1994, 126-130
- [116] R. Gahlin, M. Bromark, P. Hedenqvist, S. Hogmark, G. Hakansson
Surf. & Coat. Technol., 76-77, 1995, 174-180
- [117] J. Lin, M. Liu, J. Wu
Wear, 194, 1996, 1-11

- [118] W-D Münz, K. Vannisselroy, R. Tietema, T. Hurkmans, G. Keiren
Surf. Coat. Technol., 58, 1993, 205
- [119] G. Håkansson
Dissertation, Linköping, 1991
- [120] ASM handbook
vol. 5, Surface Engineering
3rd print, 1999
- [121] B.D. Cullity
Elements of x-ray diffraction
Addison - Wesley Publishing Company, 1978
- [122] R. Kuzel, Jr., R. Cerny, V. Valvoda, M. Blomberg, M. Merisalo
Thin Solid Films, 247, 1994, 64
- [123] C. Wagner, I. Cohen, J. Hilliard
Local Atomic Arrangements Studied by X-ray Diffraction
Gordon and Breach, New York, 1966
- [124] G. B. Harris
Phil. Mag., 43, 1952, 113
- [125] D. S. Rickerby, A. M. Jones, B. A. Bellamy
Surface and Coatings Technology, 37, 1989, 111
- [126] V. Valvoda, A. Perry, L. Hultman, J. Musil, S. Kadlec
Surface and Coatings Technology, 49, 1991, 181
- [127] A. J. Perry
Thin Solid Films, 193-194, 1990, 463
- [128] D. E. Geist, A. J. Perry, J. R. Treglio, V. Valvoda, D. Rafaja
Adv. X-ray Analysis, 38, 1995, 471
- [129] P.F. Schmidt
Praxis der Rasterelektronen Mikroskopie und Mikrobereichsanalyse.
Expert Verlag, 1994, pag. 371 - 377
- [130] C. Barret, T. Massalski
Structure of Metals
Pergamon Press, 1980
- [131] S.J. Bull
Surf. & Coat. Technol., 50, 1991, 25-32
- [132] H. Jehn, G. Reiners, N. Siegel
DIN-Fachbericht 39, 1993, Beuth Verlag GmbH, Berlin
- [133] W.-D. Münz, T. Hurkmans, G. Keiren, T. Trinh
Journal of Vac. Sci & Techn. A, Vol.11, no. 5, Sept/Oct 1993, 2583-2589
- [134] Reference normen voor de werktuigbouwkunde
NEN-bundel 1
NNI, 1983
- [135] D. Jones
Principles and prevention of corrosion, 1992. Mcmillam Publishing company,
ISBN 0-02-946439-0
- [136] Manual Minolta Spectrophometer CM-2002
- [137] ASTM E 308, 1985,
Standard method for computing the colours of objects by using the CIE
system
- [138] DIN 5033 Teil 3, 1980
Farbmessung; Farbmeßzahlen

- [139] W.D. Sproul
Surf. & Coat. Technol. 33, 1987, 73-81
- [140] S. Kadlec, J. Musil, J. Vyskocil
Vacuum 37, 10, 1987, 729-738
- [141] S. Kadlec, J. Musil, J. Vyskocil
J. Phys. D: Appl. Phys., 19, 1986, 187-190
- [142] P. Carlsson, C. Nender, H. Barankova, S. Berg
J. Vac. Sci. Technol. A, 11(4), 1993, 1534-1539
- [143] B. Sproul, M. Graham, M. Wong
Northwestern University/BIRL. Personal information exchange January 7th
2001
- [144] C. Rebholz, H. Ziegele, A. Leyland, A. Matthews
Surf. & Coat. Technol., 115, 1999, 222-229
- [145] L. Hultman, W-D Münz, J. Musil, S. Kadlec, I. Petrov, J. Greene
J. Vac. Sci. Technol. A, 9 (3), 1991, 434-438
- [146] S. Yang
Dissertation, Sheffield Hallam University, 1997
- [147] I. Brown, B. Feinberg, J. Galvin
J. Appl. Phys., 63 (10), 1998, 4889
- [148] C. Schönjahn, H. Paritong, W-D Münz, R. Twesten, I. Petrov
J. Vac. Sci. Technol. A, 19 (4), Jul/Aug 2001, 1392-1398
- [149] W.-D. Münz, I. Smith, D.B. Lewis, S. Creasey
Vacuum, Vol. 48, 5, 1997, 473-481
- [150] S. Creasey, D.B. Lewis, I. Smith, W.-D. Münz
Surf. & Coat. Technol., 97, 1997, 163-175
- [151] C. Schönjahn, L. Donohue, D.B. Lewis, W-D Münz, I. Petrov
J. Vac. Sci. Technol., A, 18 (4), 2000
- [152] P. Hovsepian, D.B. Lewis, W.-D. Münz
Surface and Coatings Technology, 133/134, 2000, 166-175
- [153] G.J. van der Kolk, T. Hurkmans, T. Trinh, W. Fleischer
40th Annual Technical Conference Proceedings SVC, 1997, 94-97
- [154] K. Bewilogua, M. Grischke, J. Schroeder, T. Michler, G.J. van der Kolk,
T. Trinh, T. Hurkmans, W. Fleischer
41st Annual Technical Conference Proceedings SVC, 1998, 75-79
- [155] Z. Huang, Y. Sun, T. Bell
Wear, 173, 1994, 13-20
- [156] A. J. Perry, D. E. Geist, K. Narasimhan, J. R. Treglio
Surface and Coatings Technology, 86-87, 1996, 364
- [157] S. Yang, D.B. Lewis, I. Wadsworth, J. Cawley, J.S. Brooks, W.-D. Münz
Surface and Coatings Technology, 131, 2000, 228-233

Current Industrial Practices

An all-round performer in the physical vapour deposition laboratory

W.-D. Münz, K. Vannisselroy, R. Tietema, T. Hurkmans and G. Keiren

Hauzer Techno Coating Europe B.V., PO Box 226, NL-5900 AE Venlo (Netherlands)

(Received March 8, 1993; accepted in final form March 14, 1993)

Abstract

Physical vapour deposition (PVD) technology is enjoying an ever-expanding range of applications. New materials are being developed. Process technology is being better understood. The HTC 625 Multilab PVD coater goes a long way toward meeting the needs that arise out of these developments. Universal cathodes, Steered Arc[®]-unbalanced-magnetron capability, ABS[®] technology and high frequency bias are standard features. Today this unit can produce coatings from materials such as TiN, TiCN, ZrN, TiAlN, TiZrN, TiNbN and hydrogenated amorphous carbon.

1. Introduction

The requirements that must be met by a physical vapour deposition (PVD) hard coater for laboratory use are growing ever stricter. Process variants are proliferating. New coating materials are always being developed, whether as monolayers or multilayer coatings. In addition to nitrides and carbonitrides, more and more work is being done with oxides, amorphous “diamond-like” carbon (hydrogenated amorphous carbon), or borides. Process automation must cope with increasing demands, going hand in hand with the need to run processes with a greater variety of subtle differences. This is particularly the case with multilayer coatings. Very often too, a coater must additionally be suitable for pilot production.

The HTC 625 Multilab coater makes it possible to carry out several different cathodic coating processes—Steered Arc[®], magnetron, unbalanced magnetron or their combinations—in parallel or simultaneously in a single unit. A universal cathode provided for this purpose can easily be switched over to the various operating modes. In addition, an automation concept has been worked out that satisfies the most demanding requirements where processes must be monitored and measurements taken.

2. Mechanical configuration

The stainless steel vessel, equipped with cooling and heating coils, has inner dimensions of 625 mm ×

625 mm × 700 mm and permits optimum access to the unit through large doors on both the front and the back. The Balzers turbomolecular pump, with oil-lubricated bearings and a nominal pumping speed of 2200 l s⁻¹, is flanged onto the side of the process chamber. A VAT gate valve separates the pump zone from the vessel. The turbomolecular pump works in combination with a 250 m³ h⁻¹ Roots pump and a 30 m³ h⁻¹ rotary-vane pump. With a clean vacuum chamber, an ultimate pressure of 2 × 10⁻⁶ mbar can readily be achieved. Under normal working conditions, a pressure of 2 × 10⁻⁵ mbar can be reached after pumping for 30 min. For high pressure processes, the vessel can also be evacuated by way of a bypass to the turbomolecular pump. Each door is equipped with a universal cathode. Two types of cathode are available: cathodes with rectangular targets measuring 400 mm × 125 mm are installed as the standard option but, on request, the unit can also be equipped with round cathodes 125 mm in diameter. Both cathode types require the appropriate door designs, which are likewise available as alternative options. Figure 1 shows a general view of the unit; Fig. 2 shows the layout of the full unit including power supplies.

3. Cathodes

In principle, the cathodes are configured like normal magnetron cathodes. The targets, selectable in versions from 6 to 12 mm thick, are clamped onto water-cooled

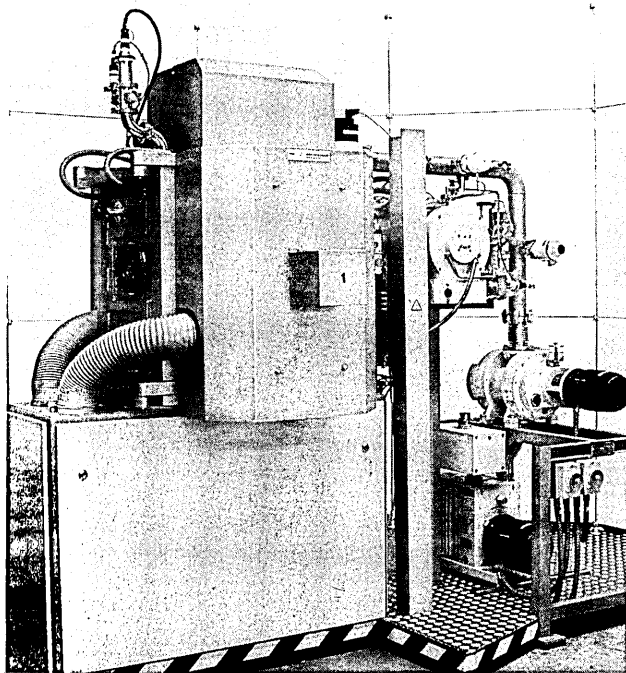


Fig. 1. Overall view of the HTC 625 Multilab coater.

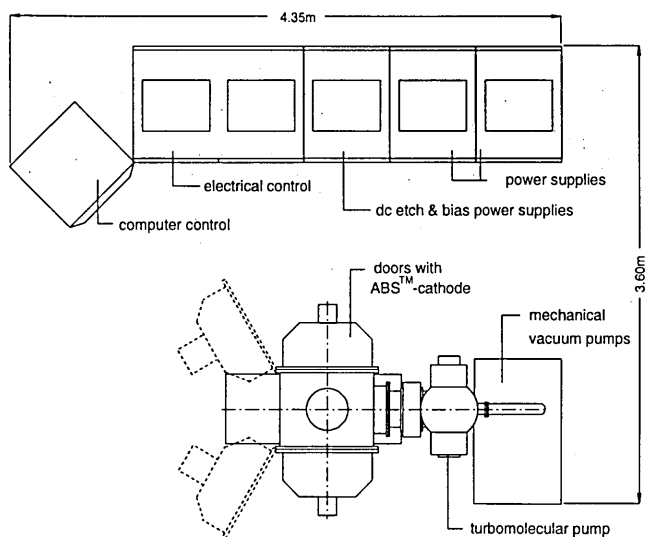


Fig. 2. Layout of the HTC 625 Multilab coater (schematic).

copper holders. The cathode unit is flanged to the outside of the door by way of a Teflon insulator. Targets can easily be replaced when the doors are open.

Figure 3 shows schematically how the magnetron cathode can also be used as an “unbalanced” magnetron or as a “Steered Arc[®]” cathode. To obtain the unbalanced-magnetron effect [1], an electromagnet with the same polarity is arranged concentrically with the outer pole of the magnetron’s permanent magnet. The level of the coil current determines the extent to which

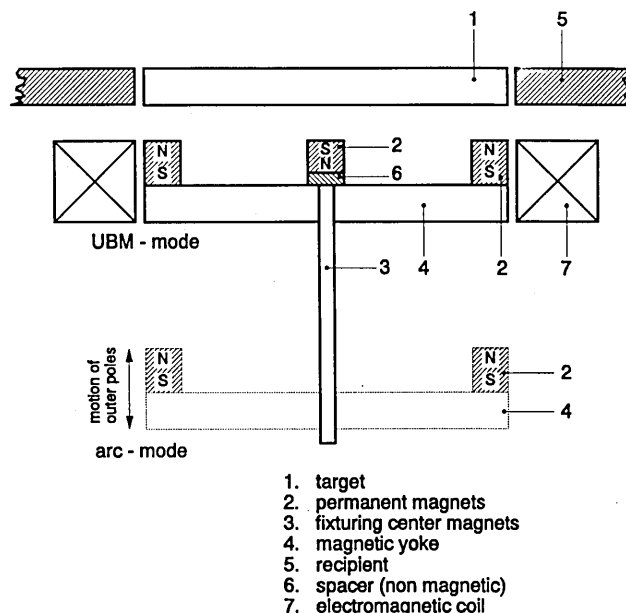


Fig. 3. Schematic of a diagram universal arc and unbalanced-magnetron (UBM) cathode.

the plasma is propagated into the vessel. Reference 2 provides a summary of the development of the unbalanced magnetron and its effects on the characteristics of hard coatings.

In contrast with the familiar combination cathode [3], “Steered Arc[®]” operation is achieved by retracting the outer pole of the permanent magnet’s field with respect to the position of the target. This reduces the total magnetic flux density in front of the target to less than 150 G. Under these conditions an arc discharge can be produced which assumes a closed ring shape, similar to that of a magnetron discharge [4, 5]. The “Steered Arc[®]” discharge also makes resourceful use of the electromagnet. By appropriately controlling the current, the diameter of the arc track can be varied continuously in such a way that the target surface is uniformly traversed and thus also uniformly stripped away. This avoids sharp “digging in” of the arc trace [3]. The permanent magnets are moved pneumatically. Figures 4 and 5 respectively show the configurations of a rectangular and a round cathode.

A particularly advantageous effect of two opposing unbalanced magnetrons can be achieved by using magnets with opposite polarities, as shown in Fig. 6 [6, 7]. With the same polarities the plasma zones positioned in front of the targets in effect repel one another, while with opposite polarities the plasma remains largely concentrated and self-enclosed within the space between the cathodes, and high plasma densities or bias current densities can be attained [7]. The HTC 625 Multilab coater offers a practical implementation of these principles, including the polarity of the electromagnets.

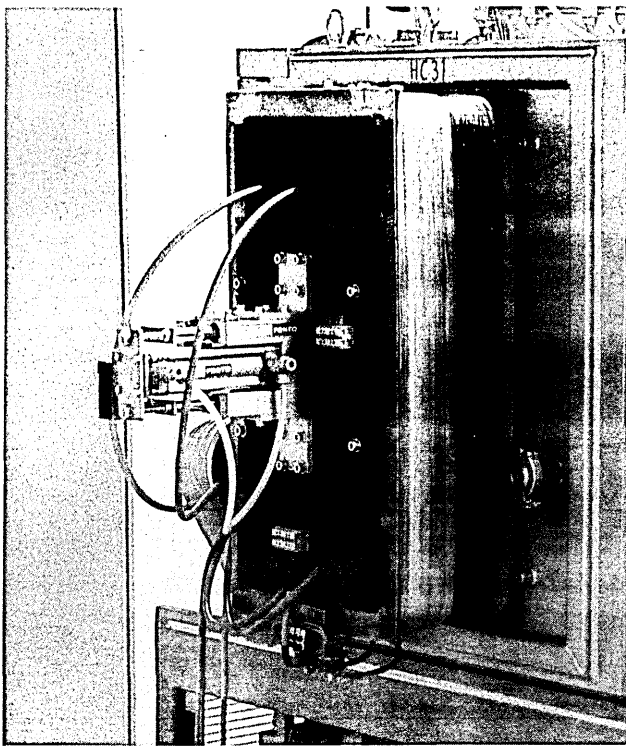
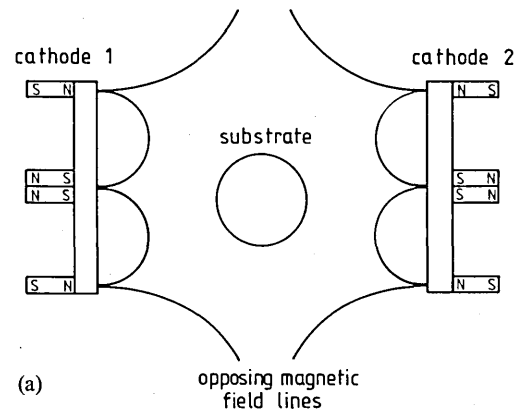
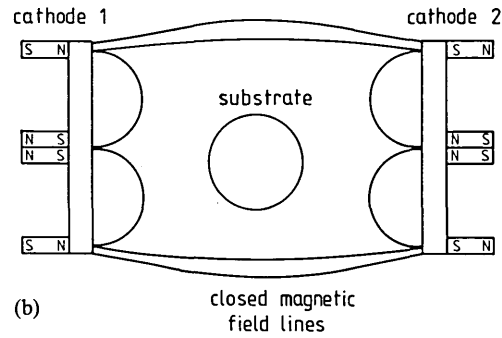


Fig. 4. Rectangular cathode: electromagnetic coil and pneumatic drive for permanent magnet motion.



(a)



(b)

Fig. 6. Principles of magnet arrangements with two cathodes: (a) opposing magnets; (b) closed-field magnetic polarization [5, 6].

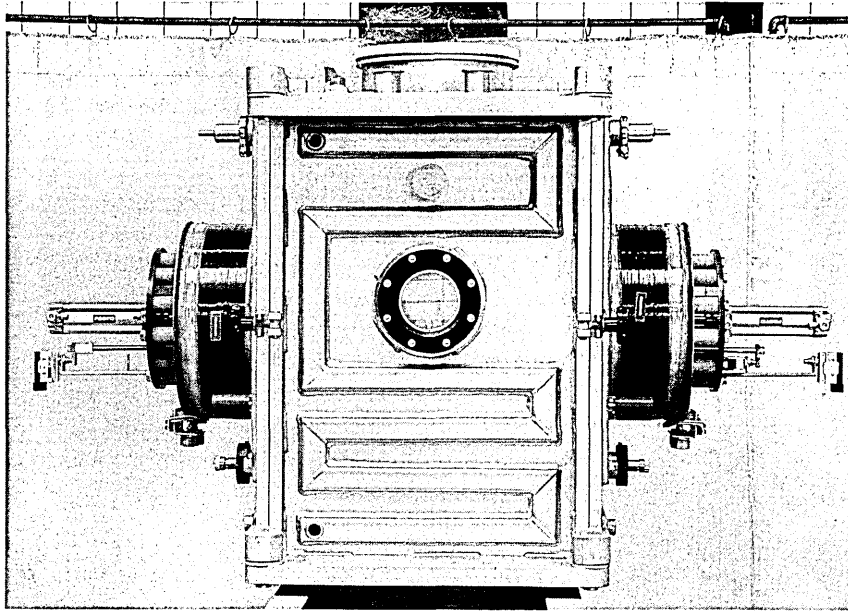


Fig. 5. Process chamber equipped with two annular ABS® cathodes, electromagnetic coils and pneumatic drives.

4. Plasma

Figure 7 provides a look through the sight glass into the process chamber with unbalanced-magnetron cathodes in operation. In the left half of the picture, the

typical appearance of a magnetron discharge can be seen. In contrast with a conventional magnetron, the plasma fills the vessel chamber virtually uniformly. As a result the structural elements of the substrate holder, filled with specimen cylinders, are clearly visible inside

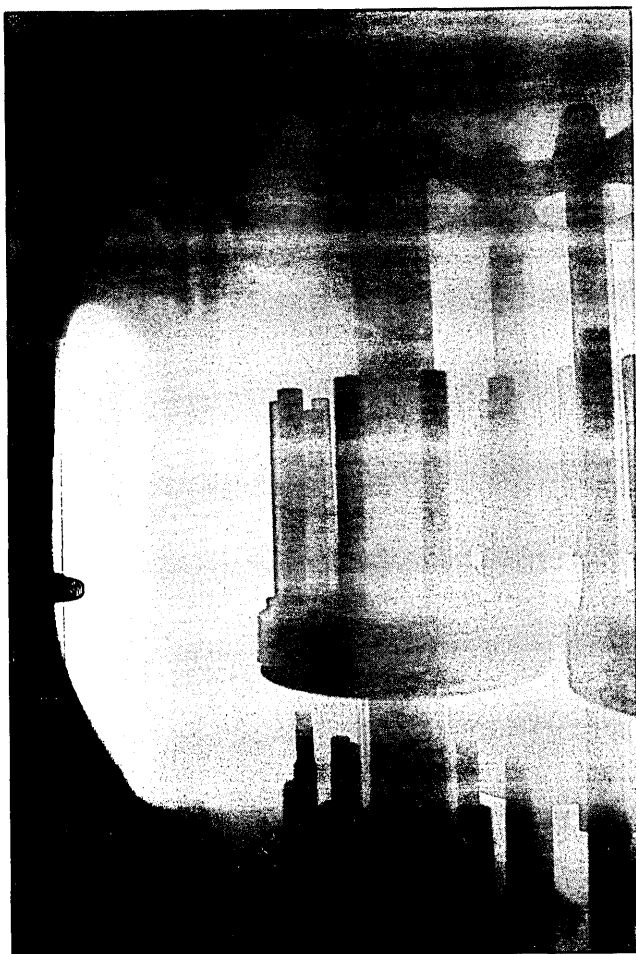


Fig. 7. View into the plasma-illuminated process chamber.

the plasma. With cathode and magnet arrangements of this kind, one can obtain plasma densities N_e of up to $10 \times 10^{10} \text{ cm}^{-3}$, as electron density measurements with Langmuir specimens have demonstrated [8].

Figure 8 shows the influence of the electromagnets' coil current on the bias current of a fully loaded substrate turntable. Using the electromagnets, the substrate current can be increased by a factor of almost 8. So a bias current of 16 A corresponds to a mean bias current density of between 5 and 8 mA cm^{-2} [4, 7]. In this experiment, the cathodes were each operated at 6.5 kW. The bias voltage was -60 V and the discharge pressure was $3 \times 10^{-3} \text{ mbar}$. The sputtered material was Ti.

The variable bias current allows the conditions for layer growth to be influenced or controlled within a broad range [9, 10]. This can be done without having to alter the coating rate, which is substantially a function of cathode power. In other words, the ratio of the number v_i of ionized particles impinging on the substrate (e.g. argon ions) to the number v_0 of neutral particles (e.g. Ti ions) can be adjusted regardless of cathode

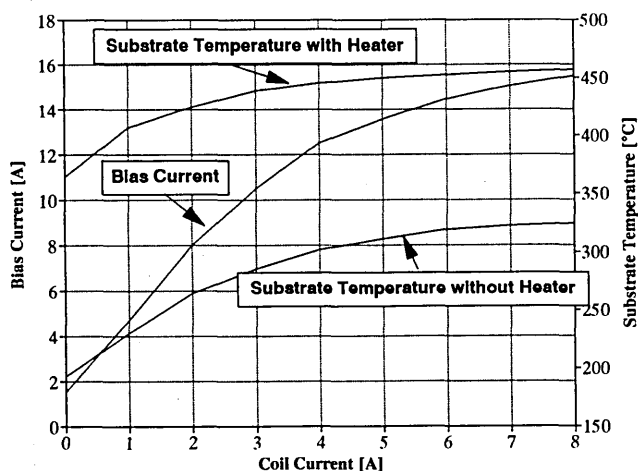


Fig. 8. Influence of the coil current (electromagnet) on bias current and substrate temperature, (parameter, auxiliary heating).

power. Appropriate measurements have shown that v_i/v_0 can be as much as a factor of 5.

Figure 8 also shows how the substrate temperature can be controlled by varying the coil current in the electromagnets. The curve labelled Substrate Temperature without Heater shows the equilibrium temperature of a test specimen 5 mm thick at a bias voltage of -60 V , for the case in which no heating is used during the coating process. With the electromagnets switched off—in other words, in the conventional balanced-magnetron mode—the substrate temperature remains distinctly below 250 °C . At a coil current of 8 A, one obtains an equilibrium temperature of around 300 °C . When an additional IR radiant heater is used, the resultant substrate temperature can be influenced still further. The curve labelled Substrate Temperature with Heater in Fig. 8 shows the equilibrium temperature of the same specimen when an IR heating power of about 2.5 kW is added in. Naturally the substrate temperature can also be increased by raising the bias voltage, with the well-known consequences for layer growth [3]. A summary look at the results in Fig. 8 gives a clear view of the variety of freely adjustable condensation conditions. The ion current at the substrate and the substrate temperature itself can be precisely adjusted to the necessary conditions. Thus low temperature processes and coating processes at a substrate temperature of 500 °C can both conveniently be carried out in a single unit. Processes can be developed for coating such temperature-sensitive materials as plastics, brass, aluminium and case-hardened steels, with no need for any substantial alterations in the coater itself.

The high ionization densities achievable with the unbalanced magnetron can also be used to advantage in etching with Ar^+ ions. In this case the magnetrons are caused to discharge at low operating voltages, such as -150 V . This generates a relatively weak plasma in

front of the magnetrons which, when associated with the electromagnets in the centre of the process chamber, is still of sufficient intensity to produce plasma densities that permit effective etching at voltages such as -500 V. During the etching process, the magnetrons are shielded with movable plates (baffles) to prevent the parts (substrates) from being coated with target material.

5. Power supplies

To operate the universal cathodes, switched-mode transistor-controlled power supply units are provided, usable in both arc and magnetron modes. The operating range is -80 V, 150 A for arc mode and -750 V, 20 A for magnetron mode. For the etching power supply the operating range is -1200 V, 20 A and for the bias power supply the range is -200 V, 20 A. The electromagnets are run with transistorized power supplies, 150 V, 10 A.

In addition to the d.c. power supplies, an optional 13.5 MHz high frequency power supply is available with a power output of 2 kW into 50Ω . This unit is connected via an automatic matchbox to the substrate turntable. The high frequency power supply can be used both to etch substrates and as a bias power supply in the deposition of electrical insulation coatings such as oxides or amorphous carbon layers. The coater complies with the high frequency emission safety requirements of the German Federal Postal Service. Every unit is tested against electromagnetic radiation by an expert service company before leaving the plant.

6. Substrate turntable

To hold substrates, the coater has a convenient substrate turntable with three-way rotation. A variety of tested and proven holder mechanisms are available. Standard equipment includes holders for cylindrical parts such as high speed steel cutting tools, which are loaded onto six rotating spindles in up to three planes. Figure 9 gives an overall view of the substrate turntable.

The loading capacity, e.g. for drill bits with a diameter of 6 mm, is 216 pieces in a three-way rotary holder, and about 600 with a "hedgehog" holder. For drill bits and milling cutters with a diameter of 25 mm it is 72 pieces; for hob cutters with a diameter of 120 mm it is 12–18 pieces, depending on length; for hard-metal indexable inserts it is about 900–1000 pieces.

A special feature of the substrate turntable is its stop-and-go capability. In this operating mode, one or more spindles, selectable in advance, can be positioned in front of either cathode, using optical position detectors, to coat the substrates with the corresponding material. This concept was specially developed for the deposition of

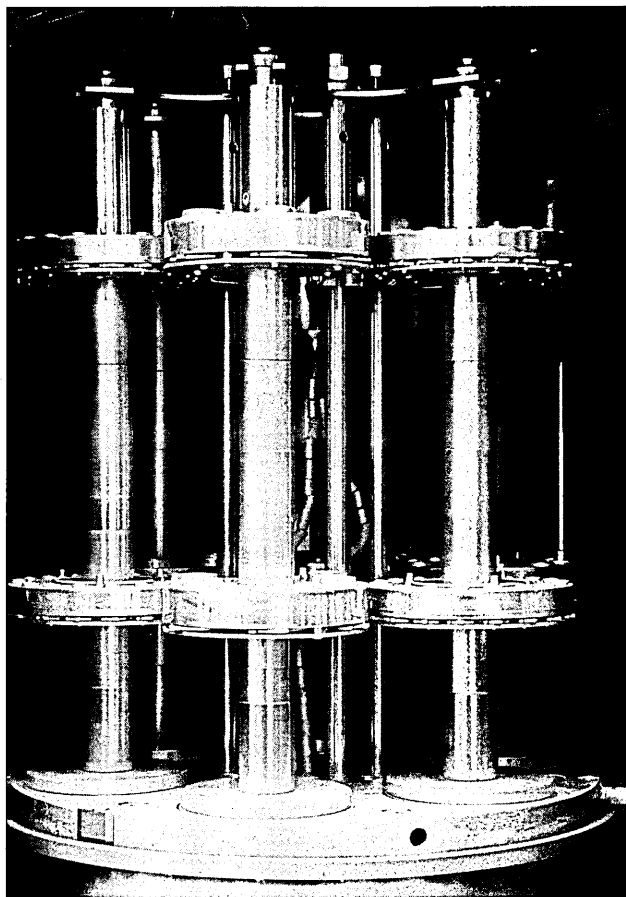


Fig. 9. Standardized threefold planetary turntable for fixturing of high speed steel cutting tools.

multilayer coatings, which may consist of different materials. In this case the two cathodes are each equipped with different targets. In stop-and-go mode, material can then be applied in front of the respective target in the appropriate gas atmosphere for each case. In addition to this sequential cathode operating mode, the multilayer coating can also be applied in simultaneous cathode operation. A shutter system to support this mode is available.

7. Special measuring equipment

The HTC 625 Multilab coater possesses two thermocouples as standard equipment, connected to the control cabinet by way of special rotary lead-throughs. This allows coating processes to be run under temperature control, with the IR heating or the bias voltage or coil current of the electromagnets, for example, being usable as a manipulated variable.

An especially important feature is the control capability for the metal ion etching process in the arc mode.

Uncontrolled substrate overheating can occur here relatively easily. For that reason, this process step is run under temperature control. Once a pre-set maximum temperature is reached, the ion etching process is interrupted and not started again until the temperature reaches a minimum.

The unit also has flow regulators for three different process gases as standard equipment. Expansion for more process gases is possible on special order. Because of the high pumping speed of the pump system, different nitride processes, such as TiAlN deposition, can be run with a completely regulated flow. Figure 10 shows the hysteresis curve [11] for this application case. Even at high flow values for nitrogen as the reactive gas, no serious target poisoning occurs.

On special order, the unit can also be equipped with an optical emission control unit for reactive processes. In this case, for example, the intensity of the emission line of one or more metal or gas ions is measured and the flow value of the reactive gas is controlled or adjusted accordingly.

Reactive arc coating and also various magnetron coating processes may also be run under absolute-pressure control. The high precision Viscovac pressure gauge (Leybold AG) serves this end, or the Baratron (MKS) is used as the control device. Reactive processes can also be run under partial-pressure control using commercial mass spectrometers.

8. Automation

The HTC 625 Multilab coater's controls use a Mitsubishi SPS as standard equipment. It handles all major switching, regulating and locking functions. For process control, process manipulation, process data

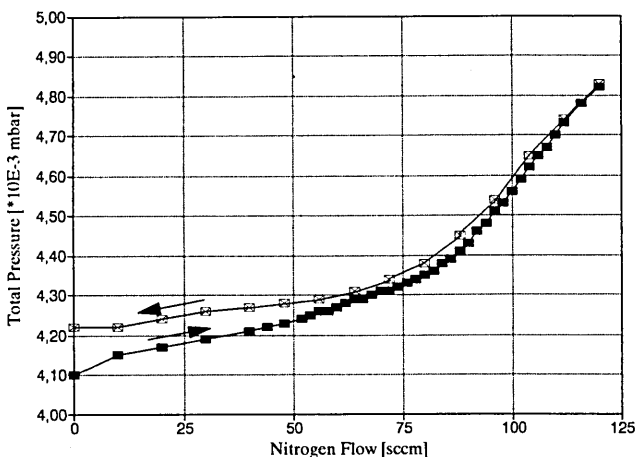


Fig. 10. "Poisoning" of $Ti_{0.5}Al_{0.5}$ target (hysteresis slope [11]): total pressure as a function of nitrogen flow ($P_{\text{target}} = 6.5 \text{ kW}$; $p_{Ar} = 4.1 \times 10^{-3} \text{ mbar}$).

acquisition, storage and documentation, the Mitsubishi SPS is combined with a computerized control unit and FactoryLink software. The latter unit also handles visual display of the process sequence, as well as filing of the process parameters. FactoryLink is a supervisory control and data acquisition package.

The computer has a database that includes all recipes and process parameters. Further information and remarks can be input by the operating personnel by way of a keyboard and then stored and printed out together with the process report. The entire process sequence is controlled and run entirely automatically via the computer. The computer hardware is housed in a special control cabinet. The software includes a colour graphics interface package, programmable logical control interface package, real-time and historic-trend package, a report generation package, batch recipe package and a data-logging package. Figure 11 gives an overall view of the computer control cabinet.

For fast customer service at a distance, a modem can be supplied that helps out with direct servicing of the unit, with maintenance and with upgrading the database, as well as in troubleshooting.

9. Operating modes

The HTC 625 Multilab coater can fundamentally be supplied even as a simple Steered Arc[®] coater. The equipment design holds to a consistent modular principle, allowing the coater to be upgraded step by step until it has the full multifunction capability described here. Depending on the upgrade level, it can be run as a plain arc, balanced-magnetron or unbalanced-magnetron system.

Increasing interest is being aroused in particular by the so-called ABS[®] process mode [4, 12, 13]—arc bond sputtering. Here the substrate surface is so to speak "pre-conditioned" in the metal vapour of the Steered Arc[®] discharge. Under the action of a bias voltage of -1200 V and the multiple ionization of the metal atoms (triple, for example, in the case of Ti), the substrate surface becomes enriched with coating material [14, 15], substantially enhancing adhesion. One study under laboratory conditions, only recently completed, found that, when the ABS[®] coater is alternately run in the unbalanced-magnetron mode (in other words, without arc pre-treatment) and in the ABS[®] mode, the latter mode substantially increases the probability of strong coating adhesion. Coating adhesion was determined here with critical-load measurements and Rockwell indentation tests. Figure 12 shows the statistical evaluation of the L_c measurements. The study was performed with TiAlN coatings deposited in different ways on hard metal [16].

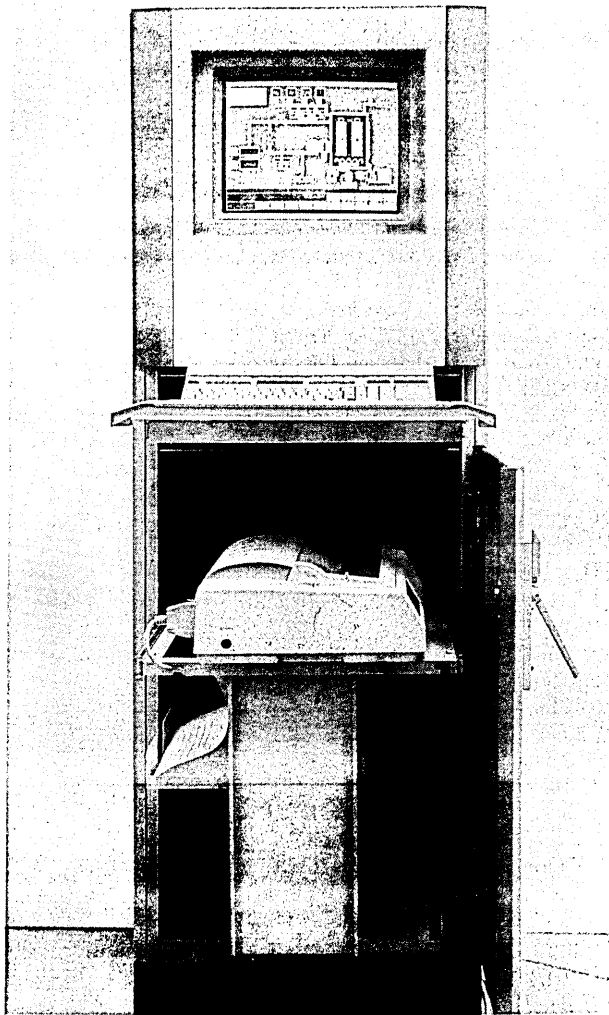
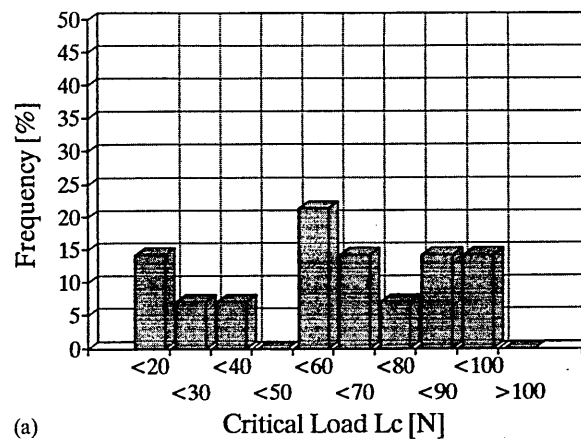
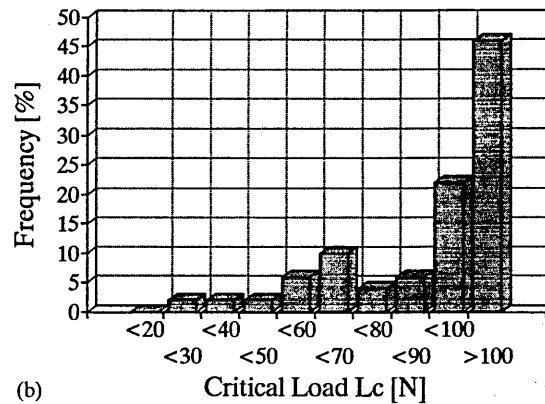


Fig. 11. View of computer control cabinet: display (colour), keyboard and printer.

As has already been noted, the necessary arrangements have been included so that the coater can also be used to produce multilayer coatings as described for example in refs. 17–24. In terms of the control equipment, one



(a)



(b)

Fig. 12. Statistical evaluation of the L_c measurements: (a) unbalanced-magnetron mode; (b) ABS[®] mode.

available capability is to deposit multilayer coatings alternately in the arc and unbalanced-magnetron modes. The capability is also available for deposition in different gas atmospheres.

Finally it should be mentioned that theoretically the unit may be used to deposit amorphous diamond-like carbon coatings. Although no specific practical results are yet available on this, the equipment itself offers no obstacles to the deposition of metal-carbon or amorphous carbon coatings [25–28].

TABLE 1. Survey results showing some characteristics of important coatings

	Colour	Temperature (°C)	HV	Critical load on HSS	Friction coefficient	Max. temp. (°C)
TiN	gold	400–500	2300–2600	40–60	0.2–0.8	500
TiN	gold	180–250	2300–2600	–	–	–
ZrN	brass	400–500	2600–2800	40–60	0.2–0.4	550
ZrN	brass	180–250	2600–2800	–	–	–
TiCN	lilac	400–500	2500–2800	40–60	0.2	400
TiAlN	black	350–450	2100–2400	50–70	0.4	800
TiAlN	black	180–250	2100–2400	–	–	–
TiNbN	pale gold	400–500	2600–2900	40–60	0.2–0.4	500
CrN	metal	180–300	2000–2200	50–80	0.8	800

10. Characteristics of ABS[®] coatings

The ABS[®] technology has been undergoing practical trials at Hauzer Techno Coating Europe B.V. since 1991. In that period, over ten ABS[®] units have been built and put into operation. A variety of layers and multilayer coatings have been studied so far. Table 1 gives a survey of some characteristics of important coatings. The typical layer thickness of these hard coatings is 2–5 µm. Only in the case of decorative coatings is the thickness in the range 0.5–1 µm.

11. Summary

As a successor to the HTC 1000-4 ABS[®] system [4, 12, 13], Hauzer Techno Coating Europe B.V. is introducing a new, compact and flexible type of coater, tailor made for the laboratory. Special emphasis was placed on making this new unit capable of handling a wide variety of possible applications. The cathode design, process conditions, superior pumping concept and convenient computer control are all intended to enhance its versatility. The result is an all-round performer for PVD laboratory operation.

References

- 1 B. Window and S. Savvides, *J. Vac. Sci. Technol. A*, 4 (1986) 196.
- 2 W.-D. Münz, *Surf. Coat. Technol.*, 48 (1991) 81.
- 3 P. Robinson and A. Matthews, *Surf. Coat. Technol.*, 43–44 (1990) 288.
- 4 W.-D. Münz, D. Schulze and F. J. M. Hauzer, *Surf. Coat. Technol.*, 50 (1992) 169.
- 5 S. Boelens and H. Veltrop, *Surf. Coat. Technol.*, 33 (1987) 63.
- 6 W. D. Sproul, P. J. Rudnik, M. E. Graham and S. L. Rohde, *Surf. Coat. Technol.*, 43–44 (1990) 270.
- 7 S. L. Rohde, A. J. Nelson, A. Mason and W. D. Sproul, *J. Vac. Sci. Technol. A*, 10 (4), (1992) 1797.
- 8 P. C. Johnson, unpublished, Culham Laboratory, Abingdon, UK, 1992.
- 9 S. Kadlec, J. Musil, V. Valvoda and W.-D. Münz, *Proc. 7th Int. Conf. on Ion and Plasma Assisted Technology, Genf*, 1989, CEP Consultants, Edinburgh, 1989, p. 100.
- 10 L. Hultman, W.-D. Münz, J. Musil, S. Kadlec, I. Petrov and J. E. Greene, *J. Vac. Sci. Technol. A*, 9 (3) (1991) 434.
- 11 W. D. Sproul, *Thin Solid Films*, 107 (1983) 141.
- 12 W.-D. Münz, F. J. M. Hauzer, D. Schulze and B. Buil, *Surf. Coat. Technol.*, 49 (1991) 161.
- 13 W. D. Sproul, P. J. Rudnik, K. O. Legg, W.-D. Münz, I. Petrov and J. E. Greene, *Surf. Coat. Technol.*, 56 (1993) 179.
- 14 G. Håkansson, L. Hultman, J.-E. Sundgren, J. E. Greene and W.-D. Münz, *Surf. Coat. Technol.*, 48 (1991) 51.
- 15 W.-D. Münz, J. Schroeder, H. Petersein, G. Håkansson, L. Hultman and J.-E. Sundgren, in A. Czichos and L. G. E. Vollrath (eds.), *Proc. Conf. on Surface Technology, Berlin, 1989*, Hanser, München, 1989, p. 61.
- 16 W.-D. Münz, T. Hurkmans, G. Keiren and T. Trinh, *J. Vac. Sci. Technol.*, in press.
- 17 H. Holleck, *Metall.*, 43 (1989) 614.
- 18 H. Holleck, M. Lahres and P. Woll, *Surf. Coat. Technol.*, 41 (1990) 179.
- 19 X. Chu, M. S. Wong, W. D. Sproul, S. L. Rohde and S. A. Barnett, *J. Vac. Sci. Technol. A*, 10 (4) (1992) 1604.
- 20 X. Chu, M. S. Wong, W. D. Sproul and S. A. Barnett, *Surf. Coat. Technol.*, 57 (1993) 13.
- 21 J. E. Sundgren, J. Birch, G. Håkansson, L. Hultman and U. Helmersson, *Thin Solid Films*, 193–194 (1990) 818.
- 22 P. B. Mirkarimi, L. Hultman and S. A. Barnett, *Appl. Phys. Lett.*, 57 (25) (1990) 2654.
- 23 L. Hultman, L. R. Wallenberg, M. Shinn and S. A. Barnett, *J. Vac. Sci. Technol. A*, 10 (4) (1992) 1618.
- 24 M. Shinn, L. Hultman and S. A. Barnett, *J. Mater. Res.*, 7 (4) (1992) 901.
- 25 H. Dimigen, H. Hübsch and J. Schaal, *Tech. Hochsch. Darmstadt, Schriftenr. Wiss. Tech.*, 30 (1986) 157.
- 26 H. Dimigen and C.-P. Klages, *Surf. Coat. Technol.*, 49 (1991) 543.
- 27 D. Repenning, *Dünne Schichten*, 2 (1992) 28.
- 28 D. Hofmann, W.-D. Münz, H. Schüssler and J. Göbel, *Proc. 5th Int. Conf. on Ion and Plasma Assisted Technology, Munich, 1985*, CEP Consultants, Edinburgh, 1985, p. 252.

Multilayered titanium tungsten nitride coatings with a superlattice structure grown by unbalanced magnetron sputtering

T. Hurkmans^a, T. Trinh^a, D.B. Lewis^b, J.S. Brooks^b and W.-D. Münz^{a,b,*}

^a Hauzer Techno Coating Europe BV, PO Box 226, 5900 AE Venlo, Netherlands

^b Materials Research Institute, Sheffield Hallam University, Pond Street, City Campus, Sheffield, South Yorkshire S1 1WB, UK

Abstract

This paper reports the deposition of TiN-W₂N superlattice coatings using unbalance magnetron sputter deposition. Three magnetrons were used to vaporise the poisoning sensitive material titanium whereas only one magnetron was needed to deposit sufficient tungsten from a pure tungsten target. The deposition process was carried out simultaneously in one single vacuum chamber using one common reactive gas atmosphere. Titanium and tungsten were present as the individual phases of TiN and W₂N and not as a TiWN solid solution.

The coatings had a (200) preferred orientation with hardness values up to 3000 HV at a surprisingly low internal stress of 1.0 GPa μm^{-1} and high adhesion, L_c 60 N, when a minimum nitrogen content was exceeded.

The superlattice period evaluated by low angle XRD was between 24.5 and 172 Å depending on the nitrogen partial pressure, the satellite rotation frequency in the vacuum chamber and whether it was single or three fold rotation

Keywords: Multilayers; Titanium tungsten nitride; Sputtering; Hard coatings; Superlattice

1. Introduction

TiWN coatings are mainly known from microelectronics applications [1,2]. TiWN coatings for mechanical applications have been prepared by reactive cathodic arc deposition using Ti/W alloy targets and have been reported as unusual hard PVD coatings particularly useful in cutting tool operations [3]. In the following work, results on TiWN phases are described which were grown from pure Ti and W metal targets by means of reactive unbalanced magnetron sputtering. It is the aim of this paper to investigate the properties of these films and to determine the influence of the multi-target arrangement to the microstructure on the deposited coatings.

2. Experimental details

2.1. Deposition parameters

All deposition runs were performed in a HTC 1000-ABSTM system of Hauzer Techno Coating Europe B.V. This system uses four vertically mounted cathodes that can be run either in a cathodic arc or unbalanced magnetron (UBM) sputtering mode. The configuration

used in this investigation was two titanium targets in the arc mode for metal ion etch and three titanium and one tungsten target in the UBM mode for film deposition. The following deposition process was used.

- (1) Pump down and heating.
- (2) Target pre-sputtering using closed shutters to avoid substrate contamination.
- (3) Titanium ion bombardment (metal etching) with biased substrates as an etching procedure using cathodic arc.

Closed field electromagnetically unbalanced magnetron sputtering [4] was used for the final deposition in the configuration shown in Fig. 1. The fixed coating parameters were 8.8 W cm⁻² target power density, a current of 5.5 A was used in each of the electromagnets to achieved the unbalancing effects of the magnetron, argon flow of 340 sccm, deposition temperature of 450 °C, table rotation speed of 8.0 rpm (1 fold rotation) and a layer thickness of approximately 3 μm (3 fold rotation).

The coatings were deposited on M2 high speed steel and type 434 stainless steel.

Film properties were measured using the following methods.

- (1) Daimler Benz Rockwell C hardness test for the determination of adhesion HR_c-DB [5].

* Corresponding author.

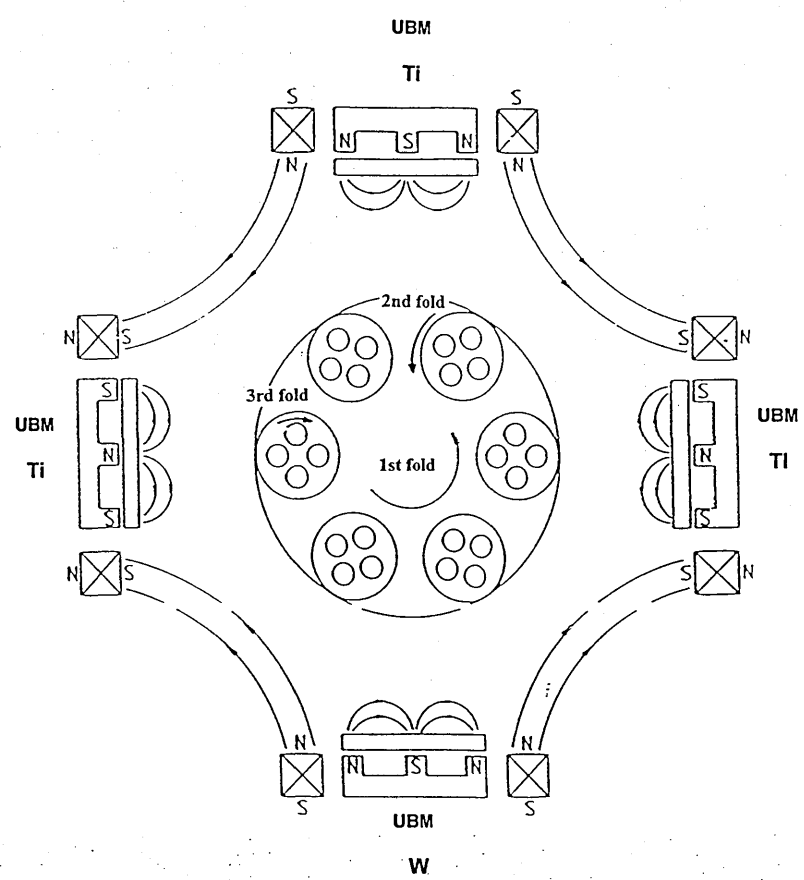


Fig. 1. Schematic diagram of the Hauzer HTC 1000-4 ABS PVD unit.

- (2) CSEM 'Revetest' scratch adhesion test to determine critical load, L_c .
- (3) Vickers microhardness measurements were made using a load of 25 g.
- (4) CSEM 'Kalotest' was used to determine coating thickness.
- (5) CIELAB colour units (L^* , a^* and b^*) were measured using a Minolta CM-2002 Spectrophotometer.
- (6) Normalised stress values were estimated by a bending test (R) of circular heat treated stainless steel samples [6].

- (7) A Philips XL 40 Scanning electron Microsc was used for the fracture morphological investigation
- (8) The coatings were analysed using both a L GDS-750 QDP glow discharge optical emission spectroscopy (GDOES) and energy dispersive X-ray analysis (EDX). Depth profile analysis was also performed using GDOES.
- (9) The specimens were analysed by X-ray diffraction in both low angle and high angle configurations using Bragg-Bretano geometry. A direct measurement of superlattice wavelength, Δ , was made in the low angle region using the standard Bragg equation

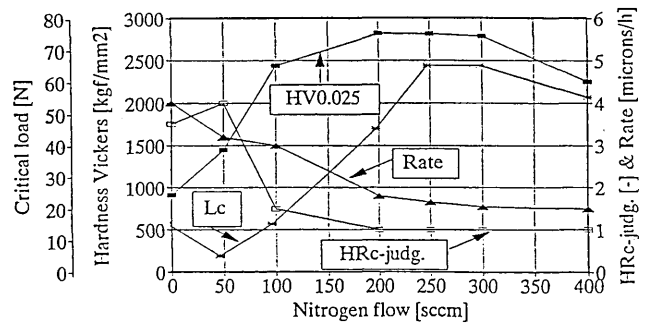


Fig. 2. The influence of the nitrogen flow rate on the Vickers Hardness (25 g), the deposition rate (3 fold planetary rotation), HR_c-DB judgement and critical load, L_c , at a negative bias voltage of -80 V.

$$\Delta = \left(\frac{n\lambda}{2 \sin \theta} \right)$$

where θ is the Bragg angle.

The superlattice period can also be calculated in high angle region using the following equation

$$\sin \theta_a = \sin \theta_b \pm \left(\frac{n\lambda}{2\Delta} \right)$$

where θ_a and θ_b are the diffraction angles of the respective satellite peaks, λ is the X-ray wavelength, Δ is superlattice period, and n is the order of the superlattice reflection.

The particle size and strain were determined using Hall-Williamson plots and the textures were determined in accordance with the inverse pole figure technique [7].

3. Experimental results and discussion

The reactive deposition process has been studied in terms of the physical, mechanical, structural, compositional and morphological properties. The influence of the nitrogen flow rate and bias voltage on the deposition rate and mechanical properties show typical trends that would be expected from a reactive sputtering process. However, this dependency was much less pronounced than those commonly observed, e.g. titanium nitride, and these results are presented in Fig. 2. The decay in the sputter rate was extraordinarily smooth compared with similar curves for titanium nitride coatings and even at a nitrogen flow rate of 350 sccm, which was identical to that of the non-reactive argon gas, the deposition rate has only decreased to 50% of that of the metallic deposition rate. The hardness dependence in the relevant operation conditions, nitrogen flow rate 200-350 sccm, is extremely flat and shows a maximum value of 2800 HV. Adhesion, as measured by HR_c -DB and critical load L_c , indicates that in the same nitrogen flow rate range satisfactory results with values of 1 for HR_c -DB and approximately 60 N for the critical load are observed. An increase in the bias voltage from -60 to -120 V shows the expected increase in the hardness. Again the influence of variation in bias voltage on the hardness was not so pronounced, in the bias range -80 to -120 V there was an increase in hardness from 2800 to 2950 HV. These values are somewhat higher than those observed for TiN (2500 HV). In parallel a rather small increase in internal stress was observed with an average value of $1.0 \text{ GPa } \mu\text{m}^{-1}$ growing stress. With increasing nitrogen flow the metallic lustre became less significant, i.e. decreasing values of L^* . Also the almost negligible increase in a^* and only slight increases in b^*

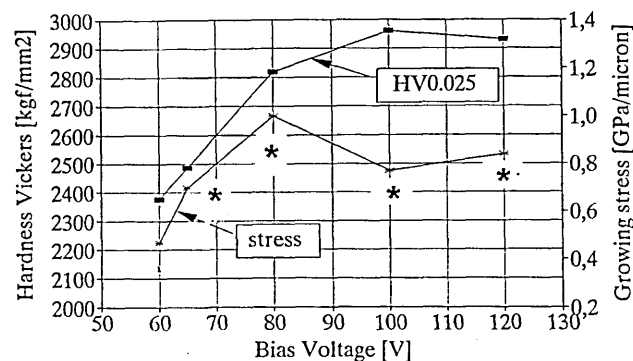


Fig. 3. (Table 2). The influence of negative bias voltage on the Vickers Hardness (25 g) and the normalised growing stress at a nitrogen flow rate of 200 sccm.

indicate a colour change from metallic to a pale champagne. It should also be mentioned that this rather low dependence of coating properties with increasing negative bias voltage and flow rate is very interesting for the process since it indicates a forgiving process control.

The results of the investigation of chemical composition by GDOES only partially confirms the impression of the smooth relationship of the influence of deposition parameters on the physical properties. As would be expected increases in the nitrogen flow rate lead to increases in the nitrogen content of the coating, see Table 1. However, when the change from metallic to nitride phases occurs (200 sccm) the titanium content of the coating has decreased to almost half of its original value. In fact the titanium content of the coating decreased from 60.5 at.% to 24.9 at.% when the nitrogen flow was increased from 100 to 400 sccm. This effect is hidden completely by the smooth decay in the deposition rate as shown in Fig. 2.

An examination of the chemical composition showed severe changes in the chemical composition although the overall deposition rate was affected to a lesser extent. The Ti:W ratio for the first fully nitride film decreases from 1.16:1 to 0.87:1 during the process. There was also no significant influence of either bias voltage or film thickness on the chemical composition of the coating (Table 1 and Fig. 5).

The X-ray diffraction results also confirm the metallic nature of the coating at low nitrogen flow rates (Table 1). It is also interesting to note that the high temperature body centred cubic (bcc) titanium phase formed rather than the lower temperature hexagonal phase. X-ray diffraction confirmed the change from the metallic phases at low nitrogen flow rates (100 sccm) to nitride phases at the higher nitrogen flow rates (200 sccm) and identification of the individual phases of TiN and W_2N was possible at the higher Bragg angle, see Fig. 6. A typical characteristic of reactive sputtering is the gradual increase in the lattice parameter of the metallic phases, owing to nitrogen incorporation in the

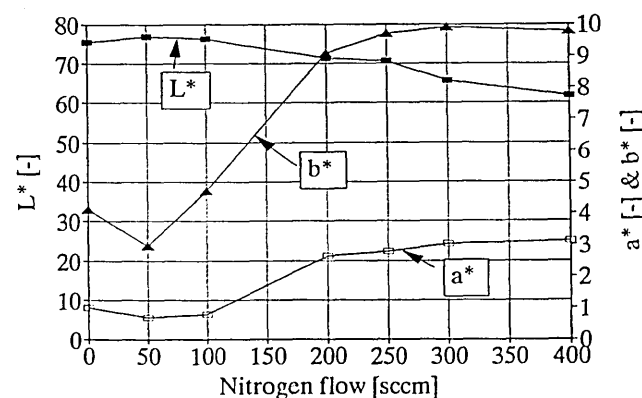


Fig. 4. The influence of the nitrogen flow rate on the colour parameters (L^* , a^* , and b^*) at a negative bias voltage of -80 V.

Table 1

Bias Voltage	N ₂ flow rate SCCM	Rotation	Composition at %			Ti W Ratio	Phases Present	Lattice Strain	Lattice Parameter A	Superlattice Spacing A
			Ti	W	N					
-80	0	3 fold 8.0 rpm	70.6	29.4	-	2.3:1	Titanium (bcc) Tungsten (bcc)	-	Ti 3.22 W 3.12	66.9
-80	50	-	65.7	28.1	6.2	2.34:1	Titanium (bcc) Tungsten (bcc) Titanium nitride (TiN)	-	Ti 3.22 W 3.14	66.9
-80	100	-	60.5	25.4	14.1	2.38:1	Titanium (bcc) Tungsten (bcc) Titanium nitride (TiN)	-	Ti 3.25 W 3.15	67.3
-80	200	-	33.4	28.7	37.9	1.16:1	Titanium nitride (TiN) Tungsten nitride (W ₂ N)	9.9 x 10 ⁻³	4.26	33.2
-80	250	-	30.5	28.8	40.7	1.06:1	Titanium nitride (TiN) Tungsten nitride (W ₂ N)	5.7 x 10 ⁻³	4.24	29.2
-80	300	-	27.5	29	43.5	0.95:1	Titanium nitride (TiN) Tungsten nitride (W ₂ N)	1.1 x 10 ⁻²	4.27	26.6
-80	400	-	24.9	28.6	46.5	0.87:1	Titanium nitride (TiN) Tungsten nitride (W ₂ N)	1.1 x 10 ⁻²	4.27	24.5
-65	200	-	29.7	29.4	40.9	1.01:1	Titanium nitride (TiN) Tungsten nitride (W ₂ N)	3.4 x 10 ⁻³	4.24	31.7
-100	200	-	29.8	30.1	40.1	0.99:1	Titanium nitride (TiN) Tungsten nitride (W ₂ N)	7.6 x 10 ⁻³	4.25	31.4
-120	200	-	29.4	30	40.6	0.98:1	Titanium nitride (TiN) Tungsten nitride (W ₂ N)	7.7 x 10 ⁻³	4.27	30.5
-80	250	1 fold 8.0 rpm	36.6	35.9	28.2	1.01:1	Titanium nitride (TiN) Tungsten nitride (W ₂ N) Titanium (bcc) Tungsten (bcc)	-	(TiW ₂)N 4.17 Ti 3.28 W 3.16	59.6
-80	250	3 fold 2.2 rpm	33.01	29.5	37.5	1.12:1	Titanium nitride (TiN) Tungsten nitride (W ₂ N) Tungsten (bcc)	-	TiN 4.23 W ₂ N 4.14	138
-80	250	1 fold 2.2 rpm	37.9	33.9	28.7	1.11:1	Titanium Nitride (TiN) Tungsten (bcc)	-	TiN 4.26 W 3.21	172

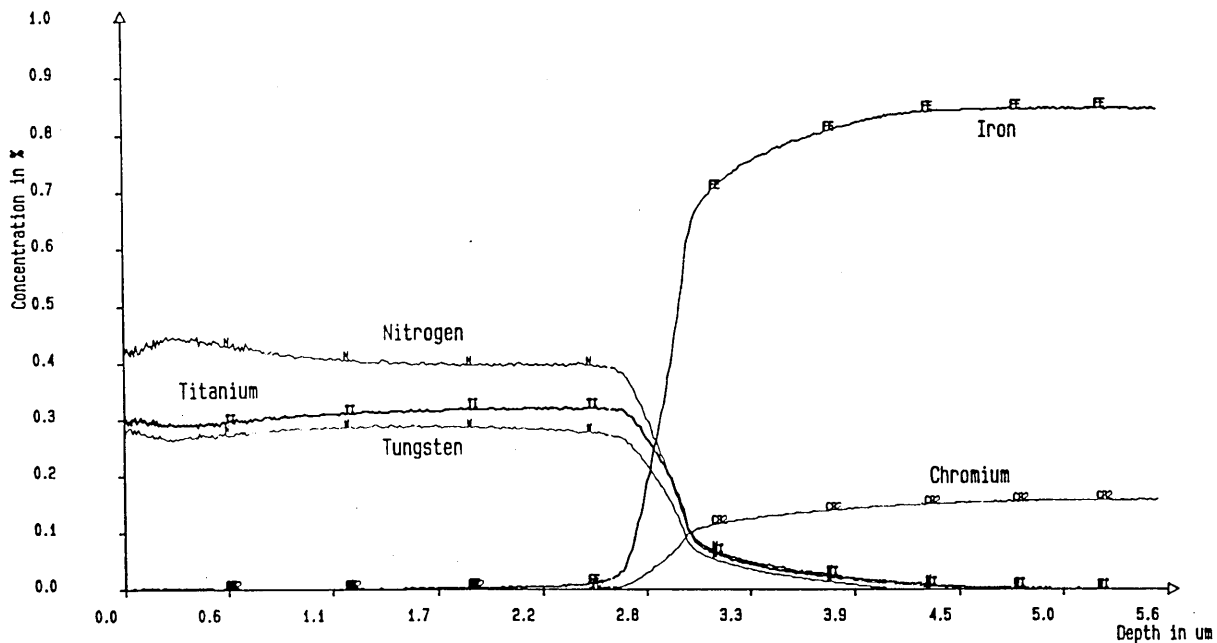


Fig. 5. Typical glow discharge optical emission spectroscopy (GDOES) depth profile from a coating deposited at a negative bias voltage of -80 V at a nitrogen flow rate of 250 sccm. Concentration in at.% $\times 100$.

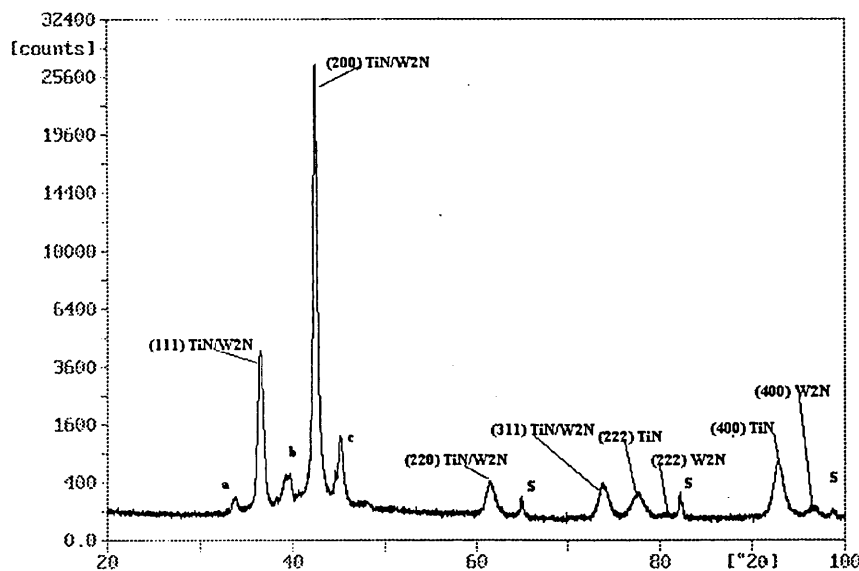


Fig. 6. X-ray diffraction trace from a coating deposited at 200 sccm nitrogen flow rate at a negative bias voltage of -65 V with 3 fold planetary rotation at 8.0 RPM rotation velocity. The small peaks marked a, b and c have been identified as satellite reflections resulting from the superlattice.

growing lattice, up to the formation of the nitride phases, see Table 1. Also the relationship between lattice parameter lattice strain, as measured by Hall–Williamson plots, and bias voltage also mirrors that of the growing stress as shown in Fig. 3 (Table 2). At this moment no explanation can be given for the decrease in lattice parameter and lattice strain at -100 and -120 V bias.

In contrast to the current theories on texture development in hard coatings [8] the (200) texture increased with increasing negative bias voltage, see Table 3.

It is shown in Fig. 1 that the specimen rotates through regimes where the deposition of either titanium or tungsten is prevalent. In order to investigate the nature of film growth the single fold rotation speed of the substrate turntable was reduced considerably from

8.0 rpm to 2.2 rpm. In Fig. 7 the X-ray diffraction traces from samples coated by single and three fold rotation are compared.

Despite the apparent uniform nature of the film, as indicated by the GDOES results, a very much different film was observed if samples were coated by single or three fold rotation. In single fold rotation a strict two phase film consisting of TiN and metallic tungsten was identified. In the TiN component of the film a (111) texture was observed with a minor (200) component, which is typically observed under deposition conditions with high bias current and low bias voltage [9]. The tungsten phase has an expanded lattice typical of a deposited film with low nitrogen incorporation. When the substrate rotation was changed from single to three fold rotation a dramatic change in the phase distribution occurs as shown in Fig. 7. The X-ray trace showed the presence of nitride phases namely (111) TiN and (111) W_2N with clear indications of (200) components of TiN and W_2N . The existence of a metallic bcc tungsten rich phase with a (110) orientation cannot be disregarded. An explanation for the appearance of mainly nitride phases in the case of three fold rotation may be given on the basis that the average deposition rate was less in the case of three fold rotation. Therefore the N:metal ratio is higher in the three fold case and under the experimental conditions the N:metal ratio in the case of the one fold rotation was already so low that the formation of metallic tungsten was allowed. As can be concluded from the analysis the titanium target must have been poisoned at a nitrogen flow rate of 250 sccm, therefore it is reasonable to assume that there exists for both cases a sufficiently high N:metal ratio to promote the formation to TiN. The probability of poisoning for

Table 2
Influence of negative bias voltage on lattice parameter and lattice strain

Bias voltage	Lattice parameter Å	Lattice strain
-65^*	4.24	3.4×10^{-3}
-80^*	4.26	9.9×10^{-3}
-100^*	4.25	7.6×10^{-3}
-120^*	4.27	7.7×10^{-3}

Table 3
The effect of bias voltage on texture development at a nitrogen flow rate of 200 sccm

Negative bias voltage	Texture parameter (hkl) reflection					
	(111)	(200)	(220)	(311)	(331)	(420)
-65	0.84	4.4	0.26	0.33	0.09	0.06
-100	0.64	5.13	0.07	0.15	0	0
-120	0.09	5.83	0.028	0.043	0	0

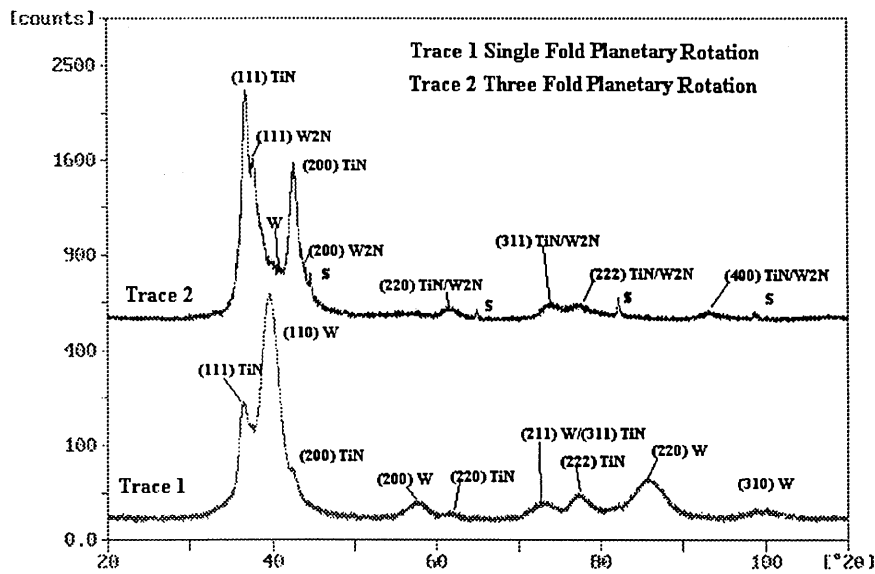


Fig. 7. X-ray diffraction traces from coatings deposited at a negative bias voltage of -80 V using 250 sccm nitrogen flow rate at 2.2 RPM rotation velocity.

the tungsten target is much less pronounced than that for the titanium target due to the well known instability of W_2N . In respect of this interpretation the presence of the (200) texture at the higher rotation velocity, Fig. 6, may be explained by the initial film growth starting with a (200) orientation [10]. This clearly leads to the conclusion that these coatings have a fine multilayered structure.

The evidence for the existence of a superlattice was confirmed by low angle X-ray diffraction, Fig. 8. This shows the presence of first and higher order diffraction peaks from a typical superlattice structure. It can also be seen that the superlattice period increased dramatically as the rotation changes from three to single fold

rotation, which is in agreement with the previously made statement on the influence of average deposition rate for the case of one and three fold rotation. All the specimens have been examined using low angle X-ray diffraction for the existence of a superlattice and the results are shown in Table 1. The dependence of the superlattice period on the nitrogen flow rate also confirms the assumption of the poisoning of the titanium target, with increasing nitrogen flow, as the spacing decreases sharply from 67.3 Å to 33.2 Å when going from a metallic to a fully nitride deposition mode. The general existence of a superlattice structure during multi-target deposition is in good agreement with data using TiN/NbN [11] and Mo/V [12] systems. Decreasing the speed of rotation

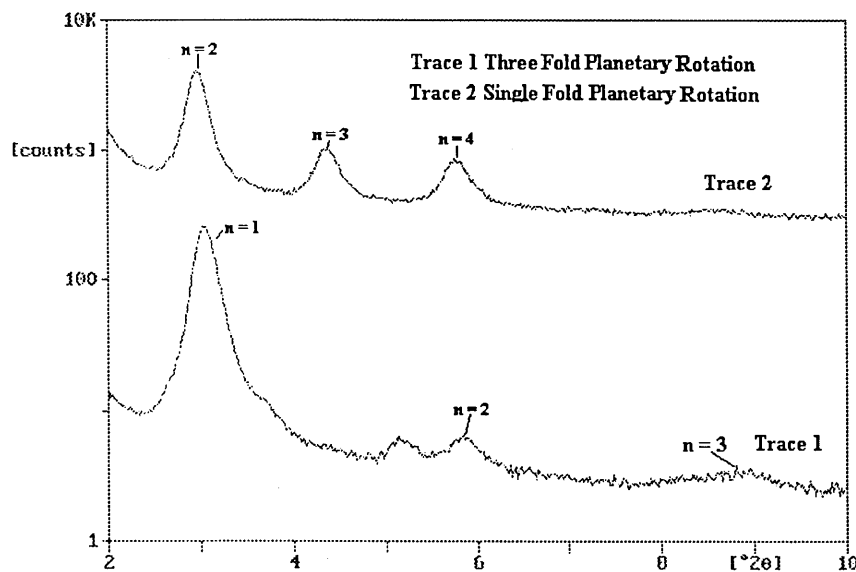


Fig. 8. Low angle X-ray diffraction traces from coatings deposited at negative bias voltage of -65 V at 8.0 RPM rotation velocity.

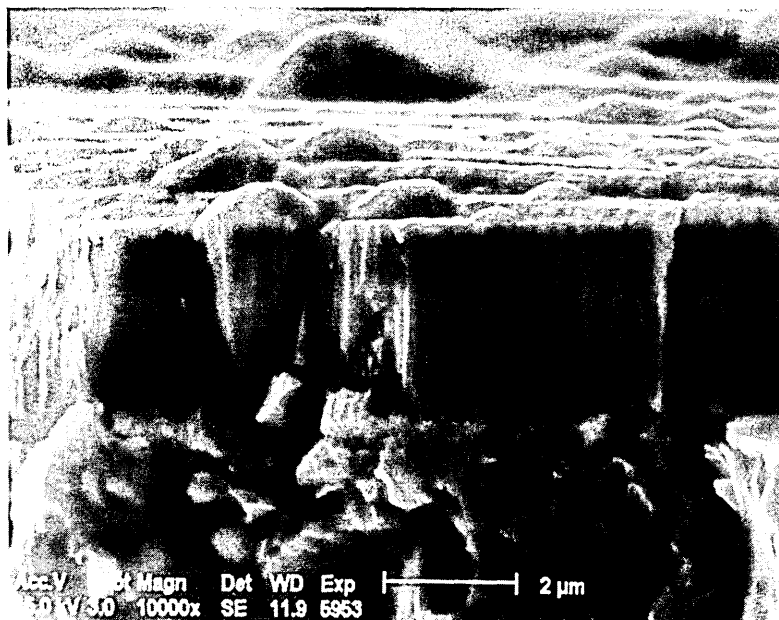


Fig. 9. A scanning electron micrograph showing a fracture cross-section from a coating deposited at -80 V bias using a nitrogen flow rate of 250 sccm.

increased the superlattice period, Table 1 and this is in good agreement with work carried out on a TiAlN/ZrN [13] where it was shown that the superlattice period could be controlled simply by the rotation speed.

A scanning electron micrograph of the coating, Fig. 9, shows a dense columnar structure with gross cone shape defects originating from droplet formation during the metal etching stage of the process [14].

4. Conclusions

(1) The low angle X-ray diffraction work clearly confirms the existence of a superlattice in TiWN coatings deposited by ABSTM using titanium and tungsten metal targets. This is in contrast to TiWN coatings prepared by cathodic arc using Ti/W alloy targets [3] where no evidence of a superlattice was found. In the latter investigation the nitride phase was identified as a TiWN solid solution whereas in the current work the nitrides were identified as separate phases TiN and W_2N .

(2) Lattice parameter measurements on TiN and W_2N individual layers indicate a TiN unit cell smaller and W_2N unit cell larger than the JCPDS standard data. This leads to the conclusion that the TiN component of the superlattice has a residual tensile stress whilst the W_2N component had a residual compressive stress. The presence of opposing residual stresses between two superlattice components was also identified in TiAlN/ZrN [13] superlattice coatings.

(3) The hardness values of the TiWN superlattice at 3000 HV were not so high as those reported for TiN/NbN [11] and TiAlN/ZrN [13] with values around 5200 HV.

(4) As a result of their low growing stress and high adhesion TiWN coatings may be suitable candidates for the production of thicker hard coatings. The very flat dependence of hardness, deposition rate and optical appearance make the TiWN an interesting system for future industrial applications.

Acknowledgements

The authors would like to express their gratitude to the following people for their generous contributions toward this publication: Mr W.v. Ijzendorp and Mr H. Willemsen, Hauzer Techno Coating Europe BV, 5900 AE Venlo, The Netherlands; Brite—Euram CoCo :BE-4118 for the financial support, and Mr T. Hudson and Dr M.R. Ives, Materials Research Institute, Sheffield Hallam University, Sheffield, UK.

References

- [1] J.H. Moser, F.Tian, O. Haller, D.B. Bergstrom, I. Petrov, J.E. Greene and C. Wiemer, *Thin Solid Films*, 253 (1994) 445.
- [2] J.M. Oparowski, D.F. Quaranta, R.R. Biederman and R.D. Sisson, Jr., in H.J. Cialoni, M.E. Blum, G.W.E. Johnson and G.F. VanderVoort (eds.), *Microstructural Science*, vol. 16, p. 379.
- [3] Company Information, O.M.T., Lübeck, Germany.
- [4] W.-D. Münz, D. Schulze and F.J.M. Hauzer, *Surf. Coat. Technol.*, 50 (1992) 169.
- [5] Verein Deutscher Ingenieure-Richtlinie 3198, Dusseldorf, Germany, 1992.
- [6] P.A. Mater, *Res. Soc. Symp. Proc.*, 130 (1989) 41.
- [7] D.B. Lewis and F.B. Pickering, *Metal. Technol.*, 10 (1981) 264.
- [8] V. Valvoda, A.J. Perry, L. Hultman, J. Musil and S. Kadlec, *Surf. Coat. Technol.*, 49 (1991) 181.

- [9] S. Kadlec, J. Musil, W.-D. Münz and V. Valvoda, *Proc. 7th Int. Conf. on Ion and Plasma Assisted Technologies*, Part 1, Geneva, Switzerland, 1989, p. 100.
- [10] S. Rickerby A.M. Jones and B.A. Bellamy, *Surf. Coat. Technol.*, 37 (1989) p. 111.
- [11] X. Chu, M.S. Wong, W.D Sproul, S.I. Rhode and S.A. Barnet, *J. Vac. Sci. Technol.*, 10 (4) (1992) p. 1604.
- [12] G. Håkansson, *PhD Dissertation No 255*, University Linköping, Sweden, 1991.
- [13] L.A. Donahue, J. Cawley, D.B.Lewis, J.S.Brooks, and W.-D. Münz, *Paper presented at the 22nd Int. Conf. on Metallurgical and Thin Films, San Diego, CA, April 24-28, 1995.*
- [14] W.-D. Münz, D.B. Lewis, S. Creasey, T. Hurkmans, T. Trinh and W. v Ijzerndorn, *Vacuum*, 46 (4) (1995), p. 323.

Comparison of TiAlN coatings grown by unbalanced magnetron and arc bond sputtering techniques

W.-D. Münz, T. Hurkmans, G. Keiren, and T. Trinh
Hauzer Techno Coating Europe B.V., P.O. Box 226, NL-5900 Venlo, The Netherlands

(Received 4 December 1992; accepted 5 June 1993)

Basic research has shown that, during the etching stage of the cathodic-arc process, metal atoms of the coating material become embedded in the surface of the substrate to be coated. If 1200-eV Ti ions are used for etching, the penetration depth may be as great as 1500 Å. Paralleling this, more recent results reveal that an unbalanced magnetron can be used to produce dense, droplet-free TiN layers in an exactly reproducible form. Hence, when the arc-mode etching process is combined with unbalanced magnetron-mode coating, the resulting coating can be expected to have excellent properties. The technical implementation of this combined technique is known as "arc bond sputtering," and is known commercially as ABS™. This article describes how the process of producing TiAl-nitride layers is used to demonstrate the advantages of metal-ion pretreatment on the adhesive strength of Ti_{0.5}Al_{0.5}N layers applied to high-speed steel and cemented-carbide substrates. The adhesive-strength criteria are the L_C and the Rockwell indentation test. The result of this study indicates that the Ti-ion pretreatment renders the measured adhesive-strength values for the subsequent films much less sensitive to uncontrolled variations of the coating-process parameters. It is also shown how the formation of TiAl droplets during the arc-based etching process can be reduced through the use of shutters.

I. INTRODUCTION

TiAl nitride films have been under investigation for several years. The first attempts to produce them made use of the conventional method of magnetron sputter deposition.¹⁻⁶ The microstructure of these films as well as their excellent oxidation resistance and mechanical properties have been thoroughly studied.⁷⁻⁹ Other deposition methods, such as cathodic arc¹⁰⁻¹³ and electron-beam ion plating,^{14,15} have come into use later.

The development of the "unbalanced magnetron"¹⁶ (UBM) began concurrently with that of TiAlN films. Surveys of this novel physical vapor deposition (PVD) coating tool and a discussion of its benefits in controlling the growth of TiN coatings were published recently.^{17,18}

A comparison of the properties of TiN coatings produced by various commercially available and industrially applied deposition methods revealed many differences in the microstructures of such films.^{19,20} Special attention was drawn to the interface composition of films deposited onto stainless steel substrates by the cathodic arc method. Ti ions diffuse into the substrate material, evidently as a consequence of the pretreatment with multiply ionized Ti atoms. A strengthening effect of the soft surface may be expected under these conditions.²⁰ These results led to the development of a combined process using the cathodic arc as an etching tool and the unbalanced magnetron as a coating tool. The process was named arc bond sputtering (ABS™).^{21,22}

In this article we compare various properties of TiAlN films deposited by the UBM and ABS™ methods in a series of 73 coating runs under conditions typical of those prevailing in laboratories and research and development (R&D) facilities. That is to say, the results were derived not only from perfect representative coating runs but also

from faulty runs characterized by, for example, unfavorable vacuum conditions, interruption of the procedure owing to a short circuit, selection of extreme, unreasonable process parameters, or improper cleaning of the coating machine or the substrates to be coated.

The aim of this study was to clarify the influence of a cathodic-arc metal-ion-vapor etch pretreatment step on the adhesion of TiAl nitride films deposited by the UBM method under extreme deposition conditions.

II. EXPERIMENTAL

All the coating experiments were performed in a single system which was described previously.^{22,23} The coating parameters are listed in Table I. A typical process sequence is outlined in Fig. 1. The targets used in these experiments, fabricated by a variety of powder metallurgical methods, were composed of 50 at. % Ti and 50 at. % Al. Some were densified by forging, others by hot isostatic pressing, with the result that their densities varied between 80% and 96% of bulk density. Consequently, different procedures were necessary for target preconditioning prior to the deposition step in order to control and minimize oxygen enrichment in the film region adjacent to the interface. The maximum power dissipation in the cathodes ranged from 4 to 7.5 W/cm², depending on the target density. With a power dissipation of 7.5 W/cm², the dynamic deposition rate was typically 2.7 μm/h. The film thickness varied between 2.0 and 6.4 μm.

The arc bond sputtering system is equipped with movable shutters which can be positioned in front of the four magnetron/arc targets when the latter are to be presputtered. They can also be used to reduce deposition of droplets, produced during the metal-vapor etching step, onto the substrates. The shutters are at floating potential at all

TABLE I. Parameter ranges used during the experiments.

		UBM	ABS™	
<i>Pump down:</i>	Pressure (mbar)	5×10^{-6} – 5×10^{-4}	5×10^{-6} – 5×10^{-4}	
<i>Heating:</i>	Temperature (°C)	200–450	200–450	
	Time (min)	30–60	30–60	
<i>Glow discharge:</i>	Bias voltage (V)	500–1000	500–1000	
	Argon pressure (mbar)	1×10^{-3} – 1×10^{-2}	1×10^{-3} – 1×10^{-2}	
	Coil current (A)	0–10	0–10	
	Source voltage (V)	100–200	100–200	
	Temperature (°C)	400–500	400–500	
	Time (min)	10	10	
<i>Ion etching</i>	Bias voltage (V)		1200	
<i>TiAl (arc):</i>	Argon pressure (mbar)	...	0.5×10^{-3}	
	Coil current (A)		0–2	
	Source current (A)		50–100	
	Temperature (°C)		400–500	
	Time (min)		10	
<i>Coating TiAlN (UBM):</i>	Source power (kW)	5–10	5–10	
	Bias voltage (V)	0–150	0–150	
	Total pressure (mbar)	2×10^{-3} – 1×10^{-2}	2×10^{-3} – 1×10^{-2}	
	Coil current (A)	5–10	5–10	
	Temperature (°C)	350–475	350–475	
	Bias curr. dens. (mA/cm ²)	0.1–5	0.1–5	
	Deposition rate (μm/h)	1.0–2.5	1.0–2.5	
	Layer thickness (μm)	2–3	2–6	
	<i>Cool down:</i>	Temperature (°C)	300	300
		Time (min)	20–120	20–120

times. In the following, the term “closed shutters” means that the shutters are shadowing the targets, while “open shutters” means that the shutters have been moved aside from the targets so that the arc and magnetron discharge is directed toward the center of the vacuum chamber without being perturbed. Samples would typically be located parallel to the axis of the vacuum chamber. The methods used to determine the films’ properties are as follows.

(1) Microhardness measurements were performed with the “Fischerscope H 100” indentation unit.^{24,25}

(2) A “Revetest” unit from centre suisse d’electronique et de microtechnique (CSEM) was used for critical-load tests.

(3) Measurements of internal stresses were obtained in standard bending tests²⁶ on circular heat-treated stainless steel samples, 0.5 mm thick, coated on one side. The stress values were normalized to a thickness value of 1 μm.

(4) The indentations from Rockwell hardness tests were examined under an optical microscope at a magnification of 100.

(5) The test method specified by Daimler Benz²⁷ was found to be very useful in determining adhesion. Its classification scheme is shown in Fig. 2.

(6) Film thickness was evaluated by the “Kalotest” method.

(7) Scanning electron microscopy (SEM) was used to examine film morphology.

(8) Values of R_a and R_z microroughness were determined with a TALYSURF 6 instrument.

(9) Film composition was measured by energy dispersive spectroscopy (EDS) techniques.

Data on film properties were evaluated from 22 runs in the UBM mode, 19 runs in the ABS™ mode with closed shutters, and 32 runs in the ABS™ mode with open shutters. All the test substrates were made of either stainless steel, high-speed steel (HSS) or cemented carbide.

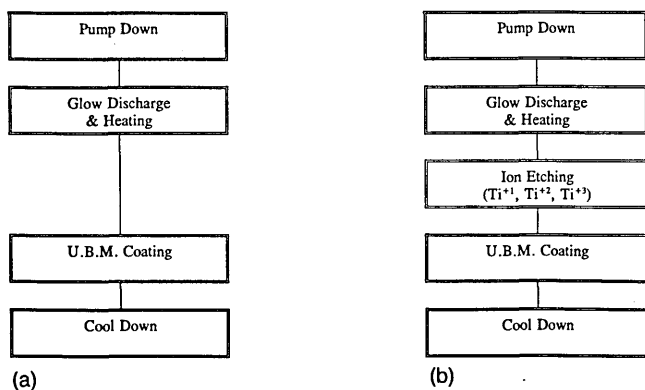


FIG. 1. Sequence of (a) UBM and (b) ABS™ processes.

III. RESULTS AND DISCUSSION

All the results of the microhardness measurements on both UBM and ABS™ coatings are compiled in Fig. 3. The most frequently observed values are in the range of $\sim 23\,500$ N/mm², which is very close to the corresponding value of $\sim 23\,000$ N/mm² found previously for films deposited by conventional magnetron sputtering.¹ The very low values seen in Fig. 3 may be attributable to incompletely dense films, while the higher values may result from defect- and stress-induced hardening effects, as suggested by the increased x-ray lattice constant and the peak broadening that are noted in such cases.⁶ It is of interest to note

Method : HRc Hardness Measurement
 Hardness of Substrate : At Least 54 HRc.
 Layer Thickness : Max. 5 μm .
 Judgement : Observe the HRc indentation with a Magnification of 100 Times.

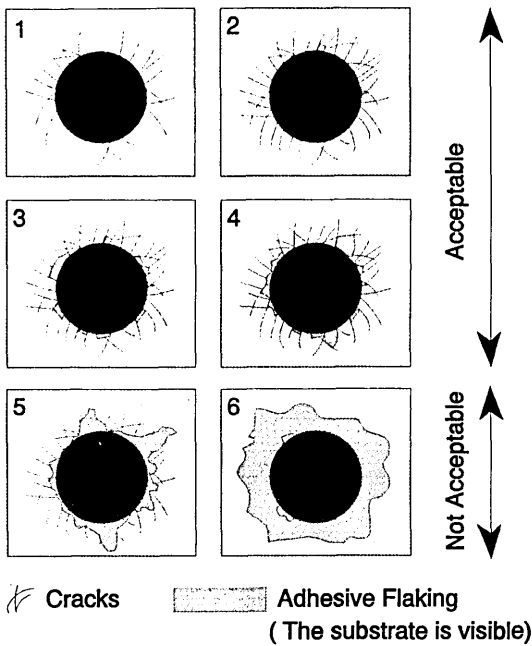


FIG. 2. Adhesion judgement of PVD layers.

that the range of most frequent values found here, i.e., around $23\,500\text{ N/mm}^2$, is far below the published values for arc-deposited films. The latter are usually above $30\,000\text{ N/mm}^2$ for 12 at. % Al films deposited by the random- and steered-arc methods¹¹ and for 50 at. % Al films deposited by the random-arc method.¹³

A statistical evaluation of the internal-stress measurements is outlined in Fig. 4. The most frequent value of the normalized stress is in the $0.4\text{ GPa}/\mu\text{m}$ range. The frequency of $1\text{ GPa}/\mu\text{m}$ values is already very low. A more detailed evaluation of the results reveals that these higher values correspond to microhardness values above $26\,000\text{ N/mm}^2$. This confirms the hypothesis that high values of microhardness are correlated with high stress levels.²⁸

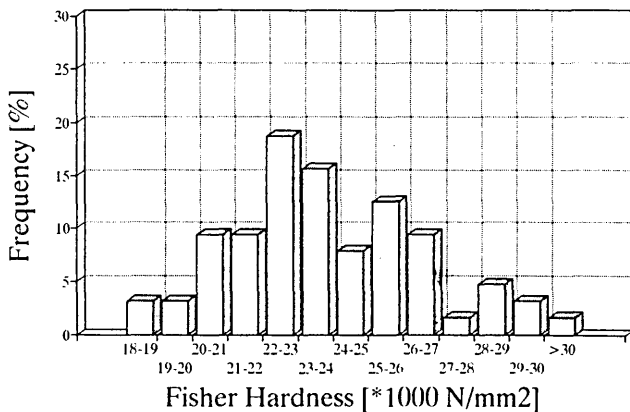


FIG. 3. Fischer hardness distribution of TiAlN coatings.

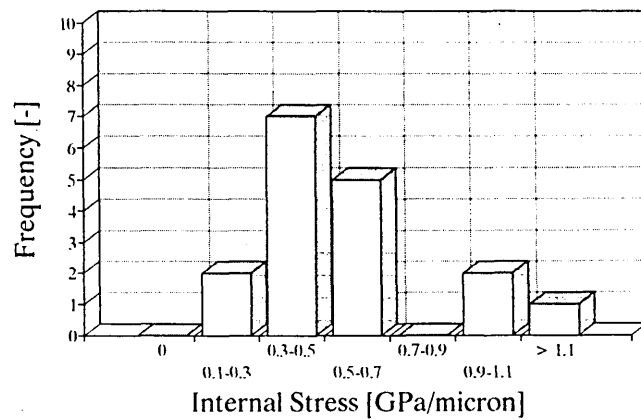


FIG. 4. Frequency distribution curve of normalized internal stress.

The results of the adhesion measurements are very interesting. Figures 5 and 6 outline the statistical evaluation of the critical-load measurements made on HSS and CC substrates. The influence of the deposition method on the measured results is clearly evident.

In Fig. 5(a) we see a rather high frequency of occurrence of low L_C values for coatings applied by the UBM method. The frequency decreases for increasing values of critical load up to the observed maximum value of 40–50 N. This trend suggests that high values of adhesion can be achieved only under a few very specific conditions for the coating parameters chosen with this method, i.e., the process appears to be highly sensitive to the deposition conditions.

Figure 5(c) reveals a rather different situation for the ABSTM case. Here the highest frequency of occurrence is observed for the same range of critical loads (40–50 N) that was found to be the maximum for UBM deposited films. While there are still low values, obviously attributable to highly defective process conditions, there are also measured L_C values extending far above the 40–50 N range. A more thorough evaluation of the results indicates that a correlation must exist between values higher than 60 N and coating thicknesses greater than $3\ \mu\text{m}$. It is well known that L_C tends to increase with film thickness. Further study is needed to determine quantitatively how much higher the maximum L_C value is for ABSTM coated samples than for UBM coated samples.

Figure 5(b) explains, that the presence of the shutter in front of the target reduces the positive influence of the metal ion bombardment. But there is still a distinct improvement to observe.

The results obtained for CC substrates complete the picture (Fig. 6). For the UBM samples we observe a wide spread of critical-load values covering a range of from 20 to 100 N, with comparable frequencies of occurrence at the low and high ends. In contrast to this fairly uniform distribution, for ABSTM coatings we observe a remarkable shift of the measured L_C values toward the high end of the scale. As was true of the coatings on HSS substrates, here too the maximum achievable values are higher for the ABSTM coatings (> 100 N) than for the UBM coatings

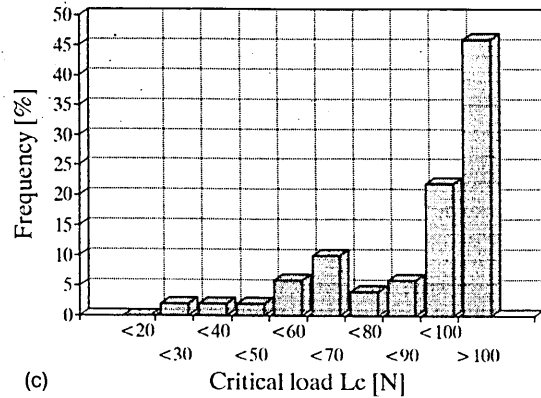
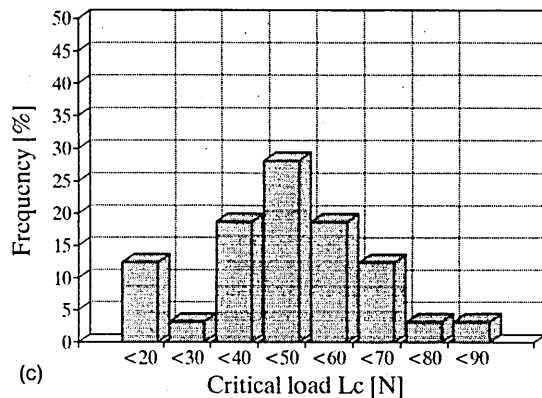
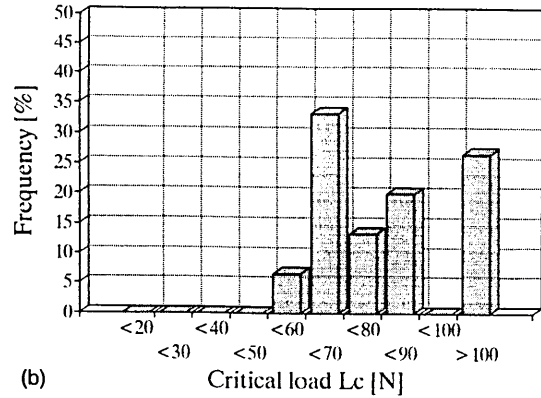
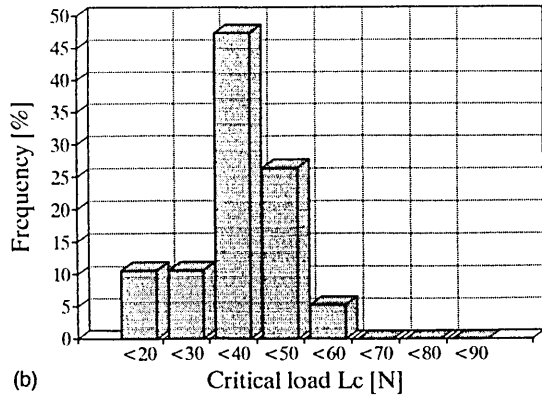
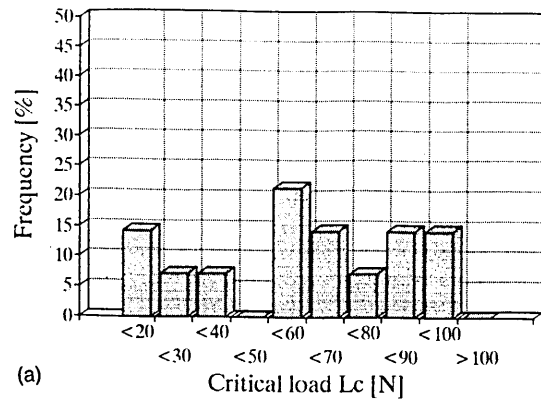
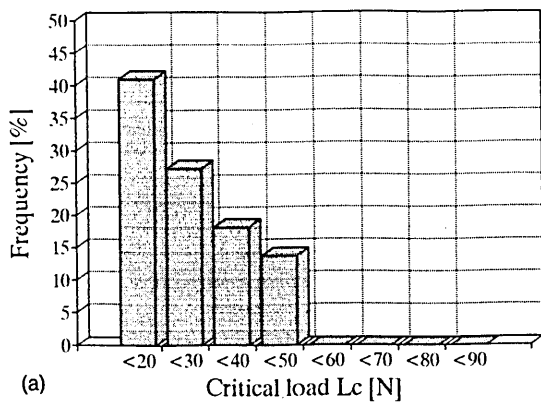


FIG. 5. Critical load L_c : TiAlN coating on HSS. (a) UBM, (b) ABS shutter closed, (c) ABS shutter open.

FIG. 6. Critical load L_c : TiAlN coating on cemented carbide. (a) UBM, (b) ABS shutter closed, (c) ABS shutter open.

(90–100 N). Unfortunately, we were unable to measure values of $L_c > 100$ N with our instrument. The ABSTM process with shutters again reduces the positive influence of the Ti ion bombardment. The dependence of L_c becomes less steep [Fig. 6(b)] than for ABSTM without shutters, but the improvement compared to the UBM case is still remarkable.

It is well known that defects may cause internal stresses in hard coatings, resulting in decreased adhesion.²⁹ Another interesting effect becomes clear when we compile the data presented above and plot L_c versus microhardness: While the UBM coated samples confirm the expectation that the critical load decreases with increasing microhardness, the same tendency could not be verified for ABSTM

coated samples with both HSS [Fig. 7(a)] and CC [Fig. 7(b)] substrates. Indeed, their L_c values seem to be completely independent of the microhardness values. This indicates that the coatings produced by the ABSTM process have a superior adhesion in which the forces generated by internal stresses are fully compensated. This result confirms the earlier hypothesis²⁰ that the adhesion of arc-deposited hard coatings such as TiN may be generally superior to that of similar coatings deposited by ion-plating techniques using electron beams or sputtering.

The results of the Rockwell indentation tests also point in the same direction. The values found for UBM coated samples exhibit a wide spread covering almost the entirety of the classification scale. Only class 1 was never reached

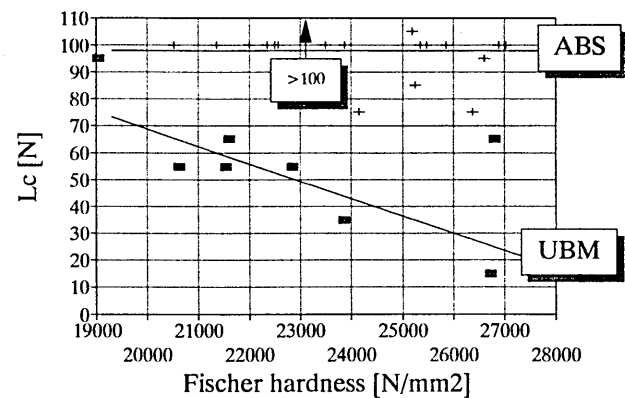
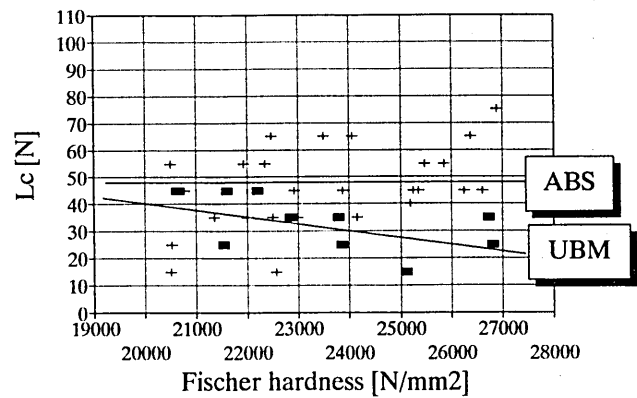
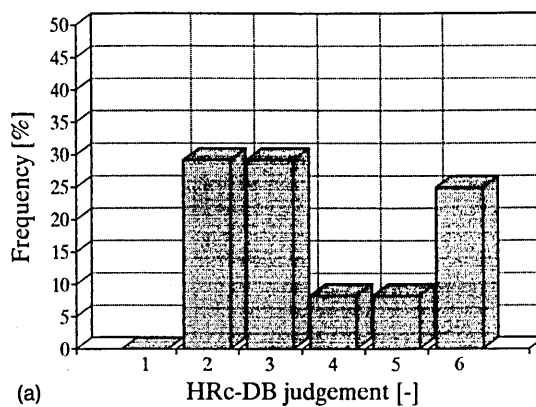


FIG. 7. Fischer hardness vs. L_c .

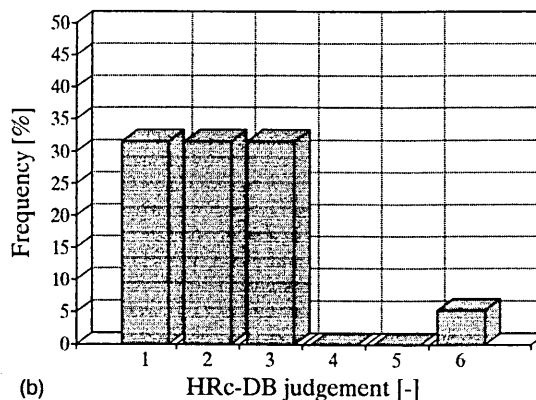
under the prevailing coating conditions [Fig. 8(a)]. In contrast to these results, the ABS™ coated samples (open shutters) display a clear trend toward the high-quality end of the classification scale, with 25% falling into class 1 and 40% into class 2. The results for ABS™ samples deposited with closed shutters are also very good. Values are again observed in class 1, but the fact that 30% of the values are in class 3 indicates that here too there is a slight tendency toward the low end of the adhesion quality scale.

The morphology of the coatings was examined in SEM cross-sectional micrographs, one of which is shown in Fig. 9. We observe a very dense, closely adhering, columnar microstructure. The same dense appearance is seen for all three types of coating, as is typical for TiAlN films deposited with a bias voltage in the range of -100 V.⁶ The UBM samples are occasionally observed to have gaps at the interface between the film and the substrate, indicative of the reduced adhesion discussed above. The cross section also reveals a single macroparticle growing from the interface all the way to the top of the surface. In general, such macroparticles are observed only in samples deposited by the ABS™ method with open shutters.

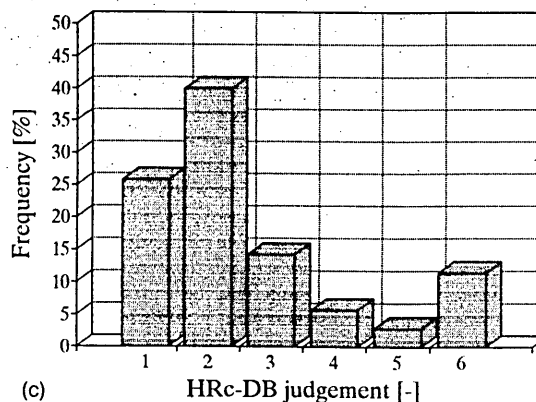
Figure 10 compares the morphologies of the three types of coating. Samples coated by the ABS™ method without shutters, in particular, exhibit a rather high concentration of macroparticles. It must be assumed that these particles originate in the metal-ion etching step. The particles or droplets are generated during the arc discharge. Hence the use of shutters is extremely important. However, it must be further optimized in order to keep the adhesion properties



(a)



(b)



(c)

FIG. 8. HRC-DB judgement: TiAlN coating on HSS. (a) UBM, (b) ABS shutter closed, (c) ABS shutter open.

to the maximum possible degree, either by prolonging the ion bombardment time or by optimizing the positions of the shutters.

As can be seen from Fig. 11, the microroughness measurements confirm the results of the SEM analyses. The R_a value of $0.05 \mu\text{m}$ for ABS™ coatings with closed shutters is only marginally higher than the value of $0.04 \mu\text{m}$ observed for UBM coatings. The microroughness values increase to $R_a=0.17 \mu\text{m}$ for samples coated by the ABS™ method without shutters. However, these values still seem very low when compared with those published for steered- and random-arc coatings. Values of R_z reported in Ref. 11 are $3 \mu\text{m}$ for steered arc and $7 \mu\text{m}$ for random arc. Additional

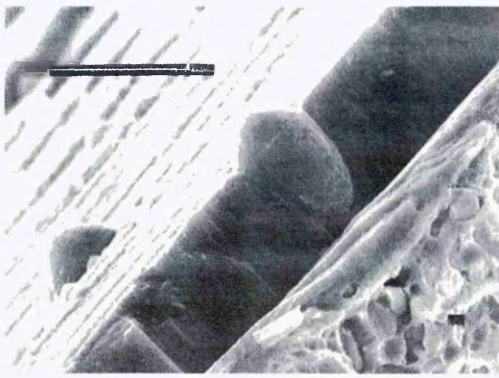
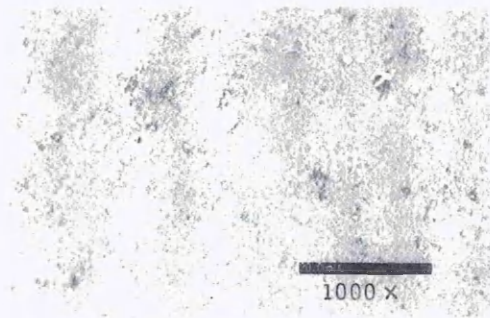


FIG. 9. SEM cross-section micrograph: dense columnar structure and macroparticle formation (shutter open).

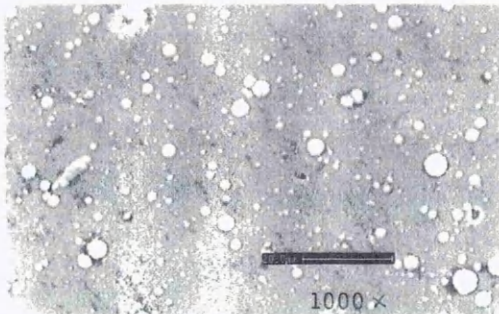
data about the roughness of arc-deposited TiAlN coatings can be found in Ref. 30. It reports a R_Z value of $4 \mu\text{m}$, although the Ti/Al ratio is not indicated. In comparison, the R_Z values evaluated in the present investigation are



(a)

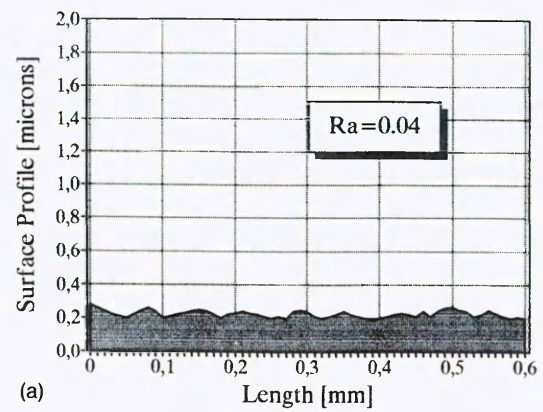


(b)

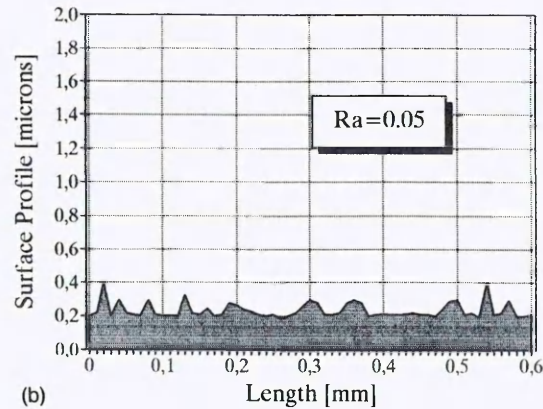


(c)

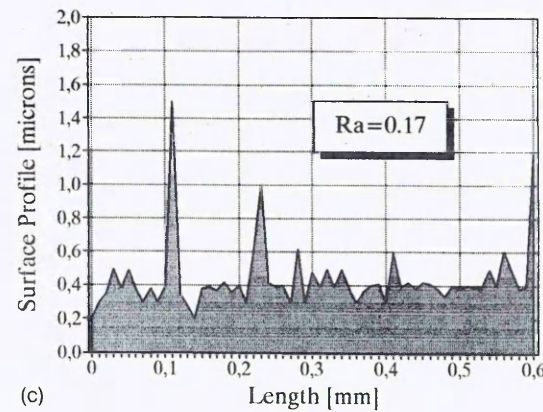
FIG. 10. SEM micrographs of TiAlN coating on HSS. (a) UBM, (b) ABS shutter closed, (c) ABS shutter open.



(a)



(b)



(c)

FIG. 11. Surface roughness of TiAlN coating on HSS. (a) UBM, (b) ABS shutter closed, (c) ABS shutter open.

$0.28 \mu\text{m}$ for UBM, $0.37 \mu\text{m}$ for ABSTM with closed shutters, and $1.14 \mu\text{m}$ for ABSTM without shutters. It must be emphasized that the values in Ref. 11 were obtained for coating with 12 at. % Al, whereas the values reported here were obtained with an alloy containing 50 at. % Al, this content being much more critical for the arc process.

The EDS analysis data yields another unexpected result. Earlier work using EDS^{6,7} and proton backscattering analyses³¹ confirmed that the atomic ratios of the main constituents of the film and target are identical. This result was derived for samples prepared by sputtering with conventional magnetrons. Under the influence of the much higher degree of ionization obtained with the unbalanced



Defects in TiN and TiAlN coatings grown by combined cathodic arc/unbalanced magnetron technology

W-D Münz, D B Lewis and S Creasey, *Materials Research Institute, Sheffield Hallam University, Pond Street, Sheffield S1 1WB, U.K.*

and

T Hurkmans, T Trinh and W v Ijzendorp, *Hauzer Techno Coating Europe bv, PO Box 226, 5900 AE Venlo, The Netherlands*

received 19 February 1994

During the cathodic arc enhanced metal ion etching process of steel substrates droplets are generated on the cathode which deposit on the substrate surface. The concentration of the droplets obviously depends upon the melting point of the target material. The number of droplets is much greater for TiAl than for Ti. The composition of the TiAl droplets also depends on their size. Large droplets tend to have the same composition as the target material, whereas smaller droplets are enriched in Ti. The adhesion of the droplets to the substrate is very poor, certainly below $L_c = 20$ N. A subsequent coating of the droplet contaminated surface with the unbalanced magnetron leads to growth defects. Nodule-like defects continue to form on the droplet itself, whereas other droplets are expelled from the coating surface during film growth, generating craters and dish-like growth defects. A simple explanation for the self-expulsion mechanism of droplets is given.

1. Introduction

The new ABSTM (Arc Bond Sputtering) PVD technique combines the cathodic arc evaporation and the unbalanced magnetron (UBM) sputter deposition methods¹. The cathodic arc discharge is used to generate a plasma consisting of multiply ionised metal atoms² which bombard the substrate surface. Under the influence of an applied voltage, typically -1200 V, these ions perform two functions: they etch the substrate surface and are also implanted into it^{1,3}. The coating procedure itself is carried out by unbalanced magnetron sputtering.

In a recent paper on TiAlN coatings grown by ABS^{TM4}, it has been pointed out that films deposited without this metal ion sputter cleaning process, exhibited a smoother surface morphology than those coatings which have undergone this *in vacuo* ion pretreatment prior to UBM coating. In the electron microscope, defects were observed in the form of 'droplets' typical of the cathodic arc deposition. Conversely, it has been clearly demonstrated in this paper⁴ that the metal ion sputter cleaning step improves the adhesion of TiAlN coatings, as measured by critical load L_c and Rockwell indentation criteria, substantially when compared to UBM coatings, where the substrates were etched *in vacuo* only with Ar⁺ ions. The increase in surface roughness could be greatly avoided if a sufficiently large shutter was used mid-way between the arc generating cathodes and the substrates, whilst still maintaining extraordinarily high adhesion values. In the case of the cathodic arc free deposition mode (only

UBM) a roughness of $R_a = 0.04$ μm was observed. With the shutter in operation, the $R_a = 0.05$ μm were evaluated. In the case of the metal ion cleaned substrates, the surface of the approximately 3 μm thick coating of TiAlN was surprisingly rough with $R_a = 0.17$ μm .

The purpose of this study was to investigate the origin of this difference in surface roughness, as UBM deposited coatings themselves should not be affected by droplet-like defects. Besides TiAlN coatings, TiN coatings have been prepared for comparison and to investigate eventual differences in the droplet formation mechanism.

2. Experimental

All the coating experiments were performed in a commercially available PVD coater HTC 1000 ABS produced by Hauzer Techno Coating Europe B.V. This machine uses four vertically mounted cathodes which can be operated either in the cathodic arc or in the unbalanced magnetron mode. The cathodes are magnetically coupled in a closed field manner, in particular by the appropriate use of strong electromagnets assembled concentrically to the cathodes.

Figure 1 shows the cathode placement and the typical closed magnetic field line distribution⁵. Figure 2 outlines, schematically, the dual purpose cathode for cathodic arc and unbalanced magnetron operation. Further details are given in Ref. (1). The pro-

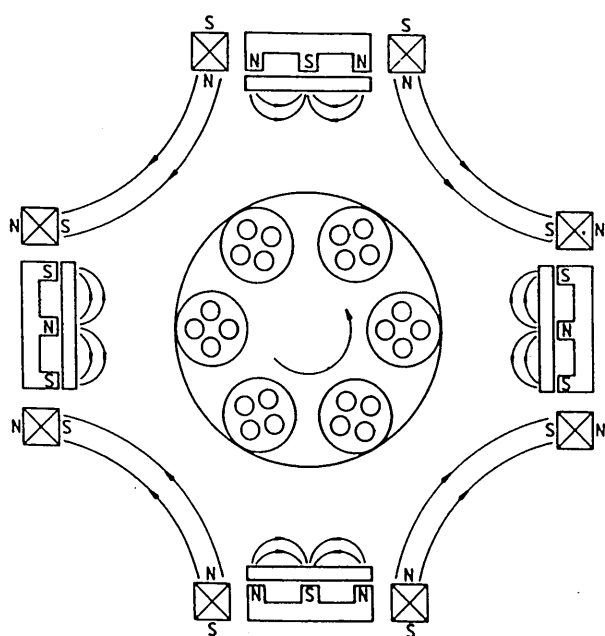


Figure 1. Cathode placement in the PVD coater HTC 1000 ABS™ with multipolar magnetic closed field.

cess sequence is outlined in Figure 3. The most important deposition parameters are summarised in Table 1.

TiAlN films were grown by reactive sputtering using powder, metallurgically prepared, hot, isostatic, pressed targets with a composition of 50 at%Ti, 50 at% Al. TiN films were prepared by reactive sputtering using vacuum cast 99.8% Ti targets. The substrates throughout these experiments were made of polished M2 high speed steel. Samples used for fracture cross-sectioning were coated on a stainless steel substrate.

The morphology of the samples was examined using either a Philips XL40 or a JEOL 840 scanning electron microscope. Droplets were subsequently analysed by energy dispersive X-ray (EDX) microanalysis.

The surface roughness was tested with a Rank Taylor Hobson Talysurf 6 instrument. The colour of the uncoated samples was

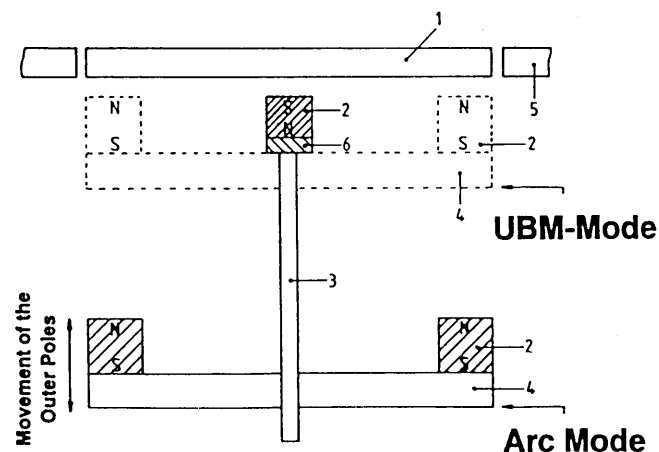


Figure 2. Schematic outline of dual purpose cathodic arc/unbalanced magnetron cathode; (1) target; (2) permanent magnets; (3) fixturing of centre poles; (4) magnetic yoke; (5) recipient; (6) magnetic neutral spacer.

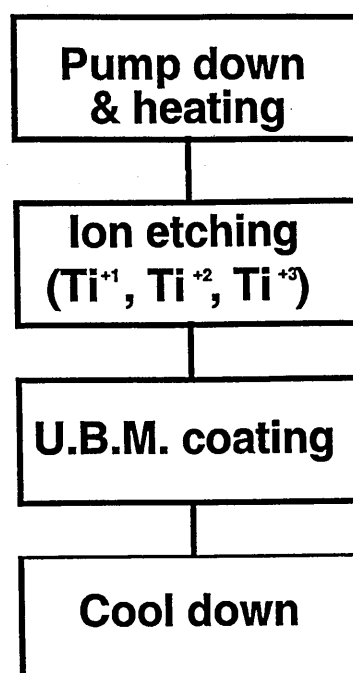


Figure 3. Process step sequence of ABS™ technology.

measured with a Minolta colorimeter in CIELAB unit (L^* , a^* , b^*). Adhesion tests were carried out using a CSEM critical load 'Revetest' instrument. The thickness of the films was evaluated by using a CSEM 'Kalotest'.

3. Results

In a first set of experiments, HSS samples were exposed to either a 5 min Ti ion etch or, alternatively, to a 5 min TiAl ion etchin

Table 1. Important process parameters

Pump down and heat		
Residual gas	mbar	2.10^{-5}
Substrate temperature	°C	300
Metal ion etching		
Pressure Ar	mbar	1.10^{-3}
Substrate bias	V	-1200
Arc current	A	200
Substrate temperature	°C	350-500
Etching time	min	5
Coating		
Total pressure	mbar	$3, 5, 10^{-3}$
Power density cathode	mW cm ⁻²	7-10
Discharge voltage cathodes	V	520
Substrate temperature	°C	450
Substrate bias	V	-75
Bias density	mW cm ⁻²	3
Coating time	h	1.5-2
Cooling		
Cooling	h	0.5-1.5

step. Figure 4 represents a secondary electron emission image of a Ti ion etched surface ($M = 250$).

The centre of the image shows the trace of a 20 N scratch test indentation. After closer examination it is clear that there is a reduction in the number of 'bright spots' inside the scratch surface compared to the outside of it. In Figure 5 a chemically cleaned surface of a HSS substrate is compared with those of Ti and the TiAl ion etched surfaces at the higher magnification of $M = 1000$. The 20 N scratch test trace covers the left part of the images and is very easily recognised by the grooves originating from the scratch stylus. There is practically no visible difference between the spot density inside and outside the scratch trace if one observes the as-chemically cleaned surface [Figure 5(a)].

However, it appears that the scratched part of the surface seems to be somewhat 'cleaner' suggesting that the stylus may have removed residues not taken away by the cleaning agent. Figure 5(b) represents the higher magnified image of Figure 4. The difference in spot density inside and outside the trace is even more difficult to recognise under these conditions. Only a careful intentional visual comparison allows the conclusion that the 'bright spot' density inside the scratch trace is lower than outside. Similarly, as with the chemically treated sample [Figure 5(a)] the trace area seems to be 'cleaner' again than the outer region. Figure 5(c) appears very different, here one observes the surface after the TiAl ion etch. It is very obvious that the trace inside is less populated by 'bright spots'. In the outside region we find many additional small spots, which cannot be found within the trace region. In general, we find a greater density of 'bright spots' outside the scratch trace when compared to the Ti ion etched samples.

Figure 6 summarises the equivalent results using elemental X-ray distribution mapping for the elements W, Al and Ti. It can be easily concluded that the majority of the 'bright spots' correlate to tungsten-rich carbide present in the HSS. Figure 6(a) is a SEM image and the corresponding X-ray mapping results show a very uniform tungsten distribution on the chemically cleaned substrate. Clearly no difference is found in the density of the 'bright spots' and the correlating tungsten signals inside and outside the scratch trace. In Figure 6(b) and Figure 6(c) the elemental mapping of Ti and Al is added, in order to analyse macroparticles

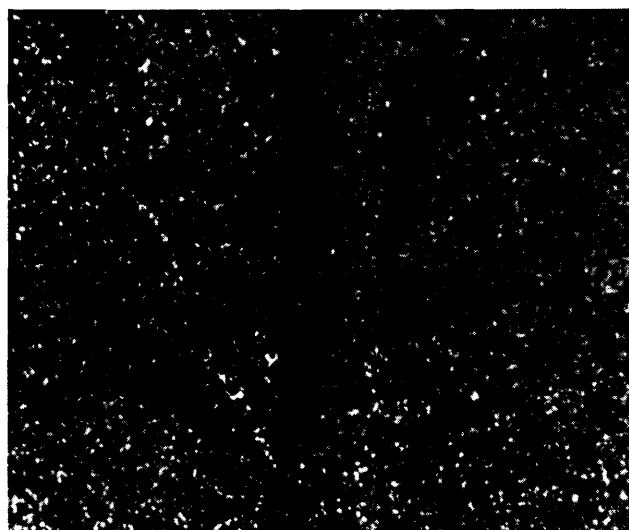


Figure 4. Secondary electron SEM image of Ti-etched sample surface ($M=250$).

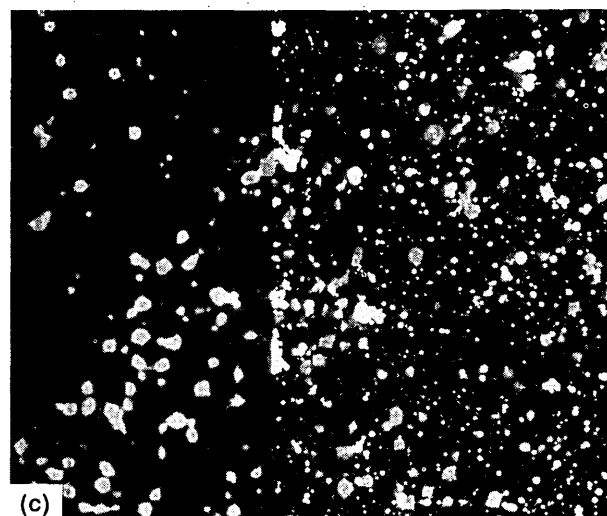
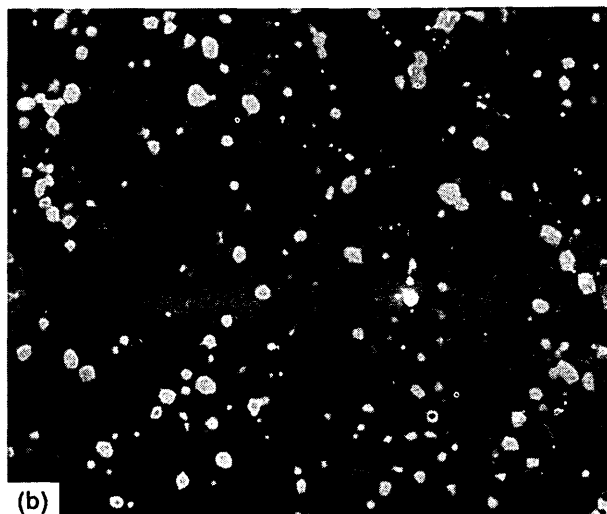
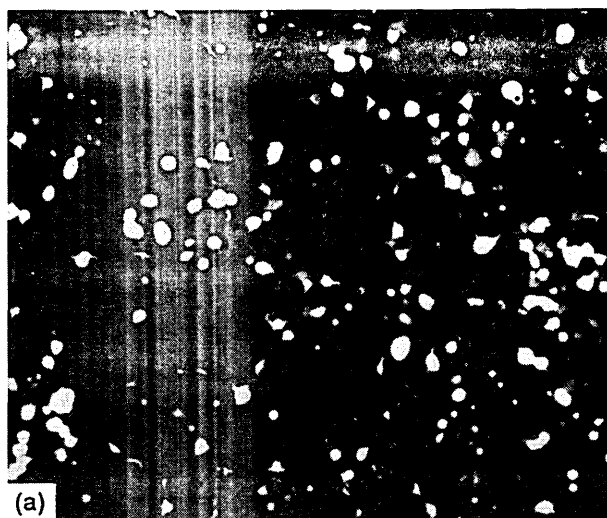


Figure 5. Secondary electron SEM image of differently pretreated sample surfaces ($M=2000$). (a) Chemically cleaned only. (b) Chemically cleaned and *in vacuo* Ti ion etched. (c) Chemically cleaned and *in vacuo* TiAl ion etched.

generated during the arc ion etching. Logically, one finds similar results for the tungsten elemental mapping, as compared to the chemically cleaned sample. The Ti and Al elemental mapping

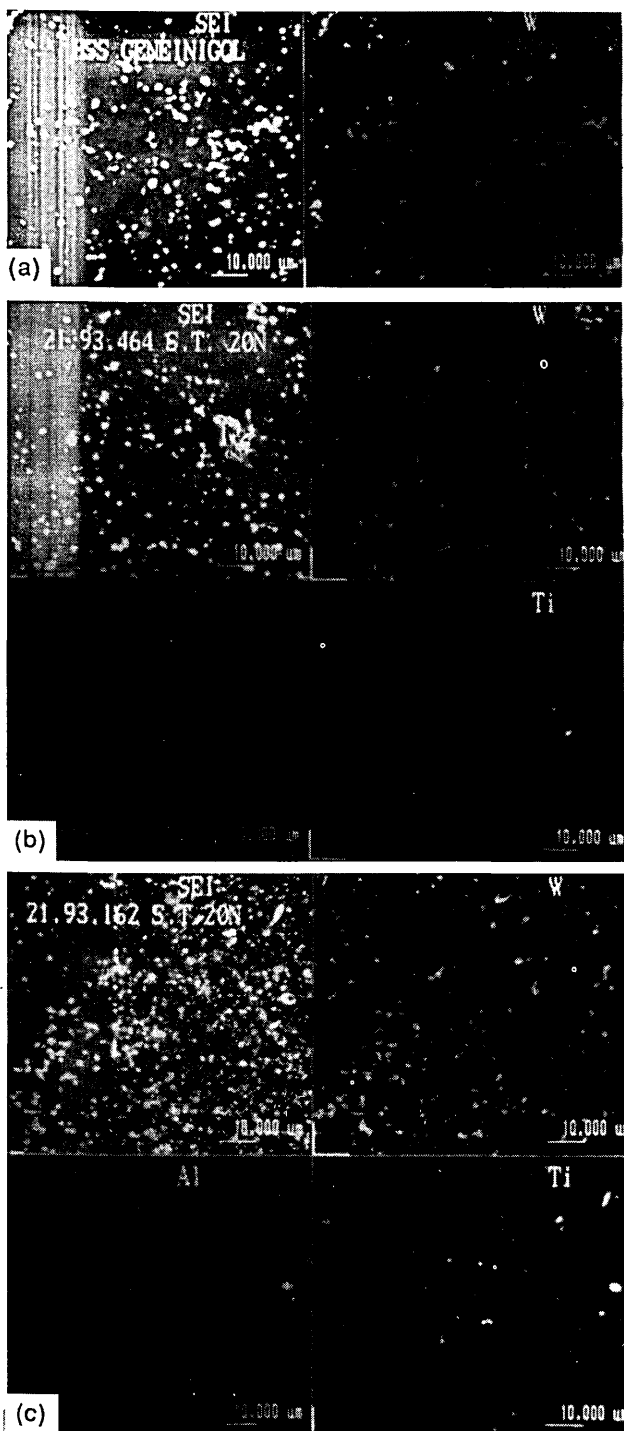


Figure 6. SEM image and EDX elemental mapping of W, Al and Ti on differently pretreated sample surfaces. (a) Chemically cleaned only. (b) Chemically cleaned and *in vacuo* Ti ion etched. (c) Chemically cleaned and *in vacuo* TiAl ion etched.

experiments, however, show (as in the case of the SEM images) quite different results. In the case of TiAl ion etching [Figure 6(c)] one recognises many signal spots in the right half of the Ti and Al mapping image, whereas in the scratch trace region, none, (except one single Ti signal) are present. One recognises also, that most of the Al signals coincide with Ti signals and that there are many more, mainly smaller, Ti signals counted than Al signals. In comparison to the TiAl ion etching case, there are

significantly fewer Ti signals present when the samples are etched with Ti ions. The density of small Ti signals is also significantly less in the specimen etched with Ti ion. Especially, the large amount of small signals is missing. There appears to be only two strong signals outside the scratch etch region, which indicates that there are really only very few droplets generated. Naturally, no Al signals were found, as no Al etching was involved.

Higher magnification images reveal that the macroparticles generated during the metal ion etching step by using the cathodic arc discharge, are strictly spherical in shape [Figure 7(a) and (c)]. This sort of defect is commonly understood as 'droplet'. During the entire investigation, only one macroparticle was found of a meteoritic impact, which is actually expected when a fluid droplet hits on the substrate surface. Figure 7(b) shows this rare object found on a Ti ion etched sample. The size of the spheres may reach up to several microns in certain cases. The average size ranges between 0.5 μm and 1.5 μm, this means that the droplets originally generated during the etching process are, in general, much smaller than the typical thickness of a hard coating, namely 3 μm. There also exist many extremely small spheres on the surface of the TiAl etched samples [Figure 7(c)]. Some of them have a diameter of only 0.05 μm. Smaller and larger spheres arrange themselves in clusters. Figure 7(c) also shows that, occasionally, one droplet sticks upon the other or that smaller spheres are covered by larger ones.

Interesting results are found by operating the SEM in the backscattering mode. In this mode of operation, elements with high atomic numbers appear bright and those with low atomic numbers appear dark to black. The very bright spots in Figure 8 represent the carbide particles in the substrate surface. The rest of the circular signals represent macroparticles or droplets characterised in varying shades of grey levels. The larger ones indicate a high Al content, since they appear darker than the smaller defects with higher Ti content. The EDX spot analysis confirmed semi-quantitatively, that the larger macroparticles had a much higher Al content than the smaller, brighter ones. In the case of the large spheres, the Al content was approximately 50 at%, practically identical with the target composition, whereas the very small spheres consist of up to 90 at% of Ti. This result satisfactorily explains the observation made in Figure 6(c), that the spot density in the case of Ti is found to be much higher than that of Al, as only Ti is present in the smaller, but more frequent, droplets.

The different pretreatments prior to coating deposition were also investigated with respect to their micro-roughness and their optical appearance. Table 2 reveals that the micro-roughness increases from the chemically cleaned case to the Ti ion etched case and, furthermore, to the TiAl ion etching pretreatment. Accordingly, the decrease of the L^* value indicates that the polished substrate loses brilliance when the surface is contaminated with droplets. The colour values for red/green a^* and blue/yellow b^* , however, are uninfluenced by the various pretreatment steps, although the enhanced b^* values of around 4 for Ti and 2.5 for TiAl pretreated samples, seem to indicate a first sign of colouration caused by oxides. Because of the higher refractive index of TiO_2 when compared to Al_2O_3 , the minor colour change is consequently more pronounced for the Ti and pretreated sample. These results therefore correspond with the SEM and EDX results.

Figure 9 and Figure 10 show SEM images of samples coated with TiN and TiAlN with a magnification of $M = 2000$ and $M = 10,000$. At the lower magnification one again observes the

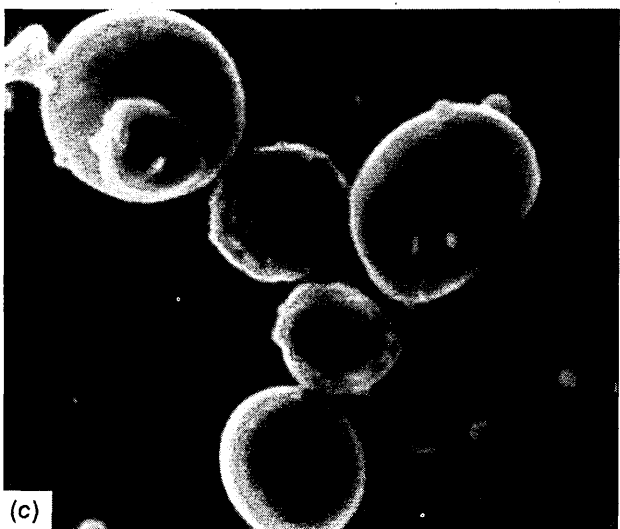
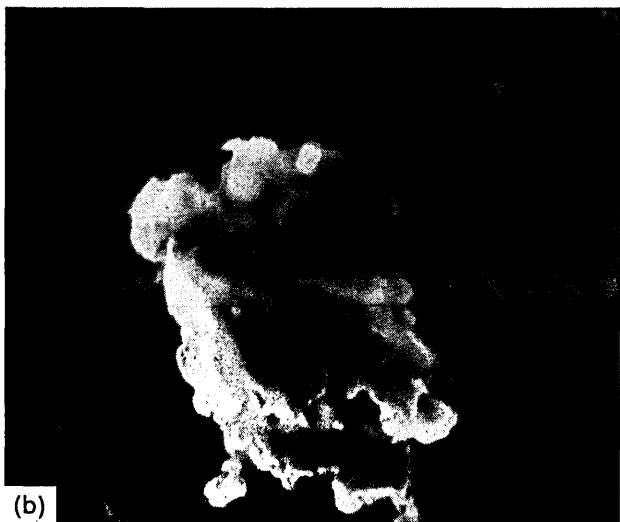


Figure 7. Various types of droplet formation ($M20000$). (a) Spherical Ti droplet. (b) Splash-like Ti droplet. (c) Cluster of TiAl droplet.

great difference in the defect density between the Ti and TiAl etched samples. The Ti ion etched and subsequently TiN coated sample, suffers apparently much less droplet deposition than do



Figure 8. Backscattered electron SEM image of TiAl ion etched surface.

the TiAl ion etched and TiAlN coated samples; but, in both cases, one finds identical defect phenomena.

There are defects in a variety of sizes, from less than $1 \mu\text{m}$ up to $5 \mu\text{m}$ diameter, and craters in similar concentrations but of larger sizes. The higher magnification gives the impression that some of the macroparticles 'sit' rather loosely bound in the film. Some of the craters appear like open dishes [Figure 10(b)].

Fracture images show that, on one hand, the craters may extend almost from the substrate up to the top surface of the coating [Figure 11(a), centre]. On the other hand, one finds defects which reach from the bottom of the coating up to the coating surface. Such defects cannot be simply designated as droplets any more.

These defects are termed as pure nodule-like growth defects. They extend with cone-shaped tops from the coating surface [Figure 11(a)]; craters or holes were found to be variable in depth; but nodule-like growth defects always extended throughout the complete film thickness [Figure 11(b)]. In general, it seems that the defects observed after coating are larger than the droplets generated during the etching process.

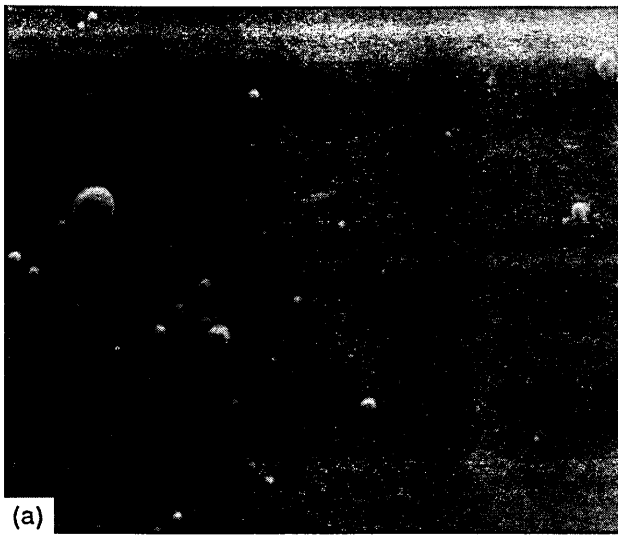
Finally, we have examined the growth defects and the dish-like craters by EDX (Figure 12). The composition of the growth defects and the inside of the craters was always identical with that of the film composition, which differed only marginally from the composition of the target, namely, 50 at% Ti, 50 at% Al.

4. Discussion

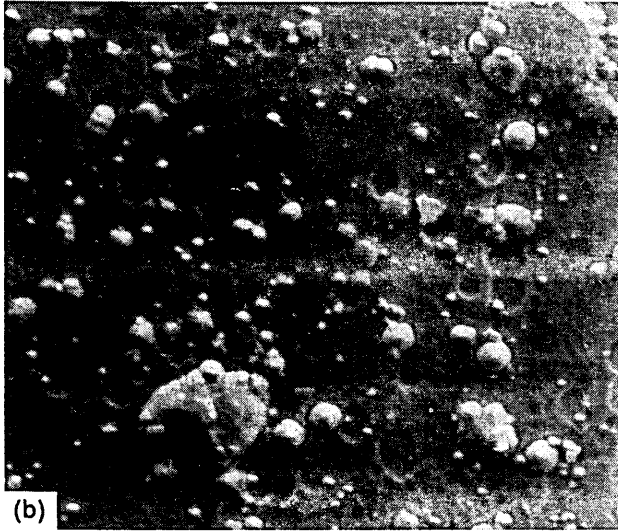
The results presented here clearly show that the origin of the unexpected high surface roughness of TiAlN coated steel samples has to be correlated directly to the metal ion etching procedure, prior to coating deposition. Obviously, depending on the melting

Table 2. Comparison of differently pretreated but uncoated samples

Sample	Ra (μm)	L^*	a^*	b^*
Chemically cleaned	0.016	82.7	0.21	0.62
Ti ion etched	0.018	79.3	0.17	7.18
TiAl ion etched	0.035	78.6	0.07	2.39



(a)



(b)

Figure 9. Secondary electron SEM image film surface ($M2000$). (a) TiN. (b) TiAlN coating.

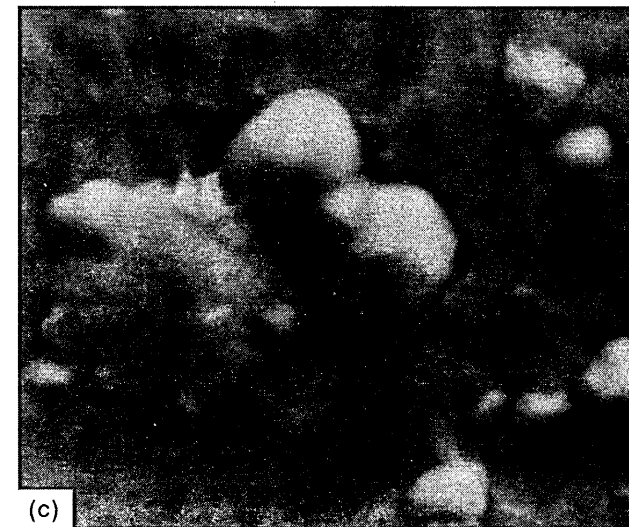
point of the target materials, 1720°C for Ti, 1450°C for the alloy TiAl and 665°C for Al⁶, droplets form under the eruptive influence of the cathodic arc discharge impinging on the target. They leave the target surface and deposit onto the substrate. Most of these droplets have an exact spherical shape, which indicates that they had already solidified before they arrived on the substrate surface (Figures 5 and 7). These findings are in good agreement with results of the excellent cross-sectional TEM study on the nature of droplet formation during the random arc evaporation of TiN⁹. Only very few droplets have a structured surface, like that droplet in the centre of the cluster in Figure 7(c) or the splash-like droplet in Figure 7(b). Here, one might conclude that the solidification process took place right on the substrate surface and that the droplet arrived in liquid phase. It is, under these circumstances, not surprising that the adhesion of the vast majority of the droplets on the uncoated surface must be rather poor. The scratch test, with a load of only 20 N, completely removes the spherical droplets. The critical load of the coating itself, either TiN or TiAlN, reveals typical values on HSS of greater than 50 N. The totally droplet-free scratch traces in Figures 4, 5 and 6 verify this conclusion.



(a)



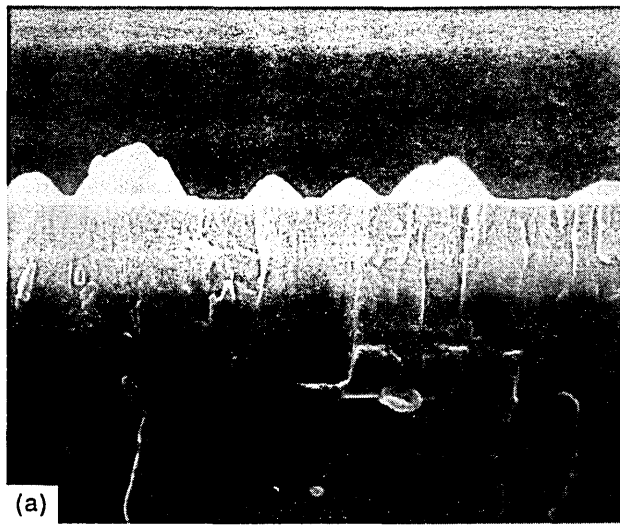
(b)



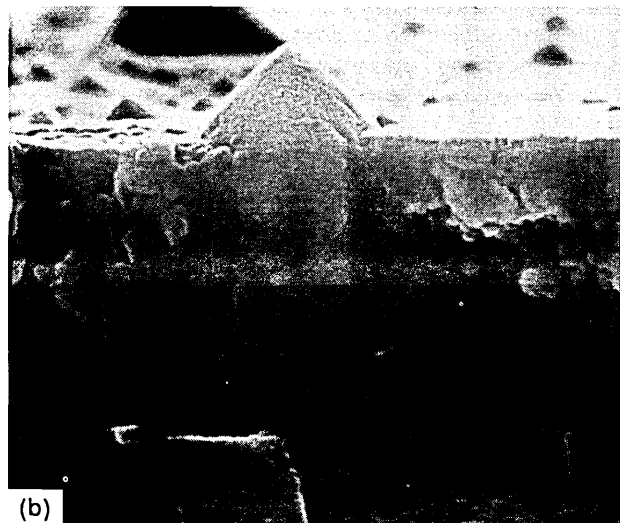
(c)

Figure 10. Various shaped growth defects ($M10000$). (a) Nodule-like defects in TiN. (b) Accumulation of dish-like growth defects in TiN. (c) Nodule-like growth defects in TiAlN.

When the cathodic arc impinges on the target surface, the and Al powder is going to melt locally and the liquid phases mi in the composition of the target. The local temperatures reporte



(a)



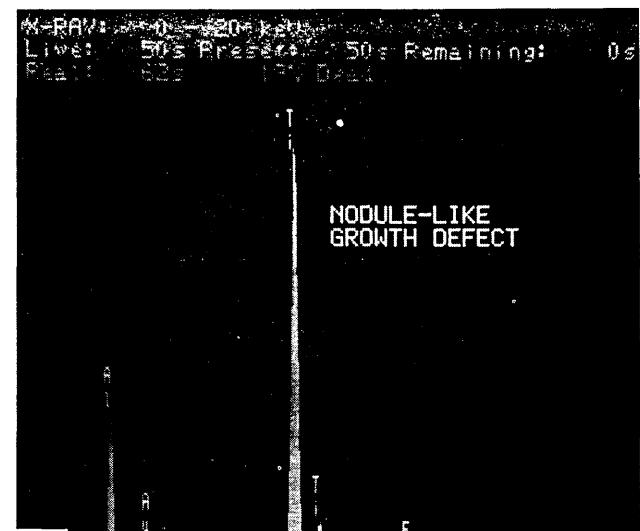
(b)

Figure 11. SEM fracture cross-section ($M10000$). (a) TiAlN with cones and craters. (b) TiN with large droplet caused growth defects.

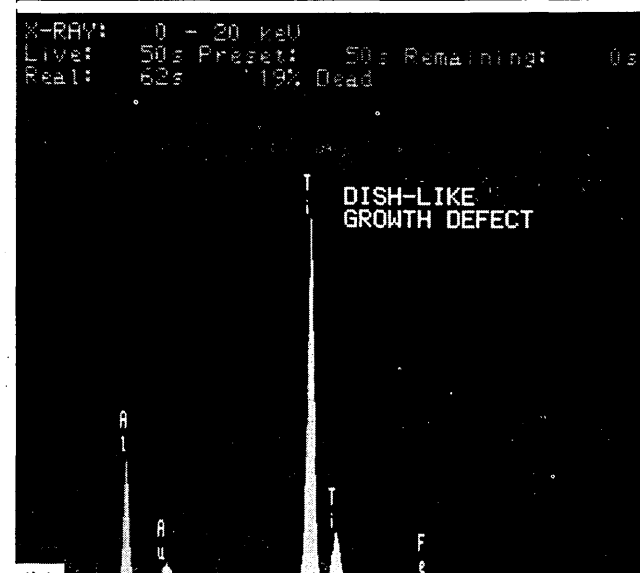
are as high as several thousand degrees⁷. For Mo, e.g., a local temperature of 7000 K is estimated⁸. It may be assumed that some of the Al and Ti is vaporised immediately and that another part of the melt is splashed towards the substrates as larger and smaller droplets. The larger spheres seem to preserve the composition of the melt, as the EDX spot analysis results showed. The smaller spheres, however, lose proportionally more of the low melting Al, presumably due to differential evaporation and their higher surface area to volume ratio. Consequently, the SEM backscattering image (Figure 8) shows the continuous gradient in the grey tone of the spherical droplets, caused by the change in concentration of the low atomic number material, Al.

The higher number of droplets produced during the TiAl ion etching procedure may be explained by the lower melting point of the liquid TiAl alloy. The expected lower viscosity of the probably superheated alloy melt may be one reason for the high amount of small sized Ti-rich droplets [Figure 6(c)] when etching with ionised TiAl vapour takes place.

The SEM images in Figures 9, 10 and 11 show that the droplets deposited during the metal ion etching step remain only partially on the substrates during film growth. However, some of them are firmly embedded within the coating and others seem to stick



(a)



(b)

Figure 12. EDX spot analysis of droplet caused growth defects. (a) Nodule shaped defects. (b) Dish shaped defect.

loosely on the substrate. In any case, the objects seen in the SEM after coating seem to be enlarged growth defects. The droplets generated during the etching step may have served as seeds for the growth of nodule-like defects which reach practically from the substrate interface to the top surface of the coating, as Figure 11(a) and (b) confirm. They enhance the surface roughness of the substrate surface after ion etching from $0.035 \mu\text{m}$ (Table 2) to $0.17 \mu\text{m}$ after coating as reported⁴ for TiAlN. This result is in contrast to very recent findings by cross-section transmission electron microscopy⁹. There, no growth defects were found in their investigations in TiN coatings originating from the substrate coating interface through the film to the coating surface, if pure random arc technology was used for metal ion etching, as well

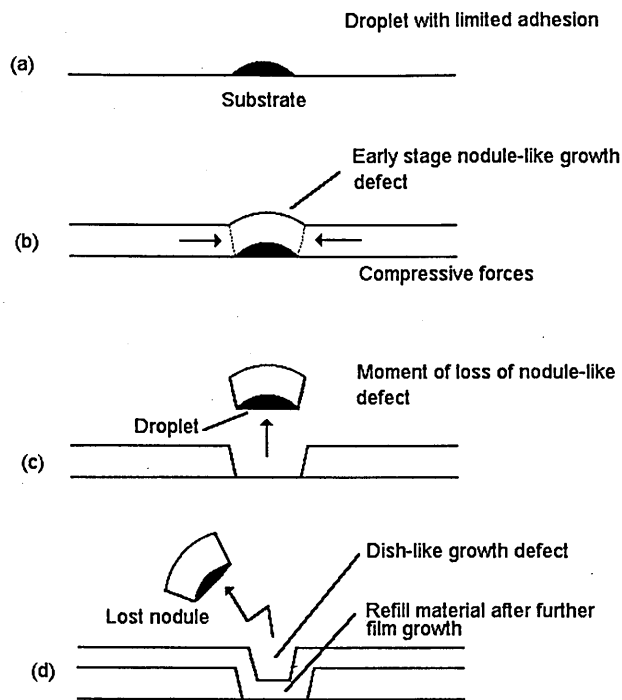


Figure 13. Schematic explanation of the self-expulsion mechanism of droplets.

as for film deposition. Only droplets were found, which were generated during the deposition phase of the film.

The craters are particularly clear, as shown in Figure 10(b). They may be related to solid droplets which have left the substrate surface during deposition. Figure 13 explains schematically a possible self-expulsion mechanism. Whether it is the increasing compressive stress of the growing coating or whether it is simply an undergrowing of the spherical droplets, the bonding strength of the droplets is in many cases not sufficient to maintain the droplet from simply being expelled out of the coating. The depth of the craters varies, obviously. EDX spot analysis showed that in the majority of the cases investigated, only the coating element, e.g. Ti, could be detected in the crater of a 3 μm thick film. The signal of the substrate material Fe was normally very weak (Figure 12); but in other cases, the Fe signal was relatively strong. This indicates that the expelling event takes place, probably shortly after the film growth is initiated. The resulting empty hole is refilled by the growing film, forming dish-like defects, as can be observed experimentally in Figure 10(b) and schematically in Figure 13. Nevertheless, it may happen that the droplets leave the substrate and the coating in a late stage of film growth. Then one has to expect rather deep holes or craters in the coating. The deep hole shown in the centre of the SEM fracture image in Figure 11(a) proves this assumption.

5. Conclusions

As mentioned previously, the investigations definitely show that the enhanced roughness of ABSTM deposited TiAlN coatings is derived from droplet deposition during the cathodic arc-generated metal ion etching process step. No specific defects could

be located which were solely caused by the unbalanced magnetron coating step. Because the growth defects observed after film deposition clearly originated from cathodic arc droplets, if one works with TiAl targets in the arc mode, the droplet formation may be reduced by magnetically steering the cathodic arc. However, this has already been the case in this study, as in the experiment carried out in the PVD coating system, HTC 1000-4 ABSTM 'Steered ArcTM', cathodes are customarily used^{1,10,11}. As an electromagnetically guided arc filtering system^{12,13} is too complicated for large scale industrial hard coating applications, the use of adjustable shutters in the coating machine seems to be the most practical method to substantially reduce the droplet formation during the etching step. This possibility has been pointed out previously^{1,4}.

However, because of the self-expulsion effect of many of the deposited droplets, the damage which may be caused by droplets is less than one may have expected solely by considering the results after the etching step. Most of the craters are 'refillable'. Practical experience has also shown that in many wear, cutting forming applications, the remaining cone-shaped growth defects which extend beyond the coating surface, are ground off to the level of the coating surface after a relatively short time of operation.

Last but not least, it should be mentioned that without shutter deposited ABSTM coatings still have an overall roughness factor lower than solely conventional random cathodic arc deposited TiAlN coatings⁴. The additional droplet deposition during the growth stage of random arc deposited coatings, as reported Ref. (9), gives an indication in the same direction.

Acknowledgement

Part of this work has been carried out within the BRIT EURAM Programme project BE-4118 'COCO'.

References

- W-D Münz, D Schulze and F J M Hauzer, *Surface Coat Technol*, 5 169 (1992).
- I G Brown and X Godediot, *IEEE Trans Plasma Science*, 19(5), 7 (1991).
- G Håkansson, L Hultman, J-E Sundgren, J E Greene and W-D Münz, *Surface Coat Technol*, 18, 51 (1991).
- W-D Münz, T Hurkmans, G Keiren and T Trinh, *J Vac Sci Technol A* 11(5), 2583 (1993).
- S Kadlec and J Musil, US Patent 5, 234, 560, Priority Date: 14 Aug 1989.
- M Hansen, *Constitution of Binary Alloys*, p 140. McGraw-Hill Book Comp Inc, New York (1958).
- G Ecker, in *Vacuum Arcs—Theory and Applications* (Edited by J Lafferty) p 229. Wiley Interscience (1980).
- H O Schrade, M Aweter-Kurtz and H L Kurtz, *IEEE Trans Plasma Science*, Vol PS-11, 103, Sept (1983).
- H Ljungerantz, L Hultman, J-E Sundgren, G Håkansson and Karlsson, *Surface Coat Technol*, 63, 123 (1994).
- S Ramalingam and C B Qi, US Patent 4, 673, 477, Priority Date: 2 March 1984.
- Ch F Morrison Jr, US Patent 4, 724, 058, Priority Date: 13 Aug 1984.
- I I Aksenov, V A Belous, V G Padalka and V M Khoroshikh, *Sov Plasma Phys*, 4, 425 (1978).
- P J Martin, R P Netherfield and T J Kinder, *Thin Solid Films*, 193/1 77 (1990).

Ion-assisted growth of $Ti_{1-x}Al_xN/Ti_{1-y}Nb_yN$ multilayers by combined cathodic-arc/magnetron-sputter deposition

I. Petrov^{a,*}, P. Losbichler^a, D. Bergstrom^a, J.E. Greene^a, W.-D. Münz^b, T. Hurkmans^c,
T. Trinh^c

^a Department of Materials Science, Coordinated Science Laboratory and Materials Research Laboratory, University of Illinois, 1101 W. Springfield Ave, Urbana, IL 61801, USA

^b Sheffield Hallam University, Pond Street, Sheffield S1 1WB, UK

^c Hauzer Techno Coating Europe S.A., Box 226, NL-5900, AE Venlo, Netherlands

Received 25 July 1996; accepted 7 November 1996

Abstract

The microstructure and microchemistry of polycrystalline $Ti_{1-x-y}Al_xNb_yN$ alloys and $Ti_{1-x}Al_xN/Ti_{1-y}Nb_yN$ multilayers grown on bcc ferritic stainless steel substrates at 450 °C by unbalanced-magnetron (UBM) sputter deposition and combined UBM/cathodic-arc (UBM/CA) deposition have been investigated using X-ray diffraction, scanning electron microscopy, Rutherford backscattering spectrometry, cross-sectional transmission electron microscopy (XTEM), and scanning transmission electron microscopy with energy-dispersive X-ray microanalyses of XTEM samples. The growth experiments were conducted in a deposition system in which the substrates are continuously rotated past one $Ti_{0.85}Nb_{0.15}$ and three $Ti_{0.50}Al_{0.50}$ cathodes, each capable of being operated independently in either UBM or CA mode. CA ion-etching of the steel substrates prior to deposition produced a polycrystalline compositionally-graded altered layer with a depth of ≈ 20 nm when operating the arc on the $Ti_{0.50}Al_{0.50}$ target and a much narrower, ≈ 6 nm, amorphous layer with the $Ti_{0.85}Nb_{0.15}$ target. Subsequent UBM or UBM/CA growth on substrates subjected to the former treatment resulted in local epitaxy with underlying grains for film thicknesses up to ≈ 200 nm before the growth front gradually broke down locally to initiate columnar deposition. Film growth on substrates CA ion-etched using the $Ti_{0.85}Nb_{0.15}$ target resulted in much smaller average column diameters with competitive grain growth. However, the fraction of the sample area covered by nodular defects arising from arc-ejected droplets was reduced by a factor of $\approx 10^2$. Thus the latter procedure was used for substrate preparation prior to multilayer growth. $Ti_{1-x}Al_xN/Ti_{1-y}Nb_yN$ multilayers with periods between 2.17 and 2.29 nm were grown by combined UBM/CA deposition. The multilayers exhibited flat, regular interfaces throughout film total thicknesses of up to 3 μm . © 1997 Elsevier Science S.A.

Keywords: Ion bombardment; Nitrides; Sputtering

1. Introduction

High-hardness transition-metal nitride films grown by physical vapor deposition (PVD) have found applications as wear-resistant layers on mechanical components such as high-speed-steel cutting tools. [1] While TiN is the primary nitride in present use, metastable NaCl-structure $Ti_{0.5}Al_{0.5}N$ alloys [2–4] which are not only hard but exhibit excellent high temperature oxidation resistance, [5,6] have also been successfully employed as coatings for high-speed tooling applications. Present materials research in this area is predominantly focused on new TiN-based alloys and multilayers. Examples of the former include

both pseudobinary ($Ti_xZr_{1-x}N$, [7,8] $Ti_xV_{1-x}N$, [9] $Ti_xNb_{1-x}N$ [10]) and pseudoternary ($Ti_{1-x-y}Al_xV_yN$ [8,11]) alloys. Following pioneering work by Helmersson et al. [12,13] on epitaxial TiN/VN superlattices exhibiting enhanced-hardness, Chu et al. [14] recently demonstrated that polycrystalline multilayer films consisting of alternating TiN (2.5 nm) and NbN (2.5 nm) layers exhibit hardnesses more than twice those of the constituent compounds.

There are four primary PVD techniques [15] presently employed for ion-assisted deposition of hard wear resistant coatings: low-voltage electron beam evaporation, triode high-voltage electron beam evaporation, cathodic-arc (CA) deposition, and unbalanced-magnetron (UBM) sputter deposition. The latter two utilize solid target sources and are

* Corresponding author.

particularly well suited for coating large three dimensional objects and for the growth of refractory materials. The combination of the two techniques offers potential synergistic advantages for multilayer alloy deposition. Magnetron sputtering eliminates the problem of droplet formation associated with arc discharges, while cathodic arc deposition provides significantly higher ion fluxes to the substrate and growing film. Arc discharges also result in a high degree of ionization (up to 90%) [16] of the vaporized material. This can be important since it has been shown that the use of Ti^+ ion-etching of steel substrates prior to nitride deposition produces a stronger film/substrate interface than obtained with the usual Ar^+ ion-etching. [15]

In this article, we report the first results on the microstructure and composition of nitride/steel interfacial regions formed with CA ion-etching using alloy targets, $Ti_{0.50}Al_{0.50}$ and $Ti_{0.85}Nb_{0.15}$ in this case. The CA ion-etched substrates are then used to grow $Ti_{1-x}Al_xN/Ti_{1-y}Nb_yN$ multilayers, with layer thicknesses controllably varied between 2.17 and 2.29 nm by combined UBM/CA deposition. The multilayers exhibit flat, regular interfaces throughout total film thicknesses of up to 3 μm .

2. Experimental procedure

The combined UBM/CA deposition system [17] is shown schematically in Fig. 1. The growth chamber contains four 19×60 cm vertically-mounted targets (two opposing pairs, each separated by 100 cm), which can function in either UBM or CA mode. The cathodes are magnetically coupled in a closed-field manner by electromagnets surrounding the targets. This allows sputtering to be carried out in a magnetically 'unbalanced' mode in

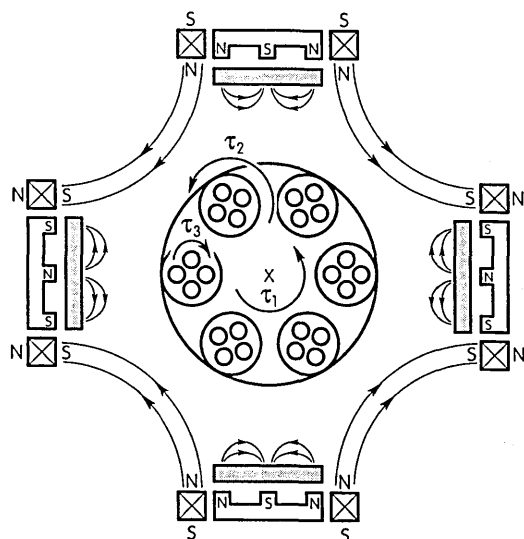


Fig. 1. Schematic diagram of the combined UBM/CA four-target deposition system used in these experiments.

order to provide higher ion currents to the substrate [18]. Three of the targets were hot-isostatically-pressed $Ti_{0.5}Al_{0.5}$ (99.9% pure) plates while the fourth was a cast $Ti_{0.85}Nb_{0.15}$ (99.9%) plate. During deposition, the substrates undergo 3-axis planetary motion at an average distance from the targets of 25 cm and a period of rotation τ_1 (see Fig. 1) with respect to a given target of 8 s. The rotational period τ_2 of individual substrate holders was 2.1 s while that of a given substrate, τ_3 , was 12.6 s in the opposite direction.

The base pressure in the deposition chamber, evacuated by two 2200 l s^{-1} turbomolecular pumps, is less than 7×10^{-6} Torr (10^{-3} Pa). Film growth was carried out in an 70:30 $Ar:N_2$ gas mixture (purity 99.999%) at a total pressure, monitored using a spinning rotor viscosity gauge, of 3.8 mTorr (0.5 Pa). After setting the Ar flow, an integrating proportional differential controller was used to regulate the N_2 flow in order to maintain the total pressure constant.

The primary substrates used in these experiments were ferritic bcc stainless-steel $5 \times 2 \times 0.08$ cm plates of composition, in at%: 83.5 Fe, 14.74 Cr, 1.08 Si, 0.36 Mn, 0.22 Ca, and 0.1 Ni. The substrates were cleaned and degreased in successive baths of hot alkali solutions (65 °C Deconex HT 107 and Banner Clean, both with $pH \approx 8.5$), an acidic solution (Borer HT07, $pH \approx 3$), de-ionized water, and acetone and then dried in hot air before mounting in the substrate holder.

A typical deposition sequence consisted of substrate heating and degassing, target sputter-cleaning, cathodic-arc substrate etching, and film deposition. Substrate temperatures T_s were measured using a chromel-alumel thermocouple attached to the surface of a dummy substrate. Reported T_s values are accurate to within ± 10 °C. During the radiant heating step, T_s was raised to ≈ 400 °C and then increased further to ≈ 450 °C during substrate etching and film deposition. Cathodic-arc etching was carried out for 20 min in Ar at a pressure of 3 mTorr (0.4 Pa) with an arc current and voltage of 100 A and 60 V. The negative substrate potential V_s during etching was 1200 V providing an average current density J_s of $\approx 0.2 \text{ mA cm}^{-2}$ ($1.25 \times 10^{15} \text{ cm}^{-2} \text{ s}^{-1}$). J_s was measured in separate runs by substituting the planetary substrate holder for a cylindrical probe with the same diameter and height.

In an initial set of experiments, film/substrate interfacial microstructures and microchemistries were investigated after substrate CA ion-etching, carried out using either $Ti_{0.50}Al_{0.50}$ or $Ti_{0.85}Nb_{0.15}$ targets, followed by UBM deposition of $Ti_{1-x-y}Al_xNb_yN$ alloy films. Based upon these results, substrate preparation for all $Ti_{1-x}Al_xN/Ti_{1-y}Nb_yN$ multilayer deposition experiments was performed using the $Ti_{0.85}Nb_{0.15}$ target for CA etching. The multilayers were grown by combined UBM/CA deposition in which the three $Ti_{0.50}Al_{0.50}$ targets were operated in the unbalanced magnetron sputter deposition mode while the $Ti_{0.85}Nb_{0.15}$ target was operated

in the arc mode. Total film thicknesses were typically 3 μm .

The negative bias V_s on the substrates during alloy and multilayer film growth was always 80 V. For UBM alloy film growth, the current density J_s at the substrate was $\approx 1 \text{ mA cm}^{-2}$ ($6.25 \times 10^{15} \text{ cm}^{-2} \text{ s}^{-1}$) with a deposition rate $R \approx 1 \mu\text{m h}^{-1}$. This yielded an ion/metal flux ratio of ≈ 4 since essentially all ions ($> 99\%$) [19] in magnetron discharges are singly charged. The majority of the ions impinging upon the growing film experience the full potential since the mean-free path for charge-exchange collisions, 16 mm, [20] is more than an order of magnitude larger than the substrate sheath width, estimated from the Child-Langmuir equation [21] to be $\approx 1 \text{ mm}$. Thus, the average energy of the ions incident on the substrate in UBM experiments was $\approx 80 \text{ eV}$.

In the combined UBM/CA deposition mode, where there is a significant fraction of metal ions in addition to Ar ions, J_s increased to 1.6–2 mA cm^{-2} as the arc current I_{arc} was varied between 70 and 150 A. R ranged from $\approx 1 \mu\text{m h}^{-1}$ with $I_{\text{arc}} = 70 \text{ A}$ to $\approx 1.1 \mu\text{m h}^{-1}$ with $I_{\text{arc}} = 150 \text{ A}$. The average ion charge in reactive arc deposition of TiN has been measured to be approximately 2 [22]. If we assume that the increased substrate current density associated with the addition of the arc results from doubly charged ions, the ion/metal flux ratios during UBM/CA multilayer growth were ≈ 5 with $I_{\text{arc}} = 70 \text{ A}$ and ≈ 6 with $I_{\text{arc}} = 150 \text{ A}$ while the average ion energies were ≈ 110 and 120 eV , respectively.

Surface morphologies of as-deposited samples were examined using a Hitachi S-800 high-resolution scanning electron microscope (SEM) while microstructures and phase compositions of films and film/substrate interfaces were determined using a combination of X-ray diffraction (XRD) and cross-sectional transmission electron microscopy (XTEM). The XRD system was operated with Cu-K α radiation and equipped with a double-crystal spectrometer to provide a resolution of $0.01^\circ 2\theta$. XTEM samples were prepared using a diamond saw to obtain $20 \times 0.3 \text{ mm}$ slabs which were further thinned to $20 \mu\text{m}$ by grinding with SiC and polishing with $0.3 \mu\text{m}$ alumina lapping film. The samples were then mounted on a Cu slot grid using carbon dag and Ar $^+$ ion milled to electron transparency by etching the sample from the substrate side while rocking the ion beams $\pm 70^\circ$ with respect to the film normal. The incident beam angle, initially 10° , was progressively reduced to 6° in the final stages of thinning. TEM observations were carried out using a Philips 400 microscope operated at 120 kV.

Average compositions of alloy and multilayer films were determined by Rutherford backscattering spectroscopy (RBS). The 1-mm-diameter probe beam consisted of 2 MeV He $^+$ ions incident normal to the substrate surface and the detector was set at a 150° scattering angle. The data were analyzed using the RUMP simulation program [23]. Cation depth distributions were investigated

using energy-dispersive X-ray (EDX) analyses of XTEM samples in a Vacuum Generators HB5 scanning TEM (STEM) equipped with a field-emission source and operated at 100 kV. Samples were traversed with respect to a stationary electron beam focused to a diameter of $\approx 1 \text{ nm}$, and X-ray spectra were collected at a take-off angle of 40° . Corrections for atomic number were carried out using the MAGIC-V computer code; [24] however, due to the thickness of the XTEM samples, $< 50 \text{ nm}$, corrections for absorption and fluorescence were insignificant.

3. Results and discussion

3.1. Substrate preparation by cathodic-arc ion-etching

Ti $_{0.50}$ Al $_{0.50}$ and Ti $_{0.85}$ Nb $_{0.15}$ were investigated as target materials for substrate preparation by CA ion-etching. The experiments were carried out in Ar at 3 mTorr (0.4 Pa) with $I_{\text{arc}} = 100 \text{ A}$, $V_{\text{arc}} = 60 \text{ V}$, and $V_s = 1200 \text{ V}$ for 20 min followed by the deposition of a 3- μm -thick UBM film in which each of the three Ti $_{0.50}$ Al $_{0.50}$ targets was operated at 8 kW and the Ti $_{0.85}$ Nb $_{0.15}$ target was operated at 0.5 kW. RBS measurements showed that the average film composition obtained under these conditions was Ti $_{0.501}$ Al $_{0.498}$ Nb $_{0.001}$ N. The films were slightly overstoichiometric with measured N/(Ti + Al + Nb) ratios of 1.05 ± 0.05 and were found to contain $1.5 \pm 0.5 \text{ at\% Ar}$. XRD patterns showed that the films crystallized in a single phase B1-NaCl structure, with all diffraction peaks indexed, as discussed below in Section 3.2. Based upon RBS, XTEM and XRD analyses, the films were homogeneous alloys with no evidence of either multilayer structure or phase separation.¹

3.1.1. Macroparticle generation

A critical issue, which has to be addressed whenever cathodic arcs are used for substrate etching or film deposition, is the formation of macroparticles [25]. Fig. 2 shows SEM images from the top surfaces of Ti $_{0.501}$ Al $_{0.498}$ Nb $_{0.001}$ N alloys deposited on steel substrates following Ti $_{0.50}$ Al $_{0.50}$ (Fig. 2(a)) and Ti $_{0.85}$ Nb $_{0.15}$ (Fig. 2(b)) CA ion-etching. The bright contrast regions correspond to the rounded tops of nodules grown on droplets deposited on the substrate surface during the CA-etch process. Occasionally, the nodules, including the initial droplet, detach leaving a hole in the film. Examples are indicated by arrows in the SEM micrograph in Fig. 2(a).

The average diameter $\langle d \rangle$ and number density N_s of nodular defects resulting from CA ion-etching using the lower melting-point Ti $_{0.5}$ Al $_{0.5}$ target ($T_m = 1472 \text{ }^\circ\text{C}$ [26])

¹ While TiN and NbN crystallize in the cubic B1-NaCl structure, AlN equilibrium structure is hexagonal wurtzite structure.

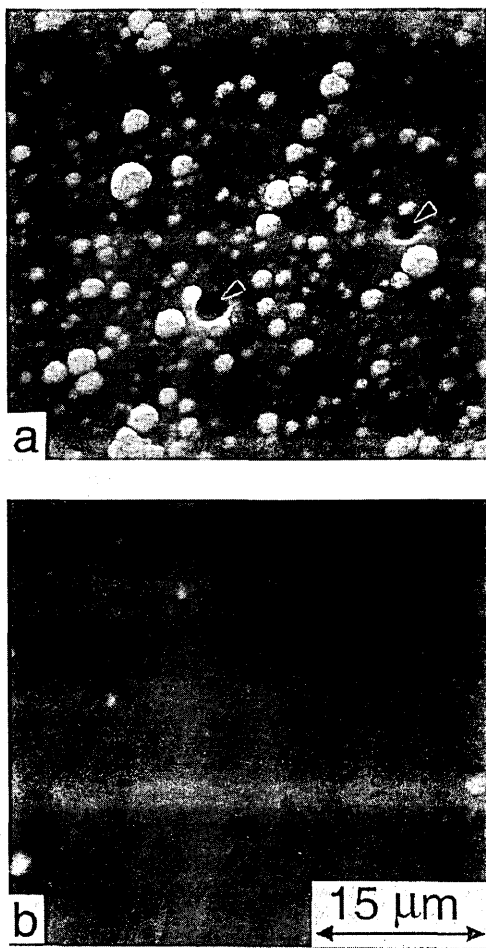


Fig. 2. SEM images from the top surfaces of 3 μm thick $\text{Ti}_{0.501}\text{Al}_{0.498}\text{Nb}_{0.001}\text{N}$ alloy films deposited on ferritic steel substrates at 450 $^{\circ}\text{C}$ following (a) $\text{Ti}_{0.50}\text{Al}_{0.50}$ and (b) $\text{Ti}_{0.85}\text{Nb}_{0.15}$ CA ion-etching.

are clearly very much larger than obtained with the $\text{Ti}_{0.85}\text{Nb}_{0.15}$ ($T_m \approx 1765$ $^{\circ}\text{C}$ [26]) target. Analyses of SEM images, using NIH image processing software [27], of $\text{Ti}_{0.5}\text{Al}_{0.5}$ -etched samples yielded $\langle d \rangle \approx 1.0$ μm with $N_s \approx 3 \times 10^7$ cm^{-2} . Thus the fraction of the sample surface area covered by nodules was ≈ 0.24 . The use of the higher melting point $\text{Ti}_{0.85}\text{Nb}_{0.15}$ target greatly decreased the rate of macroparticle generation to yield $N_s \approx 8 \times 10^5$ cm^{-2} with $\langle d \rangle \approx 0.6$ μm corresponding to a fractional film surface area coverage of less than 0.0022.

XTEM images in Fig. 3(a) illustrate the microstructure of the macroparticles and nodular defects obtained from samples in which the substrates were CA ion-etched with the $\text{Ti}_{0.50}\text{Al}_{0.50}$ target. The micrograph is a composite obtained after different stages of ion milling in order to view the entire cross-sectional thickness of the film. The high-resolution XTEM micrograph in Fig. 3(b) (from a multilayer grown by the combined UBM/CA process discussed below) shows the microstructure around the droplet in more detail. In both figures, the droplets are outlined with arrows.

The micrographs in Fig. 3 reveal that the material deposited on the droplets forms discrete nodular defects distinct in structure from the bulk of the film. The evolu-

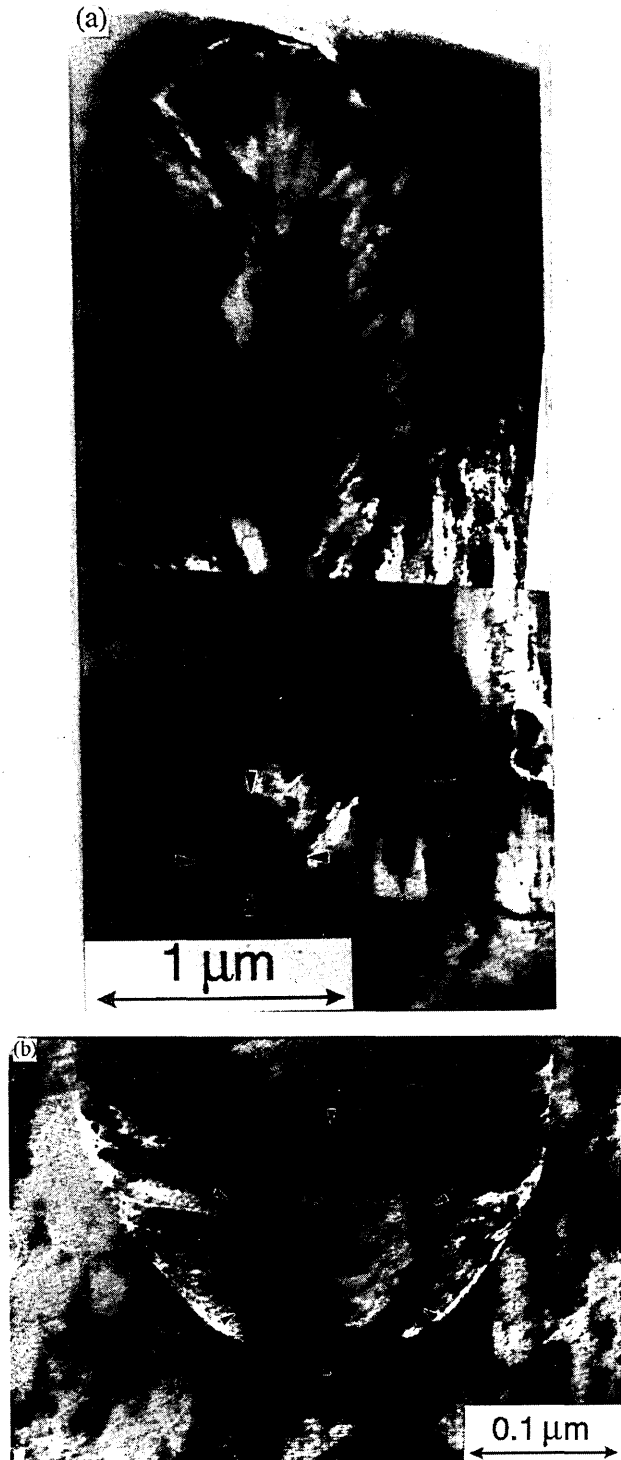


Fig. 3. Bright-field XTEM images of nodular defects: (a) from UBM-deposited samples in which the substrates were CA ion-etched with the $\text{Ti}_{0.50}\text{Al}_{0.50}$ target (the micrograph is a composite obtained after different stages of ion milling in order to view the entire cross-sectional thickness of the film) and (b) higher magnification micrograph from a multilayer grown by the combined UBM/CA process. In both figures, the droplets are outlined with arrows.

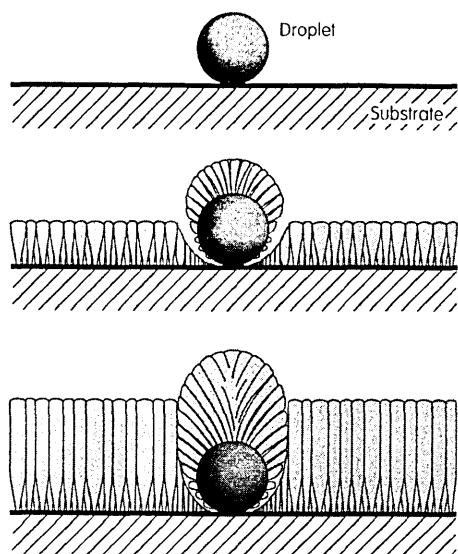


Fig. 4. Schematic illustration of the formation of a nodular defect overgrowing an arc-induced macroparticle.

tion of this structure is shown schematically in Fig. 4. The boundary between the defective and bulk film regions appears in cross-section to have a parabolic shape with a radius of curvature near the vertex approximately equal to the diameter of the original droplet. The microstructure of the nodule near the lower part of the droplet is severely underdense while the portion of the film grown on top of the droplet is composed of dense columnar grains extending outward nearly perpendicular to the local growth surface in a feather-like pattern. The final height of the nodule above the surrounding film surface is approximately equal to the diameter of the droplet indicating that the deposition rate on top of the droplet does not differ significantly from that on the surrounding flat surface. Atomic shadowing results in the formation of a voided boundary region between the nodule and the unperturbed area of the coating as shown in Figs. 3 and 4.

The dramatic differences in the observed microstructures of the film regions growing near the upper and lower edges of droplets provide significant insights regarding mechanisms associated with ion-irradiation-induced microstructural modification. The dense film on top of the droplets grows under more intense ion irradiation and is deposited at higher rates. In contrast, material deposited near the lower part of the droplet is subjected to negligible ion-irradiation and is deposited at much lower rates due to the smaller acceptance angle. Note that the latter effect, by itself, would be expected to result in a denser structure rather than the more open microstructure observed. The plasma sheath thickness at the substrate is estimated from Child's law [21] to be of the order of a mm, approximately 10^3 to 10^4 times larger than the droplet diameter and an order of magnitude larger than ion mean free paths. Thus, the shape of the plasma boundary is not strongly influenced by the presence of the droplet and ions will primar-

ily arrive at the film surface, after collisionless transport through the sheath, following paths orthogonal to the original substrate surface. The ion flux, as well as the deposition flux, in the lower regions of the droplet is therefore greatly attenuated due to shadowing by the droplet.

The differences in the microstructure of the film regions growing near the upper and lower edges of the droplets provide evidence that ion-induced microstructural changes are localized in the near-surface region, much shallower than the droplet size. The primary mechanisms giving rise to densification are forward sputtering and recoil effects which eliminate stochastically formed protrusions giving rise to atomic shadowing and the collective lattice relaxation which occurs throughout the volume of each collision cascade [28].

3.1.2. Microstructure and microchemistry of the film/substrate interfacial region

Fig. 5 shows XTEM images and selected-area electron diffraction (SAED) patterns of the film/substrate interfacial region formed by $\text{Ti}_{0.5}\text{Al}_{0.5}$ CA ion-etching followed by UBM sputter deposition. The lower magnification micrograph in Fig. 5(a) reveals that the film adjacent to the interface exhibits uniform bright-field contrast laterally, indicative of extended local epitaxy (established by SAED analyses discussed below) on individual substrate grains which have an average size of $4.6 \pm 1.2 \mu\text{m}$. After deposition of 200–300 nm, the growth front gradually breaks down locally to initiate a columnar microstructure.

A higher-magnification XTEM micrograph of the interfacial region with corresponding SAED patterns from the film and substrate sides are presented in Fig. 5(b)–(d). The bcc structure substrate diffraction pattern, obtained along the [100] zone axis, appears single crystalline since the diameter of the selected area, 200 nm, is much smaller than the average substrate grain size. The [110] zone axis SAED pattern in Fig. 5(c) shows that the film has the cubic B1-NaCl crystal structure in agreement with XRD results. The pattern is also single crystalline in nature, but with evidence of arcing, particularly in higher index reflections, indicative of local lattice distortion. The two SAED patterns are oriented such that the [002] direction in the film grain matches that of the substrate grain. The epitaxial relationship between the alloy film and the bcc steel grains imaged in Fig. 5 is $(001)\text{Ti}_{0.501}\text{Al}_{0.498}\text{Nb}_{0.001}\text{N} \parallel (001)\alpha\text{-Fe}$ and $[110]\text{Ti}_{0.501}\text{Al}_{0.498}\text{Nb}_{0.001}\text{N} \parallel [100]\alpha\text{-Fe}$. Thus, the film grains grow rotated 45° around the [001] substrate grain axis in order to decrease the lattice mismatch from ≈ 31 to 3% compression. All film/substrate interfacial regions examined exhibited analogous local epitaxial relationships.

The CA ion-etch modified layer, marked with arrows in Fig. 5(b), extends approximately 20 nm below the film/substrate interface. The dark contrast is due to strain fields associated with residual radiation-damage-induced

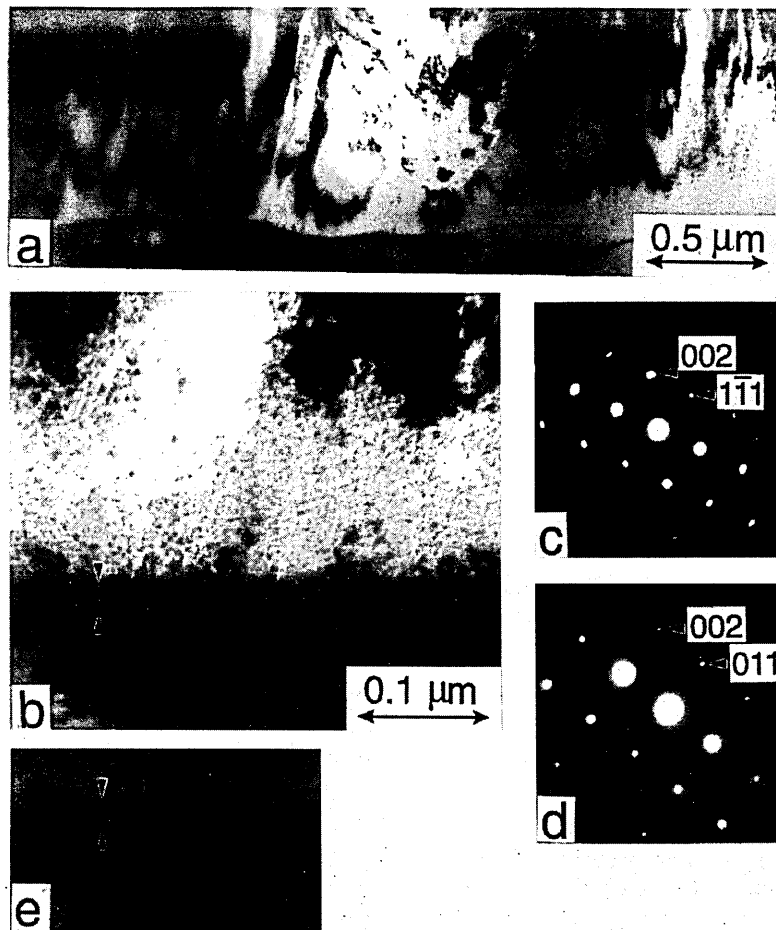


Fig. 5. XTEM images and SAED pattern from the film/ferritic-steel-substrate interfacial region formed by $\text{Ti}_{0.5}\text{Al}_{0.5}$ CA ion-etching followed by UBM sputter deposition of a $\text{Ti}_{0.501}\text{Al}_{0.498}\text{Nb}_{0.001}\text{N}$ alloy film at 450 °C. (a) Bright field micrograph, (b) higher magnification, (c) SAED pattern from the film, (d) SAED pattern from the substrate and (e) weak-beam dark-field image, obtained using the [002] diffraction vector, of the area shown in Fig. 5b.

defects within the matrix of the substrate grains as a result of the intense ion irradiation. Confirmation that the contrast is due to local strain fields (e.g. around dislocation

cores and defect clusters), rather than sample thickness variations or atomic number contrast, is provided by the weak-beam dark-field micrograph in Fig. 5(e) obtained

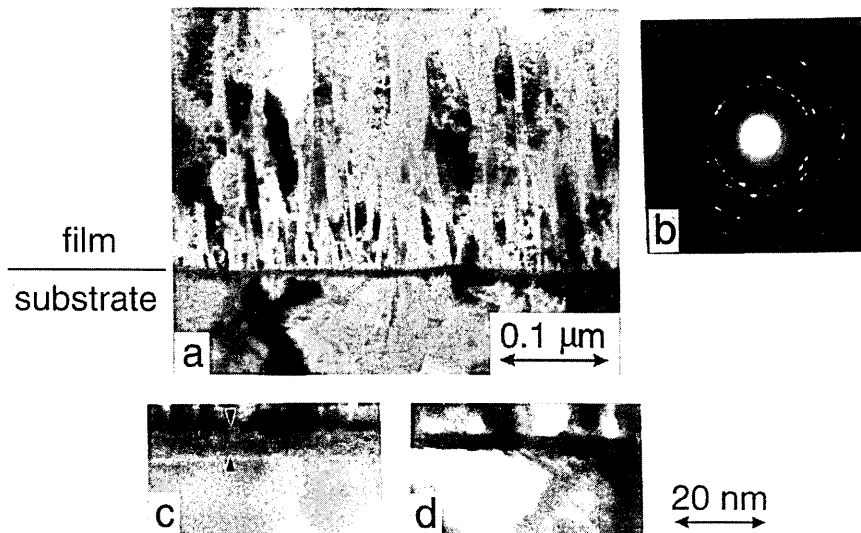


Fig. 6. XTEM images and SAED pattern of the film/ferritic-steel-substrate interfacial region formed by $\text{Ti}_{0.85}\text{Nb}_{0.15}$ CA ion-etching followed by UBM sputter deposition of a $\text{Ti}_{0.501}\text{Al}_{0.498}\text{Nb}_{0.001}\text{N}$ alloy film at 450 °C. (a) Bright field micrograph, (b) SAED pattern from the film, (c) higher magnification and (d) two-beam dark-field image, obtained using the [002] diffraction vector, of the area shown in Fig. 6c.

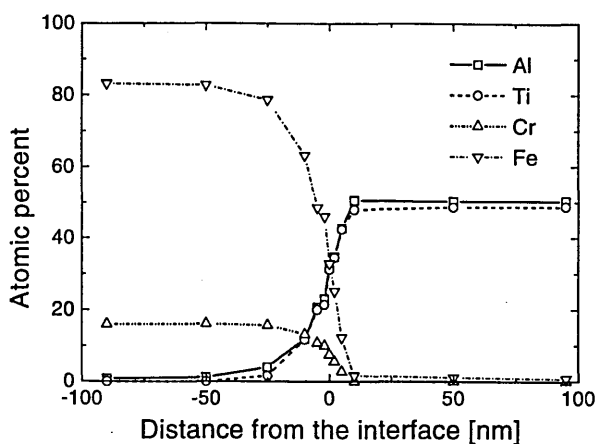


Fig. 7. STEM-EDX compositional depth profile through the interfacial region of the cross-sectional sample shown in Fig. 5.

using the [002] diffraction vector. Under this type of imaging condition, strain fields should yield brighter contrast as observed.

Fig. 6 shows typical XTEM micrographs including the interfacial region of a $\text{Ti}_{0.501}\text{Al}_{0.498}\text{Nb}_{0.001}\text{N}/\text{steel}$ sample in which the substrate was ion-etched using the $\text{Ti}_{0.85}\text{Nb}_{0.15}$ target. The bright-field image in Fig. 6(a) has approximately the same magnification as the micrograph in Fig. 5(b) corresponding to the $\text{Ti}_{0.50}\text{Al}_{0.50}$ arc-etched sample. However, a comparison of the figures shows that the microstructures of the two interfacial regions differ significantly.

Although the XTEM micrograph in Fig. 6(a) also shows a layer with darker contrast in the film/substrate interfacial region, similar to Fig. 5(b), the thickness of the modified layer formed during the $\text{Ti}_{0.85}\text{Nb}_{0.15}$ arc etch is only ≈ 6 nm, compared with ≈ 20 nm for the $\text{Ti}_{0.50}\text{Al}_{0.50}$ arc-etched sample. When examined at higher magnification in bright-field imaging, as illustrated in Fig. 6(c), the arc-modified region appears as a layer with relatively abrupt boundaries on both the film and substrate sides. Moreover, the layer contrast is independent of the angle of electron beam illumination, indicative of an amorphous structure. Further evidence of the absence of crystallinity in this layer is provided by dark-field images, such as the one shown in Fig. 6(d), taken with a large objective aperture which includes lattice spacings ranging from 0.08 to 0.4 nm. The arc modified layer appears uniformly dark in Fig. 6(d), while regions from the substrate and the film exhibit bright contrast areas corresponding to crystalline grains with orientations favorable for diffraction.

Whereas the initially-formed $\text{Ti}_{0.501}\text{Al}_{0.498}\text{Nb}_{0.001}\text{N}$ grains in the $\text{Ti}_{0.50}\text{Al}_{0.50}$ arc-etched sample are locally epitaxial with underlying substrate grains of average size 4.6 ± 1.2 μm , competitive columnar growth with an average column size of only ≈ 10 nm (more than two orders of magnitude smaller than the substrate grain size) occurs immediately upon initiation of film growth on the

$\text{Ti}_{0.85}\text{Nb}_{0.15}$ arc-etched substrate. The column size increases to ≈ 100 nm after deposition of 0.5 μm . The SAED pattern in Fig. 6(b), obtained from a 200 nm thick region of the film adjacent to the interface, consists of rings rather than spots (compare with Fig. 5(c)) consistent with the small grain size.

Figs. 7 and 8 are typical STEM-EDX compositional depth profiles through the interfacial regions of the $\text{Ti}_{0.50}\text{Al}_{0.50}$ and $\text{Ti}_{0.85}\text{Nb}_{0.15}$ arc-etched samples, respectively. In the former case, the width of the transition region over which the Fe and Cr signals decrease and the Ti and Al signals increase is ≈ 20 nm in good agreement with the bright- and dark-field XTEM images in Fig. 5. The depth resolution in these measurements is estimated to be ± 3 nm based upon the results of profiles through single-crystal Al/TiN(001) bilayers [29].

The depth profiles in Fig. 8 show that the width of the intermixed region in the $\text{Ti}_{0.85}\text{Nb}_{0.15}$ arc-etched sample is only ≈ 10 nm, half the value obtained with $\text{Ti}_{0.5}\text{Al}_{0.5}$ arc-etching. The primary difference in the composition of the two CA ion-etch-modified substrate layers is the presence of Nb, with a maximum concentration of ≈ 8 at%, in the $\text{Ti}_{0.85}\text{Nb}_{0.15}$ arc-etched sample and a reduced Al concentration due to the difference in the composition of the targets used in the two etching processes. The compositionally intermixed region is thicker than the width of the amorphized region observed in XTEM (see Fig. 6).

During arc-etching, the substrate is intensely bombarded with a mixture of Ar^+ ions and multiply-charged metal ions. The average metal-ion charge has been measured, for pure Al, Ti, and Nb arcs operated under conditions similar to those employed in the present experiments, to be 1.7, 2.1 and 3, respectively [30]. From TRIM com-

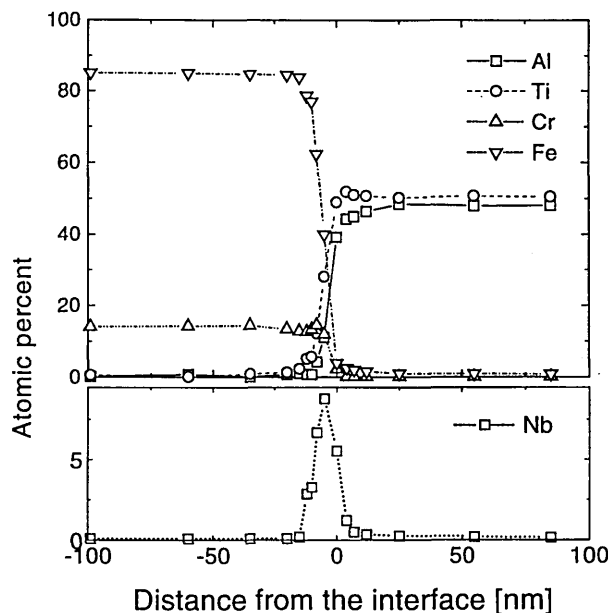


Fig. 8. STEM-EDX compositional depth profile through the interfacial region of the cross-sectional sample shown in Fig. 6.

puter simulations [31] using an acceleration potential of 1.2 kV, we estimate that the projected range R and straggle S are 2.7 and 1.5 nm for $\text{Al}^{+1.7}$, 2.5 and 1.3 nm for $\text{Ti}^{+2.7}$, 2.8 and 1.5 nm for Nb^{+3} , and 1.7 and 1.0 nm for Ar^+ ions. Fe sputtering yields for each of the incident ions were calculated, based upon the measured average ion flux of $1.25 \times 10^{15} \text{ cm}^{-2} \text{ s}^{-1}$, to be 2 ± 0.5 corresponding to the removal of $\approx 400\text{--}700$ nm of substrate material. Under these conditions, in which the thicknesses of the etched layers are approximately two orders of magnitude larger than the ion ranges, implantation profiles can be approximated by error functions extending to depths of $\approx R + S$, which is ≈ 4 nm for all metal ions. The depths corresponding to maximum interstitial and vacancy production in ion-irradiation cascades were of the same order.

For the $\text{Ti}_{0.5}\text{Al}_{0.5}$ arc-etched sample, both XTEM and STEM-EDX measurements revealed an interfacial region with a width of ≈ 20 nm, a factor of five larger than estimated $R + S$ values indicating that radiation-enhanced diffusion assists in the formation of the intermixed layer. The fact that local epitaxy occurred during subsequent alloy film deposition suggests that the $\text{Ti}_{0.5}\text{Al}_{0.5}$ arc-etch provided a relatively clean growth surface with well-preserved crystalline order. In contrast, the use of the heavier and more energetic Nb ions during the etching process increased the density of residual defect concentrations leading to the formation of an amorphous interfacial layer with a thickness of ≈ 6 nm which is consistent with the calculated ion penetration depth. Low-temperature ion-assisted deposition of the $\text{Ti}_{0.501}\text{Al}_{0.498}\text{Nb}_{0.001}\text{N}$ alloy overlayer on the amorphous interfacial layer resulted in kinetically-limited competitive columnar growth similar to that previously reported for UBM deposition of TiN [32,33] and $\text{Ti}_{0.50}\text{Al}_{0.50}\text{N}$ [34,35] on SiO_2 at comparable temperatures.

While the local epitaxial growth obtained on $\text{Ti}_{0.50}\text{Al}_{0.50}$ CA ion-etched substrates was potentially attractive for maximizing interfacial adhesion, the high rate of macroparticle production greatly reduces the utility of this process for substrate preparation. In contrast, using the higher melting point $\text{Ti}_{0.85}\text{Nb}_{0.15}$ target decreases the macroparticle production rate by more than two orders of magnitude rendering the process feasible for use during both CA

substrate etching and film growth in the combined UBM/CA mode. Based upon the above results, UBM/CA multilayer experiments were carried out using $\text{Ti}_{0.85}\text{Nb}_{0.15}$ arc-etching for substrate preparation with $I_{\text{arc}} = 100$ A, $V_{\text{arc}} = 60$ V, and $V_s = 1200$ V for 20 min.

3.2. Growth of $\text{Ti}_{1-x}\text{Al}_x\text{N}/\text{Ti}_{1-y}\text{Nb}_y\text{N}$ multilayers by UBM/CA deposition

$\text{Ti}_{1-x}\text{Al}_x\text{N}/\text{Ti}_{1-y}\text{Nb}_y\text{N}$ multilayers were grown by combined UBM/CA deposition in which the three $\text{Ti}_{0.5}\text{Al}_{0.5}$ targets were operated in a magnetically-unbalanced magnetron mode and the $\text{Ti}_{0.85}\text{Nb}_{0.15}$ target in an arc mode. The discharge power on each of the magnetron targets was maintained constant at 8 kW, while the arc current I_{arc} was varied, for different samples, between 70 and 150 A with an arc voltage of 65 V. For comparison, we also present data for purely UBM deposited films, in which the $\text{Ti}_{0.85}\text{Nb}_{0.15}$ target was operated at a power P_{TiNb} of either 0.5 or 8 kW. In the former case, UBM1, the films were of an average composition of $\text{Ti}_{0.501}\text{Al}_{0.498}\text{Nb}_{0.001}\text{N}$ (see Section 3.1) while in the latter case, the UBM 2 film composition was $\text{Ti}_{0.550}\text{Al}_{0.414}\text{Nb}_{0.036}\text{N}$, close to the average composition of multilayers grown by the combined UBM/CA process with $I_{\text{arc}} = 125$ A. Total film thicknesses in all cases were $\approx 3 \mu\text{m}$.

Typical RBS and XRD results are presented in Fig. 9 though 11 and the data summarized in Table 1. The RBS spectrum in Fig. 9 from a UBM/CA film grown with $I_{\text{arc}} = 150$ A exhibits four steps, corresponding to He scattering from Nb, Ti, Al and N. Since the depth resolution was ≈ 20 nm and individual layers are expected to be < 3 nm, these measurements provide average compositions. All films were slightly overstoichiometric with a $\text{N}/(\text{Ti} + \text{Al} + \text{Nb})$ ratio of 1.05 ± 0.05 . The Ar concentrations were below the detection limit, ≈ 0.5 at%, for UBM/CA films while UBM films contained ≈ 1.5 at% Ar. Average film cation fractions are plotted in Fig. 10 as a function of the $\text{Ti}_{0.85}\text{Nb}_{0.15}$ arc current. The Nb fraction y increased linearly, ranging from 0.02 with $I_{\text{arc}} = 70$ A to 0.039 with $I_{\text{arc}} = 150$ A. This was accompanied by a corresponding linear increase in Ti/Al ratios, $(1-x-y)/x$, from 1.15

Table 1

Average $\text{Ti}_{1-x}\text{Al}_x\text{N}/\text{Ti}_{1-y}\text{Nb}_y\text{N}$ multilayer film compositions, relative intensities ζ and FWHM β of 111 and 002 XRD peaks, lattice constants a_0 , estimated film stresses σ , and superstructure periods Λ as a function of arc current I_{arc} during deposition of CA/UBM films and $\text{Ti}_{0.85}\text{Nb}_{0.15}$ target power P_{TiNb} during deposition of UBM films

I_{arc} (A)	P_{TiNb} (kW)	$\text{Ti}_{1-x-y}\text{Al}_x\text{Nb}_y\text{N}$			$\zeta_{111} = I_{111}/\Sigma I_i$	$\zeta_{002} = I_{002}/\Sigma I_i$	β_{111} (deg)	β_{002} (deg)	a_0 (nm)	σ (GPa)	Λ (nm)
		$1-x-y$	x	y							
70	—	0.530	0.450	0.020	0.19	0.47	0.94	1.23	0.4183	−8.83	2.174
100	—	0.540	0.434	0.026	0.19	0.52	0.99	0.84	0.4192	−9.54	2.209
125	—	0.546	0.420	0.034	0.16	0.51	0.73	0.78	0.4198	−7.89	2.240
150	—	0.556	0.405	0.039	0.17	0.5	0.71	0.75	0.4210	−8.63	2.289
—	0.5	0.501	0.498	0.001	0.73	0.17	0.34	0.53	0.4178	−2.73	—
—	8.0	0.550	0.414	0.036	0.53	0.40	0.38	0.54	0.4202	−3.87	2.11

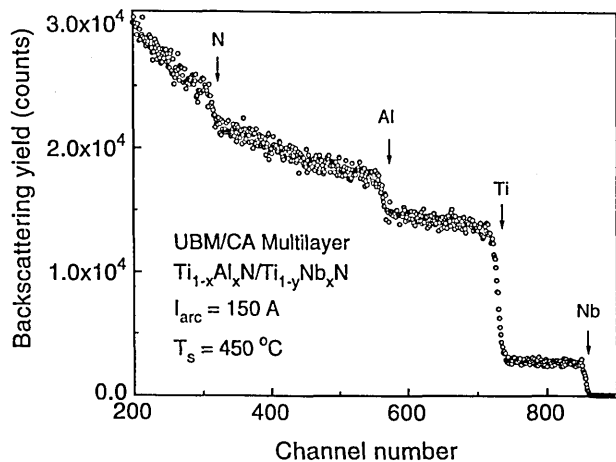


Fig. 9. RBS spectrum from a $Ti_{1-x}Al_xN/Ti_{1-y}Nb_yN$ multilayer grown by UBM/CA deposition with $I_{arc} = 150$ A.

to 1.33. Extrapolation of this data to zero arc current yields a Ti/Al ratio of 1 in agreement with results for pure UBM reactive deposition from $Ti_{0.5}Al_{0.5}$ targets [2–4]. Thus, the Ti deposition flux from the magnetron sources remains constant and equal to that of the Al flux as the arc current at the $Ti_{0.85}Nb_{0.15}$ target is increased.

From the above results, the total magnetron component of the deposited cation flux is $2x$, while the arc component is $(1 - 2x)$. We can therefore estimate the Nb fraction in

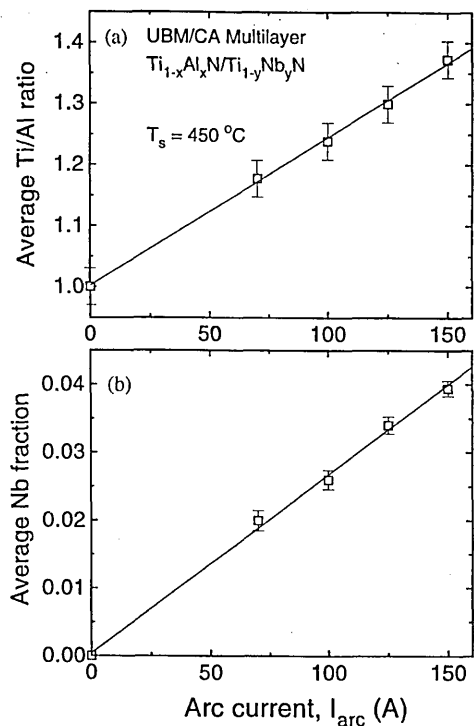


Fig. 10. (a) The average Ti/Al ratio and (b) Nb fraction in UBM/CA deposited $Ti_{1-x}Al_xN/Ti_{1-y}Nb_yN$ multilayers as a function of the arc current I_{arc} on the $Ti_{0.85}Nb_{0.15}$ target. The magnetron power on each of the three $Ti_{0.50}Al_{0.50}$ targets was maintained constant at 8 kW.

the arc cation deposition flux as $y/(1 - 2x)$. From the RBS results in Table 1, the ratio $y/(1 - 2x)$ is 0.20, 0.20, 0.21 and 0.20 with I_{arc} values of 70, 100, 125 and 150 A, respectively. Thus, the deposition flux from the arc discharge has an approximately constant composition, corresponding to Nb enrichment by ≈ 5 at% with respect to the target, as the current is varied. A small increase in the Nb fraction was expected since heavier atoms are less likely to be lost by gas-phase scattering during transport between the target and the substrate. In addition, Nb ions have the highest average cation charge and are thus accelerated toward the substrate at higher energies, further reducing scattering losses. Finally, preferential sputtering effects would also be expected to lead to enrichment in the heavier component.

Fig. 11(a) shows portions, 35 to 46° , of typical XRD $\theta-2\theta$ patterns containing the primary diffraction peaks, 111 and 002, obtained from UBM ($P_{TiNb} = 0.5$ and 8 kW) and UBM/CA ($I_{arc} = 70$ and 125 A) films. We also observed small 311, 331 and 511 peaks and second-order 222 and 004 peaks, at higher angles. All diffraction peaks,

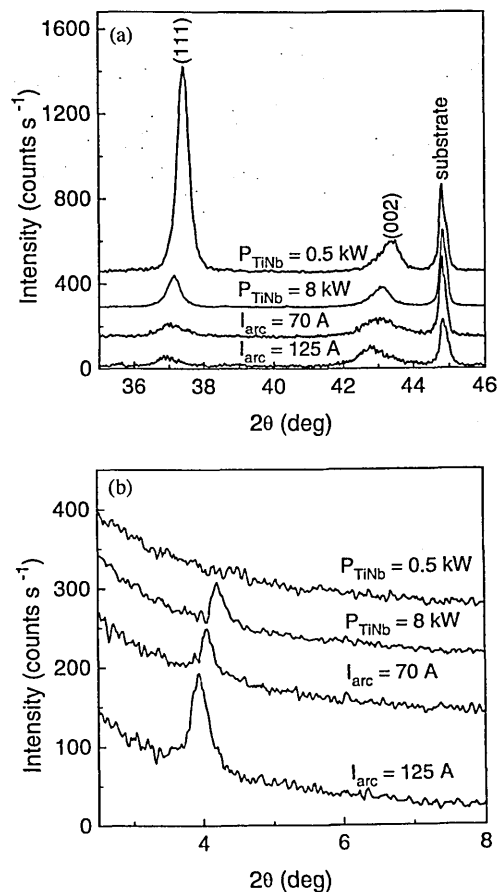


Fig. 11. Typical XRD $\theta-2\theta$ patterns from UBM and UBM/CA films: (a) $35-46^\circ$ 2θ and (b) $2.5-8^\circ$ 2θ . P_{TiNb} is the power and I_{arc} is the current applied to the $Ti_{0.85}Nb_{0.15}$ target during UBM and UBM/CA deposition, respectively.

however, were indexed as emanating from single-phase B1-NaCl structure reflections. Normalized peak intensities ($\zeta_{hkl} = I_{hkl}/\sum I_{h'k'l'}$) from TiN powder diffraction files [36] are $\zeta_{111} = 0.28$ and $\zeta_{002} = 0.37$. Comparing this with the normalized peak intensities presented in Table 1 indicates that the UBM films have a pronounced 111 texture while the UBM/CA samples have a weak 002 texture. In the latter case, $\zeta_{111} = 0.16$ – 0.19 and $\zeta_{002} = 0.47$ – 0.52 and do not vary significantly with I_{arc} . Moreover, as shown in Table 1, the full-width-at-half maximum intensities β of the UBM 111 and 002 diffraction peaks are much smaller than corresponding values for UBM/CA films.

The primary differences between deposition conditions for the UBM and UBM/CA films are the marked increase by $\approx 50\%$ in the ion fluxes incident at the growing film during the CA cycle together with an approximately 50% increase in the time-averaged ion energy due to the increased average ion charge. The observed trend in preferred orientation from strongly 111 for UBM to weakly 002 for UBM/CA is consistent with previous ion-irradiation induced transition-metal nitride results. A controllable transition from complete 111 to complete 002 preferred orientation was obtained in both TiN [32,33] and $Ti_{1-x}Al_xN$ [34,35] with increased ion-to-metal flux ratio and the ion energy maintained constant at 20 eV. A smaller but still significant shift from 111 to 002 was also observed with increasing ion energy at constant ion-to-metal flux ratio. The broadened peak widths β obtained for the UBM/CA films are indicative of the presence of ion-irradiation-induced inhomogeneous stress since XTEM investigation showed that the grain size evolution was very similar in both UBM and UBM/CA films.

The low angle θ - 2θ XRD scans from the UBM/CA samples (Fig. 11(b)) contain superstructure diffraction peaks showing, in agreement with XTEM results discussed below, that the films are multilayers. Low-angle XRD peaks were not obtained from UBM1 samples while UBM2 films had a superstructure peak corresponding to a period of 2.1 nm.

The intensity of the low-angle UBM/CA peak increased and the angular position decreased, with increasing I_{arc} . Measured 2θ values ranged from 4.06° with $I_{arc} = 70$ A to 3.86° with $I_{arc} = 150$ A corresponding to superstructure periods Λ of 2.17 to 2.29 nm. The number of layers in the multilayer films, obtained from the ratio of the total film thickness to the superstructure period, agrees in all cases with values expected based upon the substrate rotation period τ_1 . Thus, the UBM/CA films consist of alternating $Ti_{1-x}Al_xN$ and $Ti_{1-y}Nb_yN$ layers deposited when the substrates pass in front of the $Ti_{0.5}Al_{0.5}$ and $Ti_{0.85}Nb_{0.15}$ targets, respectively.

Relaxed multilayer and alloy lattice parameters a_0 together with net residual in-plane macroscopic stresses σ were estimated using the $\sin^2\Psi$ XRD technique [37] based upon measured intensities of the 111, 002, 311, 222, 331, 420 and 511 diffraction peaks at a constant X-ray beam

incidence angle of 15° . For a given sample, the set of apparent lattice parameters a_ψ varied linearly with $\sin^2\psi$. The values of a_0 and σ were then determined from the slope δ and intercept ξ of a_ψ vs. $\sin^2\Psi$ plots through least-squares fitting of the experimental data to the following equations, [37,38],

$$a_0 = \xi + \frac{2\delta\nu}{1+\nu} \quad (1)$$

and

$$\sigma = \frac{Y\delta}{2\delta\nu + (1+\nu)\xi} \quad (2)$$

where ν is Poisson's ratio and Y is Young's modulus. For TiN, $\nu = 0.3$ and $Y = 640$ GPa [38,39]. However, ν and Y are unknown for $Ti_{1-x}Al_xN$, $Ti_{1-y}Nb_yN$, and $Ti_{1-x-y}Al_xNb_yN$ alloys. Thus, in estimating a_0 and σ , we used TiN elastic constants. Known Poisson ratios and Young's moduli for other NaCl-structure transition metals vary from 0.186 and 460 GPa for ZrN to 0.35 and 380 GPa for HfN [39,40]. Variations in ν and Y of this magnitude will introduce maximum errors in a_0 of $\leq 0.1\%$ which is of the order of, or less than, the experimental uncertainty. The maximum uncertainty in σ is much larger, approximately 40%, since σ varies linearly with Y .

Published lattice constants for TiN, $Ti_{0.5}Al_{0.5}N$, and NbN are, 0.4240, [36] 0.4178, [34] and 0.4393 [41] nm, respectively. Thus, increasing the $Ti_{1-y}Nb_yN$ fraction in the multilayer films, through the use of higher I_{arc} values, would be expected to increase a_0 . Table 1 shows that this is exactly what is observed. a_0 increases monotonically from 0.4183 nm to 0.4210 nm as I_{arc} is varied from 70 to 150 A.

All films were found to exhibit an overall in-plane compressive stress. Estimated σ -values were ≈ 2.7 GPa and 3.9 GPa for UBM1 and UBM2 films, respectively, in good agreement with previous results for $Ti_{0.5}Al_{0.5}N$ deposited under similar magnetron sputtering conditions [42]. Compressive stresses in UBM/CA multilayers were more than a factor of two higher, the difference being well above experimental uncertainties, due to increased residual ion-irradiation-induced damage associated with the cathodic-arc deposition cycle. This result is consistent with the higher level of local microscopic stress indicated by increased XRD peak broadening (see Table 1). Previous studies of ion-assisted TiN growth, carried out under conditions in which either Ar^+ [43,44] or N_2^+ [32,33] were the dominant ions, demonstrated that a pronounced increase in residual defect densities occurs as acceleration energies E_i are increased above approximately 80 eV. In the present UBM experiments, the majority of the ions incident at the growing film are singly charged Ar^+ [19] with $\langle E_i \rangle$, as noted in Section 2, nearly equal to eV_s where $V_s = 80$ V. During UBM/CA depositions, however, $\langle E_i \rangle$ was higher, ≈ 110 – 120 eV, due an increased average ion charge. Such relatively high ion energies result in enhanced residual

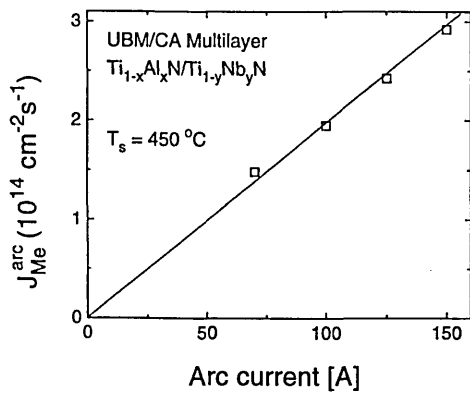


Fig. 12. The arc component J_{Me}^{arc} of the total cation deposition flux as a function of the arc current I_{arc} on the $Ti_{0.85}Nb_{0.15}$ target during UBM/CA deposition of $Ti_{1-x}Al_xN/Ti_{1-y}Nb_yN$ multilayers.

radiation damage giving rise to large lattice distortions. The increase in σ -values was thus caused predominantly by residual damage since there was no measurable Ar concentration in this case.

The arc component J_{Me}^{arc} of the total cation deposition flux J_{Me} during multilayer growth can be estimated, based upon the RBS and XRD results, as $J_{Me}^{arc} = (1 - 2x)J_{Me}$, where J_{Me} is given by

$$J_{Me}^{arc} = \frac{\Lambda N}{\tau_1} \quad (3)$$

In Eq. (3), Λ is the measured superstructure period (given as a function of I_{arc} in Table 1), $\tau_1 = 8$ s is the substrate rotation period, and N is the cation number density in the as-deposited film. Assuming that the films are dense, which is reasonable based upon the XTEM results, N can be obtained from the measured lattice parameters. Fig. 12 is a plot of J_{Me}^{arc} , from Eq. (3), vs. I_{arc} .

The curve is linear with J_{Me}^{arc} increasing from $1.5 \times 10^{14} \text{ cm}^{-2} \text{ s}^{-1}$ with $I_{arc} = 70$ A to $2.9 \times 10^{14} \text{ cm}^{-2} \text{ s}^{-1}$ with $I_{arc} = 150$ A. The ratio J_{Me}^{arc}/J_{Me} thus ranges from 0.10 to 0.19 and, in the absence of interlayer mixing, corresponds to the ratio of the $Ti_{0.8}Nb_{0.2}N$ layer thickness l_{TiNbN} to the superstructure period Λ .

Fig. 13 is a bright-field micrograph of a multilayer film deposited with $I_{arc} = 125$ A. The overall microstructure, with a small initial column size ($\langle d \rangle \approx 10$ nm) and a pronounced competitive column growth ($\langle d \rangle \approx 100$ nm at film thickness $t \approx 500$ nm), is similar to that observed in UBM1 films as shown in Fig. 6(a). The target material used in the arc etching step prior to film deposition, and the nature of the resulting altered substrate layer (see Section 3.1), thus have a much stronger effect on microstructure evolution than does the use of the arc during UBM/CA deposition.

Fig. 13 also shows an SAED pattern obtained from a 200-nm-diameter region of the UBM/CA film adjacent to the film/substrate interface. Diffraction rings, rather than spots, are observed consistent with the small grain size. The 002 ring exhibits stronger intensity along the growth direction indicating that a weak 002 preferred orientation is already present during the early stages of film growth. In addition, the SAED pattern contains satellite reflections, due to the multilayer structure, about the transmitted beam along the growth direction. The satellite separation corresponds to a periodicity of 2.2 nm in excellent agreement with values obtained from the low-angle XRD results as well as direct observations from higher-magnification XTEM micrographs such the one as shown in Fig. 14.

The vertical stripes in Fig. 14 are due to Moiré fringes from overlapping grains. The fringes disappear as column sizes become larger than the foil thickness. The multilayers

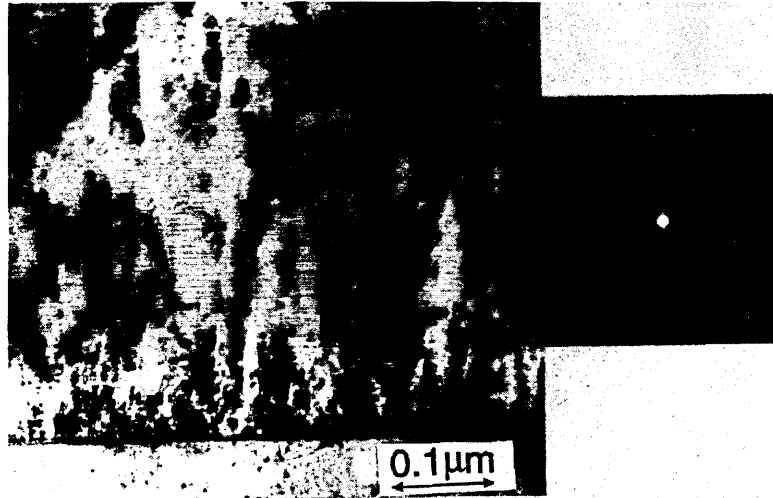


Fig. 13. XTEM image and SAED pattern from the film/ferritic-steel-substrate interfacial region formed by $Ti_{0.85}Nb_{0.15}$ CA ion-etching followed by UBM/CA deposition of a $Ti_{1-x}Al_xN/Ti_{1-y}Nb_yN$ multilayer with $I_{arc} = 125$ A.

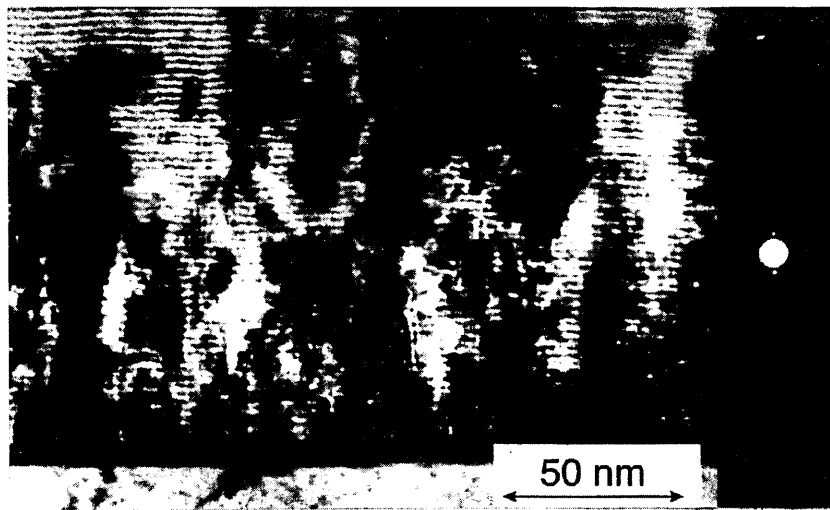


Fig. 14. A higher magnification micrograph and SAED pattern from the cross-sectional sample shown in Fig. 13.

in Fig. 14 appear as alternating darker and lighter bands parallel to the film/substrate interface. The darker bands are the higher average-atomic-number $\text{Ti}_{0.80}\text{Nb}_{0.20}\text{N}$ layers for which I_{TiNbN} is $\approx 0.4\Lambda$ while from RBS and XRD measurements, the expected value in the absence of interfacial mixing is $\approx 0.16\Lambda$. Thus, the relatively open geometry of the deposition system used in the present experiments combined with the intense ion irradiation gives rise to significant interlayer mixing during film growth.

As noted above, it was possible to obtain $\text{Ti}_{1-x}\text{Al}_x\text{N}/\text{Ti}_{1-y}\text{Nb}_y\text{N}$ multilayers in pure UBM mode by increasing the power applied to the $\text{Ti}_{0.85}\text{Nb}_{0.15}$ target during deposition. For example a multilayer film with $\Lambda = 2.1$ nm and an average Nb fraction of 0.036 was obtained with a $\text{Ti}_{0.85}\text{Nb}_{0.15}$ power of 8 kW (UBM2). However UBM multilayers, although initially flat, exhibit considerable surface roughening with continued film growth, as illustrated in Fig. 15. The film is composed of dense columns with faceted column tops. The multilayer

structure parallels the growth front and thus provides a history of the evolution of surface roughening. The reciprocal space diffraction pattern from such a structure is expected to produce arcs with radii corresponding to the inverse of the multilayer period. However, the intensity of superstructure reflections will be greatly diminished. In the present experiments, they were not resolvable as shown in Fig. 15.

In sharp contrast to the UBM case, superstructure layer interfaces in UBM/CA films were found to remain flat and parallel to the original film/substrate interface throughout the entire 3- μm thickness as shown in Fig. 16. The diffraction pattern taken from the top part of the film clearly shows satellite reflections corresponding to the layer modulation. Thus, the addition of the arc discharge in a multitarget magnetron sputtering system, whose design was optimized for providing high plasma densities, had a significant effect on film microstructure. The increased ion-to-metal flux ratios and degree of ionization enhanced

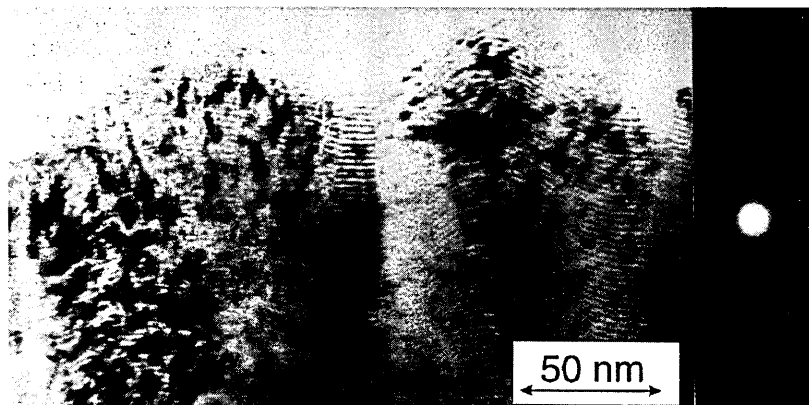


Fig. 15. A bright-field XTEM micrograph and a SAED pattern from a top portion of a 3 μm thick $\text{Ti}_{1-x}\text{Al}_x\text{N}/\text{Ti}_{1-y}\text{Nb}_y\text{N}$ multilayer grown by UBM deposition with $P_{\text{TiNb}} = 8$ kW.

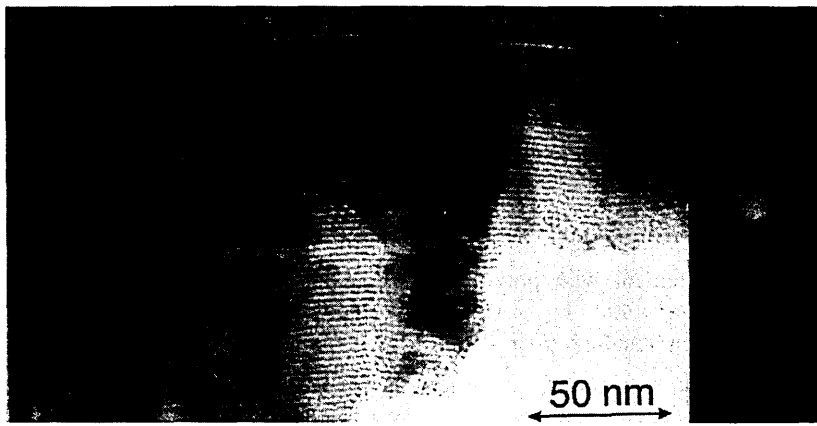


Fig. 16. A bright-field XTEM micrograph and a SAED pattern from a top portion of a 3 μm thick $\text{Ti}_{1-x}\text{Al}_x\text{N}/\text{Ti}_{1-y}\text{Nb}_y\text{N}$ multilayer deposited by UBM/CA deposition with $I_{\text{arc}} = 125$ A.

adatom mobilities sufficiently to suppress surface roughening and provide nitride multilayers with much higher structural integrity.

4. Conclusions

Polycrystalline $\text{Ti}_{1-x-y}\text{Al}_x\text{Nb}_y\text{N}$ alloys and $\text{Ti}_{1-x}\text{Al}_x\text{N}/\text{Ti}_{1-y}\text{Nb}_y\text{N}$ multilayers exhibiting smooth flat layers up to total film thicknesses of 3 μm have been grown on ferritic bcc stainless steel substrates at ≈ 450 $^{\circ}\text{C}$ using UBM/CA deposition. The final step in substrate cleaning and preparation for film growth consisted of CA etching carried out using either $\text{Ti}_{0.5}\text{Al}_{0.5}$ or $\text{Ti}_{0.85}\text{Nb}_{0.15}$ targets to remove several hundred nm of substrate material. The results obtained with the two targets were strikingly different. Operating the arc on the lower melting point $\text{Ti}_{0.5}\text{Al}_{0.5}$ target yielded a relatively high density of large macroparticles giving rise to nodular growth in the overlayer with highly underdense regions surrounding the nodules. Even after 3 μm of film deposition, the rounded tops of the nodules extended well above the surrounding film surface. The fractional surface area covered by the nodules was ≈ 0.24 . STEM and SAED measurements showed that for $\text{Ti}_{0.5}\text{Al}_{0.5}$ CA ion-etched samples, Ti and Al extended approximately 20 nm below the film/substrate interface. This was much larger than projected ranges, estimated from TRIM measurements, for the multiply-charged ions in the arc discharge and indicates defect-enhanced diffusion. Nevertheless, the substrate surface remained crystalline, although highly strained. Away from the nodules, $\text{Ti}_{1-x}\text{Al}_x\text{N}$ overlayers were found to exhibit local epitaxy over complete substrate grains with an average size of 4.6 μm .

CA ion-etching using the higher melting point $\text{Ti}_{0.85}\text{Nb}_{0.15}$ target greatly reduced the average droplet size and number density such that nodules covered less than 0.0022 of the surface of deposited overlayers. The use of heavier metal ions reduced the penetration depth to ≈ 10

nm while the heavier average ion mass resulted in considerably higher residual damage leaving the upper 6 nm of the substrate surface amorphous. The $\text{Ti}_{1-x}\text{Al}_x\text{N}$ films in this case exhibited competitive columnar growth from the earliest stages with average column sizes of ≈ 10 nm, more than two orders of magnitude smaller than the bulk substrate grain size.

While the extended local epitaxy achieved for the growth of the nitride alloy layers on the steel substrates prepared using CA etching from the $\text{Ti}_{0.5}\text{Al}_{0.5}$ target was desirable, the multilayers were grown on $\text{Ti}_{0.85}\text{Nb}_{0.15}$ arc-etched substrates in order to minimize nodule formation and maintain smooth flat interfaces.

The addition of the cathodic arc cycle during multitar-get magnetron deposition also had a dramatic effect on film microstructure, texture, stress and surface roughening due to increases, for the same substrate bias voltage V_s , in ion-to-metal flux ratios and degree of ionization. During pure UBM deposition, the dominant ion species was Ar^+ with $\langle E_i \rangle \approx eV_s = 80$ eV and an ion-to-metal flux ratio of 4. Under these conditions, we observe, consistent with previous results for TiN [32,33] and $\text{Ti}_{1-x}\text{Al}_x\text{N}$, [34,35] the kinetically-limited competitive evolution of a columnar structure with 111 texture and faceted column tops. The films are in moderate compressive stress, ≈ 3 GPa, and contain a significant concentration of trapped Ar, ≈ 1.5 at%. $\text{Ti}_{1-x}\text{Al}_x\text{N}/\text{Ti}_{1-y}\text{Nb}_y\text{N}$ interfaces in multilayer UBM films exhibited increased roughening from the earliest observable stages of growth with peak-to-peak roughnesses, as observed in XTEM of ≈ 50 nm at $t = 3$ μm .

In contrast, $\text{Ti}_{1-x}\text{Al}_x\text{N}/\text{Ti}_{1-y}\text{Nb}_y\text{N}$ multilayers grown by UBM/CA exhibited well-defined relatively flat interfaces, with peak-to-peak roughnesses in films with $\Lambda = 2.2$ nm of only ≈ 5 nm even after 3 μm of deposition. This, we believe, was primarily due to enhanced ion irradiation giving rise to sufficient increases in cation surface mobilities to suppress surface roughening. The much larger fraction of multiply-charged metal and Ar ions in the arc discharge increased both ion-to-metal flux ratios, ≈ 5 –6,

and average ion energies, $\approx 110\text{--}120$ eV, incident at the substrate. This enhanced ion irradiation also gave rise to higher compressive stresses (estimated in Table 1 to be 8–9 GPa with $V_s = 80$ V) associated with increased residual lattice damage while reducing the Ar concentration to less than detection limits, ≈ 0.5 at%. The latter was due to a combination of the higher probability of metal atom ionization in arc discharges and increased loss of trapped Ar by resputtering. Finally, in agreement with previous results obtained during low-temperature $\text{Ti}_{1-x}\text{Al}_x\text{N}$ growth, the enhanced ion irradiation resulted in a shift from 111 toward 002 texture.

Acknowledgements

The authors gratefully acknowledge the financial support of the Materials Science Division of the US Department of Energy under contract number DEAC0276ER01198. We also appreciate the use of the facilities of the Center for Microanalysis, which is partially supported by DOE, at the University of Illinois.

References

- [1] R.L. Hatschek, *Amer. Machinist*, 129 (1983) 1.
- [2] G. Håkansson, J.-E. Sundgren, D. McIntyre, J.E. Greene and W.-D. Münz, *Thin Solid Films*, 153 (1987) 55.
- [3] F. Adibi, I. Petrov, L. Hultman, U. Wahlström, T. Shimizu, D. McIntyre and J.E. Greene, *J. Appl. Phys.*, 69 (1991) 6437.
- [4] U. Wahlström, L. Hultman, J.-E. Sundgren, F. Adibi, I. Petrov and J.E. Greene, *Thin Solid Films*, 235 (1993) 62.
- [5] D. McIntyre, J.E. Greene, G. Håkansson, J.-E. Sundgren and W.-D. Münz, *J. Appl. Phys.*, 67 (1990) 1542.
- [6] W.-D. Münz, *J. Vac. Sci. Technol.*, A4 (1986) 2717.
- [7] S.B. Saut and K.S. Gill, *Surf. Coat. Technol.*, 68/69 (1994) 152.
- [8] W.D. Sproul, M.E. Graham, M.-S. Wong and P.J. Rudnik, *Surf. Coat. Technol.*, 61 (1993) 139.
- [9] O. Knotek, A. Barimani, B. Bosserhoff and F. Löffler, *Thin Solid Films*, 193/194 (1990) 557.
- [10] J.R. Roos, J.P. Celis, E. Vancoille, H. Veltrop, S. Boelens, F. Jungblut, J. Ebberink and H. Homberg, *Thin Solid Films*, 193/194 (1990) 547.
- [11] O. Knotek, T. Leyendecker and F. Jungblut, *Thin Solid Films*, 153 (1987) 83.
- [12] U. Helmersson, S. Todorova, S.A. Barnett, J.-E. Sundgren, L.C. Markert and J.E. Greene, *J. Appl. Phys.*, 62 (1987) 481.
- [13] N. Hirashita, J.E. Greene, U. Helmersson, J. Birch and J.-E. Sundgren, *J. Appl. Phys.*, 70 (1991) 4963.
- [14] X. Chu, M.S. Wong, W.D. Sproul, S.L. Rohde and S.A. Barnett, *J. Vac. Sci. Technol.*, A10 (1992) 1604.
- [15] G. Håkansson, L. Hultman, J.-E. Sundgren, J.E. Greene and W.-D. Münz, *Surf. Coat. Technol.*, 48 (1991) 51.
- [16] P.J. Martin, R.P. Netterfield, T.J. Kinder and L. Descotes, *Surf. Coat. Technol.*, 49 (1991) 239.
- [17] W.-D. Münz, D. Schulze and F.J.M. Hauzer, *Surf. Coat. Technol.*, 50 (1992) 169.
- [18] I. Petrov, F. Adibi, J.E. Greene, W.D. Sproul and W.-D. Münz, *J. Vac. Sci. Technol.*, A10 (1992) 3283.
- [19] I. Petrov, A. Myers, J.E. Greene and J.R. Abelson, *J. Vac. Sci. Technol.*, A12 (1994) 2846.
- [20] A.V. Phelps, *J. Phys. Chem. Ref. Data*, 20 (1991) 557.
- [21] B. Chapman, *Glow Discharge Processes*, Wiley, New York, 1980, p. 108.
- [22] P. Sathrum and B.F. Coll, *Surf. Coat. Technol.*, 50 (1992) 103.
- [23] R.L. Doolittle, *Nucl. Instr. Methods, B* 15 (1985) 344.
- [24] J.W. Colby, in *Quantex-ray Instruction Manual*, Keveex, Foster City, CA, 1980.
- [25] W.-D. Münz, D.B. Lewis, S. Creasey, T. Hurkmans, T. Trinh and W.v. Ijzendorp, *Vacuum*, 46 (1995) 323.
- [26] M. Hansen, *Constitution of Binary Alloys*, McGraw-Hill, New York, 1958, p. 140.
- [27] NIH Image software from the National Institute of Health, obtainable from public program site with access address 'alw.nih.gov' under the directory/pub/image/.
- [28] J.E. Greene, in *Handbook of Crystal Growth, Volume 1: Fundamentals*, D.T.J. Hurle, (ed.) Elsevier, Amsterdam, 1993, p. 639.
- [29] I. Petrov, E. Mojab, F. Adibi, J.E. Greene, L. Hultman and J.-E. Sundgren, *J. Vac. Sci. Technol.*, A11 (1993) 11.
- [30] I.G. Brown and X. Godechot, *IEEE Trans. Plasma Sci.*, 19 (1991) 713.
- [31] J. Ziegler, J.A. Biersack and U. Littmark, *The Stopping and Ranges of Ions in Matter*, Pergamon, New York 1985. TRIM-90, Version 6.0.
- [32] L. Hultman, J.-E. Sundgren, J.E. Greene, D.B. Bergstrom and I. Petrov, *J. Appl. Phys.*, 78 (1995) 5395.
- [33] J.E. Greene, J.-E. Sundgren, L. Hultman, I. Petrov and D.B. Bergstrom, *Appl. Phys. Lett.*, 67 (1995) 2928.
- [34] I. Petrov, F. Adibi, J.E. Greene, L. Hultman and J.-E. Sundgren, *Appl. Phys. Lett.*, 63 (1993) 36.
- [35] F. Adibi, I. Petrov, J.E. Greene, L. Hultman and J.-E. Sundgren, *J. Appl. Phys.*, 73 (1993) 8580.
- [36] Powder Diffraction File, JCPDC International Center for Powder Diffraction Data, Swarthmore, PA, 1989: TiN [6-642].
- [37] I.C. Noyan and J.B. Cohen, *Residual Stresses*, Springer, New York, 1987.
- [38] B.D. Cullity, *Elements of X-ray Diffraction*, Addison-Wesley, Reading, MA, 1978.
- [39] E. Török, A.J. Perry, L. Chollet and W.D. Sproul, *Thin Solid Films*, 153 (1987) 37.
- [40] A.J. Perry, *Thin Solid Films*, 193/194 (1990) 463.
- [41] Powder Diffraction File, JCPDC International Center for Powder Diffraction Data, Swarthmore, PA, 1989: NbN [38-1155].
- [42] W.D. Sproul, P.J. Rudnik, K.O. Legg, W.-D. Münz, I. Petrov and J.E. Greene, *Surf. Coat. Technol.*, 56 (1993) 179.
- [43] I. Petrov, L. Hultman, U. Helmersson, J.-E. Sundgren and J.E. Greene, *Thin Solid Films*, 169 (1989) 299.
- [44] I. Petrov, L. Hultman, J.-E. Sundgren and J.E. Greene, *J. Vac. Sci. Technol.*, A10 (1992) 265.

Chromium nitride coatings grown by unbalanced magnetron (UBM) and combined arc/unbalanced magnetron (ABSTM) deposition techniques

T. Hurkmans^a, D.B. Lewis^b, J.S. Brooks^b, W.-D. Münz^{b,*}

^a Hauzer Techno Coating Europe BV, PO Box 226 5900 AE Venlo, The Netherlands

^b Materials Research Institute, Sheffield Hallam University, Pond Street, City Campus, Sheffield, South Yorkshire S1 1WB, UK

Abstract

Increasingly chromium nitride coatings are being used as a replacement for electroplated hard chromium in various applications. This paper reports an investigation of chromium nitride coatings deposited at 250°C on various substrates at different N₂ partial pressures using both UBM sputtering and ABS techniques. The effect of process parameters on structure, composition, hardness and adhesion have been investigated by XRD, SNMS, SEM and a range of mechanical testing techniques. The presence of Cr, Cr+N, Cr₂N, CrN, and mixtures of the phases have been identified and related to both the film composition and the process parameters. Substoichiometric Cr₂N films had the greatest hardness with values up to 2100 HV. However, films of this hardness exhibited poor adhesion with critical loads, L_c , of 30 N (HSS) and HR_c-DB of “4”, if deposited with UBM only. X-ray diffraction indicated that the poor adhesion exhibited by these films was associated with high internal stress. The adhesion of substoichiometric films with comparable composition and crystal structure deposited in combination with metal ion etching (ABS) increased the critical load values up to 60 N (HSS) and improved the HR_c-DB to “1” (HSS).

Keywords: Chromium nitride; Composition; Stoichiometry; Adhesion; Cathodic arc/unbalanced magnetron

1. Introduction

Results on reactively sputtered CrN_x coatings have been reported since 1983 [1–6]. The specific advantages of this coating were soon recognised. Deposition temperatures as low as 200°C, high oxidation resistance up to 700°C and rather non-critical deposition criteria are typical. Besides magnetron sputtering the cathodic arc [7,8] and the low voltage electron beam evaporation processes [9,10] have been utilised. Independent of the deposition techniques various phases of CrN_x have been identified depending on the partial pressure of the reactive gas N₂: Cr, Cr–N solid solution, Cr₂N, Cr₂N+CrN, CrN. The hardness of these coatings depends surprisingly little on the nitrogen content, although it seems to be accepted that the maximum hardness is correlated to the Cr₂N phase. Typical range of hardness has been found between 1700 and 2400 HV over a composition range between CrN_{0.1} to CrN.

The present paper reports on CrN_x coatings which have been deposited either by reactive unbalanced magnetron sputtering or by the combined cathodic steered arc/unbalanced magnetron–arc bond sputtering (ABS)

deposition technique [11,12]. The investigations have been focused on the question of maximum hardness, internal stresses and adhesion as a function of the N content of the coating.

2. Experimental details

All coatings have been deposited in a ABSTM coating machine HTC-625-Multilab, fabricated by Hauzer Techno Coating Europe B.V., Venlo, The Netherlands. This coater is equipped with two opposing cathodes which can be used either as cathodic arc sources or as unbalanced magnetron sputtering sources. Inert Ar ion etching or Cr metal ion etching was applied to etch the samples prior to coating with the unbalanced magnetron, which was operated in the closed magnetic field mode. A detailed description of the coater is given in [12]. The most important deposition parameters are listed in Table 1.

Test samples were fabricated from ferritic stainless steel (Cr18) and high speed steel (HSS:M2). The surface was ground and polished to $R_a = 0.01 \mu\text{m}$. The coating temperature has been kept constant through all experi-

* Corresponding author. Tel.: 01142 533500; fax: 01142 533501.

Table 1
Overview of PVD process settings for CrN_x

CrN_x deposition parameters (UBM); 2-fold planetary rotation

- (1) Pump down and radiation heating
Time = 60 min:
Controlled temperature = 200°C:
Base pressure <math> < 1 \times 10^{-3}</math> Pa:
- (2) Ar ion etch/Cr ion etch:
Time = 20 min:
Controlled temperature = 240°C:
d.c.-bias voltage = -800 V (argon) -1200 V (Cr):
d.c.-target voltage = -150 V:
argon pressure = 1 Pa:
- (3) Closed field unbalanced magnetron sputtering:
Time = set to deposit 3 μm:
Controlled temperature = 250°C:
d.c.-bias voltage = -100 V:
Cr target d.c. power = 5 kW:
Argon flow rate = 160 sccm:
Nitrogen flow rate = varied between 0 and 100 sccm:
- (4) Cooling down and Venting:

ments at 250°C. To keep the coating thickness at a value of 3 μm, the deposition time had to be adjusted as the deposition rate decreases to 75% at high N₂ flow rates (compared to pure metallic), because of target poisoning. All samples were subjected to a two-fold planetary rotation during all process phases.

Film properties were measured using the following test methods:

- (1) Daimler-Benz Rockwell C hardness test (HR_c-DB judgement) [13] and CSEM "Revetest" critical load L_c test to determine the adhesion of the coating.
- (2) Leitz Vickers hardness measuring equipment (load: 0.025 N).
- (3) CSEM "Kalotest" was used to determine the coating thickness.
- (4) A JEOL JXA 840A Scanning Electron Microscope was used to investigate the morphology of the coatings.
- (5) The composition of the coatings was determined by SNMS (Secondary Neutral Mass Spectrometry V.G. SIMSLAB).
- (6) X-ray diffraction (XRD) analysis was carried out on the coatings using monochromatic Cu Kα radiation and a Philips wide range goniometer using Bragg-Brentano geometry. The diffraction traces were collected using a scan step of 0.020° in between 2θ values of 20–120°. Texture was determined in accordance with the inverse pole figure technique [14]. The reported peak-broadening values, β, were corrected for instrumental broadening.

3. Experimental results

Fig. 1 shows the amount of nitrogen incorporated into the growing film during reactive sputtering as a function

of nitrogen flow, f_{N_2} , as analysed by SNMS. Up to $f_{N_2} = 50$ sccm an almost linear increase in nitrogen content was observed. Stoichiometric β-Cr₂N is obtained at $f_{N_2} = 50$ sccm. Beyond this flow rate an asymptotic approach to stoichiometric CrN was observed. However, none of the films analysed by SNMS showed a fully stoichiometric composition.

For all samples SNMS depth profile analysis has been carried out in parallel. Fig. 2 shows a typical SNMS profile diagram for an almost stoichiometric Cr₂N hard coating. This documents that the N profile in growth direction of the coating was extremely uniform, thus giving rise to the assumption that the mechanical properties of the coating should not vary through the coating. The compositions of the coatings in atomic % are given in Table 2.

Fig. 3 shows the hardness of the deposited coating as a function of the nitrogen flow f_{N_2} . In the non-reactive mode a hardness of 800 HV was observed. This value increased rapidly and almost linearly to 2200 HV with increasing flow of N₂. The maximum value was followed by a decline to 1550 HV at a flow rate of 50 sccm. Further increases in the nitrogen flow lead to a value of 1750 HV at a flow rate of 100 sccm. A gentle minimum has been found for the coating roughness R_z at the maximum hardness value. Values as low as R_z = 0.2 μm have been found in the range $f_{N_2} = 25$ –50 sccm (Fig. 3).

The results of the HR_c-DB judgement and the critical load values are plotted in Fig. 4. At low N₂ flow rates a sharp decrease of L_c and a considerable increase of HR_c-DB judgement was observed. At a N₂ flow rate of 30 sccm the HR_c-DB value reached a maximum (classification 4) and L_c a minimum (L_c = 25 N) indicating reduced adhesion in this parameter range. At N₂ flow rates beyond 50 sccm the HR_c-DB and L_c values were consistently low and fairly high, respectively, showing superior adhesion independent of the N₂ flow rate.

X-ray diffraction analysis of five coatings produced with varying N₂ flow rates are summarised in Fig. 5(a–e). In addition to peaks originating from the coatings, substrate peaks (labelled "S" in Fig. 5(a–e)) were also identified. Measured values of interplanar spacings, d_{hkl} , and their deviation from bulk standard values (JCPDS), Δd_{hkl} , obtained from the XRD results in Fig. 5(a–e), are given in Table 2. Full width at half maximum (FWHM) peak broadening, β_{hkl} and texture coefficient, T^* (%), are included in Table 3 and Table 4, respectively. No information regarding the differences in interplanar spacing, peak broadening or texture could be determined from the XRD data for the $f_{N_2} = 30$ sccm due to broad and overlapping peaks for Cr–N and β-Cr₂N phases. In the range from zero nitrogen flow to $f_{N_2} = 25$ sccm a single phase bcc Cr was observed. With no nitrogen flow very sharp diffraction peaks corresponding to the bcc structure of bulk Cr with a (200) preferred orientation were observed. The positions of

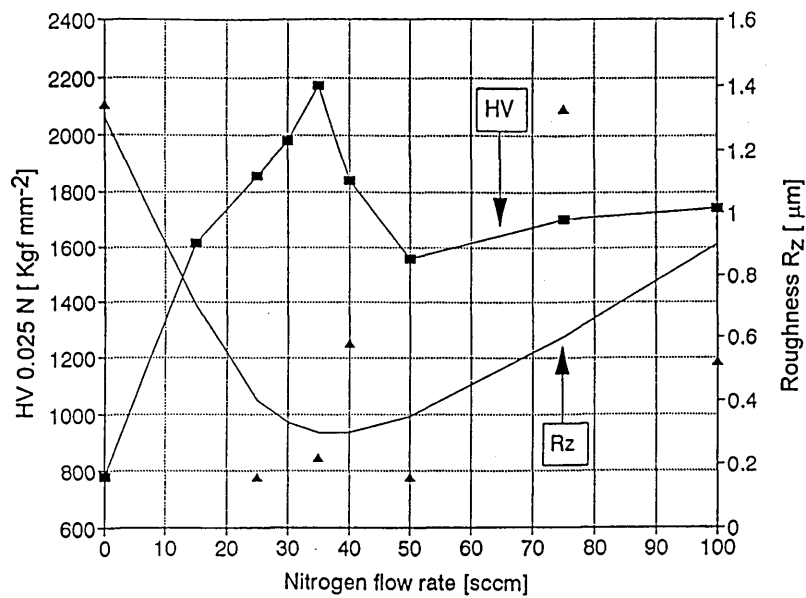


Fig. 3. Influence of nitrogen flow rate on the Vickers hardness (0.025 N) and surface roughness, R_z , at a negative bias voltage of -100 V.

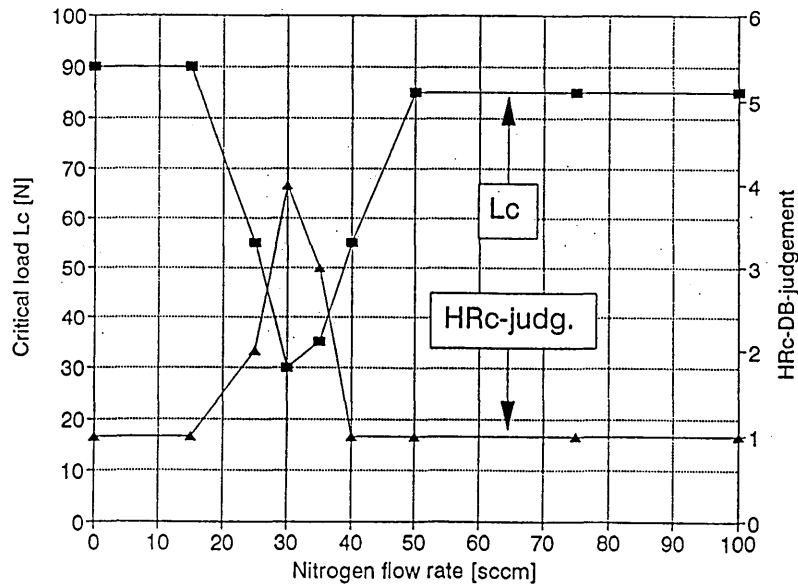


Fig. 4. Influence of nitrogen flow rate on the HR_c-DB judgement and critical load, L_c , at a negative bias voltage of -100 V.

the (hkl) reflections from Cr corresponded almost exactly with those of the JCPDS data. With increasing nitrogen flow rate the X-ray diffraction peaks showed an increase in peak broadening, β and interplanar spacing. For the (110) orientation an increase in Δd of 0.69% was observed compared with that of the bulk standard value ($f_{N_2} = 15$ sccm). The peak broadening value for the $\beta_{(110)}$ increased from 0.07 ($^{\circ}2\theta$) for $f_{N_2} = 0$ to 1.47 ($^{\circ}2\theta$) for $f_{N_2} = 15$. This gradual increase in interplanar spacing and peak broadening, β , of the metallic Cr-N phase is characteristic of reactive sputtering, due to nitrogen incorporation in the growing lattice, up to the formation of nitride phases (Tables 2 and 3).

Between $f_{N_2} = 25$ and $f_{N_2} = 35$ the metallic Cr-N phase was gradually replaced by the hexagonal close packed (hcp) β -Cr₂N nitride phase and at $f_{N_2} = 30$ sccm the structure consisted of a mixture of bcc Cr and (hcp) β -Cr₂N. A single phase β -Cr₂N coating was formed at $f_{N_2} = 35$ sccm. In this coating the peaks were broad with $\beta_{(11.1)}$ of 1.48 ($^{\circ}2\theta$) with "d-spacings" smaller than those of bulk standard β -Cr₂N, i.e., $\Delta d_{(11.1)} = -0.94\%$. This would indicate a highly stressed and understoichiometric β -Cr₂N coating. At a $f_{N_2} = 50$ sccm a single phase β -Cr₂N pattern with sharp peaks was observed. As the nitrogen flow rate was increased from 35 to 50 sccm the interplanar spacings of the β -Cr₂N phase increased to

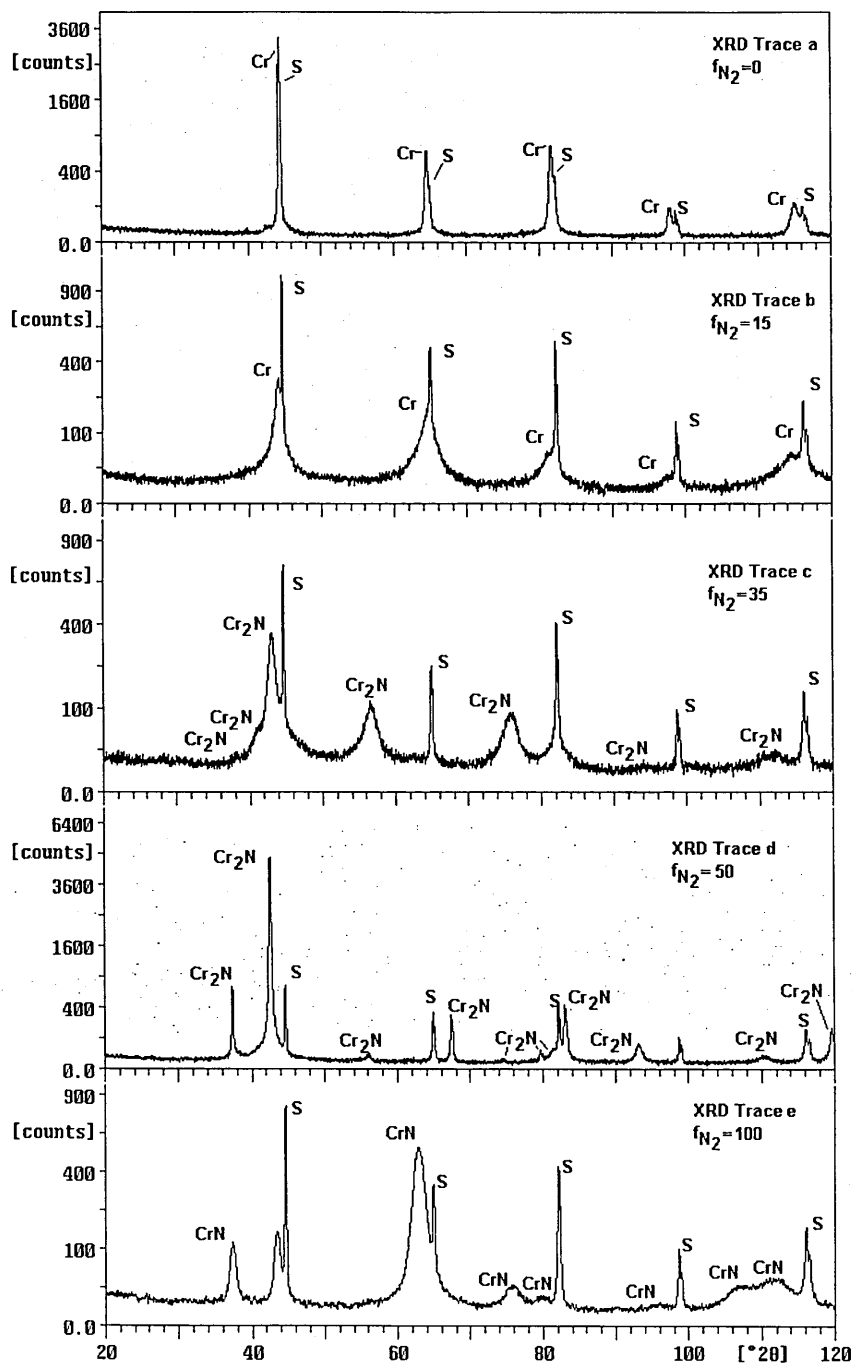


Fig. 5. X-ray diffraction diagrams from coatings deposited at (a) $f_{N_2} = 0$ sccm, (b) $f_{N_2} = 15$ sccm, (c) $f_{N_2} = 35$ sccm, (d) $f_{N_2} = 50$ sccm and (e) $f_{N_2} = 100$ sccm with a negative bias voltage of -100 V.

those of the bulk standard data (Table 2). With increasing nitrogen flow rate the texture of the β - Cr_2N phase changed from a strong (223) preferred orientation ($T^* \% 61.25$) at $f_{N_2} = 35$ to much weaker (11.1) preferred orientation ($T^* \% 26.9$) at $f_{N_2} = 50$. At nitrogen flow rates of 75 and 100 sccm the β - Cr_2N phase was not present and was replaced by CrN phase with its well-known fcc structure. The CrN coatings were characterised by rather broad X-ray diffraction peaks, $\beta_{(220)}$ 1.56 and 1.66 ($^{\circ}2\theta$)

with a strong (220) preferred orientation, $T^* \% 79$ and 67.1 for $f_{N_2} = 75$ and $f_{N_2} = 100$ respectively. The interplanar spacing of the CrN phase was larger than that of the bulk standard value and increased with increasing flow rate. Typical $\Delta d_{(111)}$ values of 0.25 and 0.53% at nitrogen flow rates of 75 and 100 sccm, respectively.

The corresponding SEM micrographs of fracture cross-sections are shown in Fig. 6(a–e). For films deposited at low nitrogen flow rate, morphology (Fig. 6(a, b)),

Table 3

f_{N_2} (sccm)	X-ray diffraction peak broadening (FWHM)								
	Cr			Cr ₂ N			CrN		
	$\beta_{(110)}$ ($^{\circ}2\theta$)	$\beta_{(200)}$ ($^{\circ}2\theta$)	$\beta_{(211)}$ ($^{\circ}2\theta$)	$\beta_{(11.1)}$ ($^{\circ}2\theta$)	$\beta_{(11.2)}$ ($^{\circ}2\theta$)	$\beta_{(22.2)}$ ($^{\circ}2\theta$)	$\beta_{(111)}$ ($^{\circ}2\theta$)	$\beta_{(200)}$ ($^{\circ}2\theta$)	$\beta_{(220)}$ ($^{\circ}2\theta$)
0	0.07	0.19	0.31						
15	1.47	2.39	2.29						
25	4.02	4.07	6.09						
30	-	-	-	-	-	-	-	-	-
35				1.48	1.84	3.84			
40				0.29	0.80	0.81			
50				0.28	0.46	0.69			
75							0.84	0.75	1.53
100							0.71	0.77	1.66

Table 4

f_{N_2} (sccm)	Texture parameter T^* (%)															
	Cr				Cr ₂ N						CrN					
	(110)	(200)	(211)	(310)	(11.0)	(11.1)	(22.1)	(22.3)	(31.3)	(41.1)	(111)	(200)	(220)	(311)	(331)	(420)
0	17	37	32	15												
15	11	65	11	12												
25	18	37	30	17												
30	-	-	-	-	-	-	-	-	-	-	-	-	-	-	-	-
35					0	4	0	10	61	0						
40					2	16	3	51	0	20						
50					15	27	18	6	0	20						
75											7	8	79	4	0	0
100											4	10	67	4	8	7

was characterised by a dense columnar structure. As the β -Cr₂N phase developed the fracture surfaces appeared to be almost featureless corresponding to very fine pore free structures (Fig. 6(c,d)). The CrN phases, Fig. 6(e), again showed dense columnar structures.

4. Discussion and conclusions

Using the unbalanced magnetron in the closed field mode CrN_x coatings may be grown with hardness values between 1500 and near 2200 HV. The maximum hardness of 2200 HV is correlated to an understoichiometric β -Cr₂N phase deposited at a flow rate of 35 sccm. The negative Δd values confirm the assumption of nitrogen deficiency. The stoichiometric β -Cr₂N phase deposited at $f_{N_2} = 50$ sccm shows a surprisingly low hardness value, only 1550 HV. The very low peak broadening and Δd values of this coating indicate a rather stress free and well crystallised film constitution. It is also interesting to note that the fracture cross-sections (Fig. 5) of coatings containing the hcp β -Cr₂N phase exhibit featureless structures. This seems to correspond to very low R_z values (about 0.3 μ m in comparison with 1.3 and 0.9 μ m, respectively, at the metallic and nitride end of the scale;

Fig. 3). However, Fig. 4 shows that the adhesion value, as described by the critical load L_c and by the HR_c-DB judgement, has a distinct minimum with L_c as low as 25 N and HR_c-DB as high as "4". These low adhesion values have been correlated to high internal stresses of these substoichiometric hcp β -Cr₂N phases.

The drawback of poor adhesion may be overcome by using the ABS technique. Pre-etching the samples with 1200 eV Cr⁺ ions prior to the UBM film deposition of the substoichiometric coatings leads to a substantial improvement of the adhesion problem. Fig. 7 documents for the special case of $f_{N_2} = 30$ sccm samples an increase of the L_c from 25 to 60 N and a decrease of the HR_c-DB value from "4" to "1" when a 20-min Cr⁺ ion bombardment is performed in comparison to an inert Ar⁺ ion etching step. The extrapolated curves show a dramatic change when compared with the UBM case (dotted lines). It should be pointed out here also that the crystallographic structure of the UBM deposited film and the coating produced in the ABS mode is completely identical. That means that there exist comparable stress conditions in both coating variants. Fig. 8 shows finally two micrographs of HR_c indentation patterns comparing the benefits of the Cr ion pre-treatment with respect to an Ar⁺ ion etch.

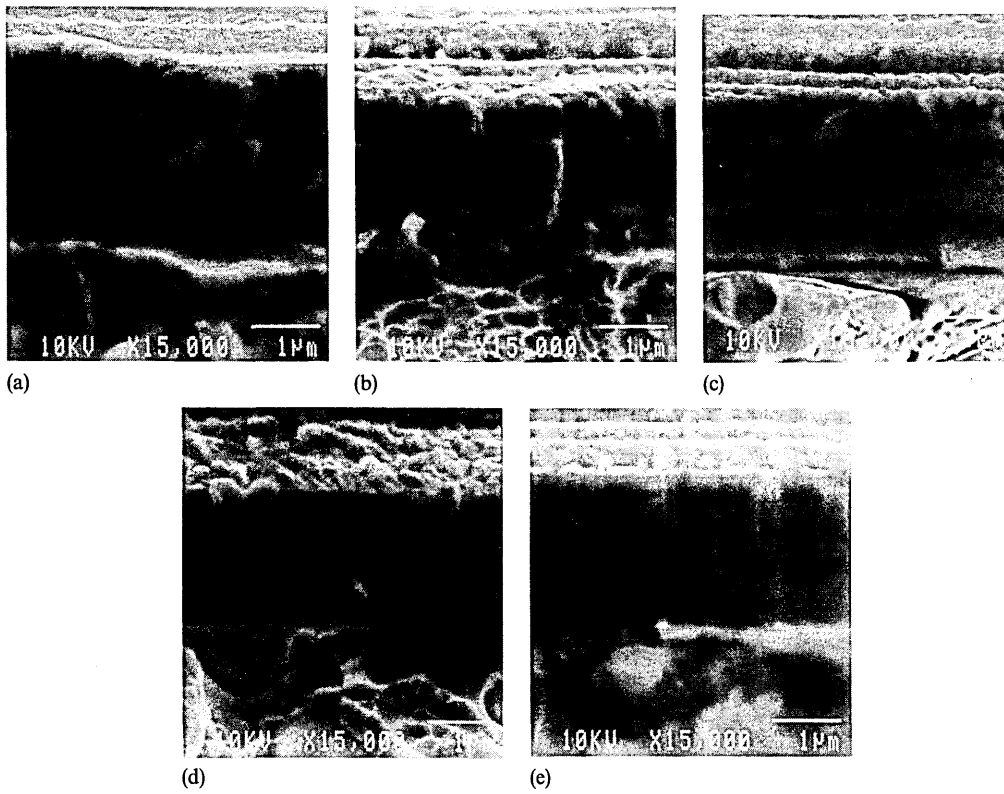


Fig. 6. Scanning electron micrographs showing fracture cross-sections from coatings deposited at (a) $f_{N_2} = 0$ sccm, (b) $f_{N_2} = 15$ sccm, (c) $f_{N_2} = 35$ sccm, (d) $f_{N_2} = 50$ sccm and (e) $f_{N_2} = 100$ sccm with a negative bias voltage of -100 V.

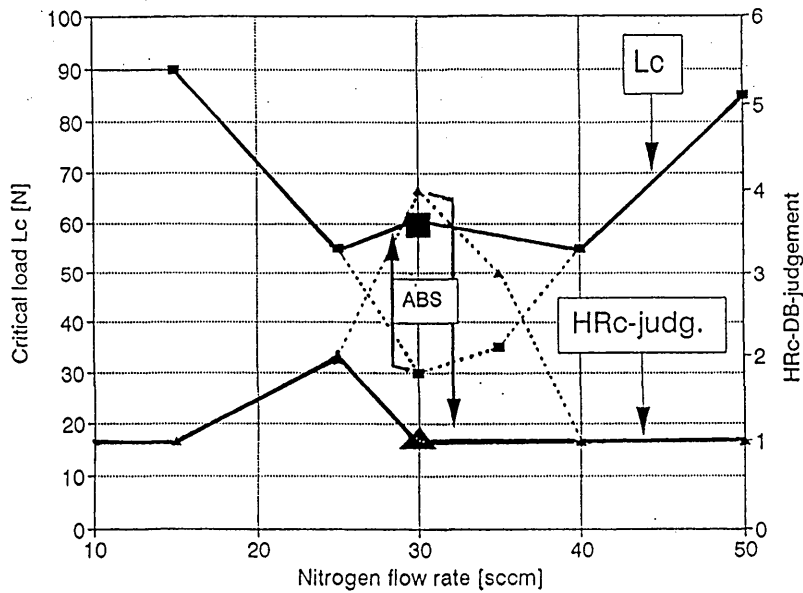
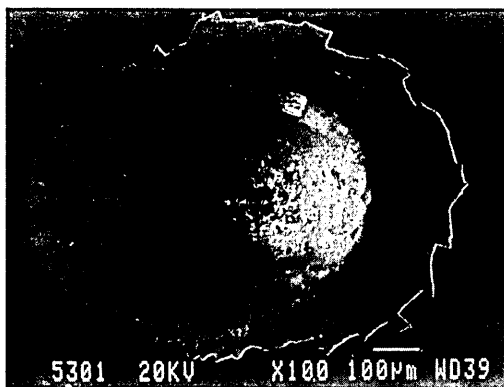


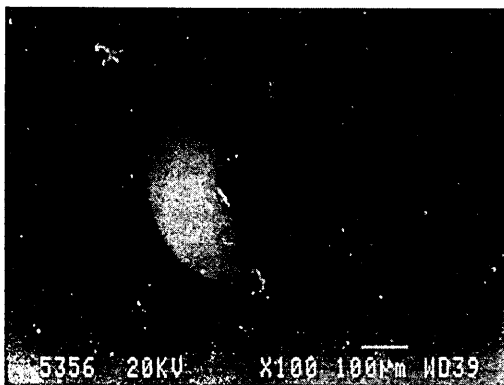
Fig. 7. Influence of using a Cr^+ ion-etching pre-treatment, ABS (solid line) instead of an Ar^+ ion-etching pre-treatment, UBM (dashed line) on the HRc-DB judgement and critical load, L_c for a coating deposited at $f_{N_2} = 30$ sccm.

The results discussed in this paper are restricted to the description of the physical properties of the coatings. Additional tribological investigations have to be carried

out to analyse the potential of the differently composed coatings with respect to wear, friction, and oxidation. In particular it is interesting to know whether the special



(a)



(b)

Fig. 8. Scanning electron micrographs comparing the HR_c indentation patterns with (a) an Ar⁺ etch only and (b) with a Cr⁺ ion pre-treatment.

positive properties (fine microstructure) of the sub-stoichiometric β -Cr₂N phase may be exploited with benefit in engineering operations.

Acknowledgement

A major part of the work has been carried out under the Exploratory Award granted by the Commission of the European Communities (Contract Number: BRST-CT95-0119).

Particular thanks are due to Drs. H. Kheyrandish and A. Brown at Mats UK Liverpool for producing the SNMS results and to Mr W.v. Ijzendor-Hauzer Techno Coating Europe BV, 5900 AE Venlo, The Netherlands, who contributed the mechanical test results.

References

- [1] A. Aubert, R. Gillet, A. Gaucher and J.P. Terrat, *Thin Solid Films*, 108 (1983) 165.
- [2] O. Knotek, W. Bosch, M. Atzor, W.-D. Münz, D. Hoffman and J. Göbel, *High Temp.-High Press.*, 18 (1986) 435.
- [3] W.-D. Münz and J. Göbel, *Surf. Eng.*, 3 (1) (1987) 47
- [4] P. Ballhause, B. Hensel, A. Rost, A. Schüssler, *Mater. Sci. Eng.*, A163 (1993) 193.
- [5] W. Herr, B. Matthes, E. Broszeit, M. Meyer and R. Suchentrunk, *Surf. Coat. Technol.*, 57 (1993) 77.
- [6] B. Navinšek, P. Panjan and A. Cvelba, *Surf. Coat. Technol.*, 74-75 (1995) 155.
- [7] O. Knotek, F. Löffler and H.-J. Scholl, *Surf. Coat. Technol.*, 45 (1991) 53.
- [8] R. Gählin, M. Bromark, P. Hedenqvist, S. Hogmark and G. Håkansson, *Surf. Coat. Technol.*, 76-77 (1995) 174.
- [9] D.D. Wang and T. Oki, *Thin Solid Films*, 185 (1990) 219.
- [10] H. Schulz and E. Bergmann, *Surf. Coat. Technol.*, 50 (1991) 53.
- [11] W.-D. Münz, D. Schulze and F. Hauzer, *Surf. Coat. Technol.*, 50 (1992) 169.
- [12] W.-D. Münz, K. Vannisselroy, R. Tietema, T. Hurkmans and G. Keiren, *Surf. Coat. Technol.*, 58 (1993) 205.
- [13] VDI-Richtlinie 3198, Düsseldorf, Germany, 1992.
- [14] D.S. Rickerby, A.M. Jones and B.A. Bellamy, *Surf. Coat. Technol.*, 37 (1989) 111.



Influence of ion bombardment on structure and properties of unbalanced magnetron grown CrN_x coatings [☆]

T. Hurkmans ^{a,*}, D.B. Lewis ^b, H. Paritong ^b, J.S. Brooks ^b, W.D. Münz ^b

^a *Hauzer Techno Coating Europe B.V., PO Box 226, 5900 AE Venlo, The Netherlands*

^b *Materials Research Institute, Sheffield Hallam University, Pond Street, City Campus, Sheffield, South Yorkshire S1 1WB, UK*

Received 1 May 1998; received in revised form 15 January 1999; accepted 19 January 1999

Abstract

The structures and properties of reactive unbalanced magnetron sputtered CrN_x can be influenced by variation of the substrate bias voltage and substrate bias current density. At floating potential ($U_f = -25$ V) the lattice parameter coincides with that of the bulk value for CrN and the compressive stress approaches almost 0 GPa. Increasing the negative bias voltage to -200 V results in a steep increase of the lattice parameter together with an observed increase in the intrinsic stress to $1 \text{ GPa } \mu\text{m}^{-1}$ at $U_b = -200$ V. In parallel a change in the texture was observed. At bias voltages below $U_b = -50$ V the (111) orientation is dominating, whereas at higher bias voltages (220) becomes the major texture.

Increasing the bias current density leads also to an increase in the lattice parameter and internal stress from zero at a bias current density of 0.9 mA cm^{-2} to $1.1 \text{ GPa } \mu\text{m}^{-1}$ at a bias current density of 4.4 mA cm^{-2} . Increasing ion bombardment densifies the coatings as can be observed from the hardness increase of HV2120 at 0.9 mA cm^{-2} to HV2440 at 4.4 mA cm^{-2} at a bias voltage level of $U_b = -100$ V. The ion energy (bias voltage) obviously influences the hardness more than does the ion flux (bias current density): At $U_b = 0$ V a hardness value of HV1300 was observed in contrast to HV2200 at $U_b = -200$ V. In parallel the composition declines to lower nitrogen contents with increasing bias voltage levels, but is more or less independent of the bias current density. © 1999 Elsevier Science S.A. All rights reserved.

Keywords: CrN_x films; Ion bombardment; Magnetron sputtering; PVD

1. Introduction

Under well-controlled reactive unbalanced magnetron sputtering conditions CrN_x coatings can be reproducibly deposited as Cr, Cr+N, Cr_2N , and CrN phases and mixtures of Cr+N and Cr_2N as a function of the nitrogen content [1]. Experiments and results outlined in this paper are to be seen as a direct continuation of work reported in Ref. [1]. There the influence of the nitrogen gas flow during reactive unbalanced magnetron sputtering on the nitrogen content of CrN_x , texture, hardness, adhesion (critical load and HR-c indentation), and morphology has been described. It has been shown that depending on the nitrogen flow Cr, Cr+N, Cr+N+ Cr_2N , Cr_2N +CrN, and CrN phases can be

identified, whilst using a constant ion bombardment energy of 100 eV and a typical bias ion current density of approx. 2 mA cm^{-2} during the growth process at a substrate temperature of 250°C .

In the present paper the influence of the bias voltage and the bias current density on the growth of nearly stoichiometric CrN_x at 250°C substrate temperature is investigated. The morphology is related to the Messiers structure zone model [2]. Mechanical properties and the microstructure are compared with results published by other researchers in the field of CrN coatings [3,4].

2. Experimental details

All coatings have been deposited again in a ABS[®] coating machine HTC-625-Multilab, fabricated by Hauzer Techno Coating Europe B.V., Venlo, The Netherlands [5]. The most important deposition parameters are summarised in Table 1. The magnetic field of the two magnetrons was enhanced by using two

[☆] Paper presented at the 25th International Conference on Metallurgical Coatings, April 26–May 1, 1998, San Diego, CA, USA.

* Corresponding author. Tel.: +31 77355 9222;

fax: +31 77354 5854.

E-mail address: thurkmans@hauzer.nl (T. Hurkmans)

Table 1.
Overview of PVD process settings for CrN_x

CrN _x deposition parameters (UBM); 2-fold planetary rotation
(1) Pump down and radiation heating: Time = 60 min Controlled temperature = 200°C Base pressure 1×10^{-3} Pa
(2) Argon ion etch: Time = 20 min Controlled temperature = 240°C D.c. bias voltage = -800 V D.c. target voltage = -150 V Argon pressure = 1 Pa
(3) Closed field unbalanced magnetron sputtering: Time = set to deposit 3 μm Controlled temperature = 250°C Cr target d.c. power = 5 kW Argon flow rate = 160 sccm Nitrogen flow rate = 100 sccm D.c. bias voltage = varied between 0 and -200 V Coil current = varied between 0 and 40 A
(4) Cooling down and venting

concentric electromagnetic coils (closed field [5]). This arrangement allows an exactly continuous control of the bias current density in the range of approx. 1–5 mA cm⁻². Test samples were fabricated from austenitic stainless steel (AISI 304) and high speed steel (HSS : M2). The substrate surface was polished to a surface roughness $R_a \approx 0.01$ μm. Thin circular substrates (annealed stainless steel, %30 × 0.5 mm) were used to measure residual stresses in accordance with the deflection method [6].

The microstructure of the coatings was analysed by SEM, XRD (monochromatic Cu Kα, Bragg Bretano geometry), and the composition determined by SNMS (secondary neutral mass spectroscopy). Further experimental details are given in Ref. [1]. Corrosion tests were carried out by dynamic polarisation measurement from -800 mV (versus SCE) to +900 mV (versus SCE) in 3% NaCl solution open to air (scan rate: 0.5 mV s⁻¹) [7].

3. Results and discussion

Figs. 1 and 2 outline the behaviour of process and machine specific parameters which are influenced by the bias voltage and the coil current, respectively. The coils are used in order to change the degree of unbalancing of the magnetrons and thereby the degree of ionisation [5,8–10]. It is clearly shown that the deposition rate decreases while increasing the bias voltage. This is a well known effect [11], also for CrN_x [4], and may be correlated with an increase of resputtering of the deposited film due to an increase of the dissipated bias power on the surface of the substrate. It is also shown that the total bias current is considerably increased. Interesting to note is that the nitrogen content of the as-deposited films is reduced by increasing the bias voltage. Obviously

it is a result of preferred resputtering of N as the lightest element in the condensed material. The results of Fig. 2 suggest that this must be an impact-controlled effect as the nitrogen content does not change with the coil current when the dependent bias current is increased from 0.35 to 1.7 A and the number of bombarding ions is therefore dramatically increased.

The marginal influence of the increased number of bombarding ions (coil current) on the composition of the coating might be explained by the fact that N₂ and N are preferably ionised having a ionisation potential lower than that of Ar (15.58, 14.53, and 15.76 eV, respectively). Therefore, the increase in the number of bombarding ions may be mainly correlated to a preferred increase in the number of N₂⁺ ions. As N₂⁺ ions are subjected to the reaction N₂⁺ → N⁺ + N⁰ when they hit the substrate surface, the effective 'resputter rate' will be lower than with the heavier Ar⁺ owing to the considerably lower sputter yield of the much lighter N⁺ ion. In addition, the preferred 'resputter effect' of condensed N will be compensated for by the high reactivity of the impinging N⁺ ions. The oxygen content stayed below 1 at.% within the experiments.

Finally fig. 2 shows the calibration of the coil current scale in units of bias current density. This calibration has been achieved by Langmuir probe measurements and reflects the wide range of ionisation which can be produced in the HTC-625-Multilab ABS® PVD system. In the following results only the bias current density will be used as second coating process parameter besides the bias voltage.

SEM fracture cross-section images show the influence of bias voltage and bias current density on the morphology, the densification, and the surface roughness of 3 μm CrN_x films. Fig. 3a–d confirms Messier's structure zone model [2], exhibiting open dendritic film growth at low bias voltages and dense structures at higher ones. It also shows a smoothing effect on the surface caused by the increased ion bombardment and 'resputter effects'. Finally, Fig. 3d shows an almost structureless fracture cross-section and a very smooth coating surface for CrN_x at a bias voltage of $U_b = -200$ V. Fig. 3e and f indicates that high ion current densities also contribute to a smoothing of the film surface at a moderate bias voltage level of $U_b = -100$ V as has been demonstrated elsewhere for TiN [12].

Fig. 4 outlines that the crystallographic structure of the CrN_x coatings is strongly affected by the bias voltage. The only phase present was CrN with the well-known B1 NaCl-type fcc structure. Films grown at $U_b = 0$ V exhibit a preferred (111) orientation [3], characterised by a sharp diffraction peak. The negative deviation from the lattice parameter and the interplanar spacings as compared to the JCPDS reference values for CrN would indicate a residual tensile stress (Table 2), which is typical for dendritic film growth [13] and shown by SEM

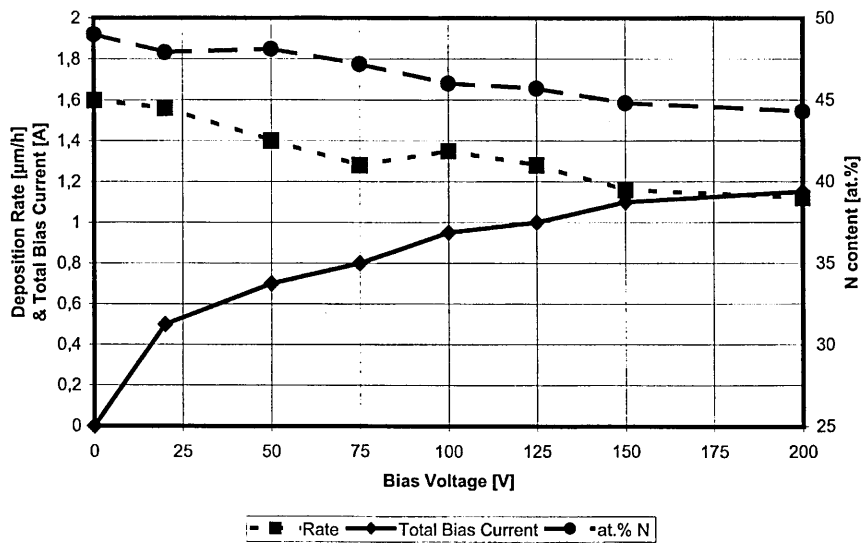


Fig. 1. Influence of bias voltage on deposition rate, nitrogen content, and bias current at a coil current of 12 A.

image Fig. 3a. Increasing the bias voltage leads to a change to positive deviation values of interplanar spacing and lattice parameter indicating the change from residual tensile to compressive stresses. In parallel, a general increase of the peak broadening is observed, indicating increased stress and decrease of grain size [3]. The texture parameter T^* listed in Table 2 confirms the change from (111) to (220) preferred orientation [3]. The results stemming from the variation of the coil current and herewith the bias current density (Table 3) complete the view which one might infer from the SEM images and the influence of the bias voltage. Enhancing the ion bombardment at a constant bias voltage of $U_b = -100$ V leads to an increase in the interplanar spacings and the lattice parameter. Accordingly the

texture parameters indicate a transformation from (111) to (220) orientation when the bias current density is increased from 0.9 to 3 mA cm^{-2} . However, at a bias current density of 4.4 mA cm^{-2} an almost randomly oriented structure is observed.

Figs. 5 and 6 outline the influence of bias voltage and bias current density on the mechanical properties of the CrN_x coatings. As can be expected from the SEM and XRD data both hardness and residual stress in the coatings increase with increasing bias voltage. Similar tendencies are published for CrN [3], TiN [13–16], NbN [17], TiAlN [15], and HfN [16]. The open structure at $U_b = 0$ V leads to low hardness values ($\text{HV}_{0.025} 1300$) and to stress values that are so low that they were very difficult to evaluate exactly enough by the deflection

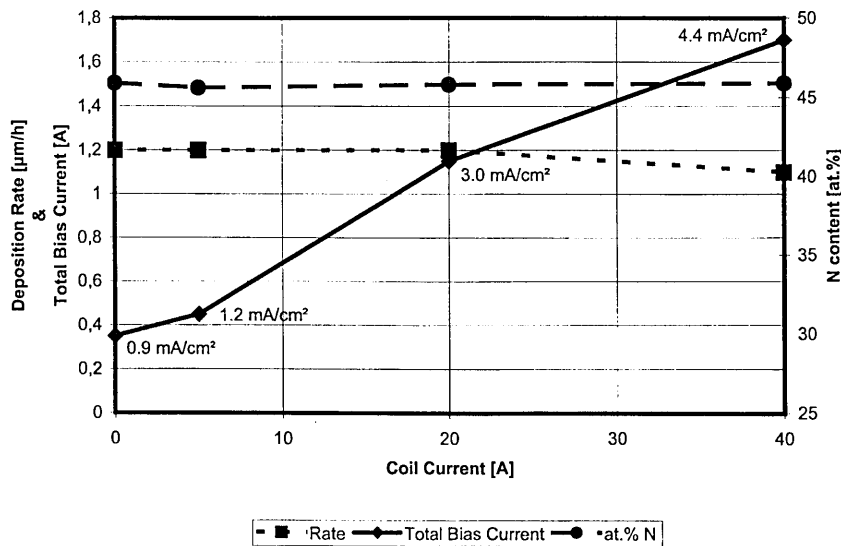


Fig. 2. Influence of coil current on deposition rate, nitrogen content, and bias current (density) at a bias voltage of -100 V.

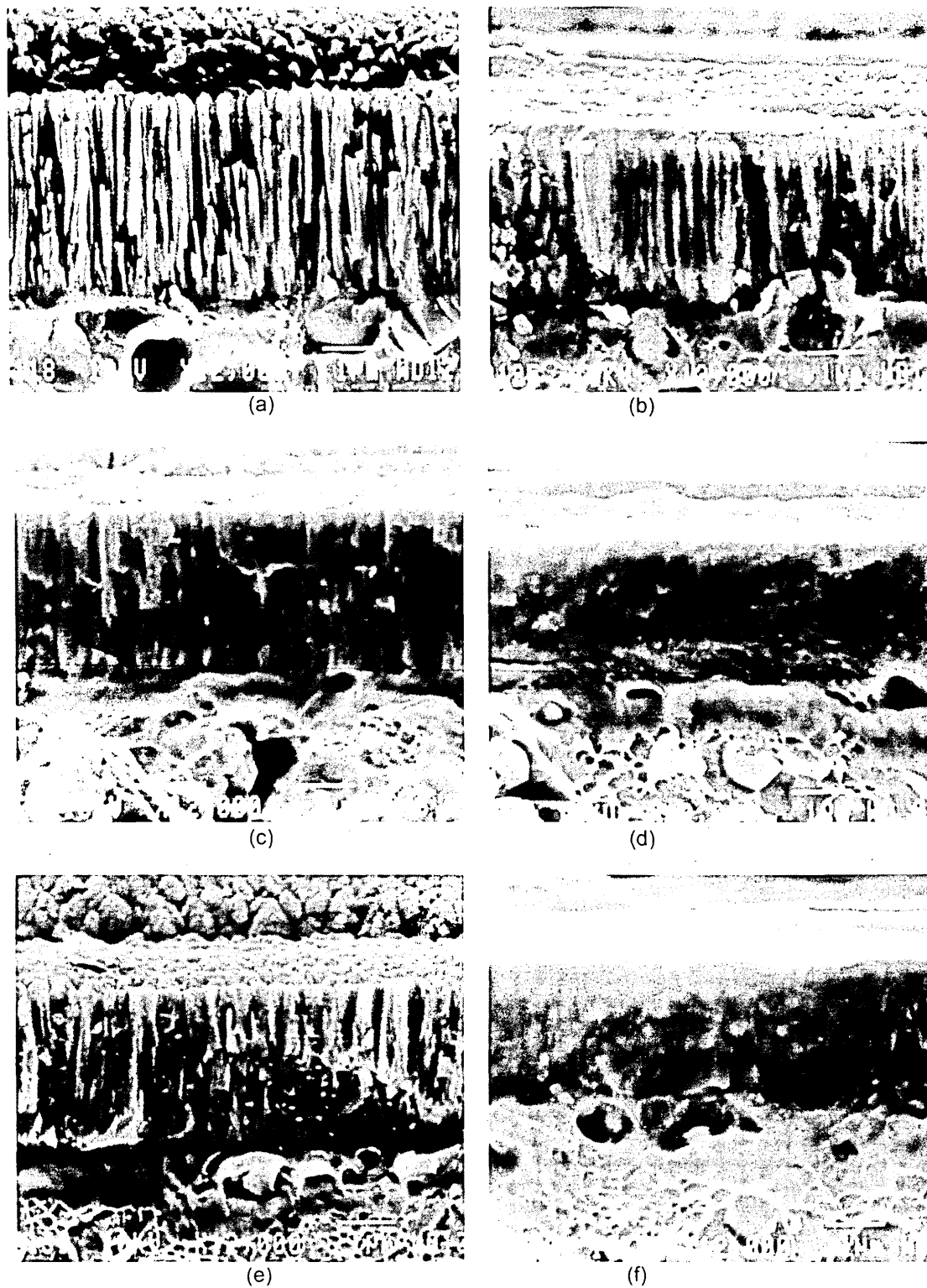


Fig. 3. Scanning electron micrographs showing fracture cross-sections from CrN_x coatings deposited at (a) $U_b=0\text{ V}/I_{\text{coil}}=12\text{ A}$, (b) $U_b=-50\text{ V}/I_{\text{coil}}=12\text{ A}$, (c) $U_b=-100\text{ V}/I_{\text{coil}}=12\text{ A}$, (d) $U_b=-200\text{ V}/I_{\text{coil}}=12\text{ A}$, (e) $U_b=-100\text{ V}/I_{\text{coil}}=0\text{ A}$ and (f) $U_b=-100\text{ V}/I_{\text{coil}}=40\text{ A}$.

method in the tensile regime (Table 2, $U_b=0\text{ V}$ and $U_b=-20\text{ V}$). The stress values in Fig. 5 were normalised to $1\text{ }\mu\text{m}$ film thickness and plotted as 'growing stress'. However, total compressive stresses in this level

(3.5 GPa) may still be considered as moderate. The critical load values L_c lie in the entire bias voltage range at a fairly high level, namely beyond $L_c=60\text{ N}$. However, in the range of U_b from -50 to -75 V , where

Table 3
Influence of coil current on X-ray data at bias voltage of -100 V

Coil current (A)	Interplanar spacing (Å)			Lattice parameter (Å)	Peak broadening 2θ (FWHM)			Texture parameter T* (%)						
	$d_{(111)} \Delta d$	$d_{(200)} \Delta d$	$d_{(220)} \Delta d$		$\beta_{(111)}$	$\beta_{(200)}$	$\beta_{(220)}$	{111}	{200}	{220}	{311}	{331}	{420}	
Ref. JCPDS	2.394	2.068	1.463	4.1465										
0	2.407 0.53%	2.089 0.99%	1.473 0.655	4.157	0.54	0.65	0.92	47.7	6.1	26.8	7.3	5.5	6.6	
5	2.406 0.52%	2.083 0.72%	1.475 0.81%	4.159	0.64	0.75	1.42	5.2	16.2	45.5	12.6	6.8	13.8	
20	2.428 1.41%	2.068 0.90%	1.492 1.95%	4.185	1.07	1.06	1.91	3.0	4.4	80.0	1.0	6.6	5.0	
40	2.435 1.73%	2.091 1.10%	1.495 2.19%	4.202	0.86	0.98	1.18	13.8	20.3	21.0	13.5	9.3	22.1	

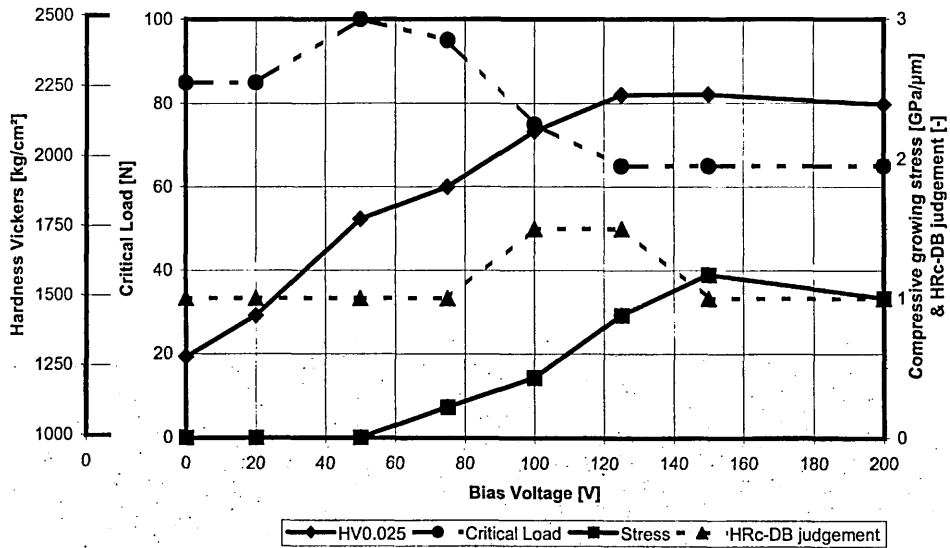


Fig. 5. Influence of bias voltage on the Vickers hardness (25 gf load), internal stress, critical load, and HRc-DB judgement at coil current of 12 A.

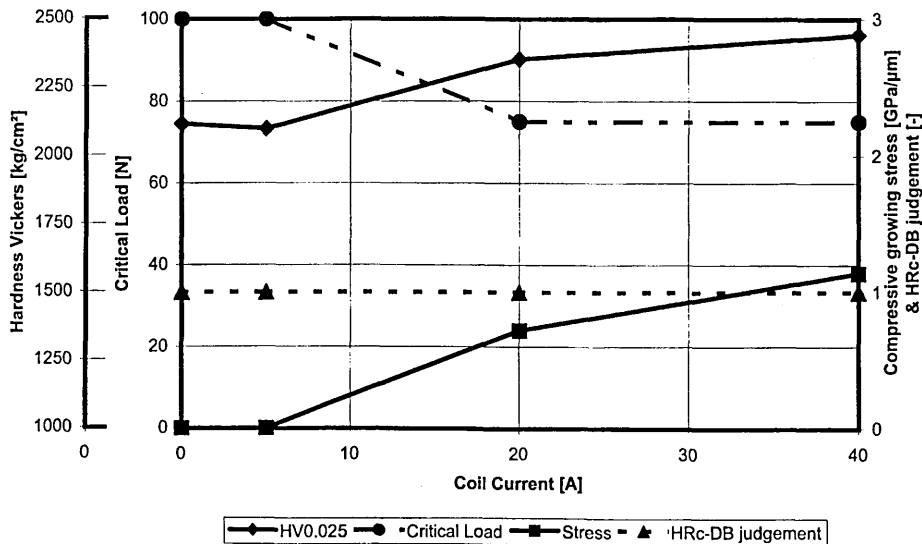


Fig. 6. Influence of coil current on the Vickers hardness (25 gf load), internal stress, critical load, and HRc-DB judgement at a Bias voltage of -100 V.

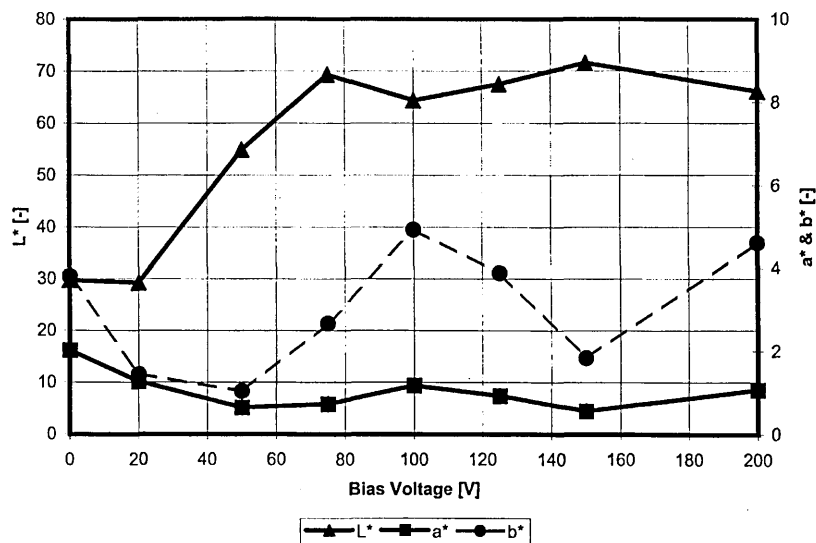


Fig. 7. Influence of bias voltage on colour values L^* , a^* , and b^* at a coil current of 12 A.

by PVD is a possible candidate to replace hard chromium in many applications, but 25 μm of CrN is still not economically feasible in most cases.

All coatings were tested on 304 stainless steel substrates. The corrosion resistance of the hard chromium coating is clearly superior to that of the CrN_x films. The hard chromium film shows a very similar behaviour to that of bulk chromium and exhibits passivation over a range of about 1100 mV. At a potential of +750 mV an increase in anodic current density indicates the transpassive dissolution of the passive oxide film. Passivation can also be observed for the two CrN coatings produced

with $U_b=0$ and -100 V. In both cases the onset of pitting, i.e. localised breakdown of the passive oxide layer occurs at +50 mV, which is indicated by the increase in anodic current. However, the corrosion performance of the coating at $U_b=-100$ V is clearly better than that for $U_b=0$ V, which is evident from the lower current densities in the passive region as well as in the transpassive region. This performance may be attributed to the porous structure of the coating in the unbiased condition (Fig. 3). With regard to the poor corrosion behaviour of the highly biased sample we can only speculate at this time: Because of the enhanced compressive stress microcracks will obviously exist within the coating. These cracks, however, are not visible in the SEM micrographs.

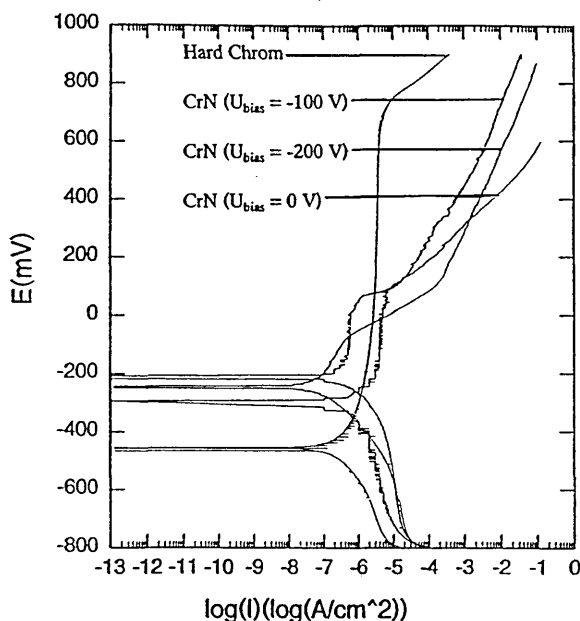


Fig. 8. Corrosion performance of approx. 3 μm CrN_x produced at $U_b=0$, -100 and -200 V compared with that of approx. 25 μm hard chromium.

4. Conclusions

CrN_x ($0.88 < x < 0.98$) coating properties are strongly affected by the state of ion bombardment during film growth. Both ion energy (by bias voltage) and number of ions (by ion current density, via coil current) are playing a role with respect to the coating composition and the microstructure. At relatively low energy levels of ion bombardment the NaCl-type coating tends to be (111) oriented, having low residual stresses, low hardness, and open columnar structure. High levels of ion bombardment show a strong (220) preferred orientation, higher residual compressive stresses, higher hardness values, and dense, smooth coatings. Adhesion results were satisfactory over the complete parameter range.

Finally, it has to be acknowledged that the corrosion performance of 3 μm CrN_x films, under the conditions described in this paper, are still inferior to that of 25 μm hard chromium.

Acknowledgements

Particular thanks are due to Dr. H. Kheyrandish of Mats UK, Liverpool for the SNMS results and Mr. T. Trinh and Mr. W. van Ijzendoorn of Hauzer Techno Coating Europe B.V. Venlo for their assistance in preparing samples and mechanical coating evaluations.

References

- [1] T. Hurkmans, D.B. Lewis, J.S. Brooks, W.D. Münz, Surf. Coat. Technol. 86 (87) (1996) 192–199.
- [2] R. Messier, A.P. Giri, R.A. Roy, J. Vac. Sci. Technol. A 2 (2) (1984) 500–503.
- [3] C. Gautier, H. Moussaoui, F. Elstner, J. Machet, Surf. Coat. Technol. 86–87 (1996) 254–262.
- [4] G. Berg, C. Friedrich, E. Broszeit, C. Berger, Surf. Coat. Technol. 86–87 (1996) 184–191.
- [5] W.-D. Münz, K. Vannisselroy, R. Tietema, T. Hurkmans, G. Keiren, Surf. Coat. Technol. 58 (1993) 205–212.
- [6] ASM Handbook, Surface Engineering Vol. 5 (1994).
- [7] D.A. Jones, Principles and Prevention of Corrosion, MacMillan, New York, 1992.
- [8] S. Kadlec, J. Musil, W.-D. Münz, G. Håkansson, J.-E. Sundgren, Surf. Coat. Technol. 39–40 (1989) 487–497.
- [9] B. Window, Surf. Coat. Technol. 71 (1995) 93–97.
- [10] M. Zlatanovic, R. Belosevac, A. Kunosic, Surf. Coat. Technol. 90 (1997) 143–149.
- [11] R.F. Bunshah, Deposition Technologies for Films and Coatings, Noyes Publications, Park Ridge, NJ, 1982.
- [12] L. Hultman, W.-D. Münz, J. Musil, S. Kadlec, I. Petrov, J.E. Greene, J. Vac. Sci. Technol. A 9 (3) (1991) 434–438.
- [13] J. Musil, S. Kadlec, V. Valvoda, R. Kuzel Jr., R. Cerney, Surf. Coat. Technol. 43–44 (1990) 259–269.
- [14] D.S. Rickerby, S.J. Bull, Surf. Coat. Technol. 39–40 (1989) 315–328.
- [15] H. Oettel, R. Wiedemann, S. Preissler, Surf. Coat. Technol. 74–75 (1995) 273–278.
- [16] C. Friedrich, G. Berg, E. Broszeit, K.-H. Kloos, Surf. Coat. Technol. 74–75 (1995) 279–285.
- [17] M.S. Wong, W.D. Sproul, X. Chu, S.A. Barnett, J. Vac. Sci. Technol. A 11 (4) (1993) 1528–1533.

Perspective for Replacement of Hard Chrome by PVD

T. Hurkmans, J. Kubinski, T. Trinh, W. Fleischer and G.J. van der Kolk,
Hauzer Techno Coating, The Netherlands

Key Words: Chrome replacement

Diamond-like carbon

ABSTRACT

In recent years hard chromium has been replaced for specific applications with PVD films that provide equivalent or superior performance. Unlike hard chrome, PVD hard chrome replacements can be tailored specifically to the application. Coatings of CrN and variants such as CrCN exhibit properties that meet or exceed the chrome they replace, and offer additional properties, such as reduced coefficient of friction. The family of coatings known as Metal containing Diamond Like Carbon (Me-DLC, also known as Me-C:H) exhibits properties of diamond like carbon, providing outstanding wear protection, toughness and low coefficients of friction. A survey of some proven replacement applications and physical characteristics will be given.

INTRODUCTION

Hard chromium is widely used in many applications. Hard chromium possesses a few characteristic properties like relatively high hardness, good corrosion resistance and a self levelling effect. Combinations of these properties have lead to use in applications where the conditions require high hardness, low friction, low wear and corrosion resistance. Hard chromium is found in a wide range of applications like hydraulic parts for aerospace, automotive and off-shore. Anti wear properties of hard chromium are used in applications such as coating of piston rings, and in the textile industry.

Physical Vapour Deposition (PVD) is a technology that has numerous applications. Well known are conducting metallic layers on semi-conductors, reflecting Al layers on CD's, selectively transmitting layers on flat glass, and ceramic wear resistant layers on professional tools. In the last few years another group of coatings is being applied industrially as well: the anti-wear PVD coating. In principle the PVD coating method has the flexibility to tune the coating properties by changing composition, creating multilayers, adjusting the mechanical properties, and influencing the microstructure. Given the flexibility of adjusting coating properties, it is possible to engineer specific coating properties that perform better than hard chromium.

Costs of PVD coatings have been high relative to hard chromium, but in many cases are now substantially decreasing.

As the cost of hard chromium increases, the applications where PVD can be competitively applied will increase as well.

In this paper a brief survey will be given of the present PVD coatings and a number of applications where they are used now. Furthermore an overview will be given of what is expected in the next five years both in coating development, as well as in equipment development.

OVERVIEW OF PRESENT PVD COATINGS

In table 1 an overview is given of PVD coatings, presently used in various applications. TiN is also shown, as it is the most frequently applied PVD coating for tools.

A number of properties are shown. Not shown is adhesion. Adhesion between coating and substrate is vital for a proper coating performance. As adhesion of the hard layers to the substrate is relatively low, adhesion interlayers like pure PVD chromium can be used. Additionally, proper adhesion relies on proper substrate cleaning and proper substrate etching processes. Another important parameter to coating performance is internal stress. Intrinsic to PVD grown coatings is internal stress which may cause adhesive flaking. As the coating layer grows, high internal stresses are generated which limit the thickness of the coating. Table 2 indicates achievable practical thicknesses.

CrN

Chromium Nitride is widely used as an anti-wear coating. Though having generally higher coefficients of friction than hard chromium, a great advantages of CrN is that the internal stresses are very low. Coatings with thicknesses of over 40 μm are routinely used in automotive applications.

DLC and Metal Containing DLC

Diamond Like Carbon offers a broad potential, as it combines very high hardness with a low friction coefficient. Unfortunately, one of the major shortcomings is, that the pure DLC has a very high internal stress, thereby limiting its thickness to about 1 μm . Another disadvantage is that pure DLC coatings show low electrical conductivity.

However, DLC coatings become viable when the coating chemistry is enhanced when low concentrations of elements

Table 1. Industrially applied PVD anti-wear coatings

	CrN	Me-C:H	a-C (pure DLC)	MoS ₂	TiN
Deposition temperature (°C)	150 - 300	150 - 250	150 - 500	150 - 250	150 - 450
Hardness (HV 0.05)	1200 - 2200	800 - 2200	3000 - 7000	300 - 600	2000 - 2500
Internal stress (Gpa/ m)	0.1 - 1	0.1 - 1.5	2 - 6	0.1 - 1	1 - 2
Thickness (µm)	1 - 50	1 - 5	1 - 2	1 - 10	1 - 6
Friction coefficient	0.4 - 0.6	0.1 - 0.2	0.02 - 0.1	0.1 - 0.2	0.5 - 0.7
Maximum temperature (°C)	750	350	450	400	450
Abrasive wear	-	+	+++	++	-
Adhesive wear	-	+++	+++	-	-
Corrosion	+++	+	+++	+	+
Practical problems	low	low	adhesive flaking	low shear	
Industrial experience	+++	+++	-	+	+++

other than Carbon are added. Examples are pure metals (1), carbide forming metals (2,3), (indicated with Me-C:H) and other carbide forming elements like Silicon (4) and Boron(5).

In principle nanostructures are formed by addition of between 5 and 15 atomic percent of carbide forming elements. Small carbide islands exist in a Carbon matrix. The hardness is considerably less than of pure DLC, but other properties like internal friction and elasticity are greatly improved. These factors improve fatigue life of the coatings.

MoS₂

Molybdenum Disulfide has well known tribological properties. A major draw back of pure MoS₂ is that the shear stress is relatively low. Coatings of pure MoS₂ are used in combination with other coatings like TiAlN to produce specific sliding wear properties (6).

TiN

Titanium Nitride has been widely used since the late seventies as a replacement for hard Chromium. It has been used because it is widely available from various sources. However, based on its specific properties it is not a suitable replacement for hard Chromium.

OVERVIEW OF PRESENT PVD APPLICATIONS

Numerous applications have been introduced the last five years. An overview is given in table 2.

The main application at present is in the automotive segment. Major applications are found in the fuel injection train. The new generation of very high pressure fuel injection systems has become economically feasible by use of PVD coatings. A considerable advantage of a PVD coating is that the coating can be made relatively thin. Because coating thickness requirements are only a few µm ±10%, allowances for coating thickness are not required, and the part to be coated can be at final dimensions.

Another application to successfully take advantage of PVD coatings are shafts of the turbo compressor. Considerable growth for PVD is expected in the next few years in the automotive industry. Applications at present are mainly for high performance cars parts. This will certainly have spin-offs for the normal car production. The continuous drive for improved energy efficiency, weight reduction, noise reduction, and volume reduction are all favourable conditions for increased use of low friction PVD coatings.

An application that is growing rapidly is for punching and forming tools. The goal is to increase the lifetime of the forming tool and improve the surface quality of the final formed part. Coatings that provide hardness and reduce mechanical forces by adding a lubricative coating during forming are possible by PVD. To get both properties simultaneously, combinations of hard and soft coatings are used, mainly CrN, CrCN and Me-C:H.

Another application is in moulds, dies and extrusion forms. Initially CrN was widely used, but use is shifting to combinations of hard and soft coatings.

PVD COATING DEVELOPMENT

Coating development is focussing on several items:

- i) corrosion resistance,
- ii) reduced friction and
- iii) proper mechanical properties like elasticity and hardness.

Corrosion Performance

A target of the present PVD developments is to reach a corrosion performance identical or better than 20 µm of hard Chromium with PVD coatings at considerably lower thicknesses.

Fig. 1 shows recent results of unbalanced magnetron deposited CrN for various substrate bias voltages in comparison with 25 µm hard chromium (7).

Table 2. Overview of present and future PVD applications

Segment	Substrate	PVD Coating	Thickness	Remark
Present applications				
Automotive	Piston ring	CrN	40 μm	Routinely used by one of the largest Japanese piston ring supplier
	Drive rods	CrN	3 μm	Used for highly loaded race engines (Formula 1)
	Turbo shafts	Cr/W-C:H	3 μm	For passenger car turbo engines
	Fuel injection	Cr/W-C:H DLC	3 μm	Diesel fuel pumps Fuel injectors Applied already on over 50% of the world production
	Valve train	Cr/W-C:H	3 μm	Tappet, Camshaft Starting to be applied on large scale
	Drive train	B ₄ C Cr/W-C:H		sun gears
Various	Forming tools	CrN, CrCN	2 μm	
	Moulds, dies	CrN, CrCN and Cr-C:H	2 μm	
Future applications				
Hydraulics	Pistons	CrN based multilayers	up to 20 μm	Improved field life expectancy
Cutlery	Cutting tools	CrN based multilayers	up to 3 μm	Use expected in cutting, slitting, medical
Aeronautical	various	various		
Textile	various	CrN based multilayers	up to 10 μm	replacement of Ni/Cr

The figure demonstrates that 25 μm of hard Chromium has better corrosion resistance than thinner PVD coatings. However, by tuning the deposition parameters such as bias voltage a considerable improvement can be achieved.

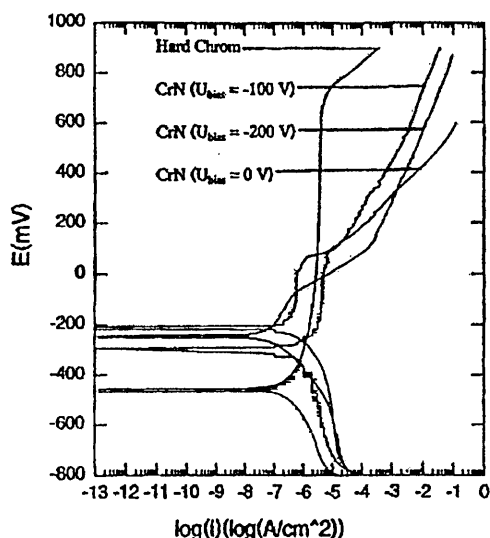


Figure 1. Corrosion performance of approx. 3 μm CrN, deposited with Bias Voltages of 0V, -100 V and -200 V, and of 25 μm hard Chromium.

Further developments are underway for multi-layers. Promising are multilayers of CrN/NbN, see e.g. Munz et al. (8). For these coatings similar corrosion resistance to hard Chromium is achieved for much smaller thicknesses.

Combinations of hard and soft coatings show a big improvement in moulding applications. In figure 2 a comparison is given between performance of plastic injection moulds coated with CrN and coated with CrN/MoS₂. The sticking forces are considerably reduced, resulting in lower ejection forces and more important better surface quality of ABS parts. The coating structure is shown in figure 3.

Further improvements are expected for multi layers. Combination layers of e.g. transition metals like Ti, Cr and W with MoS₂ have demonstrated that the low friction coefficient of MoS₂ can be attained, but that the mechanical properties like hardness, and maximum allowable shear stress and environmental stability were considerably improved, see e.g. (9).

PVD COATING EQUIPMENT DEVELOPMENTS

The development of PVD coating equipment has resulted in a number of improvements, like:

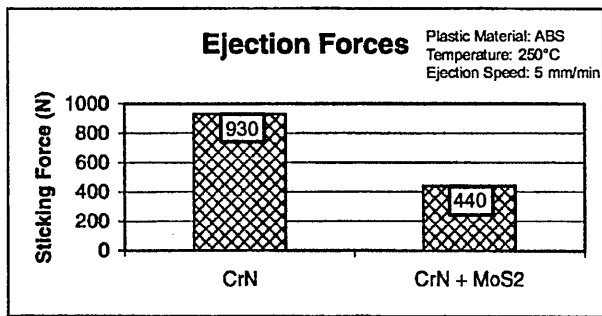


Figure 2. Sticking forces of injection moulding of ABS plastics, moulds coated with CrN and CrN + MoS₂.

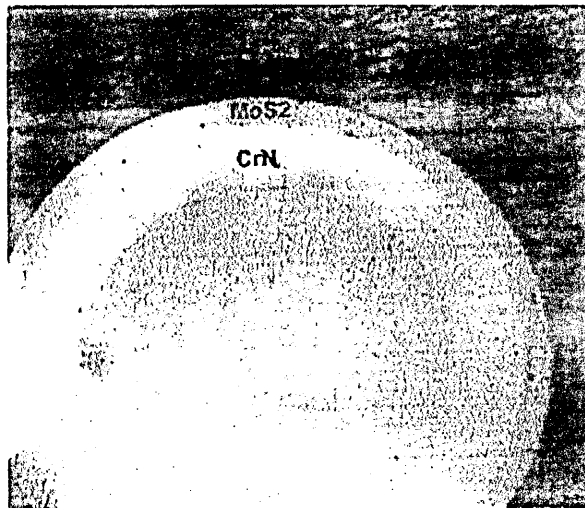


Figure 3. Ball grind cross-section by Kalo-test of CrN + MoS₂ multilayer.

- i) good equipment reliability, uptimes over 95% are routinely achieved
- ii) Reproduction of coating processes
- iii) Sophisticated multilayers with individual thicknesses of 2 nm are possible
- iv) reject levels acceptable for the automotive industry have been achieved; and
- v) PVD coating cost price has been decreased by an order of magnitude

In fig. 4 the PVD coating cost price is shown for a typical 2 µm CrN coating. For the calculations it is assumed that the coating volume fills the capacity of that one typical PVD machine. The price decrease can be attributed to a combination of matters such as: i) the availability of much larger equipment, ii) shorter cycle times, iii) utilization of large magnetron sources. The cost price can come down further, provided that product quantities are sufficiently high to fully utilize large dedicated equipment.

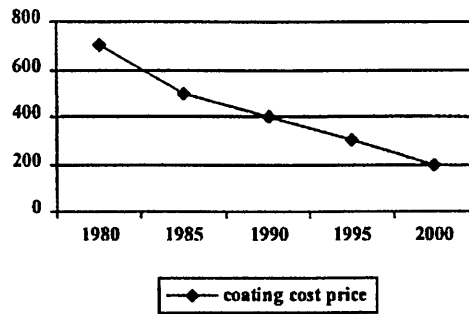


Figure 4. Indicative cost price in USD per m² of 2 µm CrN grown by unbalanced magnetron deposition.

CONCLUSIONS

Applications of PVD coating for parts traditionally coated with hard chromium is still a small activity as compared with electroplated hard chromium.

However, for specific applications requiring not only a hard and corrosion resistant surface, but also a low friction, PVD coatings are now replacing hard chromium routinely. It is expected that the coating performance will increase with a resultant decrease in the cost price. As a result, future growth is expected in applications where PVD will replace hard chromium.

REFERENCES

1. H. Biederman, P. Hlidek, J. Pesicka, D. Slavinska and V. Stundzia, *Vacuum*, 47, 1389 (1996).
2. K. Bewilogua and H. Dimigen, *Surf. Coat. Technol.*, 61, 144 (1993).
3. M. Grischke, K. Bewilogua, K. Trojan, H. Dimigen, *Surf. Coat. Technol.*, 74-75, 739 (1995).
4. V.F. Dorfman, *Thin Solid Films*, 212, 267 (1992).
5. T. Eckardt, K. Bewilogua, G.J. van der Kolk, T. Hurkmans, T. Trinh, W. Fleischer, *Proc. of ICMC 1999*.
6. E. Pfluger, A. Savan, W. Fleischer, *Proc. Of ICMC 1999*.
7. T. Hurkmans, D.B. Lewis, H. Paritong, J.S. Brooks, W.-D. Munz, *accepted by Surf. Coat. Technol.*
8. W.-D. Munz, *accepted by Surf. Coat. Technol.*
9. D.G. Teer, J. Hampshire, V. Fox, K. Laing, *Proceedings SVC*, 40, 70 (1997).

Hurkmans, Antonius P.A.
Dorpstraat 6
5862 AE Geysteren
PAYS-BAS

Datum/Date
13/12/00

en/Ref./Réf.	Anmeldung Nr./Application No./Demande n°/Patent Nr./Patent No./Brevet n°. 00122894.9-2119
holder/Applicant/Demandeur/Patentinhaber/Proprietor/Titulaire HAUZER TECHNO COATING EUROPE BV	

NENNUNG ALS ERFINDER - MITTEILUNG GEMÄSS REGEL 17(3) EPÜ

In der obenbezeichneten europäischen Patentanmeldung sind Sie als Erfinder genannt worden. Nachstehend werden Ihnen die in der Erfindernennung enthaltenen und die weiteren in Art. 128(5) EPÜ vorgesehenen Angaben mitgeteilt:

ANMELDETAG : 20.10.00
PRIORITÄT : DE/02.11.99/DE 19952549
BEZEICHNUNG : Substrate mit einer Chrom-Nitrid-Schicht
BENANNTE VERTRAGSSTAATEN: AT BE CH CY DE DK ES FI FR GB GR IE IT LI LU
MC NL PT SE

ERFINDER (VERÖFFENTLICHT = 1, NICHT VERÖFFENTLICHT = 2):
1/Hurkmans, Antonius P.A./Dorpstraat 6/5862 AE Geysteren/NL
1/Van Der Kolk, Gerrit-Jan/Hugten 14/6062 RG Maarheze/NL
1/Lewis, David Brian/5 Ratcliffe Road/Sheffield S11 8YA/GB
1/Münz, Wolf-Dieter/14 Oakland Road/Sheffield S7 1SL/GB

ERKLÄRUNG NACH ARTIKEL 81 EPÜ:
Der (Die) Anmelder hat (haben) das Recht auf das europäische Patent erlangt gemäss Vertrag vom 191099

EINGANGSSTELLE

